

Peridynamic Modelling of Thermomechanical and  
Multiphase Flow Analysis Suitable for Additive  
Manufacturing and Welding Applications

By

Bingquan Wang

*A thesis submitted in fulfilment of the requirements for the degree of*

*Doctor of Philosophy*

Department Of Naval Architecture, Ocean & Marine Engineering

University of Strathclyde, Glasgow

2025

Author statement

*This thesis is the result of the author's original research. It has been composed by the author and has not been previously submitted for examination which has led to the award of a degree.*

*The copyright of this thesis belongs to the author under the terms of the United Kingdom Copyright Acts as qualified by University of Strathclyde Regulation 3.50. Due acknowledgement must always be made of the use of any material contained in, or derived from, this thesis.*

Signed:

Date: 06/08/2025

## **Abstract**

Additive manufacturing (AM) and welding are transformative technologies extensively used across various industries due to their capability to fabricate complex, high-performance components. However, challenges such as thermal distortion, residual stresses, and defects like cracks and porosity frequently arise due to the inherent high thermal gradients and repeated thermal cycles during these processes. Traditional numerical methods, such as the Finite Element Method, often encounter difficulties in effectively addressing crack discontinuities in AM and welding processes due to their reliance on continuity assumptions in classical continuum mechanics.

This thesis has developed a peridynamics-based numerical modelling tool for simulating mechanical, thermal, thermo-mechanical, and fluid behaviours, suitable for the numerical investigation of AM and welding processes. Peridynamics, a nonlocal integral-based continuum theory, is capable of modelling discontinuities such as cracks without the need for remeshing, providing a promising alternative to conventional numerical methods.

The research includes systematic investigations into optimal horizon size (a length scale parameter determining the level of nonlocal interactions) selection criteria across different peridynamic formulations, including bond-based, ordinary state-based, and non-ordinary state-based approaches. A dual-horizon peridynamic formulation is developed and validated to effectively handle non-uniform discretisation issues, improving accuracy and computational efficiency in mechanical and thermal diffusion analyses. Furthermore, a coupled thermomechanical peridynamic model incorporating phase-change phenomena is formulated to simulate the structural deformation during welding and AM processes. To further expand peridynamic capabilities, the Peridynamic Differential Operator is utilised for modelling multiphase flow behaviours, including wetting dynamics and thermo-capillary (Marangoni) effects, which are closely related to AM and welding scenarios involving surface tension-driven fluid motion in the molten pool.

Results demonstrated that the models developed consistently produced reliable and accurate predictions of deformation, thermal diffusion characteristics, phase transitions, and multiphase flow dynamics when benchmarked against reference data.

This thesis advances peridynamic modelling capabilities for AM and welding applications by offering recommendations for horizon size selection and demonstrating the method's suitability for simulating mechanical deformation, heat conduction with phase change, and multiphase flow interactions. Overall, the work contributes to bridging fundamental peridynamic research with industrial practice, providing modelling tools and clear methodological guidelines to substantially enhance process reliability, component quality, and manufacturing efficiency.

## **Acknowledgements**

First and foremost, I would like to express my sincere gratitude to my supervisor, Professor Selda Oterkus, for her invaluable advice, constructive feedback, and constant encouragement throughout my PhD studies. Her expertise and continuous support have been fundamental to the successful completion of this thesis.

I am also deeply grateful to my co-supervisor, Professor Erkan Oterkus, whose insightful discussions, technical expertise, and practical guidance have been instrumental throughout my research journey. His perspective and advice have broadened both the quality and the scope of my work.

I would also like to thank my colleagues at the PeriDynamics Research Centre and in the Department of Naval Architecture, Ocean & Marine Engineering at the University of Strathclyde for fostering a collaborative research environment and for their valuable discussions during group meetings.

Finally, I would like to express my sincere gratitude to my family for their unconditional love, patience, and constant encouragement throughout my academic journey. Their support has been a continual source of strength and motivation at every stage of my work.

# Table of Contents

Abstract .....	I
Acknowledgements .....	III
Table of Contents .....	IV
List of Figures .....	VIII
List of Tables .....	XIV
Chapter 1 Introduction .....	1
1.1 Background and Motivations .....	1
1.2 Research Aims and Objectives .....	4
1.3 Thesis Structure .....	4
1.4 Publications Arising from this Thesis .....	6
Chapter 2 Literature Review .....	8
2.1 Introduction .....	8
2.2 Overview of Continuum Mechanics .....	8
2.3 Peridynamics: Theory and Recent Developments .....	9
2.4 Heat Source Modelling and Thermomechanical Analysis in Welding and AM .....	11
2.5 Multiphase Flow and Surface Tension Modelling .....	14
2.6 Knowledge Gaps and Thesis Contributions .....	16
Chapter 3 Methodology .....	17
3.1 Introduction .....	17
3.2 Peridynamic Theory .....	17
3.2.1 Bond-Based Peridynamics .....	19
3.2.2 Ordinary State-based Peridynamics .....	21
3.2.3 Non-ordinary State-based Peridynamics .....	23
3.3 Peridynamic Differential Operator .....	25
Chapter 4 Investigation of Horizon Size in Peridynamics .....	31
4.1 Introduction .....	31
4.2 Numerical Implementation of Peridynamic Formulations .....	31
4.2.1 Spatial Integration .....	32
4.2.2 Time Integration .....	35
4.2.3 Boundary Conditions .....	37

4.3 Numerical Investigations.....	40
4.3.1 Determination of Horizon Size .....	40
4.3.2 Vibration of a Plate .....	41
4.3.3 Plate Under Tension.....	46
4.3.4 Vibration of a Cubic Block.....	50
4.3.5 Cubic Block Under Tension .....	56
4.3.6 Comparative Results of Ordinary State-based Peridynamics, Non-ordinary State-based Peridynamics, and FEM .....	61
4.4 Chapter Summary .....	64
Chapter 5 Derivation of Dual-horizon Peridynamics Formulation.....	66
5.1 Introduction .....	66
5.2 Dual-horizon Peridynamics Formulation Based on Euler-Lagrange equation.	66
5.3 Numerical Implementation.....	70
5.4 Numerical Investigations for Dual-horizon Peridynamic Formulations .....	71
5.4.1 Plate Vibration in Nonuniform Discretization.....	71
5.4.2 Plate Under Tension in Nonuniform Discretization .....	83
5.5 Chapter Summary .....	94
Chapter 6 Thermal Diffusion Analysis by Using Dual-Horizon Peridynamics.....	96
6.1 Introduction .....	96
6.2 Peridynamic Thermal Diffusion Formulation .....	96
6.3 Dual-horizon Peridynamics for Thermal Diffusion .....	100
6.4 Thermal Diffusion Case Studies.....	102
6.4.1 Plate with Temperature and No Flux Boundary Conditions.....	102
6.4.2 Plate Under Thermal Shock with Insulated Boundaries .....	108
6.4.3 Square Plate with an Insulated Crack .....	112
6.5 Chapter Summary .....	117
Chapter 7 Thermomechanical Phase Change Peridynamic Model for Welding Analysis.....	118
7.1 Introduction .....	118
7.2 Peridynamic Thermomechanics Theory.....	119
7.2.1 Peridynamic Thermo-Mechanical Governing Equations .....	119
7.2.2 Description of Time Dependent Heat Sources .....	120
7.3 Peridynamic Thermomechanics Coupled with Phase Change .....	122

7.4 Application of Initial and Boundary Conditions .....	125
7.4.1 Temperature .....	125
7.4.2 Heat Flux.....	126
7.4.3 Time-dependent Point Heat Source .....	127
7.5 Numerical Results .....	128
7.5.1 Stefan's Solidification Problem.....	128
7.5.2 Neumann's Solidification Problem .....	132
7.5.3 Thermal Analysis for a Plate with a Moving Point Heat Source.....	135
7.5.4 Thermal Analysis for a Block with a Moving 3D Ellipsoidal Heat Source .....	138
7.5.5 Thermomechanical Analysis for a Plate with Moving 2D Gaussian Heat Source .....	141
7.6 Chapter Summary .....	146
Chapter 8 Nonlocal Modelling of Multiphase Flow Wetting and Thermo-capillary Flow by Using Peridynamic Differential Operator .....	147
8.1 Introduction .....	147
8.2 The Governing Equations of Motion for Multiphase Fluid Flow .....	148
8.2.1 Mass Conservation.....	148
8.2.2 Momentum Conservation .....	148
8.2.3 Equation of State.....	151
8.2.4 Energy Equation .....	154
8.3 PDDO Governing Equations .....	156
8.3.1 Non-local Form of Continuity Equation.....	156
8.3.2 Non-local Form of Terms in Navier-Stokes Equation.....	157
8.3.3 Thermal Model .....	166
8.4 Numerical Implementation.....	167
8.4.1 Discretized Form of Governing Equations by Using PDDO.....	168
8.4.2 Boundary Conditions .....	174
8.4.3 Time Stepping Scheme .....	176
8.4.4 Material Points Shifting Technique .....	177
8.4.5 Moving Least Square Method.....	178
8.5 Numerical Simulations .....	180
8.5.1 Droplets Deformation .....	180

8.5.2 Unit Normal Vector Correction at Triple Line Region.....	184
8.5.3 Static Contact Angle Development.....	186
8.5.4 Capillary Stress Tangential to Interface.....	189
8.5.5 Two-dimensional Droplet Migration in Thermocapillary Flow .....	193
8.6 Chapter Summary .....	199
Chapter 9 Conclusion.....	200
9.1 Achievement of Research Objectives.....	200
9.2 Significance and Implications of Research Findings .....	201
9.3 Limitations and Recommended Future Work .....	203
References .....	205

## List of Figures

Fig. 1-1 Schematic drawing of peridynamics and its discretisation. ....	3
Fig. 3-1 Peridynamic horizon and force states. ....	18
Fig. 3-2 Force states in the peridynamic framework. ....	19
Fig. 4-1 Numerical discretisation of the simulation domain and volume correction. ....	32
Fig. 4-2 Application of displacement constraints in peridynamics by introducing a fictitious region (Madenci and Oterkus, 2016). ....	38
Fig. 4-3 Application of traction boundary conditions on a surface with a normal vector in x-direction (Madenci and Oterkus, 2016). ....	39
Fig. 4-4 Square plate subjected to initial uniaxial strain condition. ....	42
Fig. 4-5 Discretisation of the square plate. ....	42
Fig. 4-6 Variation of horizontal displacement of the material point located at (0.255 m,0.255 m) by using bond-based peridynamics. ....	43
Fig. 4-7 Variation of vertical displacement of the material point located at (0.255 m,0.255 m) with time by using bond-based Peridynamics. ....	44
Fig. 4-8 Variation of horizontal displacement of the material point located at (0.255 m,0.255 m) by using ordinary state-based peridynamics. ....	44
Fig. 4-9 Variation of vertical displacement of the material point located at (0.255 m,0.255 m) with time by using ordinary state-based peridynamics. ....	45
Fig. 4-10 Variation of horizontal displacement of the material point located at (0.255 m,0.255 m) by using non-ordinary state-based peridynamics. ....	45
Fig. 4-11 Variation of vertical displacement of the material point located at (0.255 m,0.255 m) with time by using non-ordinary state-based peridynamics. ....	46
Fig. 4-12 Square plate subjected to uniaxial tension loading. ....	46
Fig. 4-13 Discretisation of the square plate. ....	47
Fig. 4-14 Horizontal displacement along (x, y=0) by using bond-based peridynamics. ....	47
Fig. 4-15 Vertical displacement along (x=0, y) by using bond-based peridynamics. ....	48
Fig. 4-16 Horizontal displacement along (x, y=0) by using ordinary state-based peridynamics. ....	48
Fig. 4-17 Vertical displacement along (x=0, y) by using ordinary state-based peridynamics. ....	49
Fig. 4-18 Horizontal displacement along (x, y=0) by using non-ordinary state-based peridynamics. .	49
Fig. 4-19 Vertical displacement along (x=0, y) by using non-ordinary state-based peridynamics. ....	50
Fig. 4-20 Three-dimensional block subjected to initial uniaxial strain condition. ....	50
Fig. 4-21 Discretisation of the block. ....	51
Fig. 4-22 Variation of horizontal displacement of the material point located at (0.0775 m, 0.0775 m, 0.0775 m) with time by using bond-based peridynamics. ....	51
Fig. 4-23 Variation of transverse displacement of the material point located at (0.0775 m, 0.0775 m, 0.0775 m) with time by using bond-based peridynamics. ....	52
Fig. 4-24 Variation of vertical displacement of the material point located at (0.0775 m, 0.0775 m, 0.0775 m) with time by using bond-based peridynamics. ....	52
Fig. 4-25 Variation of horizontal displacement of the material point located at (0.0775 m, 0.0775 m, 0.0775 m) with time by using ordinary state-based peridynamics. ....	53
Fig. 4-26 Variation of transverse displacement of the material point located at (0.0775 m, 0.0775 m, 0.0775 m) with time by using ordinary state-based peridynamics. ....	54
Fig. 4-27 Variation of vertical displacement of the material point located at (0.0775 m, 0.0775 m, 0.0775 m) with time by using ordinary state-based peridynamics. ....	54
Fig. 4-28 Variation of horizontal displacement of the material point located at (0.0775 m, 0.0775 m, 0.0775 m) with time by using non-ordinary state-based peridynamics. ....	55
Fig. 4-29 Variation of transverse displacement of the material point located at (0.0775 m, 0.0775 m, 0.0775 m) with time by using non-ordinary state-based peridynamics. ....	55
Fig. 4-30 Variation of vertical displacement of the material point located at (0.0775 m, 0.0775 m, 0.0775 m) with time by using non-ordinary state-based peridynamics. ....	56
Fig. 4-31 A three-dimensional block subjected to uniaxial tension loading. ....	57
Fig. 4-32 Discretisation of the block. ....	57

Fig. 4-33 Horizontal displacement variations along $(x, y=0, z=0)$ by using bond-based peridynamics. ....	57
Fig. 4-34 Transverse displacement variations along $(x=0, y, z=0)$ by using bond-based peridynamics. ....	58
Fig. 4-35 Vertical displacement variations along $(x=0, y=0, z)$ by using bond-based peridynamics. ...	58
Fig. 4-36 Horizontal displacement variations along $(x, y=0, z=0)$ by using ordinary state-based peridynamics.....	59
Fig. 4-37 Transverse displacement variations along $(x=0, y, z=0)$ by using ordinary state-based peridynamics.....	59
Fig. 4-38 Vertical displacement variations along $(x=0, y=0, z)$ by using ordinary state-based peridynamics.....	60
Fig. 4-39 Horizontal displacement variations along $(x, y=0, z=0)$ by using non-ordinary state-based peridynamics.....	60
Fig. 4-40 Transverse displacement variations along $(x=0, y, z=0)$ by using non-ordinary state-based peridynamics.....	61
Fig. 4-41 Vertical displacement variations along $(x=0, y=0, z)$ by using non-ordinary state-based peridynamics.....	61
Fig. 4-42 Variation of horizontal displacement of the material point located at $(0.255\text{ m}, 0.255\text{ m})$ at optimum horizon size for Ordinary State-based Peridynamics and Non-ordinary State-Based Peridynamics. ....	62
Fig. 4-43 Variation of vertical displacement of the material point located at $(0.255\text{ m}, 0.255\text{ m})$ at optimum horizon size for Ordinary State-based Peridynamics and Non-ordinary State-Based Peridynamics. ....	63
Fig. 4-44 Horizontal displacement along $(x, y=0)$ by using Ordinary State-based Peridynamics and Non-ordinary State-Based Peridynamics at their optimum horizon sizes.....	63
Fig. 4-45 Vertical displacement along $(x=0, y)$ by using Ordinary State-based Peridynamics and Non-ordinary State-Based Peridynamics at their optimum horizon sizes.....	64
Fig. 5-1 Non-uniform discretization with different horizon sizes. ....	69
Fig. 5-2 Discretisation and horizons for refined grid–coarse grid case.....	72
Fig. 5-3 Variation of horizontal displacement of the material point located at $(0.255\text{ m}, 0.255\text{ m})$ with time in bond-based formulation, locally defined horizon size. ....	73
Fig. 5-4 Variation of vertical displacement of the material point located at $(0.255\text{ m}, 0.255\text{ m})$ with time in bond-based formulation, locally defined horizon size. ....	73
Fig. 5-5 Variation of horizontal displacement of the material point located at $(0.255\text{ m}, 0.255\text{ m})$ with time in ordinary state-based formulation, locally defined horizon size. ....	74
Fig. 5-6 Variation of vertical displacement of the material point located at $(0.255\text{ m}, 0.255\text{ m})$ with time in ordinary state-based formulation, locally defined horizon size. ....	74
Fig. 5-7 Variation of horizontal displacement of the material point located at $(0.255\text{ m}, 0.255\text{ m})$ with time in non-ordinary state-based formulation, locally defined horizon size. ....	75
Fig. 5-8 Variation of vertical displacement of the material point located at $(0.255\text{ m}, 0.255\text{ m})$ with time in non-ordinary state-based formulation, locally defined horizon size. ....	76
Fig. 5-9 Discretisation and horizons for refined grid–coarse grid case.....	76
Fig. 5-10 Variation of horizontal displacement of the material point located at $(0.255\text{ m}, 0.255\text{ m})$ with time in bond-based formulation, constant horizon size. ....	77
Fig. 5-11 Variation of vertical displacement of the material point located at $(0.255\text{ m}, 0.255\text{ m})$ with time in bond-based formulation, constant horizon size. ....	78
Fig. 5-12 Comparison of horizontal displacement variation with time for the material point located at $(0.255\text{ m}, 0.255\text{ m})$ between locally defined and constant horizon size in the bond-based formulation. ....	78
Fig. 5-13 Comparison of vertical displacement variation with time for the material point located at $(0.255\text{ m}, 0.255\text{ m})$ between locally defined and constant horizon size in the bond-based formulation. ....	79
Fig. 5-14 Variation of horizontal displacement of the material point located at $(0.255\text{ m}, 0.255\text{ m})$ with time in ordinary state-based formulation, constant horizon size.....	80

Fig. 5-15 Variation of vertical displacement of the material point located at (0.255 m,0.255 m) with time in ordinary state-based formulation, constant horizon size.....	80
Fig. 5-16 Comparison of horizontal displacement variation with time for the material point located at (0.255 m,0.255 m) between locally defined and constant horizon size in the ordinary state-based formulation. ....	81
Fig. 5-17 Comparison of vertical displacement variation with time for the material point located at (0.255 m,0.255 m) between locally defined and constant horizon size in the ordinary state-based formulation. ....	81
Fig. 5-18 Variation of horizontal displacement of the material point located at (0.255 m,0.255 m) with time in non-ordinary state-based formulation, constant horizon size. ....	82
Fig. 5-19 Variation of vertical displacement of the material point located at (0.255 m,0.255 m) with time in non-ordinary state-based formulation, constant horizon size. ....	82
Fig. 5-20 Comparison of horizontal displacement variation with time for the material point located at (0.255 m,0.255 m) between locally defined and constant horizon size in the non-ordinary state-based formulation. ....	83
Fig. 5-21 Comparison of vertical displacement variation with time for the material point located at (0.255 m,0.255 m) between locally defined and constant horizon size in the non-ordinary state-based formulation. ....	83
Fig. 5-22 Variation of horizontal displacements along the central axis ( $x, y = 0$ ) in bond-based formulation, locally defined horizon size. ....	85
Fig. 5-23 Variation of vertical displacement along the central axis ( $x = 0, y$ ) in bond-based formulation, locally defined horizon size. ....	85
Fig. 5-24 Variation of horizontal displacements along the central axis ( $x, y = 0$ ) in ordinary state-based formulation, locally defined horizon size. ....	86
Fig. 5-25 Variation of vertical displacement along the central axis ( $x = 0, y$ ) in ordinary state-based formulation, locally defined horizon size. ....	86
Fig. 5-26 Variation of horizontal displacements along the central axis ( $x, y = 0$ ) in non-ordinary state-based formulation, locally defined horizon size. ....	87
Fig. 5-27 Variation of vertical displacement along the central axis ( $x = 0, y$ ) in non-ordinary state-based formulation, locally defined horizon size. ....	87
Fig. 5-28 Variation of horizontal displacements along the central axis ( $x, y = 0$ ) in bond-based formulation, constant horizon size.....	88
Fig. 5-29 Variation of vertical displacement along the central axis ( $x = 0, y$ ) in bond-based formulation, constant horizon size.....	88
Fig. 5-30 Comparison of horizontal displacements along the central axis ( $x, y = 0$ ) between locally defined and constant horizon size in the bond-based formulation.....	89
Fig. 5-31 Comparison of vertical displacements along the central axis ( $x = 0, y$ ) between locally defined and constant horizon size in the bond-based formulation.....	89
Fig. 5-32 Variation of horizontal displacements along the central axis ( $x, y = 0$ ) in ordinary state-based formulation, constant horizon size.....	90
Fig. 5-33 Variation of vertical displacement along the central axis ( $x = 0, y$ ) in ordinary state-based formulation, constant horizon size.....	90
Fig. 5-34 Comparison of horizontal displacements along the central axis ( $x, y = 0$ ) between locally defined and constant horizon size in ordinary state-based formulation.....	91
Fig. 5-35 Comparison of vertical displacements along the central axis ( $x = 0, y$ ) between locally defined and constant horizon size in ordinary state-based formulation.....	91
Fig. 5-36 Variation of horizontal displacements along the central axis ( $x, y = 0$ ) in non-ordinary state-based formulation, constant horizon size.....	92
Fig. 5-37 Variation of vertical displacement along the central axis ( $x = 0, y$ ) in non-ordinary state-based formulation, constant horizon size.....	92
Fig. 5-38 Comparison of horizontal displacements along the central axis ( $x, y = 0$ ) between locally defined and constant horizon size in non-ordinary state-based formulation.....	93
Fig. 5-39 Comparison of vertical displacements along the central axis ( $x = 0, y$ ) between locally defined and constant horizon size in non-ordinary state-based formulation.....	93

Fig. 5-40 Comparison of horizontal displacements along the central axis ( $x, y = 0$ ) between locally defined and constant horizon size in non-ordinary state-based formulation.....	94
Fig. 5-41 Comparison of vertical displacements along the central axis ( $x = 0, y$ ) between locally defined and constant horizon size in non-ordinary state-based formulation.....	94
Fig. 6-1 Material points and the horizon (Oterkus et al., 2017). .....	97
Fig. 6-2 Non-uniform discretization with different horizon sizes. ....	101
Fig. 6-3 Peridynamic model of the plate. ....	102
Fig. 6-4 Peridynamic model with uniform discretisation and identical horizon sizes. ....	104
Fig. 6-5 Temperature variations from peridynamic and FEM predictions at $y = 0$ when $k = 1, m = 1$ .....	104
Fig. 6-6 Peridynamic model with uniform discretisation but different horizon sizes.....	105
Fig. 6-7 Temperature variations from PD and FEM predictions at $y = 0$ when $k = 1, m = 2$ .....	105
Fig. 6-8 Peridynamic model with non-uniform discretisation but identical horizon sizes. ....	106
Fig. 6-9 Temperature variations from PD and FEM predictions at $y = 0$ when $k = 0.5, m = 1$ ....	106
Fig. 6-10 Peridynamic model with non-uniform discretisation but different horizon sizes. ....	107
Fig. 6-11 Temperature variations from PD and FEM predictions at $y = 0$ when $k = 0.5, m = 0.5$ . ....	108
Fig. 6-12 Peridynamic model of the plate under thermal shock loading. ....	108
Fig. 6-13 Temperature variations from PD and FEM predictions when (a) $t = 3$ s, (b) $t = 6$ s at $y = 0, k = 1, m = 1$ . ....	109
Fig. 6-14 Temperature variations from PD and FEM predictions when (a) $t = 3$ s, (b) $t = 6$ s at $y = 0, k = 1, m = 2$ . ....	110
Fig. 6-15 Temperature variations from PD and FEM predictions when (a) $t = 3$ s, (b) $t = 6$ s at $y = 0, k = 0.5, m = 1$ .....	111
Fig. 6-16 Temperature variations from PD and FEM predictions when (a) $t = 3$ s, (b) $t = 6$ s at $y = 0, k = 0.5, m = 0.5$ .....	111
Fig. 6-17 Peridynamic model of the plate with an insulated crack. ....	112
Fig. 6-18 PD model with uniform discretisation and identical horizon sizes. ....	113
Fig. 6-19 Temperature variations from PD and FEA predictions at $x = 0$ when $k = 1, m = 1$ . ....	113
Fig. 6-20 PD model with uniform discretisation and different horizon sizes. ....	114
Fig. 6-21 Temperature variations from PD and FEA predictions at $x = 0$ when $k = 1, m = 0.5$ . ....	114
Fig. 6-22 PD model with non-uniform discretisation and identical horizon sizes.....	115
Fig. 6-23 Temperature variations from PD and FEM predictions at $x = 0$ when $k = 2, m = 1$ . ....	115
Fig. 6-24 PD model with non-uniform discretisation and different horizon sizes.....	116
Fig. 6-25 Temperature variations from PD and FEM predictions at $x = 0$ when $k = 2, m = 2$ . ....	116
Fig. 7-1 Point heat source moving on the surface of a thick workpiece. ....	120
Fig. 7-2 Semi-ellipsoidal heat source model. ....	122
Fig. 7-3 Peridynamic horizon and its thermal-mechanical bonds (green line). ....	124
Fig. 7-4 Material real domain, $R_t$ and its fictitious domain, $R_c$ . ....	126
Fig. 7-5 Demonstration of implementing moving point heat source in numerical model. ....	127
Fig. 7-6 Physical illustration of Stefan's solidification problem. ....	128
Fig. 7-7 Stefan's solidification problem illustration (a) geometry and (b) peridynamic discretization. ....	129
Fig. 7-8 Temperature comparison along axial axis at ( $x, y = 0$ ). ....	131
Fig. 7-9 Temperature variation at ( $x = L/2, y = 0$ ). ....	131
Fig. 7-10 Temperature distribution at $t = 600$ s (a) peridynamic (b) FEM model. ....	132
Fig. 7-11 Temperature distribution at ( $x, y = 0$ ) at $t = 900$ s. ....	132
Fig. 7-12 Physical illustration of Neumann's solidification problem. ....	133
Fig. 7-13 Temperature comparison along ( $x, y = 0$ ) at several time intervals.....	134
Fig. 7-14 Temperature variation at $Mx = -4L/5, y = 0$ and $Nx = L/2, y = 0$ . ....	135
Fig. 7-15 Temperature distribution at $t = 600$ s (a) peridynamic (b) FEM model.....	135
Fig. 7-16 Point heat source model illustration (a) geometry and (b) peridynamic discretization.....	136
Fig. 7-17 Point heat source converted to heat generation.....	136

Fig. 7-18 Temperature variation at along $(x, y = 0)$ at $t = 4$ s.....	137
Fig. 7-19 Geometrical illustration of ellipsoidal heat source acting on a rectangular block. ....	138
Fig. 7-20 Temperature variation at $(x, y = 0, z = H2)$ at $t = 4$ s. ....	139
Fig. 7-21 Temperature distribution at $t = 4$ s (a) peridynamic (b) FEM model. ....	140
Fig. 7-22 Temperature variation at $(x, y = 0, z = H2)$ at $t = 4$ s. ....	141
Fig. 7-23 Temperature distribution at $t = 4$ s with phase change considered in peridynamic model. ....	141
Fig. 7-24 Gaussian heat source model illustration (a) geometry and (b) peridynamic discretization. ....	142
Fig. 7-25 Temperature variation along $(x, y = 0)$ at $t = 0.08$ s.....	143
Fig. 7-26 Displacement variation along $(x, y = 0)$ at $t = 0.08$ s.....	143
Fig. 7-27 Temperature field distribution at $t = 0.08$ s (a) peridynamic (b) FEM model. ....	144
Fig. 7-28 Temperature variation along $(x, y = 0)$ at $t = 0.08$ s.....	145
Fig. 7-29 Horizontal displacement variation along $(x, y = 0)$ at $t = 0.08$ s.....	145
Fig. 7-30 Horizontal displacement field at $t = 0.08$ s(a) With phase change (b) without phase change.....	146
Fig. 8-1 The transition band and unit normal vectors between two fluids. ....	150
Fig. 8-2 Two fluids come into contact at a solid surface, and the triple line region at the point of contact.....	160
Fig. 8-3 Unit normal vector $n_{lg}$ , $cor_x$ at the triple line region and ordinary computed unit normal vector $n_{lgx}$ . ....	161
Fig. 8-4 Corrected unit normal vectors distributed along the fluid interface. ....	163
Fig. 8-5 Location of material point $x_{in}$ with its family members at $t = t_n$ , and the updated location at $t = t_n + 1$ . ....	167
Fig. 8-6 Schematic drawing of interface between two fluids and the boundary material points. ....	174
Fig. 8-7 Investigation of square droplet deformation (a) geometry (b) PDDO discretisation. ....	181
Fig. 8-8 Evolution of droplet deformation at (a) $t = 0.128$ s, (b) $t = 0.384$ s, (c) $t = 0.64$ s, (d) $t =$ $1.28$ s, (e) $t = 1.92$ s, (f) $t = 2.56$ s. ....	183
Fig. 8-9 Pressure profile (a) time history of pressure difference between the droplet and surrounding fluid (b) distribution at $t = 2.56$ s. ....	183
Fig. 8-10 Demonstration of two droplets lying on a solid surface with $30^\circ$ contact angle and $90^\circ$ contact angle. ....	184
Fig. 8-11 PDDO discretisation of droplet contact on solid interface (a) $30^\circ$ contact angle (b) $90^\circ$ contact angle. ....	184
Fig. 8-12 The unit normal vectors between fluid domains before correction (a) $30^\circ$ contact angle (b) $90^\circ$ contact angle. ....	185
Fig. 8-13 The corrected unit normal vectors at triple line region (a) $30^\circ$ contact angle (b) $90^\circ$ contact angle. ....	185
Fig. 8-14 Smoothed unit normal vectors at fluid interface (a) $30^\circ$ contact angle (b) $90^\circ$ contact angle. .....	186
Fig. 8-15 Investigation of square droplet wetting on a solid surface (a) geometry of the fluid domain (b) PDDO discretisation of the simulation domain.....	187
Fig. 8-16 Evolution of liquid droplet wetting on a solid surface for various contact angles. ....	189
Fig. 8-17 Investigation of Marangoni force at the interface between two fluids (a) geometry (b) PDDO discretisation. ....	190
Fig. 8-18 Temperature distribution of the simulation domain at $t = 0.1$ s (a) PDDO (b) ANSYS. ....	191
Fig. 8-19 Marangoni force vectors distributed along the interface with $\Delta x = 9.0 \times 10^{-5}$ m. ....	192
Fig. 8-20 Volumetric Marangoni force distribution computed at interfaces of different mesh sizes using PDDO.....	193
Fig. 8-21 Comparison between the PDDO prediction and analytical solution of interfacial Marangoni force.....	193
Fig. 8-22 Thermocapillary flow migration (a) geometry (b) PDDO discretisation. ....	194
Fig. 8-23 Fluid field pressure distribution at $t = 0.12$ s. ....	196
Fig. 8-24 Migration of the droplet at (a) $t = 0.04$ s (b) $t = 0.08$ s (c) $t = 0.12$ s. ....	197
Fig. 8-25 Dimensionless velocity of the droplet migration over the dimensionless time. ....	198

Fig. 8-26 Isothermal distribution of the fluid domain at $t=0.12$ s.....	198
Fig. 8-27 Velocity profile of the thermocapillary migration of the droplet at $t=0.12$ s.....	199

## List of Tables

Table 3-1 Peridynamic parameters in different dimensions .....	22
Table 3-2 Bulk modulus and shear modulus in different dimensions.....	22
Table 4-1 Summary of optimal horizon sizes for different peridynamic formulations in 2D and 3D ..	65
Table 7-1 Temperature-dependent Young's Modulus .....	144

# **Chapter 1 Introduction**

AM and welding technology are rapidly changing the modern engineering landscape, allowing the production of complex, customised parts across a wide range of industries. However, as adoption expands, the need for robust predictive modelling tools has become vital. This chapter introduces the motivations for the research, provides background on AM, welding and peridynamic theory, outlines the research objectives, and presents an overview of the thesis structure as well as research contributions.

## **1.1 Background and Motivations**

AM, commonly known as 3D printing, incorporates a family of technologies that build three-dimensional objects directly from digital models (Wong and Hernandez, 2012). Unlike traditional subtractive manufacturing, which removes material from a pre-formed block to achieve the desired shape, AM introduces material only where it is needed. This approach allows the production of highly complex geometries, offers design freedom with minimal material waste (Adam and Zimmer, 2015). As a tool-less, data-driven production method, AM supports shorter production cycles, lower tooling costs, and greater environmental sustainability, establishing itself as a core driver of Industry 4.0 and an attractive solution across diverse industries (Adam and Javaid, 2019).

AM technologies are compatible with a wide range of materials, including polymers, metals, ceramics, and composites (Yang et al., 2019), making them applicable across diverse sectors. The aerospace (Katz-Demyanetz et al., 2019), automotive, and healthcare industries (Mohanavel et al., 2021) have adopted AM for producing highly customised, lightweight, or geometrically intricate components, revolutionising both product development and supply chain strategies. Although oil & gas and maritime applications initially comprised only a small fraction of the global AM market (Bikas et al., 2016), the technology's maturity is now prompting a steady expansion into these fields.

Within the marine industry, challenges such as lengthy lead times for spare parts, complex logistics, and high inventory costs have made AM more attractive. Recent developments have shown an industry shift towards decentralised and on-demand manufacturing, with 3D-printed spare parts now being produced for ships, and yachts.

For example, pilot projects in the U.S. Navy, the deployment of a metal 3D printer aboard the USS Essex, have demonstrated the value of producing components directly onboard, which increases operational efficiency and reduces dependence on external supply chains (Strieby, 2024). In addition, the creation of the world's first 3D-printed propeller demonstrates the transformative potential of AM in marine manufacturing, showcasing new possibilities in design innovation (Taşdemir and Nohut, 2021). Nevertheless, the widespread industrial adoption of AM is constrained by technical challenges. High thermal gradients and repeated heating-cooling cycles, inherent in metal AM processes, contribute to the development of residual stresses, cracks, and porosity, defects that can compromise the integrity and reliability of components in safety-critical applications (Abdulhameed et al., 2019; Brennan et al., 2021).

Alongside the rise of AM, welding continues to play a foundational role in manufacturing, serving as an essential technology for joining metals and alloys in industries such as shipbuilding, construction, energy, and automotive engineering. Welding processes, including arc welding, laser welding, and electron beam welding, are inherently characterised by localised, intense heating and rapid solidification, leading to complex thermal cycles and steep temperature gradients (Shravan et al., 2021). Notably, the distinction between AM and welding is increasingly blurred by the development of hybrid processes such as Wire Arc Additive Manufacturing and Laser Metal Deposition, which leverage welding-based energy sources to build components layer by layer (Paskual et al., 2018; Rumman et al., 2019). In both conventional and hybrid approaches, the resulting thermal history and the risk of defects such as cracks or porosity can have a direct impact on the service life and structural integrity of ship hulls and pressure vessels (Gannon, 2011).

To address these challenges, researchers and engineers have employed a combination of experimental and numerical methodologies, each offering advantages and limitations. Experimental methods provide empirical data for understanding defect formation, validating process parameters (Chen et al., 2019; Sola and Nouri, 2019; Brennan, 2021) but can be time-consuming. In response, numerical modelling has become popular, allowing researchers and engineers to virtually investigate thermal histories, stress evolution, material flow, and defect development under varied processing conditions. Finite element analysis (FEA) and computational fluid

dynamics (CFD) are the most common simulation tools that allow the systematic exploration of process-structure-performance relationships without extensive physical experiments (Vastola et al., 2016; Yang et al., 2016; Schoinochoritis et al., 2017; Luo and Zhao, 2018; ).

However, traditional numerical approaches like FEA encounter challenges when simulating cracks. Classical Finite Element Method (FEM) is built upon differential equations that assume continuity across elements, making it difficult to accurately capture crack initiation and propagation without extensive remeshing or specialised enrichment techniques (Anderson, 2016), motivating the research for more robust computational frameworks.

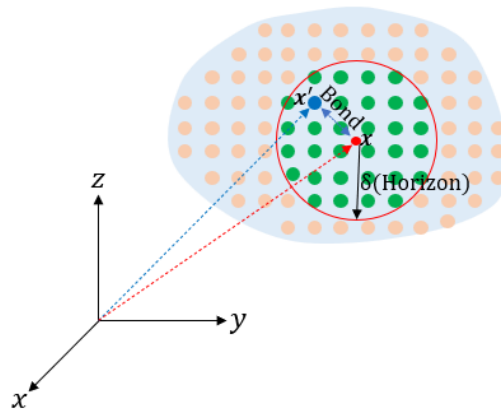


*Fig. 1-1 Schematic drawing of peridynamics and its discretisation.*

To overcome these limitations, peridynamics, a nonlocal, integral-based, continuum theory, has emerged as a promising alternative (Silling, 2000). In peridynamics, the simulation domain is discretised into a series of material points. As shown in Fig. 1-1, peridynamics represents the material response, i.e., the interaction between a material point at  $\mathbf{x}$  and its surrounding material points at  $\mathbf{x}'$  within a finite distance named the horizon  $\delta$ . The “bonds” connecting material points deform as the structure is loaded, and a bond-breaking criterion (e.g., critical stretch) naturally controls crack initiation and propagation (Silling and Askari, 2005; Foster et al., 2011). As adjacent bonds fail, microcracks form and merge into macrocracks, enabling the simulation of complex crack patterns and failure modes (Silling and Askari, 2005). The meshless nature of peridynamics is ideally suited for studying complex geometries in AM and welding processes, making it a promising tool in advanced predictive modelling.

## **1.2 Research Aims and Objectives**

Accordingly, the primary aim of this thesis is to advance and validate peridynamic modelling tools, which are suitable for numerical investigation of AM and welding processes. This research specifically focuses on improving simulation tools to handle deformation, thermal diffusion, phase transformations, and multiphase flow behaviour, which are areas where traditional modelling methods face limitations. To achieve this aim, the following objectives have been established:

- To investigate the influence of horizon size in peridynamics and provide optimal selection guidelines for achieving accurate and efficient numerical simulations.
- To develop and implement a peridynamic formulation with variable horizon sizes and non-uniform discretisation, thereby reducing numerical simulation time while maintaining accuracy.
- To extend and validate the dual horizon peridynamic formulation for heat transfer analysis, addressing the challenges of non-uniform discretisation in thermal diffusion problems.
- To develop and validate a coupled thermomechanical peridynamic model incorporating phase change, thereby supporting predictive simulation of deformation during AM and welding processes.
- To extend the peridynamic modelling framework to simulate multiphase flow using a non-local differential operator, thereby improving the analysis of complex interfacial behaviours relevant AM and welding.

## **1.3 Thesis Structure**

This thesis is organised into nine chapters, each addressing a specific aspect of peridynamic modelling techniques for AM and welding processes. The structure is as follows.

Chapter 1 introduces the research by outlining the motivation, context, and significance of the study. It articulates the research aims and objectives and presents an overview of the thesis structure.

Chapter 2 provides a comprehensive literature review, tracing the evolution of continuum mechanics approaches from classical to nonlocal methods. It discusses

recent advances in peridynamics for mechanical, thermal, and multiphysics modelling, and identifies current challenges.

Chapter 3 details the methodology adopted in this work, presenting the theoretical foundations of peridynamic theory and the mathematical formulations of peridynamic models.

Chapter 4 investigates the influence of horizon size on the accuracy of peridynamic models. It provides a theoretical discussion of horizon size selection and presents numerical studies to illustrate its impact on static and dynamic problems, offering guidance for effective modelling in various engineering applications.

Chapter 5 introduces the dual-horizon peridynamic formulation, which extends the peridynamic approach to accommodate non-uniform discretisation. This chapter presents the mathematical development of the dual-horizon concept and demonstrates its capability through a series of numerical examples.

Chapter 6 extends the dual horizon peridynamic framework to thermal diffusion analysis, addressing the need for accurate heat transfer modelling in non-uniform discretisation domains. The effectiveness of the method is validated through numerical case studies and benchmark simulations.

Chapter 7 develops a coupled thermomechanical peridynamic framework incorporating phase change phenomena, capturing the interactions between thermal and mechanical fields in AM and welding processes. The chapter presents the theoretical formulation, numerical implementation, and validation through simulation results.

Chapter 8 expands the peridynamic modelling framework into the fluid domain to address multiphase flow, wetting, and thermo-capillary (Marangoni) effects in AM and welding processes. It introduces the peridynamic differential operator for simulating complex interfacial phenomena and demonstrates the framework's capability through numerical examples.

Chapter 9 concludes the thesis by summarising the main findings and contributions. It discusses the limitations encountered, provides recommendations for future work, and outlines potential directions for further development of peridynamic modelling in AM.

## 1.4 Publications Arising from this Thesis

The research presented in this thesis has resulted in the following peer-reviewed publications

1. Wang, B., Oterkus, S. and Oterkus, E., 2023. Determination of horizon size in state-based peridynamics. *Continuum Mechanics and Thermodynamics*, 35(3), pp.705-728.
2. Oterkus, S., Wang, B. and Oterkus, E., 2020. Effect of horizon shape in peridynamics. *Procedia Structural Integrity*, 28, pp.418-429.
3. Wang, B., Oterkus, S. and Oterkus, E., 2020. Closed-form dispersion relationships in bond-based peridynamics. *Procedia Structural Integrity*, 28, pp.482-490.
4. Wang, B., Oterkus, S. and Oterkus, E., 2024. Closed-form wave dispersion relationships for ordinary state-based peridynamics. *Journal of Peridynamics and Nonlocal Modeling*, 6(3), pp.394-407.
5. Wang, B., Oterkus, S. and Oterkus, E., 2023. Derivation of dual-horizon state-based peridynamics formulation based on Euler–Lagrange equation. *Continuum Mechanics and Thermodynamics*, 35(3), pp.841-861.
6. Wang, B., Oterkus, S. and Oterkus, E., 2020. Thermal diffusion analysis by using dual horizon peridynamics. *Journal of Thermal Stresses*, 44(1), pp.51-74.
7. Wang, B., Oterkus, S. and Oterkus, E., 2022. Thermomechanical phase change peridynamic model for welding analysis. *Engineering Analysis with Boundary Elements*, 140, pp.371-385.
8. Wang, B., Oterkus, S. and Oterkus, E., 2024. Non-local modelling of multiphase flow wetting and thermo-capillary flow using peridynamic differential operator. *Engineering with Computers*, 40(3), pp.1967-1997.

Several chapters of this thesis are based on the work presented in the publications listed above. The relationship between each chapter and the relevant publications is as follows:

- Chapter 2: Based on [1, 2, 3, 4, 5, 6, 7, 8].
- Chapter 3: Based on [1, 2, 3, 4].
- Chapter 4: Based on [1].
- Chapter 5: Based on [5].

- Chapter 6: Based on [6].
- Chapter 7: Based on [7].
- Chapter 8: Based on [8].

Where appropriate, material from these publications has been adapted, revised, and supplemented with additional context and discussion to ensure coherence and completeness within the thesis.

## **Chapter 2 Literature Review**

### **2.1 Introduction**

The continued advancement of AM and welding processes has highlighted the need for predictive modelling frameworks to accurately capture thermomechanical behaviour, phase changes, and multiphase flow phenomena. This chapter provides a review of the evolution of continuum mechanics approaches, from classical formulations to peridynamic nonlocal integral-based methods. The literature review addresses the foundations of peridynamic theory, advances in mechanical and thermal analysis, multiphysics modelling, and recent progress in applying nonlocal methods to complex interfacial phenomena. The chapter concludes by identifying key gaps in the literature, thus motivating the research directions pursued in this thesis.

### **2.2 Overview of Continuum Mechanics**

Solid mechanics is a fundamental discipline in engineering that focuses on understanding the deformation and failure of materials and structures when subjected to external loads. Over the past two centuries, Classic Continuum Mechanics (CCM) has provided the principal theoretical framework for describing such behaviour, with various formulations developed to address different classes of problems. The most common continuum mechanics formulation was developed by Cauchy (Reddy, 2013), where the equations of motion for the objects of continuum mechanics, "material points," are expressed in the form of partial differential equations.

Owing to the complexity of most engineering problems, analytical solutions are generally restricted to idealised cases involving simple geometries, boundary conditions, and material properties. To address more engineering scenarios, numerical methods such as the FEM have been widely adopted. However, the reliance of classical formulations on spatial derivatives poses a challenge: when discontinuities exist in the domain (such as cracks or material separation), standard numerical methods become inapplicable because spatial derivatives become singularities in the presence of these discontinuities (Anderson, 2016). Consequently, traditional FEM requires supplementary techniques such as enrichment functions, adaptive mesh refinement, or remeshing to model crack propagation and material failure (Anderson, 2016). These approaches, however, can increase computational complexity and may compromise the accuracy of the simulation because the crack pattern is not naturally defined.

### **2.3 Peridynamics: Theory and Recent Developments**

As an alternative to CCM, Silling (2020) introduced the concept of peridynamics. Unlike Cauchy's continuum mechanics, where the equations of motion are formulated using spatial derivatives, peridynamics expresses these equations in an integral form that is inherently nonlocal and free from spatial derivatives (Silling and Askari, 2005). As a result, peridynamics is not subject to the limitations associated with discontinuities such as cracks.

A key difference between peridynamics and CCM is the nature of material point interactions. In CCM, a material point interacts only with its immediate neighbours; by contrast, peridynamics allows each material point to interact with all other points within a finite distance (Silling, 2000; Silling et al., 2007; Silling, 2017; Gu et al., 2018). The distance of interactions between material points is denoted as "horizon", which is a length scale parameter in peridynamics. Such a parameter does not exist in Cauchy's formulation. CCM does not have a length scale parameter. Hence, it cannot represent non-classical material behaviour which usually appears at micro-scale. "Horizon" is a fundamental concept in peridynamics, and the term "peri" in the name corresponds to "horizon" in the Greek language (Madenci and Oterkus, 2013).

Since its introduction, there has been rapid progress in peridynamics research. As a generalised continuum theory, it can be applied to a wide range of materials, including metals (Madenci and Oterkus, 2013), composites (Oterkus and Madenci, 2012), polycrystalline materials (De et al., 2016), concrete (Oterkus et al., 2012), ceramics (Guski et al., 2020), ice (Vazic et al., 2020), and graphene (Liu et al., 2018). The versatility of peridynamics extends to the simulation of complex phenomena such as fatigue (Oterkus et al., 2010), plasticity (Madenci and Oterkus, 2016), and viscoelasticity (Madenci and Oterkus, 2017). Furthermore, peridynamics has been successfully extended to address multiphysics problems, with formulations available for thermal (Oterkus et al., 2014 Gao and Oterkus, 2019), electrical (Oterkus et al., 2013), and porous flow fields (Oterkus et al., 2017).

Among the various areas where peridynamics has expanded, thermal process modelling has become an active area. There are various studies in the literature focused on peridynamic analysis of thermal diffusion. Gerstle et al. (2008) developed a 1-

dimensional multiphysics model coupling thermal diffusion, electrical, mechanical and vacancy diffusion fields to investigate the electromigration phenomenon. Bobaru and Duangpanya (2012) introduced a multidimensional bond-based peridynamic formulation for transient heat transfer analysis. Oterkus et al. (2014) developed an ordinary state-based peridynamic heat conduction equation based on Lagrangian formalism. To analyse failure prediction in electronic packages, Oterkus et al. (2014) proposed a coupled hygro-thermo-mechanical model. Xue et al. (2018) developed a state-based peridynamic formulation for heat transfer analysis by utilising the domain decomposition method. Wang et al. (2016) utilised the Green's function method to develop a peridynamic diffusion model. Liao et al. (2017) performed peridynamic simulations for heat conduction analysis of functionally gradient materials by considering cracks.

Despite these wide range of applications for peridynamics developed over the past twenty-five years, research on the fundamental length parameter, the horizon size, remains relatively limited. The current size selection in numerical simulation mainly depends on suggestions made in the influential paper written by Silling and Askari (Silling and Askari, 2005). They suggested using a horizon size equivalent to three times the grid spacing between material points based on the experiences of these researchers for their simulations. However, their conclusion was obtained based on the original peridynamic formulation, named bond-based Peridynamics (Silling, 2000). Although bond-based peridynamics is an effective approach, it has certain limitations in material properties (Madenci and Oterkus, 2017), as Poisson's ratio is not a free parameter. To overcome these limitations, advanced peridynamic formulations, such as ordinary state-based peridynamics (Silling et al., 2007) and non-ordinary state-based Peridynamics (Warren et al., 2009; Silling, 2017), were developed.

In addition to the gaps associated with horizon size selection, the implementation of peridynamic models presents further computational considerations. Closed-form solutions to peridynamic equations are generally not available; therefore, numerical methods are typically employed to obtain solutions (Madenci and Oterkus, 2013). For spatial discretization, uniform discretization scheme is widely used. However, for some problems, using uniform discretization can unnecessarily increase the computational time since only some part of the solution domain can be solved by using

fine discretization whereas other parts can be modelled by using coarse discretization. Moreover, variable horizon size can also be required to reduce the computational time or due to the nature of the problem. To overcome these concerns, Dual-horizon Peridynamics was developed by Ren et al. (2016a; 2016b) which allows both non-uniform discretization and variable horizon for mechanical analysis.

In summary, the horizon size influences the computational time significantly; it is important to determine optimum horizon sizes for ordinary state-based and non-ordinary state-based peridynamics formulations to provide a decent level of accuracy within a reasonable computational time. In addition, a Dual-horizon Peridynamics formulation specifically addressing thermal diffusion has not been available in the literature.

#### **2.4 Heat Source Modelling and Thermomechanical Analysis in Welding and AM**

Welding remains a widely utilised fabrication process in the manufacturing industry, relying on high temperatures to melt and join metallic components. The resulting thermal field not only governs the development of residual stresses but is also closely linked to the metallurgical, crystallisation, and phase transformation phenomena that occur during solidification. Building upon similar principles of localised melting and solidification, AM has emerged as a transformative production technology that enables layer-by-layer fabrication of complex components. Its unique advantages, including design freedom, customisation, and material efficiency, have led to increasing adoption across sectors such as aerospace, healthcare, and automotive. However, the widespread industrial application of AM is still limited by the lack of understanding of the underlying processes required for accurate process modelling (Tofail et al., 2018).

One of the challenges in both welding and AM is the development of reliable mathematical models, which are necessary to minimise dependence on costly and time-consuming trial-and-error procedures during process optimisation. An important aspect of these modelling approaches is the representation of the heat source, which provides a mathematical description of the fraction of input energy absorbed by the material and its spatial distribution within the heat-affected zone. In AM modelling, heat source models are employed to assess the impact of powder deposition on thermal

transport and to inform the optimisation of powder nozzle designs (Arrizubieta et al., 2014), as well as to characterise the complex interaction between the melt pool and the energy input (e.g., laser or electron beam) (Hamahmy and Deiab, 2020).

Heat source models for AM are, in most cases, adapted from approaches in the welding literature (Thompson et al., 2015). Various heat source models have been proposed in the past decades to investigate heat transfer mechanisms for welding and AM processes. The welding heat source model can be classified as a concentrated heat source, a planar distribution heat source, or a volumetric distributed heat source, which depends on different welding methods in the manufacturing process (Hamahmy and Deiab, 2020). While the part of the workpiece concerned is far away from the weld's centreline, the welding heat source can be treated as a centralised heat source model. Rosenthal (1941) stated an analytical solution of the temperature field for a semi-infinite body subjected to a constant heat source. For general arc welding, the welding arc's heat flow is distributed in a particular area on the weldment. Hence, a plane distribution of the heat source can be considered in the numerical model. Eagar and Tsai (1983) applied Rosenthal's theory to a two-dimensional heat source model and found the analytical solution of the temperature field. However, for high-energy beam welding, due to the large depth-to-width ratio of the weld, it shows that the heat flow of the welding heat source has a great influence along the thickness direction of the workpiece, and it must be treated according to a certain volumetric distributed heat source model. Goldak (1985) proposed a three-dimensional double ellipsoidal model to overcome the penetration effect due to the surface heat model, and Nguyen et al. (1999) provided the analytical solutions for the transient temperature of the three-dimensional heat source.

Moreover, due to the complexity of the heat transfer in welding and AM processes, rapid temperature change can induce residual stresses and macro-thermal deformations (Bian et al., 2019). Therefore, in the investigation of the welding manufacturing process, the thermomechanical coupling effects needs to be considered in thermal and structural fields. Goldak et al. (1984) proposed a finite element model (FEM) for welding heat sources to investigate the temperature distribution. Van Elsen et al. (2007) used a finite difference model (FDM) for moving heat sources in a semi-infinite medium. Ning et al. (2019) utilised an analytical model with a moving point heat

source in metal AM to predict the temperature field and thermal gradient. Sepe et al. (2021) developed an FEM butt welding and performed a sensitivity analysis on temperature-dependent material properties such as thermal conductivity, specific heat, Young's modulus, and thermal expansion coefficient. The results showed that temperature-dependent thermal expansion has little effect, whereas temperature-dependent Young's modulus strongly influences the displacement field.

In addition, heat transfer during welding is often accompanied by phase change. It is considered a moving boundary problem due to the undetermined moving boundary between the liquid phase and the solid phase (Jiji, 2009). Due to its non-linear characteristic, only a small number of exact solutions exist (Jiji, 2009). When a substance undergoes a phase change such as solidification, modelling of the latent heat at the solid-liquid interface is crucial in heat transfer analysis. The latent heat can be mainly handled by front-tracking methods and fixed grid methods.

Jiji Latif (2009) applied the front tracking method to explicitly track the moving phase boundary during melting or solidification, which sets an additional node at the solid-liquid interface that splits a single element that contain both solid and liquid regions. This can accurately predict the location of the moving interface and precisely handle the latent heat. However, it merely can be used for simple geometries, which restricts its application in modelling the solidification process (Hu and Argyropoulos, 1996).

The fixed-grid method treats the entire computational domain as a continuous region (Voller et al., 1990), where the Stefan condition is implicitly incorporated into the heat conduction equation. The Stefan condition represents the energy balance at the moving phase interface, so that the heat conducted to the interface is exactly equal to the energy required to melt or solidify the material at that interface (Jiji, 2009).

In fixed-grid method, the phase boundary is represented indirectly through variables such as effective heat capacity, or heat generation, thus latent heat in phase change can be applied using standard heat transfer solvers without complex interface tracking. However, when applying the effective heat capacity method to account for latent heat during phase transitions, the time step needs to be relatively small due to the effective heat capacity in the phase-change interval calculated by integrating over the temperature range. If the temperature in a control volume jumps from below the

solidus to above the liquidus in a single time step, the model will fail to capture the latent heat release during the phase change (Hu and Argyropoulos, 1996).

In summary, the accurate representation of heat source models and the incorporation of thermomechanical coupling effects are fundamental for advancing the predictive capability of welding and AM simulations. While the development of analytical and numerical approaches, such as finite element and finite difference methods, has improved our understanding of thermal fields, residual stress, and phase change phenomena, many existing models remain limited by their reliance on classical continuum mechanics and the challenges of handling complex geometries and discontinuities. This has led to growing interest in alternative modelling approaches, such as peridynamics, which offer a promising framework for addressing these limitations and capturing the complex, multiphysics behaviour intrinsic to advanced manufacturing processes.

## **2.5 Multiphase Flow and Surface Tension Modelling**

AM and welding processes involve not only heat transfer and mechanical deformation but also complex fluid flow and interfacial phenomena within the melt pool. During laser or electron beam AM, a molten pool forms where liquid metal interacts with surrounding solid and gaseous phases, creating a multiphase system. In such systems, surface tension, where the force acting along the interface between two phases, plays an important role in stabilising the melt pool and controlling its shape. Furthermore, when the characteristic length scale of the system is sufficiently small in AM, the effect of surface tension on the flow field is more prominent than the inertial effect.

When temperature gradients form across the melt pool surface, the molten metal is subjected to thermo-capillary effects. Since surface tension generally decreases with increasing temperature, a non-uniform temperature distribution along the liquid–gas interface produces a surface tension gradient (Wozniak et al., 2001). This gradient induces Marangoni forces, which act tangentially along the interface and drive fluid motion from hotter regions with lower surface tension toward cooler regions with higher surface tension (Ma and Bothe, 2011). The thermo-capillary effects strongly influence melt pool dynamics in AM and welding, affecting pool shape, microstructure evolution, and eventually the mechanical integrity of manufactured components.

Accurate simulation of these multiphase flows and interfacial phenomena is therefore important for predictive modelling in AM.

Over the past few decades, extensive research has been conducted on modelling multiphase fluid flows. Based on the Navier–Stokes equations, there are two common computational fluid dynamics methods for modelling the multiphase fluid flow motion from the nanoscale to the macroscale. The first category is Euler methods based on grids, such as the volume of fluid (VOF) method (Hirt and Nichols, 1981). Cano-Lozano et al. (2015) performed a numerical study on rising bubbles in still liquids using the VOF method to track the interface between two fluids. Hoang et al. (2013) performed numerical simulations of the contact angle and wetted surface properties using the fluid volume interface tracking method and the continuum surface force method. Ma et al. (2011) developed a numerical method for directly simulating the thermal Marangoni effect at the interface in two-phase incompressible fluids and quantitatively comparing the numerical results of liquid droplet thermal capillary migration with experimental and theoretical results. Another class of numerical methods that can be used for multiphase simulations are meshless methods (Belytschko et al., 1996). The meshless method is a particle method, such as the smoothed particle hydrodynamics method (Morris, 2000) and peridynamics method (Gao and Oterkus, 2020). Morris (2020) proposed a technique based on smooth particle hydrodynamics for simulating two-phase flow with surface tension. This method addresses problems involving fluids of similar density and viscosity. Adami et al. (2010) extended the method to higher density and viscosity ratios, using a density-weighted colour gradient formulation to reflect the asymmetric distribution of surface tension. Describing wetting phenomena, in addition to including surface tension effects at the interfaces between fluids, the interaction of fluids with solid substrates also requires the implementation of appropriate boundary conditions at the solid interface. Breinlinger et al. (2013) extended the surface tension model using additional boundary conditions to explicitly include interactions with solid walls. Moreover, if the temperature or concentration gradient vector is tangent to the interface between the two fluids, an additional force known as the Marangoni force develops. Hopp-Hirschler et al. (2018) proposed a smoothed particle hydrodynamics model of surface

tension gradient-driven thermo-capillary flow based on a continuum of surface force methods, including Marangoni forces.

As a promising meshless method, peridynamics is a new formulation of non-local continuum mechanics (Silling, 2000; Silling et al., 2017; Madenci and Oterkus, 2013). Inspired by peridynamic formulations, Peridynamic Differential Operator (PDDO) (Madenci et al., 2016) is developed to transfer the differential equations to their integral forms. Various applications of PDDO can be found in the literature (Madenci et al., 2017; Madenci et al., 2019; Dorduncu et al., 2023). Gao et al. (2019) developed a non-local Lagrangian model for Newtonian fluids with low Reynolds number laminar flow and subsequently extended the model for multiphase fluid flow (Gao and Oterkus, 2020). Using PDDOs, Nguyen et al. (2021) modelled a truly incompressible fluid based on Euler's method, in which the pressure field is no longer calculated by a weakly compressible fluid model.

Despite progress in both grid-based and meshless approaches for modelling multiphase flows, accurately capturing the interface interaction remains challenging. The PDDO has shown promise in extending peridynamic theory to fluid dynamics; however, existing studies reveal a gap in the development of peridynamic models capable of addressing multiphase flow problems that involve interfacial wetting and coupled thermo-fluid behaviour.

## **2.6 Knowledge Gaps and Thesis Contributions**

While peridynamic modelling has seen significant advances in recent years for mechanical, thermal, and multiphase fluid systems, several challenges remain only partially resolved. For example, approximate guidelines for horizon size selection have been suggested, but mainly for bond-based formulations and without systematic validation across different peridynamic formulations. Variable discretisation methods have been proposed, but their stability and efficiency are still not fully established. Similarly, surface-tension-driven multiphase flows, such as those involving Marangoni effects, are only beginning to be addressed and require further development. This thesis aims to address these gaps through developing, implementing, and validating advanced peridynamic models suited for the multiscale, multiphysics demands of AM and welding applications.

## Chapter 3 Methodology

### 3.1 Introduction

The accurate modelling of material deformation is a key challenge in computational mechanics, specifically when dealing with complex phenomena such as crack initiation, propagation, and coalescence. As previously discussed, traditional approaches based on Classical Continuum Mechanics (CCM) are limited by their reliance on local partial differential equations, which become invalid at discontinuities and require additional treatments to model fractures.

To address these challenges, the peridynamic theory was introduced as a fundamentally nonlocal reformulation of continuum mechanics, replacing classical spatial derivatives with integral equations that remain well-defined in the presence of discontinuities. This chapter presents the theoretical framework and mathematical formulation of peridynamic methods, laying the foundation for the subsequent numerical investigations.

### 3.2 Peridynamic Theory

In CCM, the motion of a material body is described by partial differential equations based on the local balance of linear momentum. For a body occupying region, the equation of motion at position  $\mathbf{x}$  is given as (Reddy, 2013)

$$\rho(\mathbf{x})\ddot{\mathbf{u}}(\mathbf{x}, t) = \nabla \cdot \boldsymbol{\sigma}(\mathbf{x}, t) + \mathbf{b}(\mathbf{x}, t) \quad (3.1)$$

in which  $\rho$  is the mass density,  $\mathbf{u}$  is the displacement,  $t$  is the time,  $\nabla$  is the nabla operator,  $\boldsymbol{\sigma}$  is the Cauchy stress tensor, and  $\mathbf{b}$  is the body force per unit volume. Eq.( 3.1 ) presents that internal forces at a point are governed by the spatial gradients of stress in its immediate neighbourhood.

However, this reliance on spatial derivatives introduces inherent limitations when modelling problems with discontinuities such as cracks, since derivatives become undefined at those locations. This necessitates supplementary mathematical techniques, such as remeshing, enrichment to represent fracture processes, thereby complicating the simulation framework.

To overcome the limitations of CCM, Silling (2020) proposed the peridynamic theory, which removes the requirement for spatial derivatives by reformulating the equations

of motion as nonlocal integral equations. In peridynamics, each material point interacts with surrounding material points within a finite spatial domain known as the horizon  $H_x$ , as shown in Fig. 3-1.

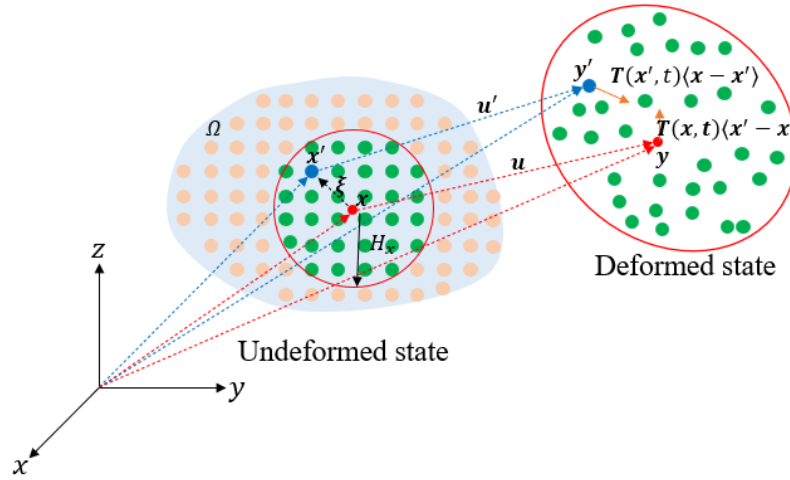


Fig. 3-1 Peridynamic horizon and force states.

Within the horizon, a force density vector acts on the material point  $x$  because of its interaction with neighbouring material points  $x'$ . The collection of all such force density vectors at material point  $x$  constitutes the force state  $T(x, t)$ .

The concept of state in peridynamics is a mathematical object that generalises the concept of a vector or tensor field, and represented by  $\langle \cdot \rangle$ , allowing the description of interactions between a reference material point and all its neighbours within the horizon (Silling et al., 2007). For instance, the force density vectors on material points  $x$  from  $x'$  can be denoted in state notation as  $T(x, t)\langle x' - x \rangle$ .

With these definitions, the general peridynamic equation of motion can be expressed as (Madenci and Oterkus, 2013)

$$\rho(x)\ddot{u}(x, t) = \int_{H_x} [T(x, t)\langle x' - x \rangle - T(x', t)\langle x - x' \rangle] dV' + b(x, t) \quad (3.2)$$

where  $V'$  represents the volume associated with each neighbouring material point  $x'$  within the horizon.

Generally, peridynamics can be classified into three main categories: bond-based (Silling, 2000), ordinary state-based (Silling, 2007), and non-ordinary state-based (Madenci and Oterkus, 2013) formulations, which are distinguished according to the direction and magnitude of the force density vector between a pair of material points (Fig. 3-2).

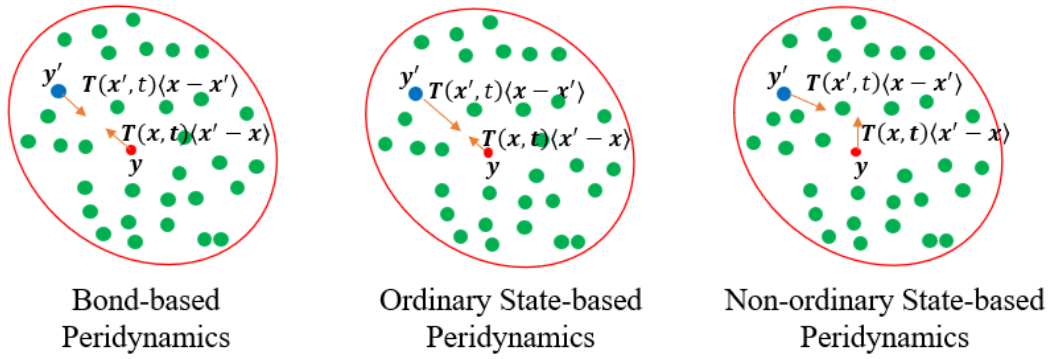


Fig. 3-2 Force states in the peridynamic framework.

### 3.2.1 Bond-Based Peridynamics

Bond-based peridynamics is the original formulation (Silling, 2000), in which the force density vectors acting on a pair of material points are determined only by the stretch of the bond connecting them. These forces are assumed to be equal in magnitude and opposite in direction.

The force density vector  $\mathbf{T}(\mathbf{x}, t)\langle\mathbf{x}' - \mathbf{x}\rangle$  in linear elastic isotropic materials at material points  $\mathbf{x}$  in Eq.( 3.2 ) can be expressed in the form as (Madenci and Oterkus, 2013)

$$\mathbf{T}(\mathbf{x}, t)\langle\mathbf{x}' - \mathbf{x}\rangle = \frac{1}{2}cs(\mathbf{u}' - \mathbf{u}, \mathbf{x}' - \mathbf{x}) \frac{\mathbf{y}' - \mathbf{y}}{|\mathbf{y}' - \mathbf{y}|} \quad (3.3)$$

and at material point  $\mathbf{x}'$  as

$$\mathbf{T}(\mathbf{x}', t)\langle\mathbf{x} - \mathbf{x}'\rangle = -\frac{1}{2}cs(\mathbf{u}' - \mathbf{u}, \mathbf{x}' - \mathbf{x}) \frac{\mathbf{y}' - \mathbf{y}}{|\mathbf{y}' - \mathbf{y}|} \quad (3.4)$$

where  $\mathbf{u}$  and  $\mathbf{u}'$  represent the displacement of material points  $\mathbf{x}$  and its neighbouring points  $\mathbf{x}'$ , the term  $\mathbf{y}$  represent the position of material points in the deformed configuration, thus  $\mathbf{y} = \mathbf{x} + \mathbf{u}$ , and similarly, for its family material point  $\mathbf{x}'$  within the horizon, it can be represented as  $\mathbf{y}' = \mathbf{x}' + \mathbf{u}'$ .

The term  $s$  denotes the stretch of the bond between a pair of material points  $\mathbf{x}$  and  $\mathbf{x}'$  after deformation, this can be defined as

$$s(\mathbf{u}' - \mathbf{u}, \mathbf{x}' - \mathbf{x}) = \frac{|\mathbf{y}' - \mathbf{y}| - |\mathbf{x}' - \mathbf{x}|}{|\mathbf{x}' - \mathbf{x}|} \quad (3.5)$$

The bond constant, denoted as  $c$ , in Eq.( 3.3 ) and Eq.( 3.4 ) is related to the elastic modulus and geometry, derived by equating strain energy densities from peridynamics and CCM (Madenci and Oterkus, 2013).

To establish this relationship, the strain energy density at a material point is calculated for a given loading condition using both the peridynamic formulation and CCM. By equating these results, a direct correspondence between the peridynamic and classical material parameters can be established.

For a linear elastic isotropic material, the bond constant in the two-dimensional case is given by (Madenci and Oterkus, 2013)

$$c = \frac{9E}{\pi h \delta^3} \quad (3.6)$$

and for a three-dimensional structure is given by (Madenci and Oterkus, 2013)

$$c = \frac{12E}{\pi \delta^4} \quad (3.7)$$

in which  $E$  is the elastic modulus,  $h$  is the thickness, and  $\delta$  is the horizon size.

As can be observed from the expression for the bond constant, bond-based formulations incorporate only the elastic modulus,  $E$ , from CCM, while disregarding the Poisson's ratio,  $\tilde{\nu}$ . This simplification implies that Poisson's ratio is not a free parameter in bond-based peridynamics; instead, the formulation inherently imposes a fixed value of  $\tilde{\nu} = 1/3$  for two-dimensional geometries and  $\tilde{\nu} = 1/4$  for three-dimensional problems (Silling, 2000).

For materials with Poisson's ratios different from these fixed values, more general peridynamic models, such as the ordinary state-based or non-ordinary state-based formulations, are required.

### 3.2.2 Ordinary State-based Peridynamics

The ordinary state-based formulation generalises the bond-based approach by relaxing the requirement that the forces between two material points must be equal in magnitude and opposite in direction (Silling, 2000). While the direction of the force density vectors remains opposed, their magnitudes are no longer required to be equal (Fig. 3-2). Furthermore, the force acting on a material point depends not only on its own motion and that of its immediate neighbour, but also on the collective motion of all family members within their horizons.

The pairwise force density vector at material point  $\mathbf{x}$  for ordinary state-based formulation is given by (Madenci and Oterkus, 2013)

$$\mathbf{T}(\mathbf{x}, t) \langle \mathbf{x}' - \mathbf{x} \rangle = \frac{1}{2} A \frac{\mathbf{y}' - \mathbf{y}}{|\mathbf{y}' - \mathbf{y}|} \quad (3.8)$$

and at material point  $\mathbf{x}'$  as (Madenci and Oterkus, 2013)

$$\mathbf{T}(\mathbf{x}', t) \langle \mathbf{x} - \mathbf{x}' \rangle = -\frac{1}{2} B \frac{\mathbf{y}' - \mathbf{y}}{|\mathbf{y}' - \mathbf{y}|} \quad (3.9)$$

where  $A$  and  $B$  are auxiliary parameters dependent on the material constants, the deformation field, and the horizon.

For a linear elastic isotropic material, the auxiliary parameter  $A$  can be written as (Madenci and Oterkus, 2013)

$$A = \frac{4ad\delta}{|\mathbf{x}' - \mathbf{x}|} \theta(\mathbf{x}, t) + 4\delta bs(\mathbf{u}' - \mathbf{u}, \mathbf{x}' - \mathbf{x}) \quad (3.10)$$

while  $B$  for the paired material point is (Madenci and Oterkus, 2013)

$$B = \frac{4ad\delta}{|\mathbf{x}' - \mathbf{x}|} \theta(\mathbf{x}', t) + 4\delta bs(\mathbf{u}' - \mathbf{u}, \mathbf{x}' - \mathbf{x}) \quad (3.11)$$

The term  $\theta(\mathbf{x}, t)$  in the above expressions represents the dilatation, or volumetric strain, and is given by (Madenci and Oterkus, 2013)

$$\theta(\mathbf{x}, t) = \int_{H_x} (d\delta s) dV' \quad (3.12)$$

where  $a$ ,  $b$  and  $d$  are the peridynamic parameters.

As discussed previously, these peridynamic parameters can be derived by considering a common parameter in both peridynamics and CCM. For instance, the relationships between these parameters can be established by comparing dilatation and strain energy density under isotropic expansion and simple shear conditions in peridynamics and CCM. The detailed list of peridynamic parameters in different dimensions is provided in Table 3-1 (Madenci and Oterkus, 2013).

*Table 3-1 Peridynamic parameters in different dimensions*

2D	$a = \frac{1}{2}(\kappa - 2\mu)$	$b = \frac{6\mu}{\pi h \delta^4}$	$d = \frac{2}{\pi h \delta^3}$
3D	$a = \frac{1}{2}\left(\kappa - \frac{5\mu}{3}\right)$	$b = \frac{15\mu}{2\pi \delta^5}$	$d = \frac{9}{4\pi \delta^4}$

in which  $\kappa$  is the bulk modulus and  $\mu$  is shear modulus. Table 3-2 provides the calculation of the bulk modulus  $\kappa$  and shear modulus  $\mu$  in different dimensions.

*Table 3-2 Bulk modulus and shear modulus in different dimensions*

2D	$\kappa = \frac{E}{2(1 - \nu)}$	$\mu = \frac{E}{2(1 + \nu)}$
3D	$\kappa = \frac{E}{3(1 - 2\nu)}$	$\mu = \frac{E}{2(1 + \nu)}$

It is noteworthy that, for two-dimensional calculations when the Poisson's ratio  $\tilde{\nu} = 1/3$ , there has  $\kappa = 2\mu$ ; and for three-dimensional calculations when  $\tilde{\nu} = 1/4$ , there has  $\kappa = \frac{5\mu}{3}$ . Under these specific conditions, the peridynamic parameter,  $a$ , becomes zero, causing the first terms ( $\frac{2ad\delta}{|x'-x|}\theta(\mathbf{x}, t)$  and  $\frac{2ad\delta}{|x'-x|}\theta(\mathbf{x}', t)$ ) in Eq.( 3.10 ) and Eq.( 3.11 ) to vanish.

Furthermore, substituting these values of  $\mu$  into the peridynamic parameter,  $b$ , from Table 3-1, the factor '4 $\delta b$ ' in the second term of Eq.( 3.10 ) and Eq.( 3.11 ) becomes

equivalent to the factor  $c$  given in Eq.( 3.3 ) and Eq.( 3.4 ). As a result, the ordinary state-based formulation reduces to the bond-based formulation for these special values of Poisson's ratio (Poisson's ratio  $\tilde{\nu} = 1/3$  at 2D, and  $\tilde{\nu} = 1/4$  for 3D).

### 3.2.3 Non-ordinary State-based Peridynamics

The force density vector restriction is further relaxed in the non-ordinary state-based formulation, wherein the directions of the forces are permitted to be arbitrary. However, once the force direction is no longer constrained to the bond direction, it becomes necessary to explicitly ensure conservation of angular momentum, a condition that is automatically satisfied in both bond-based and ordinary state-based peridynamics. Therefore, the following condition must be met (Madenci and Oterkus, 2013)

$$\int_{H_x} \{ (\mathbf{y}' - \mathbf{y}) \times \mathbf{T}(\mathbf{x}, t) \langle \mathbf{x}' - \mathbf{x} \rangle \} dV' = 0 \quad (3.13)$$

Within the non-ordinary state-based formulation, the force vector  $\mathbf{T}(\mathbf{x}, t) \langle \mathbf{x}' - \mathbf{x} \rangle$  acting on material point  $\mathbf{x}$  may be directly expressed using stress definitions from CCM. This approach allows the integration of established material models from CCM into the peridynamic framework (Madenci and Oterkus, 2013).

For example, the force state in non-ordinary state-based peridynamics may be related to the first Piola-Kirchhoff stress tensor,  $\mathbf{P}$ , as (Madenci and Oterkus, 2013)

$$\mathbf{T}(\mathbf{x}, t) \langle \mathbf{x}' - \mathbf{x} \rangle = w \langle \mathbf{x}' - \mathbf{x} \rangle \mathbf{P} \mathbf{K}^{-1} \langle \mathbf{x}' - \mathbf{x} \rangle \quad (3.14)$$

where  $\mathbf{K}$  is the shape tensor, defined as

$$\mathbf{K} = \int_{H_x} w \langle \mathbf{x}' - \mathbf{x} \rangle (\mathbf{X} \langle \mathbf{x}' - \mathbf{x} \rangle \otimes \mathbf{X} \langle \mathbf{x}' - \mathbf{x} \rangle) dV' \quad (3.15)$$

Here,  $w \langle \mathbf{x}' - \mathbf{x} \rangle$  is the influence state, characterising the strength of the interaction between material points,  $\otimes$  denotes the dyadic product of two vectors, and  $\mathbf{X} \langle \mathbf{x}' - \mathbf{x} \rangle$  is the position state, describing the relative position of material points associated with a particular bond.

The first Piola-Kirchhoff stress tensor  $\mathbf{P}$  in Eq.( 3.14 ) can be determined using the deformation gradient tensor  $\mathbf{F}$  and the second Piola-Kirchhoff stress tensor  $\mathbf{S}$  as follows

$$\mathbf{P} = \mathbf{F}\mathbf{S} \quad (3.16)$$

The second Piola-Kirchhoff stress tensor  $\mathbf{S}$ , can be calculated from the Green-Lagrange strain tensor  $\mathbf{E}$  by (Madenci and Oterkus, 2013)

$$\mathbf{S} = \lambda \text{tr}(\mathbf{E})\mathbf{I} + 2\mu\mathbf{E} \quad (3.17)$$

where  $\lambda$  and  $\mu$  are Lamé constants, related to Young's modulus and Poisson's ratio,  $\text{tr}$  is trace operation,  $\mathbf{I}$  is identity matrix, and the Green-Lagrange strain tensor  $\mathbf{E}$  is computed as (Madenci and Oterkus, 2013)

$$\mathbf{E} = \frac{1}{2}(\mathbf{F}^{-1}\mathbf{F} - \mathbf{I}) \quad (3.18)$$

To incorporate CCM-based material models into peridynamics, it is necessary to relate the stress and strain components. In peridynamics, the deformation gradient  $\mathbf{F}$  can be defined as (Madenci and Oterkus, 2013)

$$\mathbf{F} = \frac{\int_{H_x} w\langle \mathbf{x}' - \mathbf{x} \rangle (\mathbf{Y}\langle \mathbf{x}' - \mathbf{x} \rangle \otimes \mathbf{X}\langle \mathbf{x}' - \mathbf{x} \rangle) dV'}{\int_{H_x} w\langle \mathbf{x}' - \mathbf{x} \rangle (\mathbf{X}\langle \mathbf{x}' - \mathbf{x} \rangle \otimes \mathbf{X}\langle \mathbf{x}' - \mathbf{x} \rangle) dV'} \quad (3.19)$$

where the term  $\mathbf{Y}\langle \mathbf{x}' - \mathbf{x} \rangle$  denotes the position state in the deformed configuration.

Although non-ordinary state-based peridynamics allows the direct utilisation of CCM material models, typical particle discretisations are prone to zero-energy mode instabilities (Gu et al., 2018). To overcome this, the stabilisation method proposed by Silling (2017) is employed, whereby a stabilisation term is introduced into the force formulation (Madenci and Oterkus, 2013)

$$\mathbf{T}(\mathbf{x}, t)\langle \mathbf{x}' - \mathbf{x} \rangle = w\langle \mathbf{x}' - \mathbf{x} \rangle \left( \mathbf{PK}^{-1}(\mathbf{x}' - \mathbf{x}) + \frac{Gc}{\omega_{NOPD}\delta} \mathbf{z}\langle \mathbf{x}' - \mathbf{x} \rangle \right) \quad (3.20)$$

where  $G$  is a positive constant, and  $c$  is the bond constant as given in Eq.( 3.6 ) and Eq.( 3.7 ) for two-dimensional and three-dimensional structures, respectively, and  $\omega_{NOPD}$  is given by

$$\omega_{NOPD} = \int_{H_x} w \langle \mathbf{x}' - \mathbf{x} \rangle dV' \quad (3.21)$$

The deformation state  $\underline{\mathbf{z}} \langle \mathbf{x}' - \mathbf{x} \rangle$  in Eq.( 3.20 ) is defined as (Madenci and Oterkus, 2013)

$$\underline{\mathbf{z}} \langle \mathbf{x}' - \mathbf{x} \rangle = \mathbf{Y} \langle \mathbf{x}' - \mathbf{x} \rangle - \mathbf{F} \langle \mathbf{x}' - \mathbf{x} \rangle \quad (3.22)$$

### 3.3 Peridynamic Differential Operator

While the peridynamic theory introduced in Section 3.2 reformulates continuum mechanics using integral equations to overcome the limitations of classical partial differential equations. Building on this non-local concept, the Peridynamic Differential Operator (PDDO) has been recently proposed by Madenci et al. (2016), enabling the representation of any order of partial differentials within an integral form. The first and second order partial differentials of a function  $f(\mathbf{x})$  in two-dimensional domain can be calculated using PDDO as

$$\begin{pmatrix} \frac{\partial f(\mathbf{x})}{\partial x_1} \\ \frac{\partial f(\mathbf{x})}{\partial x_2} \\ \frac{\partial^2 f(\mathbf{x})}{\partial x_1^2} \\ \frac{\partial^2 f(\mathbf{x})}{\partial x_2^2} \\ \frac{\partial^2 f(\mathbf{x})}{\partial x_1 \partial x_2} \end{pmatrix} = \int_{H_x} [f(\mathbf{x} + \boldsymbol{\xi}) - f(\mathbf{x})] \begin{pmatrix} g_1^{10}(\boldsymbol{\xi}) \\ g_1^{01}(\boldsymbol{\xi}) \\ g_2^{20}(\boldsymbol{\xi}) \\ g_2^{02}(\boldsymbol{\xi}) \\ g_2^{11}(\boldsymbol{\xi}) \end{pmatrix} dV' \quad (3.23)$$

where  $V'$  represents the volume associated with each neighbouring material point  $\mathbf{x}'$  within the horizon. The parameters  $g_1^{10}(\boldsymbol{\xi})$ ,  $g_1^{01}(\boldsymbol{\xi})$ ,  $g_2^{11}(\boldsymbol{\xi})$ ,  $g_2^{02}(\boldsymbol{\xi})$ ,  $g_2^{20}(\boldsymbol{\xi})$  are peridynamic functions.

Here,  $\xi = \mathbf{x}' - \mathbf{x} = \xi_1 \mathbf{e}_1 + \xi_2 \mathbf{e}_2$  is the relative position vector between material point  $\mathbf{x}$  and its family material points  $\mathbf{x}'$  within its horizon  $H_x$  with

$$\xi_1 = x'_1 - x_1 \quad (3.24)$$

$$\xi_2 = x'_2 - x_2$$

where  $\xi_1$  and  $\xi_2$  represent the projections of the vector  $\xi$  with respect to  $x_1$  and  $x_2$  axes, and  $\mathbf{e}_1, \mathbf{e}_2$  are the unit vectors in the coordinate directions.

Peridynamic functions,  $g_1^{10}(\xi)$ ,  $g_1^{01}(\xi)$ ,  $g_2^{11}(\xi)$ ,  $g_2^{02}(\xi)$  and  $g_2^{20}(\xi)$  in Eq.( 3.23 ), are constructed to satisfy orthogonality properties (Madenci et al., 2016) that ensure the peridynamic integral operator correctly recovers the desired derivatives. The orthogonality properties for peridynamic functions can be given in the compact form as (Madenci et al., 2016)

$$\frac{1}{n_1! n_2!} \int_{H_x} \xi_1^{n_1} \xi_2^{n_2} g_N^{P_1 P_2}(\xi) d\xi_1 d\xi_2 = \delta_{n_1 P_1} \delta_{n_2 P_2} \quad (3.25)$$

where  $g_N^{P_1 P_2}(\xi)$  is the peridynamic function up to second order,  $n_i = 1, 2$ ,  $P_i = 1, 2$  is the order of differentiation with respect to  $x_i$ , and  $\delta_{n_i P_i}$  is the Kronecker delta ( $\delta_{n_i P_i} = 1$  if  $n_i = P_i$ , otherwise  $\delta_{n_i P_i} = 0$ ).

Eq. ( 3.25 ) can also be written in an explicit form as (Madenci et al., 2016)

$$\int_{H_x} \begin{bmatrix} \xi_1^0 \xi_2^1 & \xi_1^0 \xi_2^1 & \xi_1^0 \xi_2^1 & \xi_1^0 \xi_2^1 & \xi_1^0 \xi_2^1 \\ \xi_1^0 \xi_2^2 & \xi_1^0 \xi_2^2 & \xi_1^0 \xi_2^2 & \xi_1^0 \xi_2^2 & \xi_1^0 \xi_2^2 \\ \xi_1^1 \xi_2^0 & \xi_1^1 \xi_2^0 & \xi_1^1 \xi_2^0 & \xi_1^1 \xi_2^0 & \xi_1^1 \xi_2^0 \\ \xi_1^1 \xi_2^1 & \xi_1^1 \xi_2^1 & \xi_1^1 \xi_2^1 & \xi_1^1 \xi_2^1 & \xi_1^1 \xi_2^1 \\ \xi_1^2 \xi_2^0 & \xi_1^2 \xi_2^0 & \xi_1^2 \xi_2^0 & \xi_1^2 \xi_2^0 & \xi_1^2 \xi_2^0 \end{bmatrix} \begin{bmatrix} g_1^{01}(\xi) \\ g_2^{02}(\xi) \\ g_1^{10}(\xi) \\ g_2^{11}(\xi) \\ g_2^{20}(\xi) \end{bmatrix} dV' = \begin{bmatrix} 1 & 0 & 0 & 0 & 0 \\ 0 & 2 & 0 & 0 & 0 \\ 0 & 0 & 1 & 0 & 0 \\ 0 & 0 & 0 & 1 & 0 \\ 0 & 0 & 0 & 0 & 2 \end{bmatrix} \quad (3.26)$$

in which the superscript on relative position vector components represents the power of  $\xi_1$  and  $\xi_2$ .

Each peridynamic function  $g_N^{P_1 P_2}(\xi)$  in Eq. ( 3.26 ) at a given material point can be constructed as (Madenci et al., 2016)

$$g_{P_1+P_2}^{P_1P_2}(\xi) = \sum_{q_1=0}^2 \sum_{q_2=0}^{2-q_1} a_{q_1q_2}^{P_1P_2} \omega(|\xi|) \xi_1^{q_1} \xi_2^{q_2} \quad (3.27)$$

in which  $a_{q_1q_2}^{P_1P_2}$  are the coefficients to be determined, and  $\omega(|\xi|)$  is a weight function that describes the level of nonlocal interaction between material points in PDDO.

The weight function typically decays with increasing distance; for example, in this study, the weight function is chosen as (Madenci et al., 2016)

$$\omega(|\xi|) = \exp\left(-\left(\frac{2|\xi|}{\delta}\right)^2\right) \quad (3.28)$$

The unknown coefficients  $a_{q_1q_2}^{P_1P_2}$  in Eq.( 3.27 ) can be arranged in matrix form as

$$a_{q_1q_2}^{P_1P_2} = \begin{Bmatrix} a_{01}^{01} & a_{02}^{01} & a_{10}^{01} & a_{11}^{01} & a_{20}^{01} \\ a_{01}^{02} & a_{02}^{02} & a_{10}^{02} & a_{11}^{02} & a_{20}^{02} \\ a_{01}^{10} & a_{02}^{10} & a_{10}^{10} & a_{11}^{10} & a_{20}^{10} \\ a_{01}^{11} & a_{02}^{11} & a_{10}^{11} & a_{11}^{11} & a_{20}^{11} \\ a_{01}^{20} & a_{02}^{20} & a_{10}^{20} & a_{11}^{20} & a_{20}^{20} \end{Bmatrix} \quad (3.29)$$

By substituting these coefficients into the definition of the peridynamic functions  $g_N^{P_1P_2}$  in Eq.( 3.27 ) the explicit forms up to second order can be represented as

$$\begin{aligned} g_2^{01}(\xi) &= \sum_{q_1=0}^2 \sum_{q_2=0}^{2-q_1} a_{q_1q_2}^{01} \omega(|\xi|) \xi_1^{q_1} \xi_2^{q_2} \\ &= a_{01}^{01} \omega(|\xi|) \xi_1^0 \xi_2^1 + a_{02}^{01} \omega(|\xi|) \xi_1^0 \xi_2^2 + a_{10}^{01} \omega(|\xi|) \xi_1^1 \xi_2^0 \\ &\quad + a_{11}^{01} \omega(|\xi|) \xi_1^1 \xi_2^1 + a_{20}^{01} \omega(|\xi|) \xi_1^2 \xi_2^0 \\ g_2^{02}(\xi) &= \sum_{q_1=0}^2 \sum_{q_2=0}^{2-q_1} a_{q_1q_2}^{02} \omega(|\xi|) \xi_1^{q_1} \xi_2^{q_2} \\ &= a_{01}^{02} \omega(|\xi|) \xi_1^0 \xi_2^1 + a_{02}^{02} \omega(|\xi|) \xi_1^0 \xi_2^2 + a_{10}^{02} \omega(|\xi|) \xi_1^1 \xi_2^0 \\ &\quad + a_{11}^{02} \omega(|\xi|) \xi_1^1 \xi_2^1 + a_{20}^{02} \omega(|\xi|) \xi_1^2 \xi_2^0 \end{aligned} \quad (3.30)$$

$$\begin{aligned}
g_2^{10}(\xi) &= \sum_{q_1=0}^2 \sum_{q_2=0}^{2-q_1} a_{q_1 q_2}^{10} \omega(|\xi|) \xi_1^{q_1} \xi_2^{q_2} \\
&= a_{01}^{10} \omega(|\xi|) \xi_1^0 \xi_2^1 + a_{02}^{10} \omega(|\xi|) \xi_1^0 \xi_2^2 + a_{10}^{10} \omega(|\xi|) \xi_1^1 \xi_2^0 \\
&\quad + a_{11}^{10} \omega(|\xi|) \xi_1^1 \xi_2^1 + a_{20}^{10} \omega(|\xi|) \xi_1^2 \xi_2^0 \\
g_2^{11}(\xi) &= \sum_{q_1=0}^2 \sum_{q_2=0}^{2-q_1} a_{q_1 q_2}^{11} \omega(|\xi|) \xi_1^{q_1} \xi_2^{q_2} \\
&= a_{01}^{11} \omega(|\xi|) \xi_1^0 \xi_2^1 + a_{02}^{11} \omega(|\xi|) \xi_1^0 \xi_2^2 + a_{10}^{11} \omega(|\xi|) \xi_1^1 \xi_2^0 \\
&\quad + a_{11}^{11} \omega(|\xi|) \xi_1^1 \xi_2^1 + a_{20}^{11} \omega(|\xi|) \xi_1^2 \xi_2^0 \\
g_2^{20}(\xi) &= \sum_{q_1=0}^2 \sum_{q_2=0}^{2-q_1} a_{q_1 q_2}^{20} \omega(|\xi|) \xi_1^{q_1} \xi_2^{q_2} \\
&= a_{01}^{20} \omega(|\xi|) \xi_1^0 \xi_2^1 + a_{02}^{20} \omega(|\xi|) \xi_1^0 \xi_2^2 + a_{10}^{20} \omega(|\xi|) \xi_1^1 \xi_2^0 \\
&\quad + a_{11}^{20} \omega(|\xi|) \xi_1^1 \xi_2^1 + a_{20}^{20} \omega(|\xi|) \xi_1^2 \xi_2^0
\end{aligned}$$

Alternatively, these can be concisely written in matrix form as

$$\begin{Bmatrix} g_2^{01}(\xi) \\ g_2^{02}(\xi) \\ g_2^{10}(\xi) \\ g_2^{11}(\xi) \\ g_2^{20}(\xi) \end{Bmatrix} = \begin{pmatrix} a_{01}^{01} & a_{02}^{01} & a_{10}^{01} & a_{11}^{01} & a_{20}^{01} \\ a_{01}^{02} & a_{02}^{02} & a_{10}^{02} & a_{11}^{02} & a_{20}^{02} \\ a_{01}^{10} & a_{02}^{10} & a_{10}^{10} & a_{11}^{10} & a_{20}^{10} \\ a_{01}^{11} & a_{02}^{11} & a_{10}^{11} & a_{11}^{11} & a_{20}^{11} \\ a_{01}^{20} & a_{02}^{20} & a_{10}^{20} & a_{11}^{20} & a_{20}^{20} \end{pmatrix} \begin{Bmatrix} \omega(|\xi|) \xi_1^0 \xi_2^1 \\ \omega(|\xi|) \xi_1^0 \xi_2^2 \\ \omega(|\xi|) \xi_1^1 \xi_2^0 \\ \omega(|\xi|) \xi_1^1 \xi_2^1 \\ \omega(|\xi|) \xi_1^2 \xi_2^0 \end{Bmatrix} \quad (3.31)$$

To determine the unknown coefficients  $a_{q_1 q_2}^{P_1 P_2}$ , substituting Eq.( 3.31 ) into orthogonal condition in Eq.( 3.26 ) resulting in a linear system

$$\mathbf{A} \mathbf{a} = \bar{\mathbf{b}} \quad (3.32)$$

Here,  $\mathbf{A}$  is the shape matrix with

$$\mathbf{A} = \int_{H_x} \omega(|\xi|) \begin{bmatrix} \xi_1^0 \xi_2^2 & \xi_1^0 \xi_2^3 & \xi_1^1 \xi_2^1 & \xi_1^1 \xi_2^2 & \xi_1^2 \xi_2^1 \\ \xi_1^0 \xi_2^3 & \xi_1^0 \xi_2^4 & \xi_1^1 \xi_2^2 & \xi_1^1 \xi_2^3 & \xi_1^2 \xi_2^2 \\ \xi_1^1 \xi_2^1 & \xi_1^1 \xi_2^2 & \xi_1^2 \xi_2^0 & \xi_1^2 \xi_2^1 & \xi_1^3 \xi_2^0 \\ \xi_1^1 \xi_2^2 & \xi_1^1 \xi_2^3 & \xi_1^2 \xi_2^1 & \xi_1^2 \xi_2^2 & \xi_1^3 \xi_2^1 \\ \xi_1^2 \xi_2^1 & \xi_1^2 \xi_2^2 & \xi_1^3 \xi_2^0 & \xi_1^3 \xi_2^1 & \xi_1^4 \xi_2^0 \end{bmatrix} dV' \quad (3.33)$$

$\mathbf{a}$  is the unknown coefficients matrix with

$$\mathbf{a} = \begin{bmatrix} a_{01}^{01} & a_{01}^{02} & a_{01}^{10} & a_{01}^{11} & a_{01}^{20} \\ a_{02}^{01} & a_{02}^{02} & a_{02}^{10} & a_{02}^{11} & a_{02}^{20} \\ a_{10}^{01} & a_{10}^{02} & a_{10}^{10} & a_{10}^{11} & a_{10}^{20} \\ a_{11}^{01} & a_{11}^{02} & a_{11}^{10} & a_{11}^{11} & a_{11}^{20} \\ a_{20}^{01} & a_{20}^{02} & a_{20}^{10} & a_{20}^{11} & a_{20}^{20} \end{bmatrix} \quad (3.34)$$

and matrix  $\bar{\mathbf{b}}$  is presented as

$$\bar{\mathbf{b}} = \begin{bmatrix} 1 & 0 & 0 & 0 & 0 & 0 \\ 0 & 1 & 0 & 0 & 0 & 0 \\ 0 & 0 & 2 & 0 & 0 & 0 \\ 0 & 0 & 0 & 1 & 0 & 0 \\ 0 & 0 & 0 & 0 & 1 & 0 \\ 0 & 0 & 0 & 0 & 0 & 2 \end{bmatrix} \quad (3.35)$$

As a result, in unknown coefficients matrix,  $\mathbf{a}$ , can be obtained by

$$\mathbf{a} = \mathbf{A} \bar{\mathbf{b}} \quad (3.36)$$

Therefore, peridynamic functions  $g_N^{P_1 P_2}$  can then be constructed using Eq.( 3.31 ). Consequently, the derivative of  $f(\mathbf{x})$  can be obtained through Eq.( 3.23 ).

The linear system from Eq.( 3.32 ) can be solved either analytically or numerically. When the neighbouring material points  $\mathbf{x}'$  of material point  $\mathbf{x}$  are distributed symmetrically within the horizon, and the weight function from Eq.( 3.28 ) is used, analytical integration of Eq.( 3.33 ) leads to a closed-form expression for the shape matrix

$$\mathbf{A} = \begin{bmatrix} \frac{\delta^4(-5+e^4)\pi}{32e^4} & 0 & 0 & 0 & 0 \\ 0 & \frac{3\delta^6(-13+e^4)\pi}{256e^4} & 0 & 0 & \frac{\delta^6(-13+e^4)\pi}{256e^4} \\ 0 & 0 & \frac{\delta^4(-5+e^4)\pi}{32e^4} & 0 & 0 \\ 0 & 0 & 0 & \frac{\delta^6(-13+e^4)\pi}{256e^4} & 0 \\ 0 & \frac{\delta^6(-13+e^4)\pi}{256e^4} & 0 & 0 & \frac{3\delta^6(-13+e^4)\pi}{256e^4} \end{bmatrix} \quad (3.37)$$

Accordingly, the unknown coefficients  $\mathbf{a}$  is obtained by analytical solving Eq.( 3.32 ) as

$$\mathbf{a} = \begin{bmatrix} \frac{32e^4}{\delta^4(-5+e^4)\pi} & 0 & 0 & 0 & 0 \\ 0 & \frac{192e^4}{\delta^6(-13+e^4)\pi} & 0 & 0 & -\frac{64e^4}{\delta^6(-13+e^4)\pi} \\ 0 & 0 & \frac{32e^4}{\delta^4(-5+e^4)\pi} & 0 & 0 \\ 0 & 0 & 0 & \frac{256e^4}{\delta^6(-13+e^4)\pi} & 0 \\ 0 & -\frac{64e^4}{\delta^6(-13+e^4)\pi} & 0 & 0 & \frac{192e^4}{\delta^6(-13+e^4)\pi} \end{bmatrix} \quad (3.38)$$

Substituting these coefficients, the analytical forms of the peridynamic functions is presented as

$$\begin{aligned} g_1^{01}(\boldsymbol{\xi}) &= \frac{32e^4}{\delta^4(-5+e^4)\pi} e^{-\left(\frac{2|\boldsymbol{\xi}|}{\delta}\right)^2} \xi_1^0 \xi_2^1 & (3.39) \\ g_2^{02}(\boldsymbol{\xi}) &= \frac{192e^4}{\delta^6(-13+e^4)\pi} e^{-\left(\frac{2|\boldsymbol{\xi}|}{\delta}\right)^2} \xi_1^0 \xi_2^2 - \frac{64e^4}{\delta^6(-13+e^4)\pi} e^{-\left(\frac{2|\boldsymbol{\xi}|}{\delta}\right)^2} \xi_1^2 \xi_2^0 \\ g_1^{10}(\boldsymbol{\xi}) &= \frac{32e^4}{\delta^4(-5+e^4)\pi} e^{-\left(\frac{2|\boldsymbol{\xi}|}{\delta}\right)^2} \xi_1^1 \xi_2^0 \\ g_2^{11}(\boldsymbol{\xi}) &= \frac{256e^4}{\delta^6(-13+e^4)\pi} e^{-\left(\frac{2|\boldsymbol{\xi}|}{\delta}\right)^2} \xi_1^1 \xi_2^1 \\ g_2^{20}(\boldsymbol{\xi}) &= -\frac{64e^4}{\delta^6(-13+e^4)\pi} e^{-\left(\frac{2|\boldsymbol{\xi}|}{\delta}\right)^2} \xi_1^0 \xi_2^2 + \frac{192e^4}{\delta^6(-13+e^4)\pi} e^{-\left(\frac{2|\boldsymbol{\xi}|}{\delta}\right)^2} \xi_1^2 \xi_2^0 \end{aligned}$$

For general, non-symmetric distributions or complex geometries, the coefficients are determined numerically. The detailed numerical procedure is provided in Chapter 8.

## **Chapter 4 Investigation of Horizon Size in Peridynamics**

### **4.1 Introduction**

The accuracy of peridynamic simulations is governed by two key numerical parameters: the discretisation size and, most importantly, the horizon size, which defines the spatial extent of nonlocal interactions between material points. The choice of horizon size not only affects the fidelity of simulation results but also has direct implications for computational cost. The horizon size selection is based on an early recommendation associated with the original bond-based peridynamics (Silling and Askari, 2005), which suggests setting the horizon to approximately three times the grid spacing. While this rule of thumb has been widely used, it was derived specifically for bond-based formulation, whose formulation imposes certain material property constraints, such as a fixed Poisson's ratio.

With the development of state-based peridynamics, both ordinary and non-ordinary formulations, the mathematical structure have evolved (Madenci and Oterkus, 2013). These generalised frameworks overcome the limitations of the bond-based approach, permitting a broader range of material models. However, whether the selection of horizon size for bond-based peridynamics remain valid for state-based formulations is not fully understood. The different nature of the interactions and constitutive models in state-based peridynamics may require different considerations for determining the optimal horizon size.

This chapter addresses this gap by systematically investigating the influence of horizon size in bond-based, ordinary state-based, and non-ordinary state-based peridynamics. A range of two- and three-dimensional benchmark problems, including both static and dynamic cases, are examined to evaluate how horizon size affects simulation accuracy and computational efficiency. The aim is to establish recommendations for selecting the horizon size in different peridynamic formulations, thereby improving the reliability and predictive capability of peridynamic modelling for applications in structural engineering.

### **4.2 Numerical Implementation of Peridynamic Formulations**

This section presents the numerical procedures employed for the implementation of the peridynamic models. The approach accommodates both static and dynamic

problems and covers bond-based, ordinary state-based, and non-ordinary state-based formulations. Key aspects include the spatial discretisation of the solution domain, numerical integration of the peridynamic equations of motion, imposition of boundary conditions, and the incorporation of correction techniques to address nonlocal effects at boundaries and interfaces.

#### 4.2.1 Spatial Integration

In numerical implementation, the solution domain is discretised into a finite set of material points, each representing a finite volume with assigned material properties. The spatial discretisation forms the basis for all subsequent calculations, as each material point interacts nonlocally with neighbouring points located within its horizon radius.

As illustrated in Fig. 4-1, material point  $k$  at location  $\mathbf{x}_k$  interacts with all neighbouring points  $j$  at location  $\mathbf{x}_j$  whose centres fall within a horizon of radius  $\delta$ .

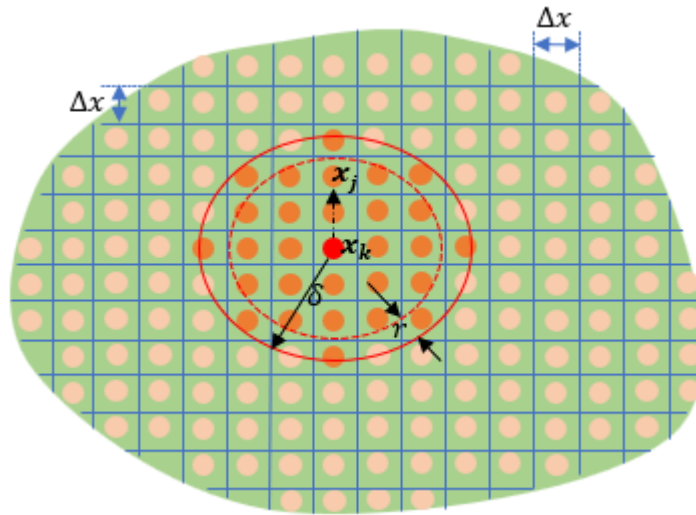


Fig. 4-1 Numerical discretisation of the simulation domain and volume correction.

The peridynamic equation of motion, originally formulated as an integral from Eq.( 3.2 ), is approximated numerically by summing the contributions of all family members within the horizon as

$$\rho_k \ddot{\mathbf{u}}_k = \sum_{j=1}^{N_k} [\mathbf{t}_{kj} - \mathbf{t}_{jk}] V_j + \mathbf{b}_k \quad (4.1)$$

where  $\mathbf{t}_{kj}$  is the force density vector acts on material point  $\mathbf{x}_k$  by  $\mathbf{x}_j$ ,  $\mathbf{t}_{jk}$  the reciprocal force, and  $N_k$  denotes the number of neighbouring material points within the horizon of material point  $k$ .

To reduce numerical integration errors in Eq.( 4.1 ), two correction factors are introduced: a volume correction factor and a surface correction factor.

#### 4.2.1.1 Volume Correction

For neighbours near the edge of the horizon, only a portion of their volume is contained within the horizon. The volume correction factor compensates for this partial overlap (Madenci and Oterkus, 2013)

$$v_{cor} = \frac{(\delta + r - |\mathbf{x}_j - \mathbf{x}_k|)}{2r} \quad (4.2)$$

in which  $r$  is defined as

$$r = \frac{\Delta x}{2} \quad (4.3)$$

where  $\Delta x$  is the discretion size. This correction applies if  $|\mathbf{x}_j - \mathbf{x}_k| > (\delta - r)$ ; otherwise,  $v_{cor} = 1$ .

#### 4.2.1.2 Surface Correction

For material points at or near boundaries, horizons are truncated, resulting in incomplete nonlocal interactions. To address this, a surface correction factor is therefore applied. The necessity and magnitude of this correction depend on the presence of free surfaces, which is determined by the specific problem setup.

The correction is typically computed numerically by integrating both the dilatation and the strain energy density at each material point under simple loading conditions and comparing these results with those from CCM.

First, a fictitious uniaxial stretch is applied in the x-, y-, and z-directions before time integration. The dilatation in peridynamic framework is then computed as (Madenci and Oterkus, 2013)

$$\theta_m^{PD} x_k = d\delta \sum_{j=1}^{N_k} s_{kj} V_j \quad (4.4)$$

where  $s_{kj}$  is the stretch between material point  $x_k$  and  $x_j$ . The parameter  $d$  is given by Table 3-1. The corresponding dilatation in CCM is determined as

$$\theta_m^{CCM} = \xi_{CCM} \quad (4.5)$$

where  $\xi_{CCM}$  is the applied normal strain in the x-, y-, and z-directions, with  $m = 1,2,3$ .

Consequently, the surface correction factor for dilatation term is computed as

$$s_{cor}^d = \frac{\theta_m^{CCM}}{\theta_m^{PD} x_k} \quad (4.6)$$

Now the dilatation term in Eq.( 3.10 ) and Eq.( 3.11 ) has corrected via Eq.( 4.6 ).

The strain energy density is used to correct the bond constant,  $c$ , in the bond-based formulation (see Eq.( 3.3 ) and Eq.( 3.4 )) or parameter,  $b$ , in the ordinary state-based formulation (see Eq.( 3.10 ) and Eq.( 3.11 )). This surface correction factor is computed as

$$s_{cor}^W = \frac{W_m^{CCM}}{W_m^{PD} x_k} \quad (4.7)$$

Here  $W_m^{PD} x_k$  is the strain energy density in peridynamic framework.  $W_m^{CCM}$  denotes the strain energy density in CCM and varies according to the dimensionality of the problem. Its general form can be written as

$$W_m^{CCM} = \frac{1}{2} \sigma \epsilon \quad (4.8)$$

where  $\sigma$  and  $\epsilon$  represents the stress and strain, respectively. As a result, the force term in  $t_{kj}$  and  $t_{jk}$  in Eq.( 4.1 ) is corrected via Eq.( 4.6 ) for dilatation and Eq.( 4.7 ) for peridynamic parameters. The integral volume  $V_j$  in is corrected via volume correction factor in Eq.( 4.2 ). Consequently, the equation of motion in Eq.( 4.1 ) is reformed as

$$\rho_k \ddot{\mathbf{u}}_k = \sum_{j=1}^{N_k} [\bar{\mathbf{t}}_{kj} - \bar{\mathbf{t}}_{jk}] v_{cor} V_j + \mathbf{b}_k \quad (4.9)$$

#### 4.2.2 Time Integration

##### 4.2.2.1 Dynamic Problems

For dynamic simulations, either implicit or explicit time integration methods can be employed. While implicit schemes are unconditionally stable and permit larger time steps, they involve solving large systems of equations at each time step, which can be computationally demanding. In this study, an explicit time integration scheme (Madenci and Oterkus, 2013) is adopted for its simplicity and computational efficiency. The explicit approach updates the displacement and velocity at each time step using only information from the previous steps, thereby avoiding the need for solving large systems of equations.

Given the acceleration of a material point at time step  $n$  from Eq.( 4.9 ), the velocity and displacement at the next time step  $n + 1$  can be calculated as

$$\dot{\mathbf{u}}_{x_k}^{n+1} = \dot{\mathbf{u}}_{x_k}^{n+1} \Delta t + \dot{\mathbf{u}}_{x_k}^n \quad (4.10)$$

and

$$\mathbf{u}_{x_k}^{n+1} = \dot{\mathbf{u}}_{x_k}^{n+1} \Delta t + \mathbf{u}_{x_k}^{n+1} \quad (4.11)$$

where  $\Delta t$  is the time step size.

It should be noted that explicit schemes are only conditionally stable. To ensure numerical stability, the time step must be chosen according to the critical value determined by von Neumann stability analysis as (Lapidus and Pinder, 1999; Madenci and Oterkus, 2013)

$$\Delta t < \sqrt{\frac{2\rho_k}{\sum_{j=1}^{N_k} \left[ 2ad\delta \frac{\left( \sum_{l=1}^{N_l} \left[ \frac{1}{|\mathbf{x}_l - \mathbf{x}_k|} + \frac{1}{|\mathbf{x}_j - \mathbf{x}_j|} \right] \right) V_l}{|\mathbf{x}_j - \mathbf{x}_k|} + \frac{4b\delta}{|\mathbf{x}_j - \mathbf{x}_k|} \right] v_{cor} V_j}} \quad (4.12)$$

#### 4.2.2.2 Static Problems

Static analyses require the system to reach an equilibrium state where both acceleration and velocities are zero. Owing to the nonlocal nature and large size of the system, directly solving for static equilibrium can be computationally challenging. Here, the Adaptive Dynamic Relaxation (ADR) method is used (Underwood, 1983; Kilic and Madenci, 2010), in which the equations of motion are integrated in a pseudo-time domain with artificial inertia and damping, gradually leading the system to a static equilibrium.

The ADR method introduces fictitious mass and damping terms, leading to the following reformulation (Madenci and Oterkus, 2013)

$$\mathbf{D}\ddot{\mathbf{U}}(\mathbf{X}, t) + \mathbf{C}\mathbf{D}\dot{\mathbf{U}}(\mathbf{X}, t) = \mathbf{F}(\mathbf{U}, \mathbf{U}', \mathbf{X}, \mathbf{X}') \quad (4.13)$$

where  $\mathbf{D}$  is fictitious diagonal mass matrix,  $\mathbf{C}$  is the damping coefficient. The vectors  $\mathbf{X}$  and  $\mathbf{U}$  represent the initial positions and the displacements of all material points, respectively, and these are expressed as

$$\mathbf{X}^T = \{\mathbf{x}_1, \mathbf{x}_2, \mathbf{x}_3, \dots, \mathbf{x}_M\} \quad (4.14)$$

and

$$\mathbf{U}^T = \{\mathbf{u}(\mathbf{x}_1, t), \mathbf{u}(\mathbf{x}_2, t), \mathbf{u}(\mathbf{x}_3, t), \dots, \mathbf{u}(\mathbf{x}_M, t)\} \quad (4.15)$$

with  $M$  denoting the total number of material points.

The vector  $\mathbf{F}$  consists of peridynamic interaction forces and external body forces. Its  $i$ th component can be expressed as

$$\mathbf{F}_i = \sum_{j=1}^{N_i} [\bar{\mathbf{t}}_{ij} - \bar{\mathbf{t}}_{ji}] v_{cor} V_j + \mathbf{b}_i \quad (4.16)$$

By applying the central-difference explicit integration scheme, the velocity and displacement of each material point at the next time step can be calculated as (Madenci and Oterkus, 2013)

$$\dot{U}_i^{n+\frac{1}{2}} = \frac{(2 - C^n \Delta t) \dot{U}_i^{n-\frac{1}{2}} + 2\Delta t \mathbf{D}_i^{-1} \mathbf{F}_i^n}{(2 + C^n \Delta t)} \quad (4.17)$$

and

$$U_i^{n+1} = U_i^n + \mathbf{b}_i \Delta t \dot{U}_i^{n+\frac{1}{2}} \quad (4.18)$$

where  $\Delta t$  is the time step size and is typically set to unity in ADR scheme. The damping coefficient  $C^n$  is determined at each time step, and it is computed as (Underwood, 1983)

$$C^n = 2 \sqrt{\frac{(\mathbf{U}_i^n)^T \mathbf{K}_i^n \mathbf{U}_i^n}{(\mathbf{U}_i^n)^T \mathbf{U}_i^n}} \quad (4.19)$$

with  $\mathbf{K}^n$  is the stiffness matrix, which is given as (Madenci and Oterkus, 2013)

$$\mathbf{K}_i^n = -\frac{\frac{\mathbf{F}_i^n}{\mathbf{D}_i} - \frac{\mathbf{F}_i^{n-1}}{\mathbf{D}_i}}{\Delta t \dot{U}_i^{n-\frac{1}{2}}} \quad (4.20)$$

#### 4.2.3 Boundary Conditions

The imposition of boundary conditions in peridynamics differs from CCM due to the nonlocal nature of the formulation. Instead of prescribing values directly at discrete nodes or along boundaries, as is standard in finite element methods, peridynamics enforces boundary conditions over finite volumes.

##### 4.2.3.1 Displacement Constraints

Displacement boundary conditions are implemented by prescribing the displacements of material points located within a fictitious region adjacent to the boundary (Madenci and Oterkus, 2016). To achieve this, fictitious regions,  $R_f$ , are introduced adjacent to the physical boundaries of the solution domain (see Fig. 4-2). The thickness of this region is typically set to twice the horizon size ( $2\delta$ ).

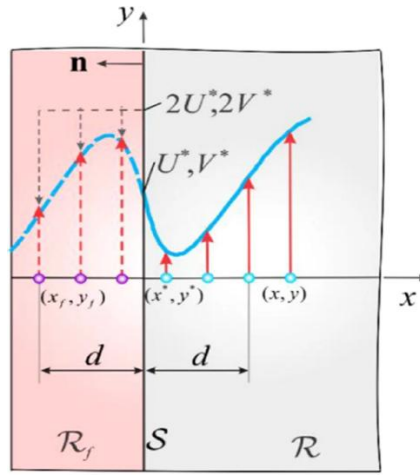


Fig. 4-2 Application of displacement constraints in peridynamics by introducing a fictitious region (Madenci and Oterkus, 2016).

Let  $U^*$ ,  $V^*$ , and  $W^*$  denote the prescribed displacements in the x-, y-, and z-directions, respectively. The displacement of a material point within the fictitious region is then defined for x direction as (Madenci and Oterkus, 2016)

$$u_f(x_f, y_f, z_f, t + \Delta t) = 2U^*(x^* y^* z^*, t + \Delta t) - u(x, y, z, t) \quad (4.21)$$

for y direction as

$$v_f(x_f, y_f, z_f, t + \Delta t) = 2V^*(x^* y^* z^*, t + \Delta t) - v(x, y, z, t) \quad (4.22)$$

and for z direction as

$$w_f(x_f, y_f, z_f, t + \Delta t) = 2W^*(x^* y^* z^*, t + \Delta t) - w(x, y, z, t) \quad (4.23)$$

where  $u_f$ ,  $v_f$ , and  $w_f$  denote the displacement of material points within the fictitious region, while  $u$ ,  $v$  and  $w$  denotes the corresponding material points in the adjacent position in the physical domain. By directly specifying the displacement field in the fictitious region, the desired boundary behaviour is achieved at the interface.

#### 4.2.3.2 Traction Boundary Conditions

Traction boundary conditions are implemented by prescribing the displacements of material points within the fictitious region in such a way that the intended stress state is reproduced at the boundary (Madenci and Oterkus, 2016). The explicit expression

for these imposed displacements depends on both the problem's dimensionality and the orientation of the boundary normal.

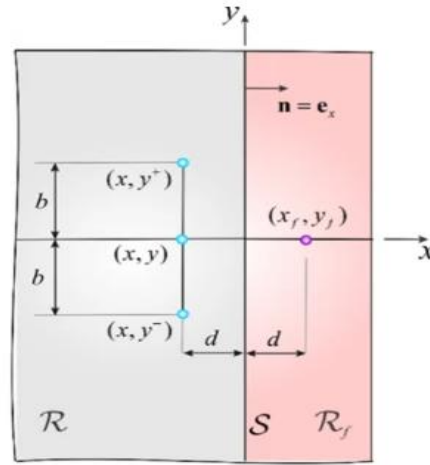


Fig. 4-3 Application of traction boundary conditions on a surface with a normal vector in x-direction (Madenci and Oterkus, 2016).

For two-dimensional problems, considering a boundary with a unit normal in the x-direction, the displacements within the fictitious region are obtained for x direction as (Madenci and Oterkus, 2016)

$$\begin{aligned}
 u_f(x_f, y_f, t + \Delta t) & \quad (4.24) \\
 &= \left[ \frac{(1 - \tilde{\nu}^2)\sigma_{xx}^*}{E} - \tilde{\nu} \frac{v(x, y^+, t) - v(x, y^-, t)}{y^+ - y^-} \right] (x_f - x) \\
 &+ u(x, y, t)
 \end{aligned}$$

and for y direction as

$$\begin{aligned}
 v_f(x_f, y_f, t + \Delta t) & \quad (4.25) \\
 &= \left[ \frac{2(1 + \tilde{\nu})\sigma_{xy}^*}{E} - \frac{u(x, y^+, t) - u(x, y^-, t)}{y^+ - y^-} \right] (x_f - x) \\
 &+ v(x, y, t)
 \end{aligned}$$

where  $\sigma_{xx}^*$  and  $\sigma_{xy}^*$  are applied stresses normal and tangent to the boundary, respectively,  $E$  is Young's modulus, and  $\tilde{\nu}$  is Poisson's ratio.

For three-dimensional problems, the methodology for imposing traction boundary conditions using fictitious regions is readily extended. When the traction boundary

possesses a unit normal in the x-direction, the displacement fields are computed for the x-direction as

$$\begin{aligned}
u_f(x_f, y_f, z_f, t + \Delta t) & \quad (4.26) \\
&= \frac{1}{(1 - \tilde{\nu})} \left[ \frac{(1 + \tilde{\nu})(1 - 2\tilde{\nu})\sigma_{xx}^*}{E} \right. \\
&\quad - \tilde{\nu} \frac{v(x, y^+, t) - v(x, y^-, t)}{y^+ - y^-} \\
&\quad \left. - \tilde{\nu} \frac{w(x, y^+, t) - w(x, y^-, t)}{z^+ - z^-} \right] (\mathbf{x}_f - \mathbf{x}) + u(x, y, t)
\end{aligned}$$

for y direction as

$$\begin{aligned}
v_f(x_f, y_f, z_f, t + \Delta t) & \quad (4.27) \\
&= \left[ \frac{2(1 + \tilde{\nu})\sigma_{xy}^*}{E} - \tilde{\nu} \frac{u(x, y^+, t) - u(x, y^-, t)}{y^+ - y^-} \right] (\mathbf{x}_f - \mathbf{x}) \\
&\quad + v(x, y, t)
\end{aligned}$$

and for z direction as

$$\begin{aligned}
w_f(x_f, y_f, z_f, t + \Delta t) & \quad (4.28) \\
&= \left[ \frac{2(1 + \tilde{\nu})\sigma_{xz}^*}{E} - \tilde{\nu} \frac{u(x, y^+, t) - u(x, y^-, t)}{z^+ - z^-} \right] (\mathbf{x}_f - \mathbf{x}) \\
&\quad + w(x, y, t)
\end{aligned}$$

Note that this procedure is only valid if the traction boundary region is elastic.

### 4.3 Numerical Investigations

#### 4.3.1 Determination of Horizon Size

The horizon size is a decisive numerical parameter in peridynamic theory, as it determines the extent of nonlocal interactions between material points. In the context of uniform discretisation, each point interacts with neighbouring points within a circular (in 2D), or spherical (in 3D) region defined by the horizon radius  $\delta$ . The choice of  $\delta$  directly affects the accuracy and computational cost of the peridynamic simulation. If the horizon is chosen too small, the interaction network becomes sparse, which limits the model's ability to capture basic deformation modes (i.e., if a material

point interacts only with its nearest neighbours, shear deformation will not be captured). Conversely, a larger horizon increases computational expense without proportionate gains in accuracy.

A commonly adopted guideline, originally developed for bond-based peridynamics, is to select the horizon size as three times the grid spacing ( $\delta = 3\Delta x$ ). This recommendation ensures that each point maintains enough interacting neighbours, supporting reliable approximation of both tensile and shear responses. However, with the emergence of more general state-based peridynamic formulations, this rule requires re-examination. Moreover, it is important to verify whether these guidelines are robust for both static and dynamic loading scenarios, as well as for two- and three-dimensional structures.

This section systematically investigates horizon size selection through a series of uniform discretisation simulations, analysing both 2D and 3D problems in bond-based, ordinary state-based, and non-ordinary state-based peridynamics. By considering simple benchmark geometries and loading conditions, and by analysing both static and dynamic scenarios, this investigation aims to establish guidelines for horizon size selection that balance computational efficiency with solution accuracy. For validation, peridynamic predictions are compared with FEM by ANSYS simulations under equivalent settings.

FEM simulations were carried out in ANSYS for verification. Plane182 elements (four-node quadrilateral) were employed for two-dimensional models, while Solid185 elements (eight-node hexahedral) were used for three-dimensional cases. The mesh configuration was generated to match the nodal spacing of the peridynamic discretisation, and identical material properties were applied, including Young's modulus, Poisson's ratio, and density as given in each case description. For dynamic analyses, the time step size was kept consistent with the peridynamic simulations.

#### *4.3.2 Vibration of a Plate*

In the first simulation case, the dynamic response of a square plate in Fig. 4-4 with dimensions  $L = W = 1$  m and thickness 0.01 m is investigated. The plate is composed of a linear elastic and homogeneous material, with Young's modulus  $E = 200$  GPa and density  $\rho = 7850$  kg/m<sup>3</sup>. Vibration is initiated by imposing an initial

uniaxial strain of 0.001 in the horizontal direction. The left edge of the plate is fully constrained using a fictitious region, while all other edges are traction-free, as shown in Fig. 4-5.

Uniform discretisation is adopted, with a grid spacing of  $\Delta x = 0.01$  m. Each material point interacts with its neighbours within a horizon of radius  $\delta$ , which is varied systematically to assess its influence on simulation results.

The dynamic analysis is performed using an explicit time integration scheme, with a time step size of  $1 \times 10^{-7}$  seconds.

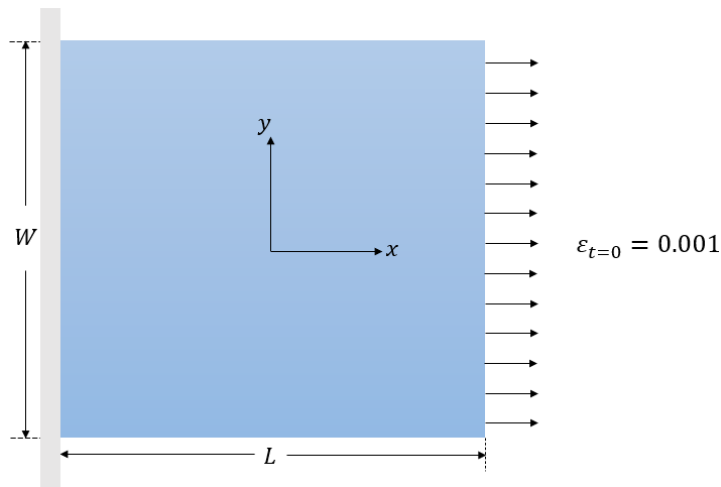


Fig. 4-4 Square plate subjected to initial uniaxial strain condition.

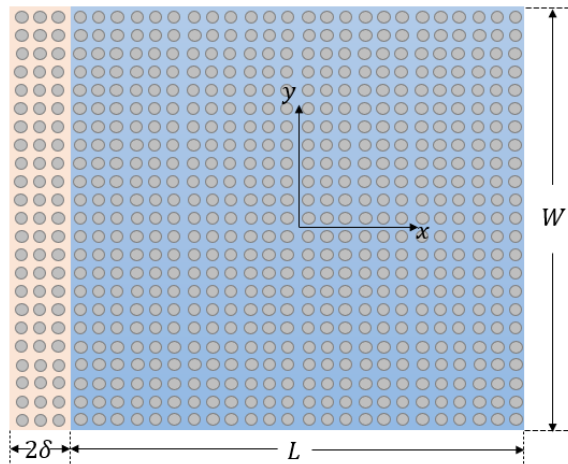


Fig. 4-5 Discretisation of the square plate.

### 4.3.2.1 Bond-based Peridynamics

The analysis begins with the bond-based formulation. Five different horizon sizes ( $\delta = n\Delta x$ ,  $n = 1,2,3,4,5$ ) are investigated. Owing to the nature of bond-based formulation for two-dimensional structure, Poisson's ratio is fixed at  $\tilde{\nu} = 1/3$ .

A monitoring point at (0.255 m, 0.255 m), distant from boundaries, is used to record horizontal and vertical displacements. The time histories of both horizontal and vertical displacements at this point are recorded throughout the simulation. Results are compared with FEM solutions.

As shown in Fig. 4-6 and Fig. 4-7, a close agreement between peridynamics and FEM is observed for  $\delta = 3\Delta x$  and  $\delta = 4\Delta x$ , indicating these as optimal choices for bond-based formulation for this dynamic case (square plate vibration).

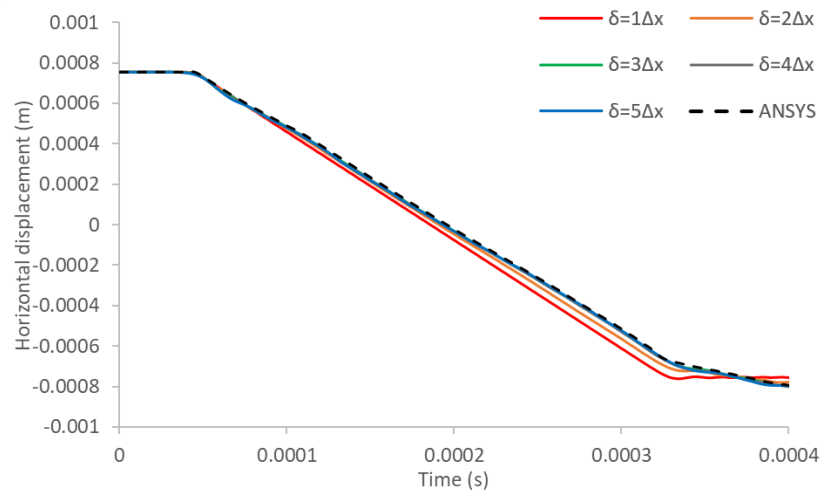
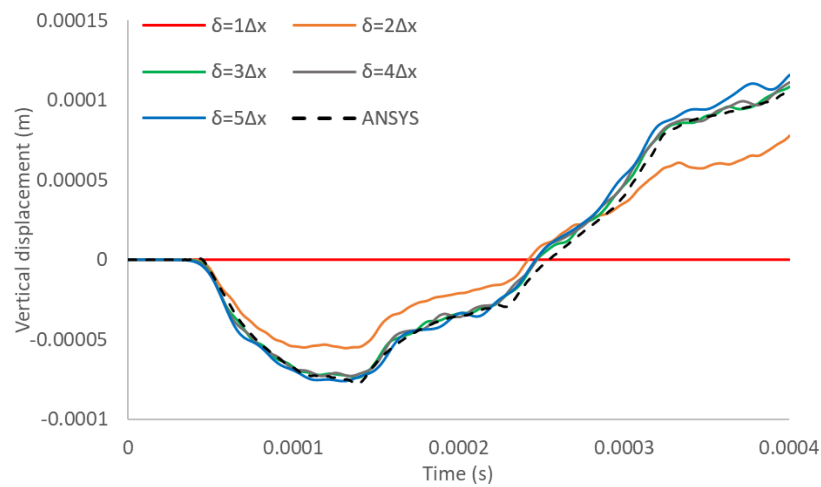


Fig. 4-6 Variation of horizontal displacement of the material point located at (0.255 m, 0.255 m) by using bond-based peridynamics.



*Fig. 4-7 Variation of vertical displacement of the material point located at (0.255 m, 0.255 m) with time by using bond-based Peridynamics*

#### 4.3.2.2 Ordinary State-based Peridynamics

For the ordinary state-based formulation, the restriction on Poisson's ratio is lifted; here,  $\tilde{\nu} = 0.25$  is used to avoid the formulation being reduced to bond-based peridynamics as explained in section 3.2.2. The same range of horizon sizes and monitoring point are adopted.

Fig. 4-8 and Fig. 4-9 compare the peridynamic predictions with the FEM. As observed, while horizontal displacements are captured closely for all horizon sizes, the vertical displacement is most closely predicted with  $\delta = 3\Delta x$  and  $\delta = 4\Delta x$ . For smaller horizons,  $\delta = 1\Delta x$  and  $\delta = 2\Delta x$ , the model fails to accurately capture the vertical displacement response.

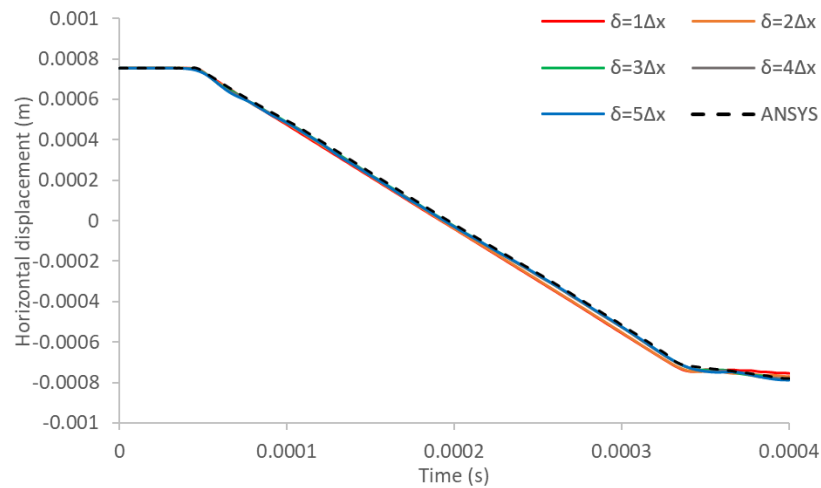


*Fig. 4-8 Variation of horizontal displacement of the material point located at (0.255 m, 0.255 m) by using ordinary state-based peridynamics.*

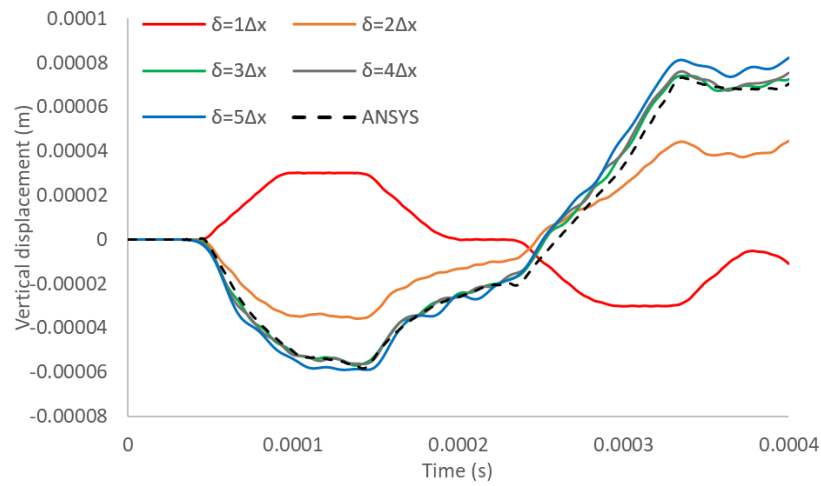


Fig. 4-9 Variation of vertical displacement of the material point located at (0.255 m, 0.255 m) with time by using ordinary state-based peridynamics.

#### 4.3.2.2 Non-ordinary State-based Peridynamics

The non-ordinary state-based analysis uses Poisson's ratio  $\tilde{\nu} = 1/3$ . As before, five horizon sizes are considered, and the same monitoring point is used. As presented in Fig. 4-10 and Fig. 4-18, a better agreement with FEM is found for the smaller horizons  $\delta = 1\Delta x$  and  $\delta = 2\Delta x$ , with increasing horizon size not yielding significant improvement and, in some cases, reducing accuracy.

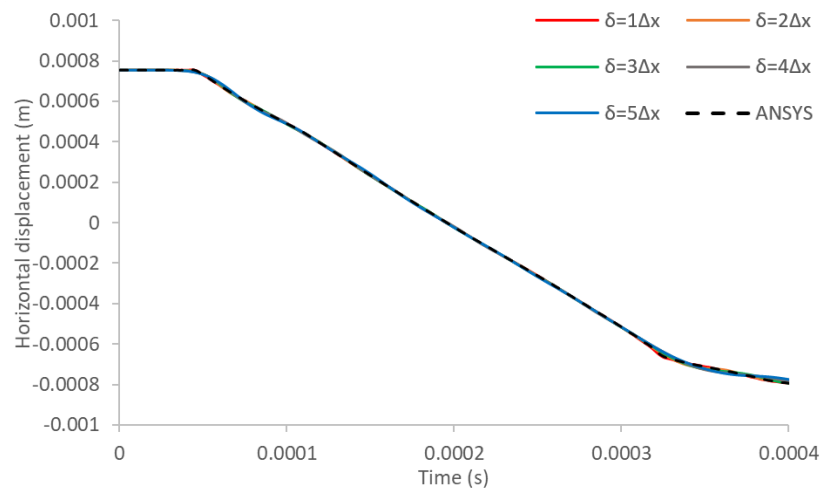


Fig. 4-10 Variation of horizontal displacement of the material point located at (0.255 m, 0.255 m) by using non-ordinary state-based peridynamics.

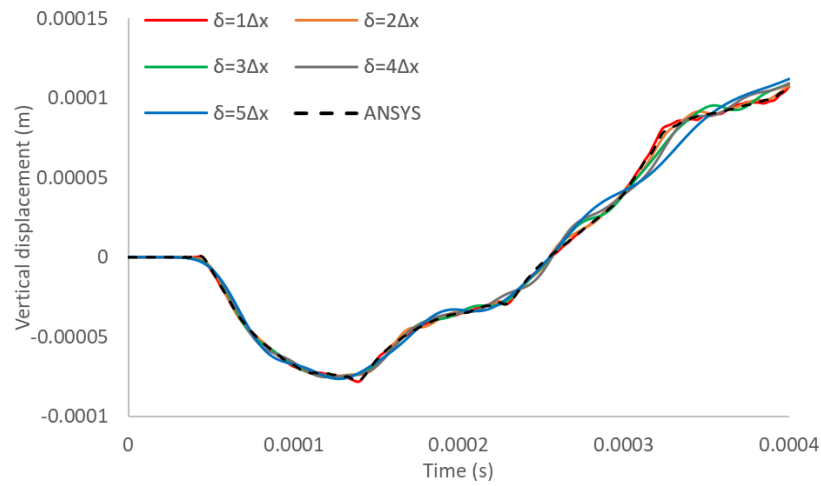


Fig. 4-11 Variation of vertical displacement of the material point located at  $(0.255\text{ m}, 0.255\text{ m})$  with time by using non-ordinary state-based peridynamics.

#### 4.3.3 Plate Under Tension

In the second case, the square plate described previously is subjected to uniaxial tensile loading, with a prescribed stress of  $\sigma^* = 200\text{ MPa}$  applied to the right edge, as shown in Fig. 4-12. The loading is implemented via a fictitious region at the right boundary (Fig. 4-13), following the methodology outlined in Section 4.2.3.2. The steady-state solution is obtained using the Adaptive Dynamic Relaxation technique (Underwood, 1983; Kilic and Madenci, 2010). All geometric, discretisation, and material properties remain as specified in the plate vibration case.

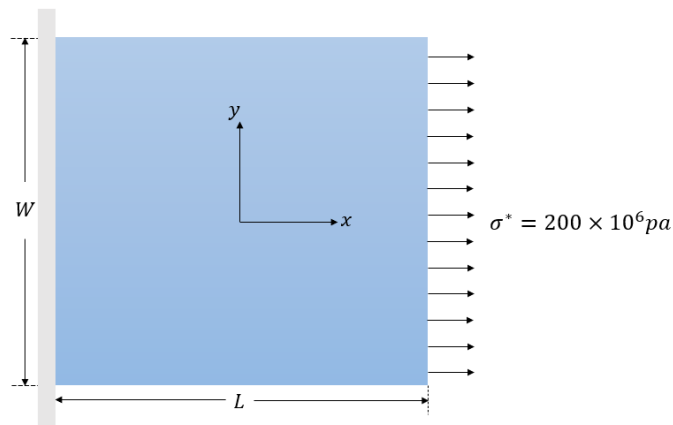


Fig. 4-12 Square plate subjected to uniaxial tension loading.

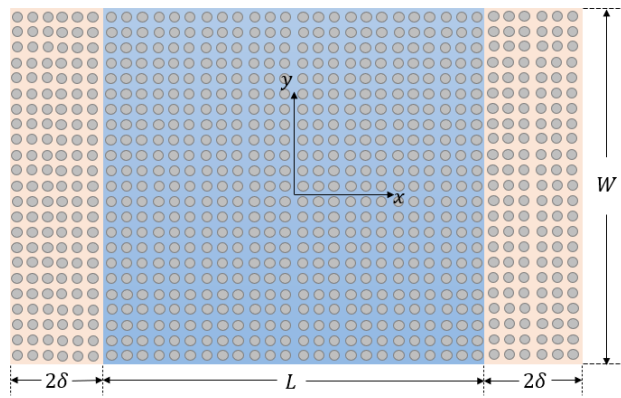


Fig. 4-13 Discretisation of the square plate.

#### 4.3.3.1 Bond-based Peridynamics

For the uniaxial tension problem, bond-based formulation is first employed. The horizontal and vertical displacements along the plate's central axes are evaluated for various horizon sizes and compared to FEM reference solutions.

As shown in Fig. 4-14 and Fig. 4-15, the closest agreement with FEM is achieved for horizon sizes  $\delta = 3\Delta x$ ,  $\delta = 4\Delta x$ , and  $\delta = 5\Delta x$ . For smaller horizon sizes, discrepancies arise in both displacement components. These results confirm the findings from the dynamic vibration analysis; an intermediate horizon size (three to four times the grid spacing) optimally balances accuracy and efficiency in bond-based simulations.

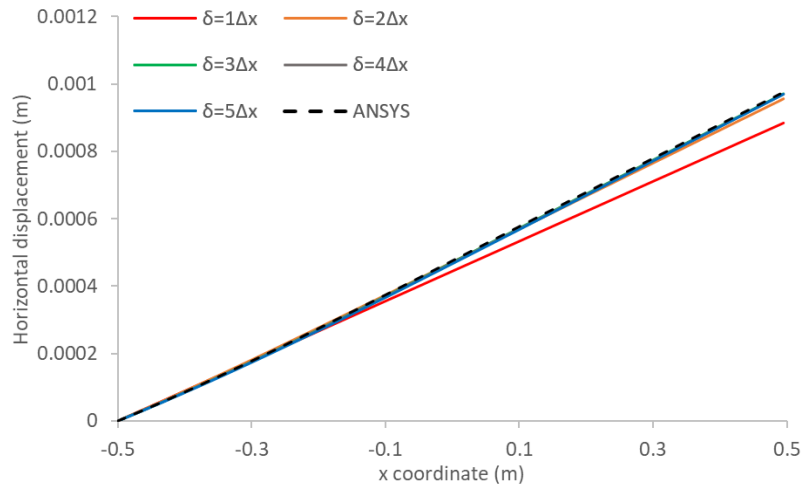


Fig. 4-14 Horizontal displacement along  $(x, y=0)$  by using bond-based peridynamics.

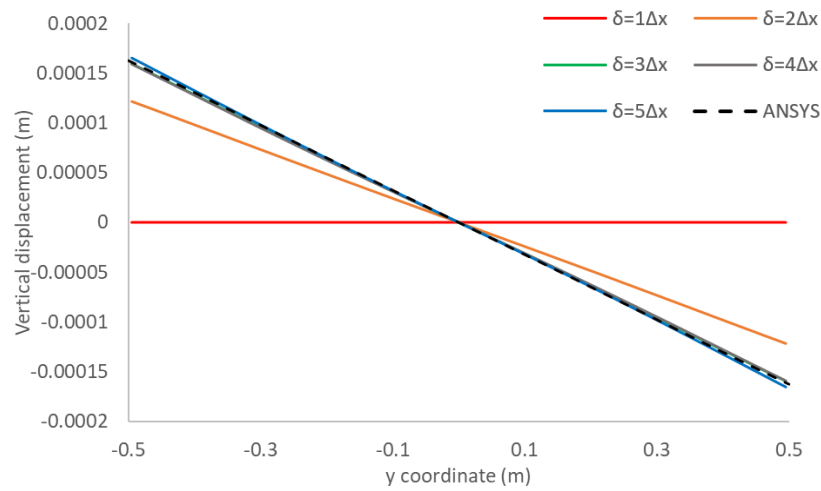


Fig. 4-15 Vertical displacement along  $(x=0, y)$  by using bond-based peridynamics.

#### 4.3.3.2 Ordinary State-based Peridynamics

The ordinary state-based formulation is next applied. As shown in Fig. 4-16 and Fig. 4-17, the simulation results reveal that horizon size values of  $\delta = 3\Delta x$ ,  $\delta = 4\Delta x$ , and  $\delta = 5\Delta x$  offer a better agreement with the FEM solutions. In contrast, smaller horizons  $\delta = 1\Delta x$  and  $\delta = 2\Delta x$  do not sufficiently capture the static vertical displacement field, which is consistent with the observations made for the dynamic (vibration) case.

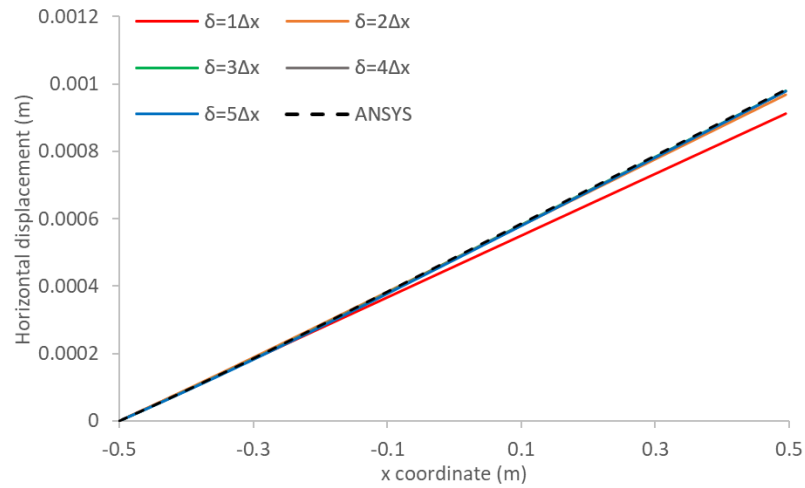


Fig. 4-16 Horizontal displacement along  $(x, y=0)$  by using ordinary state-based peridynamics.

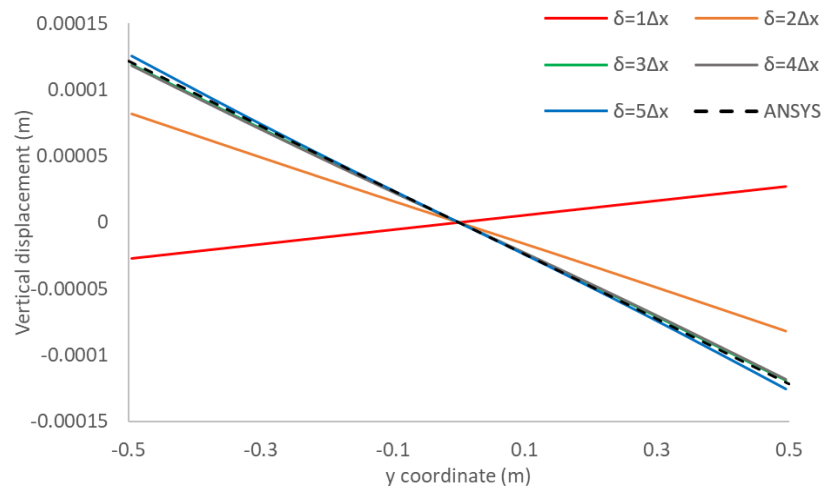


Fig. 4-17 Vertical displacement along ( $x=0, y$ ) by using ordinary state-based peridynamics.

#### 4.3.3.3 Non-ordinary State-based Peridynamics

Finally, the non-ordinary state-based peridynamic model is assessed. As observed previously in the vibration case, this formulation achieves close correspondence with FEM solutions for all tested horizon sizes (see Fig. 4-18 and Fig. 4-19). However, the best agreement is observed for the smallest horizons  $\delta = 1\Delta x$  and  $\delta = 2\Delta x$ , suggesting that smaller horizons suffice to accurately capture the static response. Larger horizons ( $\delta = 3\Delta x, 4\Delta x,$  and  $5\Delta x$ ) also yield reliable results, but the best match is observed at the lower end of the tested range.

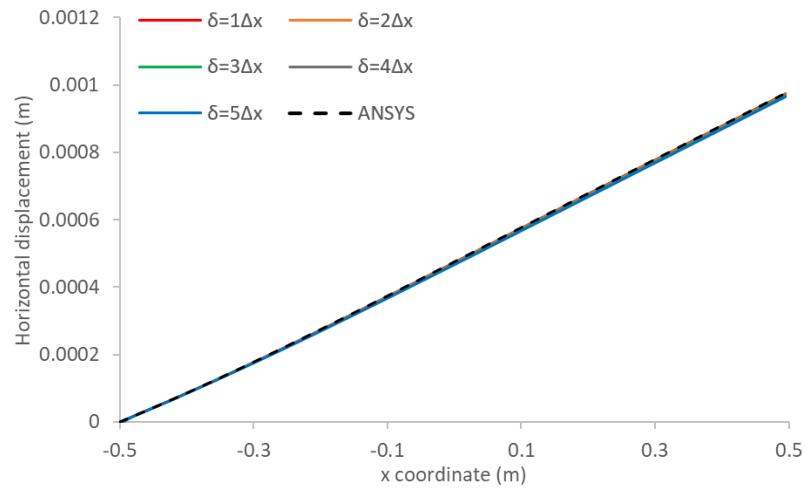


Fig. 4-18 Horizontal displacement along ( $x, y=0$ ) by using non-ordinary state-based peridynamics.

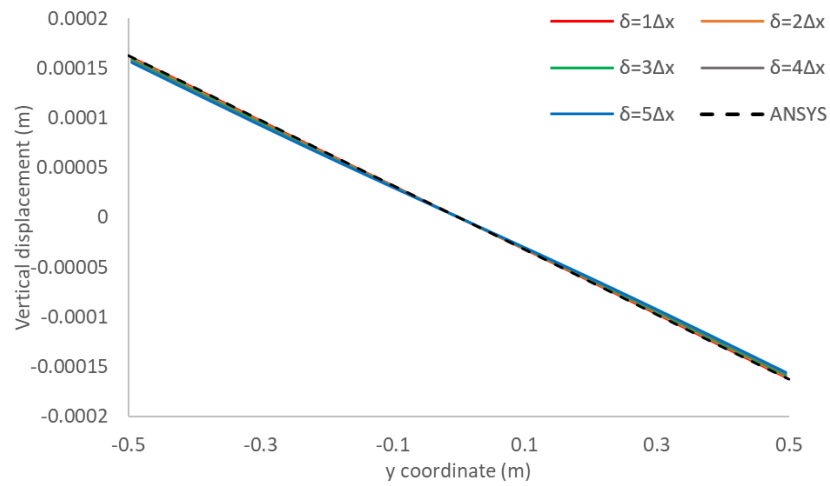


Fig. 4-19 Vertical displacement along ( $x=0, y$ ) by using non-ordinary state-based peridynamics.

#### 4.3.4 Vibration of a Cubic Block

The third benchmark investigates the dynamic response of a three-dimensional cubic block subjected to uniform discretisation. As represented in Fig. 4-20, the block has dimensions  $L = H = W = 0.3$  m and is initially loaded with a uniaxial strain of 0.001 in horizontal direction. The left face is fully constrained using a fictitious region, as shown in Fig. 4-21, while all remaining faces are traction-free. The block is modelled as a linear, elastic, homogeneous material, with Young’s modulus  $E = 200$  GPa and density  $\rho = 7850$  kg/m<sup>3</sup>. Poisson’s ratio is taken as 0.25 for bond-based simulations, and non-ordinary state-based simulations, and 1/3 for ordinary state-based simulations.

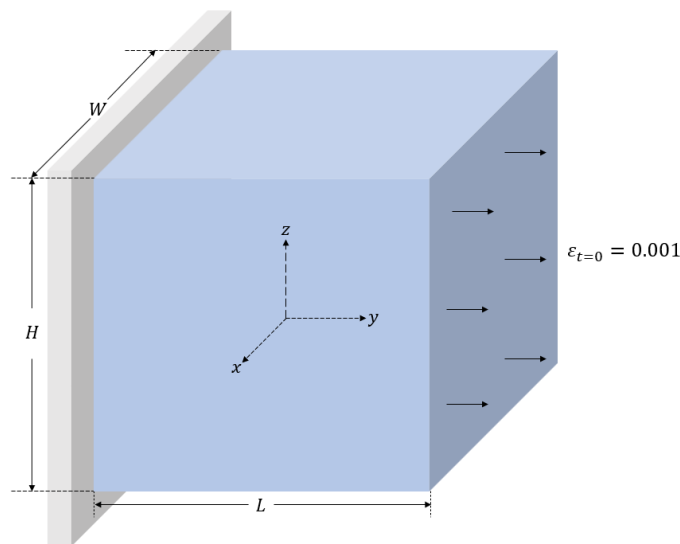


Fig. 4-20 Three-dimensional block subjected to initial uniaxial strain condition.

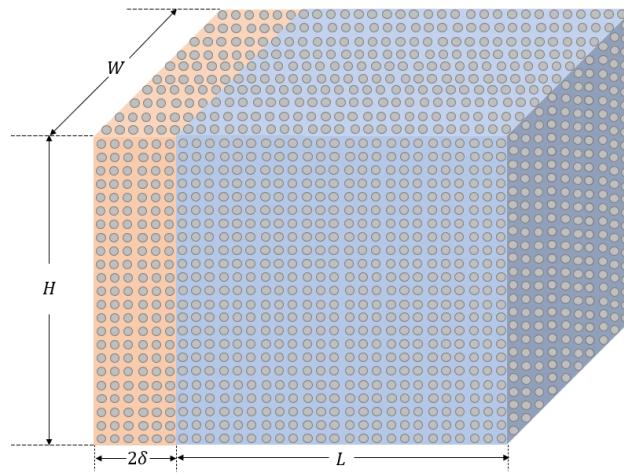


Fig. 4-21 Discretisation of the block.

For computational efficiency, the domain is discretised uniformly with a grid size of  $\Delta x = 0.005$  m, resulting in a computational mesh of  $60 \times 60 \times 60$  material points. Explicit time integration is used with a time step of  $1 \times 10^{-7}$  s. The effect of horizon size is systematically evaluated by expressing  $\delta$  as an integer multiple of  $\Delta x$ .

#### 4.3.4.1 Bond-based Peridynamics

In the bond-based simulation, the response at a representative internal material point (0.0775 m, 0.0775 m, 0.0775 m) is monitored. The histories of the horizontal, transverse, and vertical displacement components ( Fig. 4-22, Fig. 4-23 and Fig. 4-24) demonstrate that a horizon size of  $\delta = 3\Delta x$  yields a better agreement with FEM reference results.

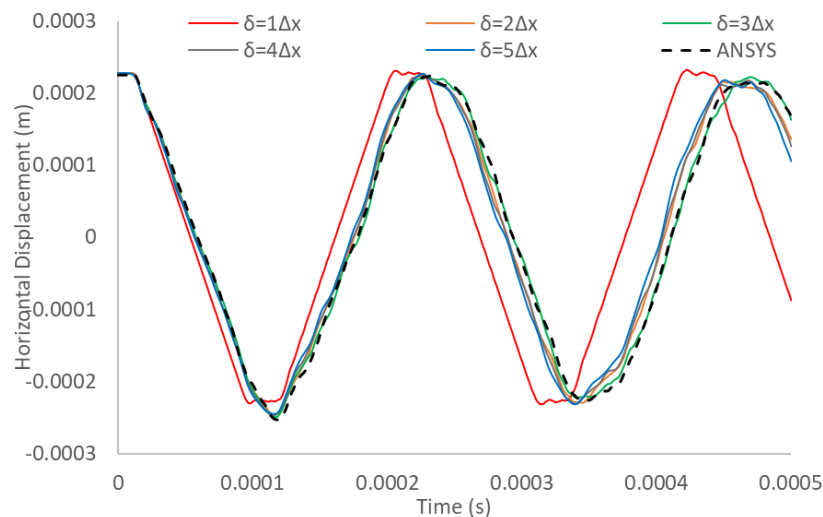
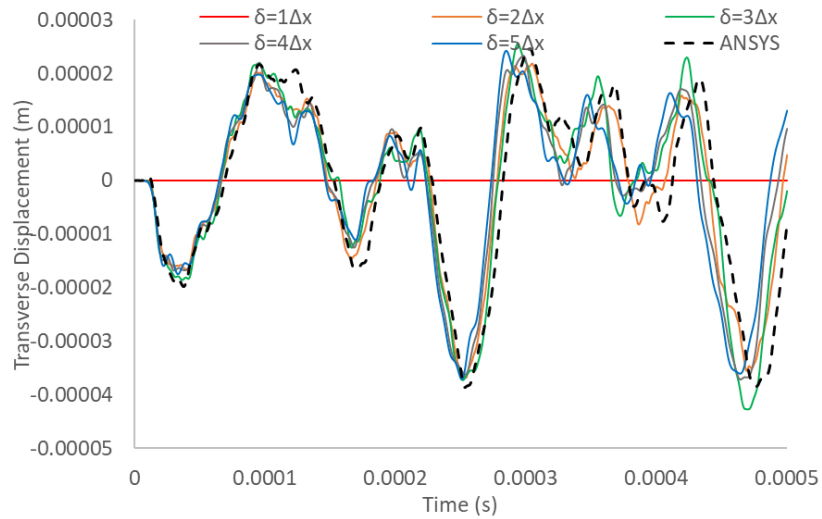
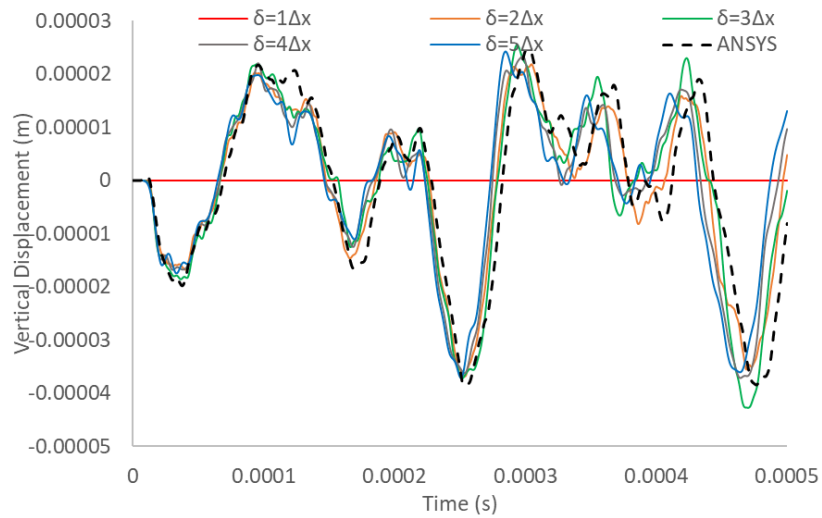


Fig. 4-22 Variation of horizontal displacement of the material point located at (0.0775 m, 0.0775 m, 0.0775 m) with time by using bond-based peridynamics.



*Fig. 4-23 Variation of transverse displacement of the material point located at (0.0775 m, 0.0775 m, 0.0775 m) with time by using bond-based peridynamics.*



*Fig. 4-24 Variation of vertical displacement of the material point located at (0.0775 m, 0.0775 m, 0.0775 m) with time by using bond-based peridynamics.*

It is noted, that as the time progresses, discrepancies between peridynamic and FEM results increase. This accumulation of error over time is primarily attributed to the relatively coarse discretisation required to keep the computational cost reasonable in three dimensions. With fewer material points, small numerical errors can accumulate and affect the later stages of the simulation. As such, early-time simulation results are more reliable for determining the optimal horizon size.

In comparison, this issue is less pronounced in two-dimensional cases where finer meshes can be used. Overall, for 3D dynamic simulations using bond-based

formulation, a horizon size of  $\delta = 3\Delta x$  continues to offer a good compromise between accuracy and computational cost.

#### 4.3.4.2 Ordinary State-based Peridynamics

The ordinary state-based peridynamic formulation produces similar trends. Displacement histories at the monitoring point for all three components are shown in Fig. 4-25 to Fig. 4-27. The results indicate that a better agreement with FEM is again achieved for  $\delta = 3\Delta x$ . While other horizon sizes can also produce reasonable results, the  $\delta = 3\Delta x$  case consistently shows the close match for both the amplitude and phase of the displacement histories.

As in the bond-based case, the error relative to FEM increases at later simulation times, reflecting the influence of the coarser discretisation in three dimensions. These findings suggest the recommendation of  $\delta = 3\Delta x$  for accurate and efficient modelling with ordinary state-based peridynamics.

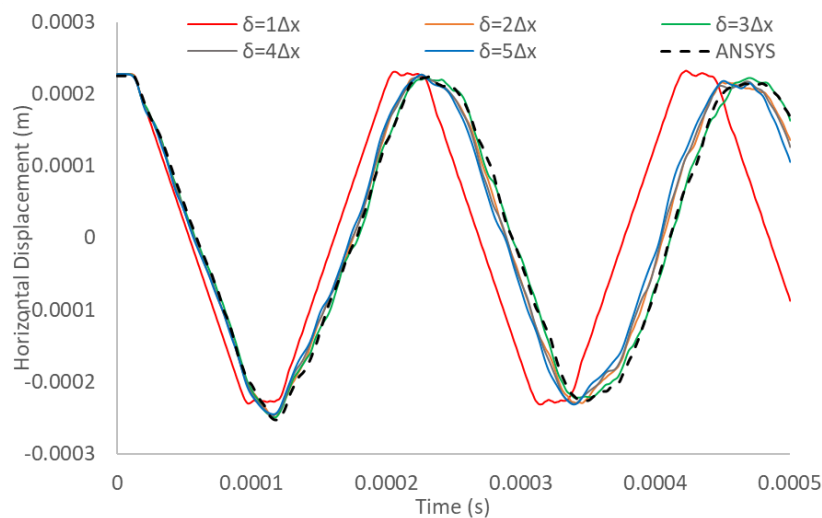


*Fig. 4-25 Variation of horizontal displacement of the material point located at (0.0775 m, 0.0775 m, 0.0775 m) with time by using ordinary state-based peridynamics.*

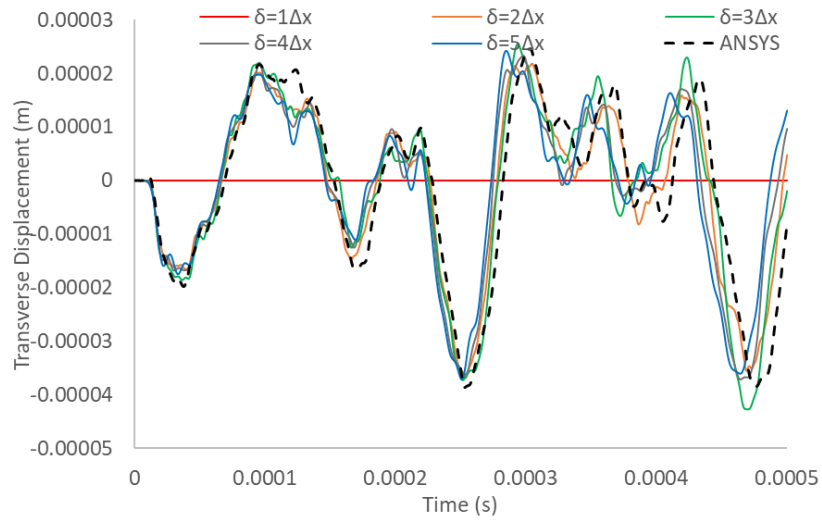


*Fig. 4-26 Variation of transverse displacement of the material point located at (0.0775 m, 0.0775 m, 0.0775 m) with time by using ordinary state-based peridynamics.*

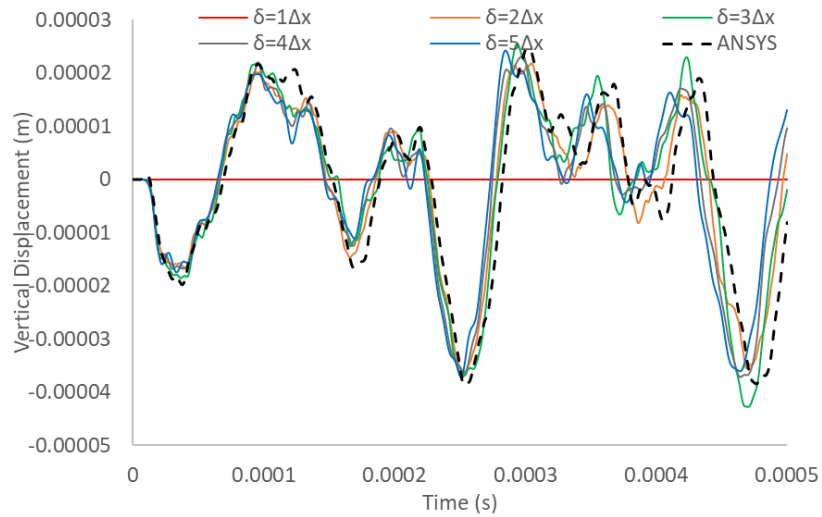


*Fig. 4-27 Variation of vertical displacement of the material point located at (0.0775 m, 0.0775 m, 0.0775 m) with time by using ordinary state-based peridynamics.*

#### 4.3.4.3 Non-ordinary State-based Peridynamics

For the non-ordinary state-based formulation, displacement time histories for the horizontal, transverse, and vertical components at the monitoring point are shown in Fig. 4-38, Fig. 4-39 and Fig. 4-40. The results indicate that all horizon size values provide reasonably agreement with the reference FEM solution, capturing both the amplitude and phase of the dynamic response across all displacement components.

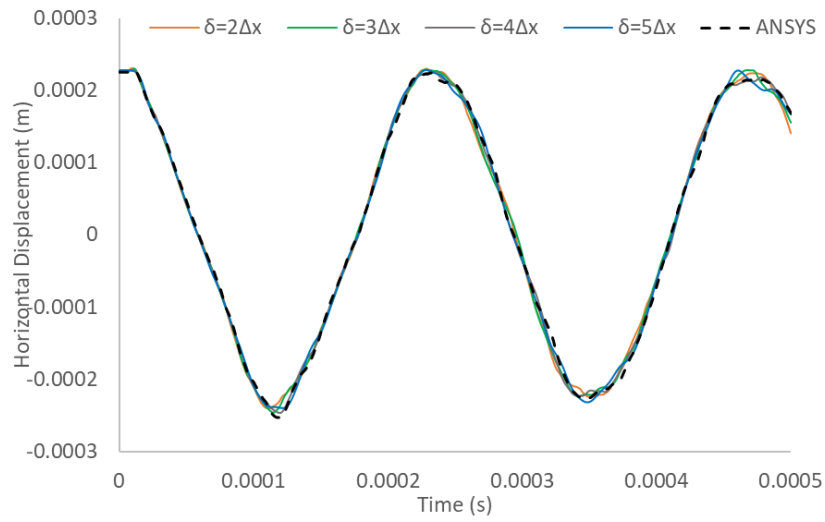


*Fig. 4-28 Variation of horizontal displacement of the material point located at (0.0775 m, 0.0775 m, 0.0775 m) with time by using non-ordinary state-based peridynamics.*

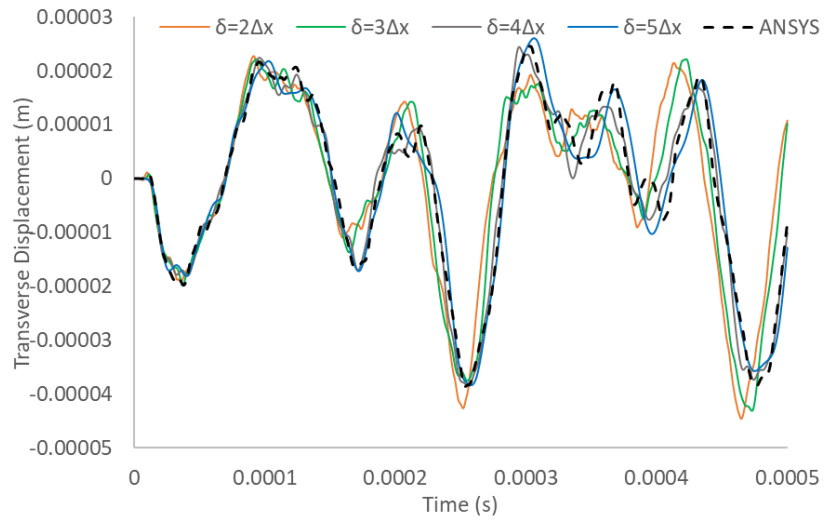


*Fig. 4-29 Variation of transverse displacement of the material point located at (0.0775 m, 0.0775 m, 0.0775 m) with time by using non-ordinary state-based peridynamics.*

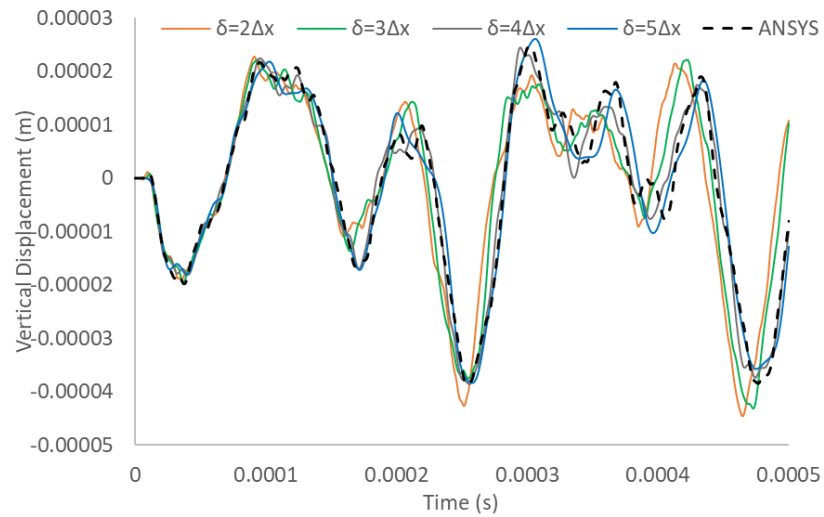


Fig. 4-30 Variation of vertical displacement of the material point located at (0.0775 m, 0.0775 m, 0.0775 m) with time by using non-ordinary state-based peridynamics.

#### 4.3.5 Cubic Block Under Tension

For the static analysis, the same three-dimensional block geometry, material properties, and uniform discretisation adopted in the vibration study are used. As illustrated in Fig. 4-31, the block is subjected to a uniaxial tensile loading of  $\sigma^* = 200$  MPa applied at the right face. The loading is implemented through a fictitious region at the boundary of the right face, following the procedure outlined in Section 4.3.3.2 and depicted in Fig. 4-32. The left face of the block is fully constrained, while all other surfaces are traction-free. The steady-state response is obtained using the Adaptive Dynamic Relaxation technique (Underwood, 1983; Kilic and Madenci, 2010), with a time step size  $\Delta t=1$  s.

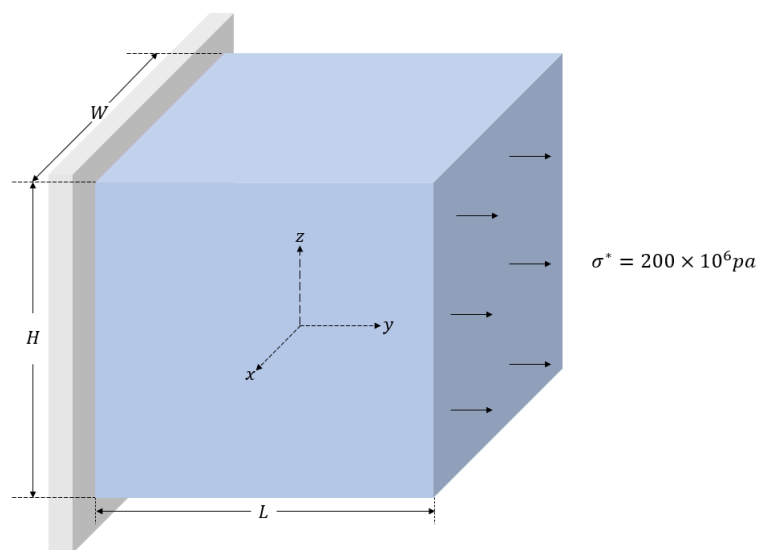


Fig. 4-31 A three-dimensional block subjected to uniaxial tension loading.

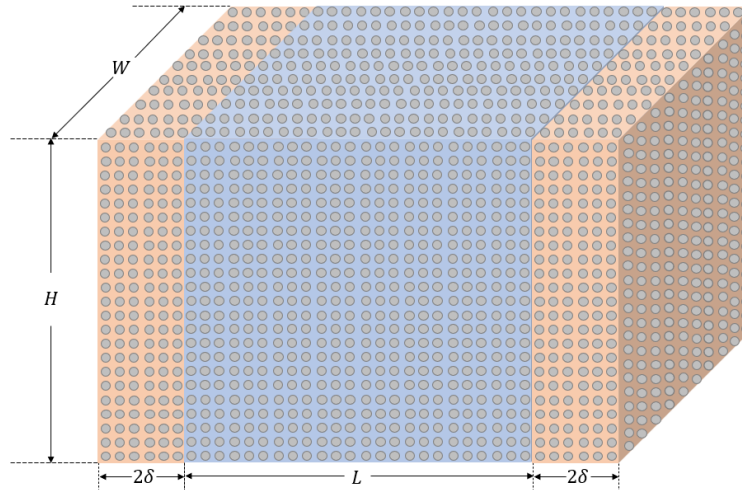


Fig. 4-32 Discretisation of the block.

#### 4.3.5.1 Bond-based Peridynamics

The effect of horizon size on the displacement field is first examined using the bond-based formulation. The horizontal, transverse, and vertical displacement distributions along the respective central axes of the block are computed and compared against FEM reference solutions.

As shown from Fig. 4-33 to Fig. 4-35, the peridynamic predictions exhibit good agreement with the FEM results for all displacement components when the horizon size is greater than or equal to  $2\Delta x$ . In contrast, the smallest horizon size ( $\delta = 1\Delta x$ ) fails to capture the correct displacement behaviour.

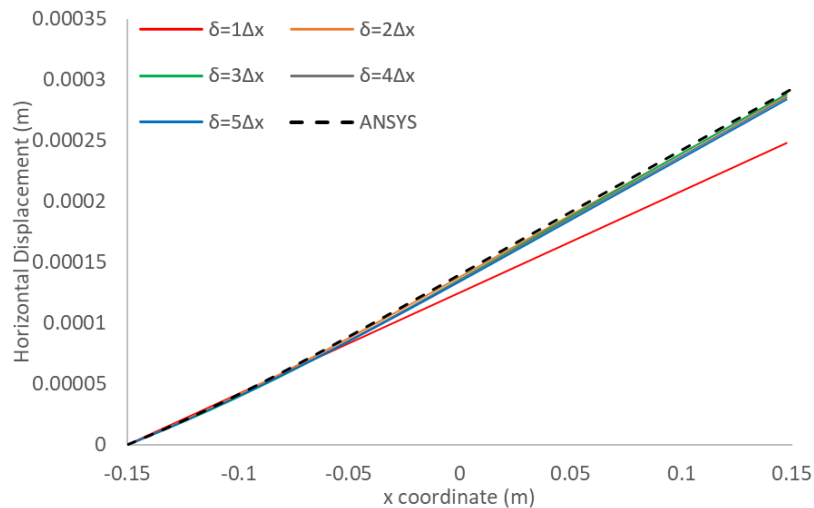


Fig. 4-33 Horizontal displacement variations along  $(x, y=0, z=0)$  by using bond-based peridynamics.

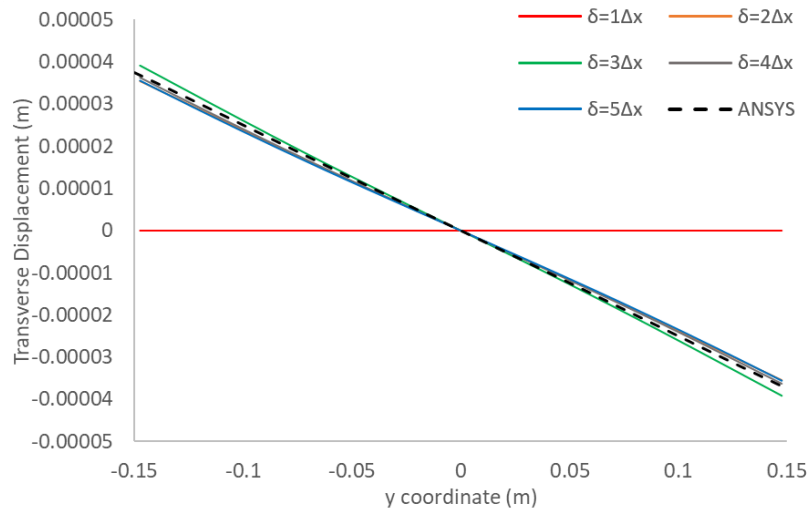


Fig. 4-34 Transverse displacement variations along ( $x=0, y, z=0$ ) by using bond-based peridynamics.

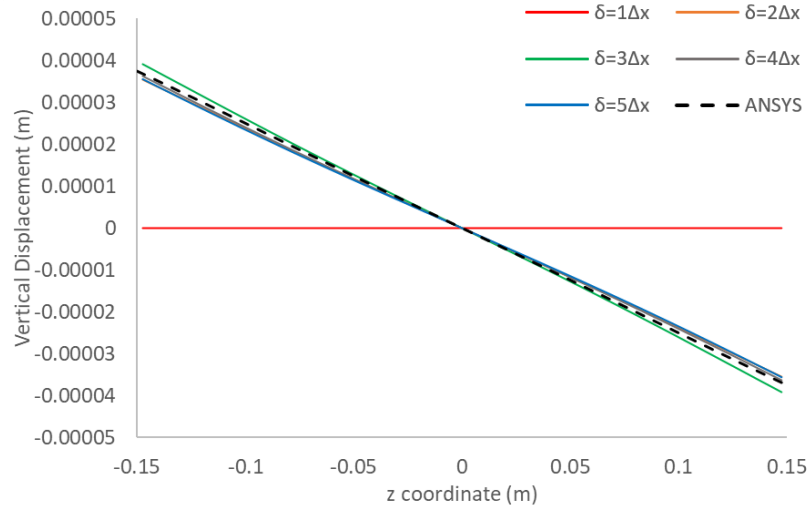


Fig. 4-35 Vertical displacement variations along ( $x=0, y=0, z$ ) by using bond-based peridynamics.

#### 4.3.5.2 Ordinary State-based Peridynamics

The ordinary state-based formulation demonstrates a similar trend to the bond-based formulation. Displacement distributions for the horizontal, transverse, and vertical components are evaluated along the central axes for the same set of horizon sizes. As illustrated in from Fig. 4-36 to Fig. 4-38, the peridynamic results show good agreement with FEM solutions for all horizon sizes except  $\delta = 1\Delta x$ . The best correspondence is observed for  $\delta = 3\Delta x$  corroborating the findings from the two-dimensional simulations.

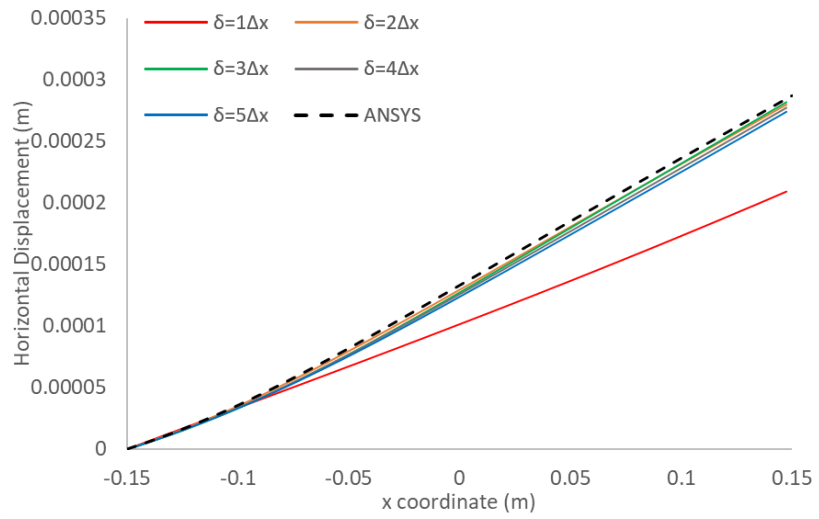


Fig. 4-36 Horizontal displacement variations along ( $x, y=0, z=0$ ) by using ordinary state-based peridynamics.

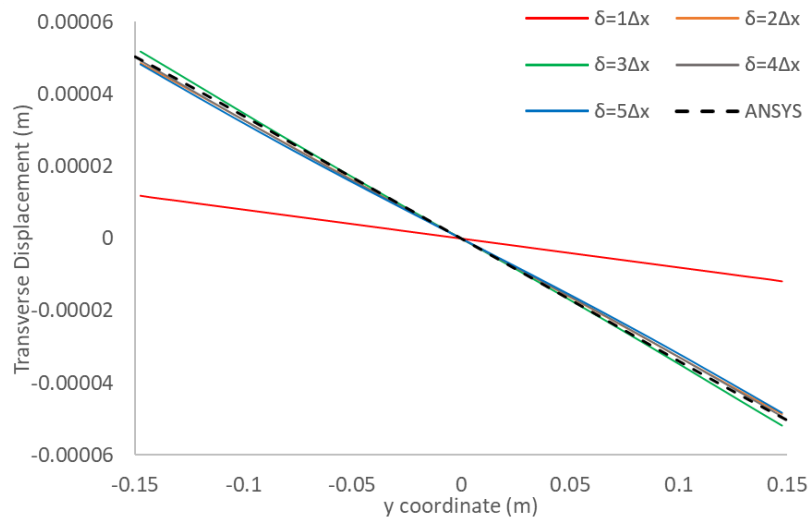


Fig. 4-37 Transverse displacement variations along ( $x=0, y, z=0$ ) by using ordinary state-based peridynamics.

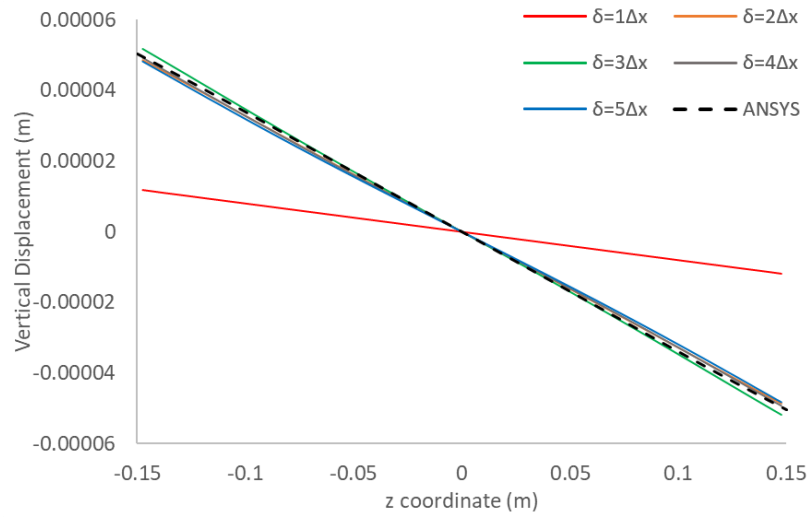


Fig. 4-38 Vertical displacement variations along ( $x=0, y=0, z$ ) by using ordinary state-based peridynamics.

#### 4.3.5.3 Non-ordinary State-based Peridynamics

Finally, the non-ordinary state-based formulation is assessed. Displacement profiles along the central axes are computed for a range of horizon sizes and compared to FEM results. As shown in Fig. 4-39, Fig. 4-40 and Fig. 4-41, all horizon sizes except for  $\delta = 1\Delta x$  exhibit close agreement with the FEM results. Specifically, a horizon size of  $\delta = 2\Delta x$  provides an optimal solution, accurately capturing the displacement behaviour in all directions.

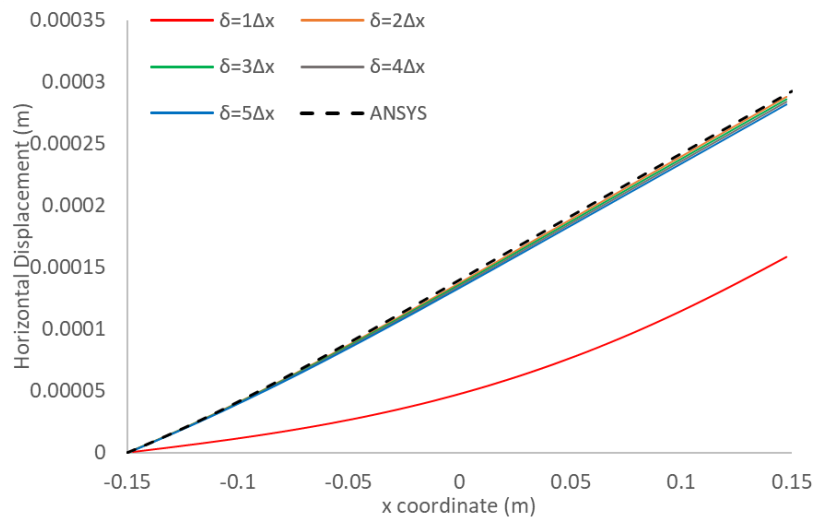


Fig. 4-39 Horizontal displacement variations along ( $x, y=0, z=0$ ) by using non-ordinary state-based peridynamics.

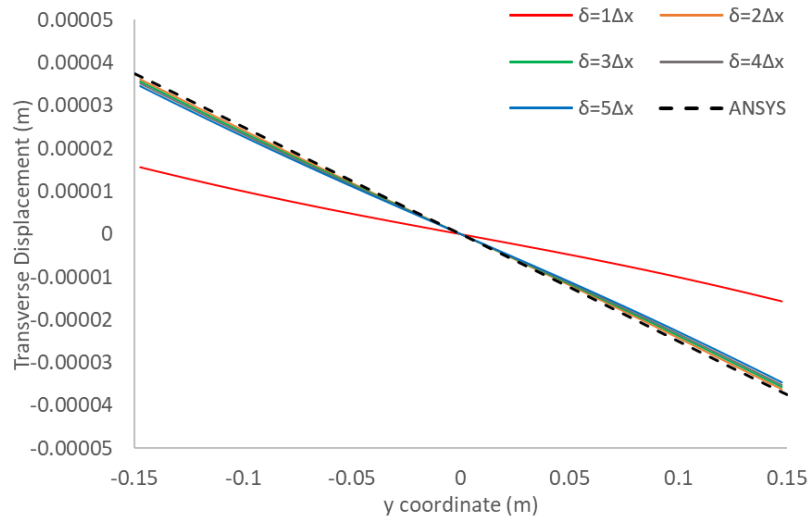


Fig. 4-40 Transverse displacement variations along ( $x=0, y, z=0$ ) by using non-ordinary state-based peridynamics.

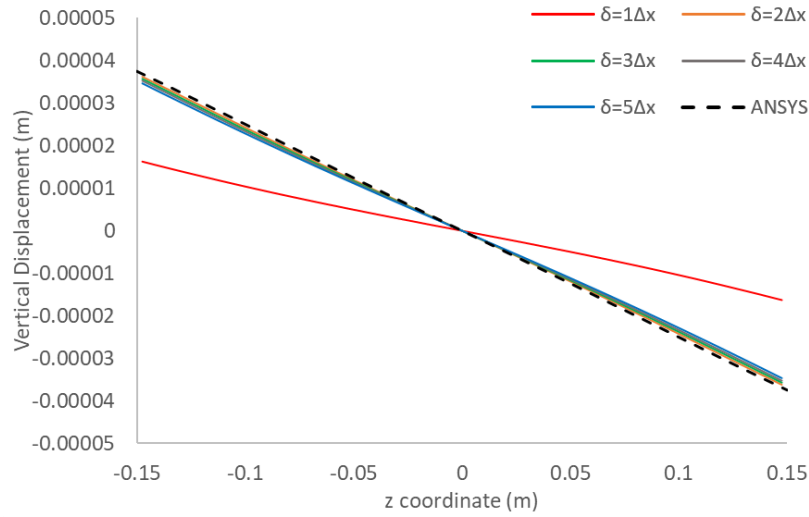


Fig. 4-41 Vertical displacement variations along ( $x=0, y=0, z$ ) by using non-ordinary state-based peridynamics.

#### 4.3.6 Comparative Results of Ordinary State-based Peridynamics, Non-ordinary State-based Peridynamics, and FEM

To provide a direct comparison under identical settings, additional results are presented for the 2D plate in vibration and in tension with Poisson's ratio fixed at  $\tilde{\nu} = 1/3$  for both the ordinary state-based and non-ordinary state-based formulations. This choice matches the fixed Poisson's ratio of bond-based peridynamics in 2D, so the bond-based elastic response is effectively represented by the ordinary state-based curves at  $\tilde{\nu} = 1/3$ ; the bond-based curves are therefore omitted to avoid clutter.

The comparisons are performed with the same discretisation and material parameters and with the horizon set to the formulation-specific optimum identified earlier:  $\delta = 3\Delta x$  for ordinary state-based formulations and  $\delta = 2\Delta x$  for non-ordinary state-based formulations. The same trends were observed in the corresponding 3D studies, so 2D comparisons are reported here for brevity.

#### 4.3.6.1 Vibration of a Plate

Fig. 4-42 and Fig. 4-43 show the horizontal and vertical displacement time histories of the material point located at (0.255 m,0.255 m), obtained using ordinary state-based peridynamics, non-ordinary state-based peridynamics, and FEM. Both formulations reproduce the FEM results closely in terms of horizontal displacement. In the vertical displacement, non-ordinary state-based peridynamics provides slightly improved agreement despite employing a smaller horizon.

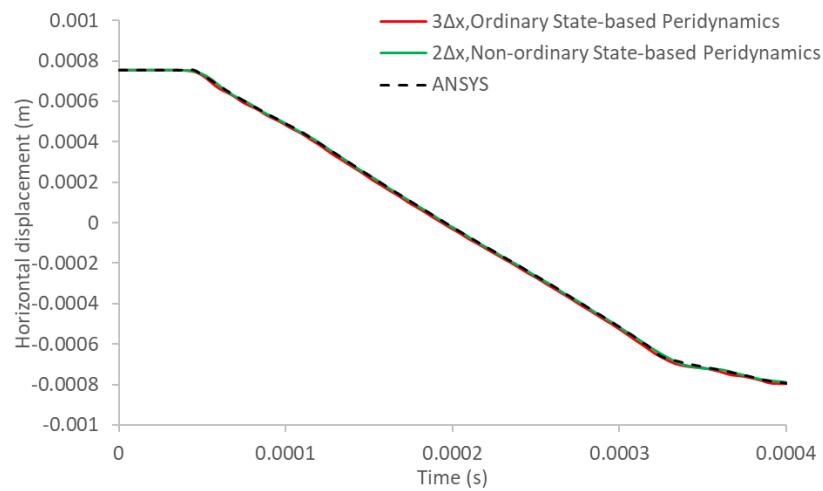


*Fig. 4-42 Variation of horizontal displacement of the material point located at (0.255 m,0.255 m) at optimum horizon size for Ordinary State-based Peridynamics and Non-ordinary State-Based Peridynamics.*

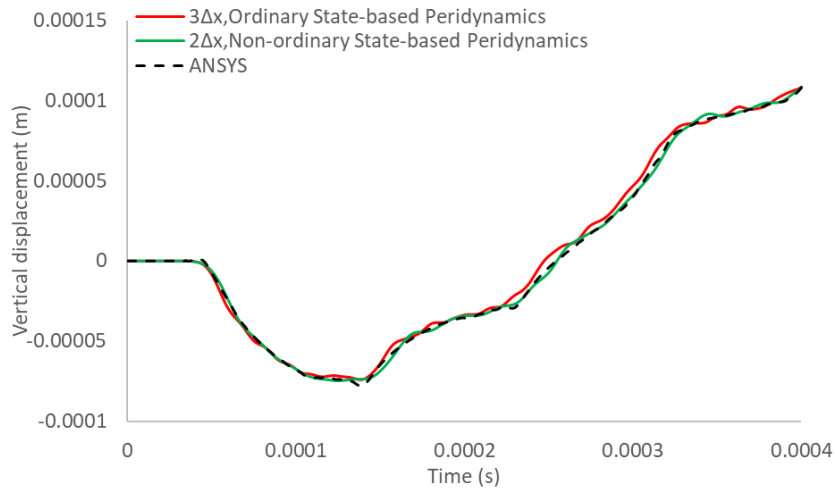


*Fig. 4-43 Variation of vertical displacement of the material point located at (0.255m,0.255m) at optimum horizon size for Ordinary State-based Peridynamics and Non-ordinary State-Based Peridynamics.*

#### 4.3.6.1 Plate Under Tension

Fig. 4-44 and Fig. 4-45 present the horizontal and vertical displacement distributions along the midlines of the plate under uniform tension, obtained using ordinary state-based peridynamics, non-ordinary state-based peridynamics, and FEM at their respective optimum horizon sizes. In both cases, the peridynamic predictions are in good agreement with FEM, with nearly coincident displacement profiles.

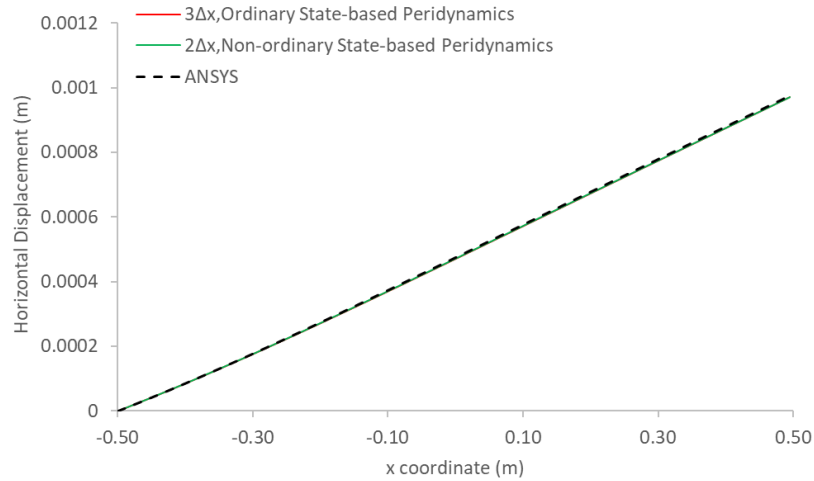


*Fig. 4-44 Horizontal displacement along (x, y=0) by using Ordinary State-based Peridynamics and Non-ordinary State-Based Peridynamics at their optimum horizon sizes.*

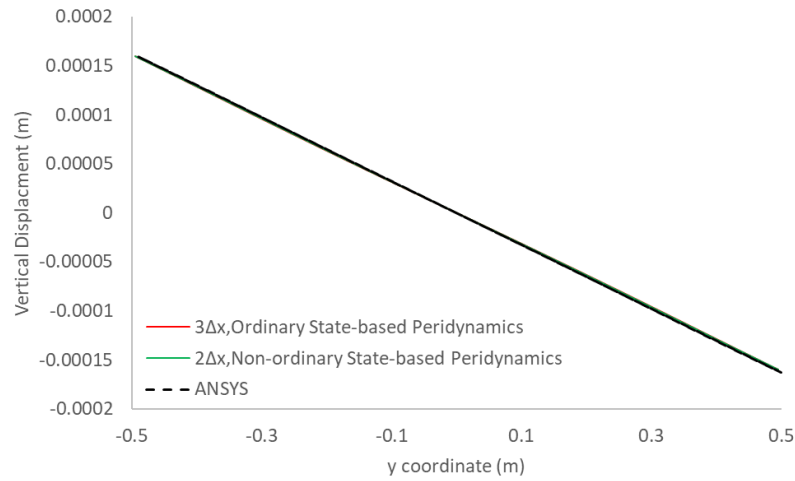


*Fig. 4-45 Vertical displacement along ( $x=0$ ,  $y$ ) by using Ordinary State-based Peridynamics and Non-ordinary State-Based Peridynamics at their optimum horizon sizes.*

In summary, the choice of peridynamic formulation depends on the balance between simplicity, flexibility, and computational cost. The bond-based model is the simplest and computationally most efficient, but its limitations include a fixed Poisson's ratio ( $\tilde{\nu} = 1/3$  in 2D and  $\tilde{\nu} = 0.25$  in 3D) and the inability to capture more complex material responses. The ordinary state-based formulation removes this restriction by decoupling volumetric and deviatoric contributions, enabling a wider range of Poisson's ratios while retaining moderate efficiency. The non-ordinary state-based formulation provides the generality by lifting the requirement that forces act along bonds, allowing established constitutive models from classical continuum mechanics to be incorporated directly into the peridynamic framework. However, this increased versatility comes at a higher computational cost.

Accordingly, bond-based peridynamics may be suitable for simple, proof-of-concept studies, ordinary state-based peridynamics for structural problems requiring flexibility in Poisson's ratio, and non-ordinary state-based peridynamics for applications involving complex materials.

#### **4.4 Chapter Summary**

This chapter presented a systematic numerical investigation of horizon size effects in peridynamic models, focusing on uniform discretisation for both two- and three-dimensional structures subjected to static and dynamic loading. Through detailed comparison of bond-based, ordinary state-based, and non-ordinary state-based

peridynamics with reference FEM solutions, the optimal horizon size for each formulation is revealed as in the Table 4-1.

*Table 4-1 Summary of optimal horizon sizes for different peridynamic formulations in 2D and 3D*

Peridynamic models	2D	3D
Bond-based Peridynamics	$\delta = 3\Delta x$	$\delta = 3\Delta x$
Ordinary State-based Peridynamics	$\delta = 3\Delta x$	$\delta = 3\Delta x$
Non-ordinary State-based Peridynamics	$\delta = 2\Delta x$	$\delta = 2\Delta x$

For both the 2D plate and 3D block cases, the analyses demonstrated that bond-based and ordinary state-based peridynamics achieve good agreement with FEM solutions when the horizon size is set to three times the grid spacing ( $\delta = 3\Delta x$ ). By contrast, the non-ordinary state-based formulation consistently delivers accurate displacement and stress predictions with smaller horizons, with  $\delta = 2\Delta x$  identified as optimal for both static and dynamic scenarios. It was also observed that increasing the horizon size beyond these optimal values does not significantly improve accuracy and can incur unnecessary computational cost.

Another important finding is the increased sensitivity of three-dimensional simulations to numerical errors arising from coarse discretisation, mostly in dynamic analyses. Consequently, early-time responses provide a more reliable basis for horizon size assessment in dynamic problems, whereas static cases are less affected by discretisation-induced errors.

In summary, the findings of this chapter offer practical guidance for horizon size selection in peridynamic modelling with uniform discretisation. For most engineering applications, a horizon size of three times the grid spacing is recommended for bond-based and ordinary state-based formulations, while a value of two times the grid spacing is sufficient for non-ordinary state-based peridynamics. These insights are expected to contribute to more reliable and efficient peridynamic modelling in future research.

## Chapter 5 Derivation of Dual-horizon Peridynamics Formulation

### 5.1 Introduction

While the previous chapter discussed guidelines for horizon size selection in peridynamics using uniform discretisation, many engineering problems may require non-uniform meshes to capture complex geometries or local features. Although uniform discretisation is easy to implement, it increases computational time for some applications, as only certain parts of the solution domain require a finer discretisation, while other parts can be discretised using a coarser mesh. Non-uniform discretisation, therefore, offers benefits in terms of both computational efficiency and modelling flexibility. In addition to non-uniform discretisation, the horizon size can also be different at different parts of the solution domain, either to reduce the computational time or to capture the correct physics of the problem.

In this chapter, a new derivation of the dual-horizon peridynamics formulation is presented, using the Euler-Lagrange equations as a theoretical basis. The effectiveness of this approach is demonstrated through numerical verification on two benchmark problems: a plate under tension and a plate undergoing vibration, both discretised with non-uniform meshes and variable horizon sizes.

### 5.2 Dual-horizon Peridynamics Formulation Based on Euler-Lagrange equation

The equation of motion for a material point  $k$  at location  $\mathbf{x}_k$  in the reference configuration can be expressed as (Madenci and Oterkus, 2013)

$$\frac{d}{dt} \left( \frac{\partial L}{\partial \dot{\mathbf{u}}_k} \right) - \frac{\partial L}{\partial \mathbf{u}_k} = 0 \quad (5.1)$$

where  $L$  denotes the Lagrangian, defined as the difference between the total kinetic energy,  $T$ , and the total potential energy,  $U$ , of the body.

In the peridynamic framework, the total kinetic energy is evaluated as the sum over all material points as

$$T = \sum_i \frac{1}{2} \rho_i \dot{\mathbf{u}}_i \cdot \dot{\mathbf{u}}_i V_i \quad (5.2)$$

where  $\rho_i$  is the density and  $V_i$  is the volume associated with material point  $i$ .

The total potential energy,  $U$ , is defined as the difference between the total strain energy and the work done by external forces

$$U = \sum_i W_i V_i - \sum_i (\mathbf{b}_i \cdot \mathbf{u}_i) V_i \quad (5.3)$$

where,  $\mathbf{b}_i$  is the body force per unit volume acting on material point  $i$ .

The strain energy density,  $W_k$ , for a given material point  $k$  is defined as (Madenci and Oterkus, 2013)

$$W_k = \frac{1}{2} \sum_{j=1}^{N_k} \frac{1}{2} \left\{ \begin{array}{l} \omega_{kj} [\mathbf{y}_{(1^k)} - \mathbf{y}_{(k)}, \dots, \mathbf{y}_{(N_k^k)} - \mathbf{y}_{(k)}] + \\ \omega_{jk} [\mathbf{y}_{(1^j)} - \mathbf{y}_{(j)}, \dots, \mathbf{y}_{(N_j^j)} - \mathbf{y}_{(j)}] \end{array} \right\} V_j \quad (5.4)$$

where  $N_k$  and  $N_j$  are the number of family members (i.e., neighbouring material points) within the horizon of points  $k$  and  $j$ , respectively,  $\mathbf{y}$  denotes the position in the deformed configuration, and  $\omega_{kj}$  is the micropotential arising from the interaction between material points  $k$  and  $j$ . Generally,  $\omega_{kj}$  and  $\omega_{jk}$  are not equal, as each is evaluated over a different domain of influence (the horizon of material points  $k$  and  $j$ , respectively).

Substituting Eq.( 5.2 ), Eq.( 5.3 ) and Eq.( 5.4 ) into Eq.( 5.1 ), the equation of motion for material point  $k$  becomes

$$\rho_k \ddot{\mathbf{u}}_k = \sum_{j=1}^{N_k} [\mathbf{t}_{kj} - \mathbf{t}_{jk}] V_j + \mathbf{b}_k \quad (5.5)$$

where the force density vectors  $\mathbf{t}_{kj}$  and  $\mathbf{t}_{jk}$  are given in terms of the micropotentials as (Madenci and Oterkus, 2013)

$$\mathbf{t}_{kj} = \frac{1}{2} \frac{1}{V_j} \left[ \sum_{i=1}^{N_k} \frac{\omega_{ki}}{\partial(\mathbf{y}_j - \mathbf{y}_k)} V_i \right] \quad (5.6)$$

and

$$\mathbf{t}_{jk} = \frac{1}{2} \frac{1}{V_k} \left[ \sum_{i=1}^{N_j} \frac{\omega_{ji}}{\partial(\mathbf{y}_k - \mathbf{y}_j)} V_i \right] \quad (5.7)$$

For the bond-based peridynamic formulation, the force between two material points at  $\mathbf{x}_k$  and  $\mathbf{x}_j$  only depends on their interaction. Therefore, Eq.( 5.6 ) and Eq.( 5.7 ) simplify to

$$\mathbf{t}_{kj} = \frac{1}{2} \frac{\omega_{kj}}{\partial(\mathbf{y}_j - \mathbf{y}_k)} \quad (5.8)$$

and

$$\mathbf{t}_{jk} = \frac{1}{2} \frac{\omega_{jk}}{\partial(\mathbf{y}_k - \mathbf{y}_j)} \quad (5.9)$$

For variable horizon sizes, these force density vectors can be rewritten as

$$\mathbf{t}_{kj} = \alpha_{kj} \frac{1}{2} c s_{kj} \frac{\mathbf{y}_j - \mathbf{y}_k}{|\mathbf{y}_j - \mathbf{y}_k|} \quad (5.10)$$

and

$$\mathbf{t}_{jk} = \alpha_{kj} \frac{1}{2} c s_{kj} \frac{\mathbf{y}_k - \mathbf{y}_j}{|\mathbf{y}_j - \mathbf{y}_k|} \quad (5.11)$$

where  $\alpha_{kj}$  and  $\alpha_{kj}$  are defined as

$$\alpha_{kj} = \begin{cases} 1, & \omega_{kj} \neq 0 \\ 0, & \omega_{kj} = 0 \end{cases} \quad (5.12)$$

and

$$\alpha_{jk} = \begin{cases} 1, & \omega_{jk} \neq 0 \\ 0, & \omega_{jk} = 0 \end{cases} \quad (5.13)$$

As shown in Fig. 5 1, that due to different horizon sizes, a material point with a smaller horizon (e.g., shown in blue) may be within the horizon of another point with a larger

horizon (red), but not vice versa. In such cases, the micropotential in Eq.( 5.12 ) or Eq.( 5.13 ) is considered zero if is zero if a point lies outside the other's horizon.

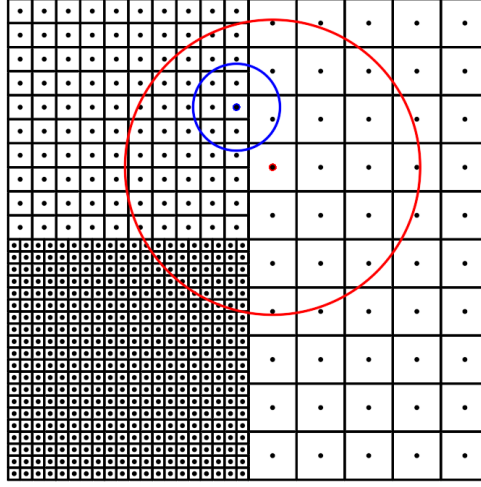


Fig. 5-1 Non-uniform discretization with different horizon sizes.

The bond constant  $c$  in Eq.( 5.10 ) and Eq.( 5.11 ) is as defined previously (Eq.( 3.6 ) for two-dimensional structures), and the stretch between material points is given by

$$s_{kj} = \frac{|\mathbf{y}_j - \mathbf{y}_k| - |\mathbf{x}_j - \mathbf{x}_k|}{|\mathbf{x}_j - \mathbf{x}_k|} \quad (5.14)$$

For the ordinary state-based peridynamics, the force terms can be adapted for the variable horizon case as

$$\mathbf{t}_{kj} = \alpha_{kj} \left( \frac{2ad\delta_k}{|\mathbf{x}_j - \mathbf{x}_k|} \theta_k(\mathbf{x}_k, t) + 2\delta_k b s_{kj} \right) \frac{\mathbf{y}_j - \mathbf{y}_k}{|\mathbf{y}_j - \mathbf{y}_k|} \quad (5.15)$$

and

$$\mathbf{t}_{jk} = \alpha_{jk} \left( \frac{2ad\delta_j}{|\mathbf{x}_j - \mathbf{x}_k|} \theta_j(\mathbf{x}_j, t) + 2\delta_j b s_{kj} \right) \frac{\mathbf{y}_k - \mathbf{y}_j}{|\mathbf{y}_j - \mathbf{y}_k|} \quad (5.16)$$

where  $a$ ,  $b$  and  $d$  are the peridynamic parameters, and these can be obtained through Table 3-1.

The dilatation term in Eq.( 5.15 ) and Eq.( 5.16 ) for material points material points  $k$  and  $j$  are defined, respectively, as

$$\theta_k = \sum_{i=1}^{N_k} d\delta_k s_{ki} V_i \quad (5.17)$$

and

$$\theta_j = \sum_{i=1}^{N_j} d\delta_j s_{ji} V_i \quad (5.18)$$

For non-ordinary state-based peridynamics, the force density vector for material points  $k$  and  $j$  for variable horizon size can be written as

$$\mathbf{t}_{kj} = \alpha_{kj} \mathbf{P}[\mathbf{x}_k] \mathbf{K}^{-1}[\mathbf{x}_k] (\mathbf{x}_j - \mathbf{x}_k) \quad (5.19)$$

and

$$\mathbf{t}_{jk} = \alpha_{jk} \mathbf{P}[\mathbf{x}_j] \mathbf{K}^{-1}[\mathbf{x}_j] (\mathbf{x}_k - \mathbf{x}_j) \quad (5.20)$$

where the shape tensor,  $\mathbf{K}$ , can be obtained as

$$\mathbf{K}[\mathbf{x}_k] = \sum_{i=1}^{N_k} (\mathbf{x}_i - \mathbf{x}_k) \otimes (\mathbf{x}_i - \mathbf{x}_k) V_i \quad (5.21)$$

and

$$\mathbf{K}[\mathbf{x}_j] = \sum_{i=1}^{N_j} (\mathbf{x}_i - \mathbf{x}_j) \otimes (\mathbf{x}_i - \mathbf{x}_j) V_i \quad (5.22)$$

where the symbol  $\otimes$  represents dyadic product. It should be noted that the non-ordinary state-based formulation may exhibit zero-energy modes (Gu et al., 2018); as discussed in section 3.2.3, in this study, these are addressed using the approach outlined by Silling (2017).

### 5.3 Numerical Implementation

The general procedures for the numerical implementation, including the imposition of boundary conditions, application of surface correction techniques, and time integration

schemes, are detailed in Chapter 4 (see Sections 4.2). The reader is referred to Chapter 4 for the description of the underlying algorithms and standard computational procedures.

#### **5.4 Numerical Investigations for Dual-horizon Peridynamic Formulations**

As previously discussed, while uniform discretisation is common in the peridynamic literature, the use of variable mesh sizes offers computational advantages and is widely adopted in other numerical methods, such as FEM.

In this section, the effectiveness of the dual-horizon peridynamics approach is demonstrated through case studies involving non-uniform discretisation, where both the grid size and the horizon radius may vary across the domain.

For clarity and comparison, each problem divides the solution domain into two regions with different grid sizes and corresponding horizon sizes. Two benchmark problems are considered: (1) the vibration of a plate (Section 5.4.1), which evaluates the method dynamically; and (2) a plate under tension (Section 5.4.2), which assesses static performance. Each case is studied using bond-based, ordinary state-based, and non-ordinary state-based formulations to demonstrate the flexibility and capability of the dual-horizon framework with non-uniform discretisation.

##### *5.4.1 Plate Vibration in Nonuniform Discretization*

In the first simulation case, the dynamic response of a square plate (Fig. 4-4) with dimensions  $L = W = 1$  m and thickness 0.01 m is investigated. The plate is modelled as a linear elastic and homogeneous material, with Young's modulus  $E = 200$  GPa and density  $\rho = 7850$  kg/m<sup>3</sup>. Poisson's ratio is taken as 1/3 for bond-based simulations, and non-ordinary state-based simulations, and 0.25 for ordinary state-based simulations.

Vibration is initiated by imposing an initial uniaxial strain of 0.001 in the horizontal direction. The left edge of the plate is fully constrained by a fictitious region (see Fig. 4-5), while all other edges are traction-free. Time integration is carried out using an explicit scheme with a time step size of  $1 \times 10^{-7}$  sec.

For clarity and direct comparison, a material point at  $(x, y) = (0.255 \text{ m}, 0.255 \text{ m})$  is selected as a monitoring point. The horizontal and vertical displacements of this point

are recorded as functions of time and compared against the finite element solution obtained in ANSYS.

#### 5.4.1.1 Effect of Locally Defined Horizon Size

In this scenario, as shown in Fig. 5-2, the right half of the plate (Region 2) is discretised with a coarse grid of  $\Delta x_2 = 0.005$  m, while the left half (Region 1) employs a refined grid of  $\Delta x_1 = 0.01$  m. The mesh ratio,  $k$ , between these two regions is defined as  $k = \frac{\Delta x_2}{\Delta x_1} = 2$ .

For each region, the horizon size is defined as an integer multiple of the local discretisation size:  $\delta_1 = nhor_1 \Delta x_1$  for Region 1, and  $\delta_2 = nhor_2 \Delta x_2$  for Region 2, where  $nhor_1$  and  $nhor_2$  denote the horizon-to-grid spacing ratios in the two regions. In this study,  $nhor_1$  and  $nhor_2$  are varied simultaneously from 1 to 5, meaning that the horizon size of material points in Region 1 is always half of that in Region 2. Although the mesh differs across the two regions, the number of family material points remains the same for every material point across the simulation domain.

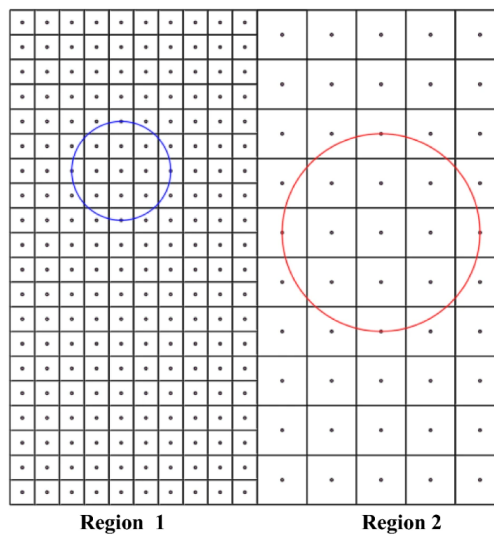
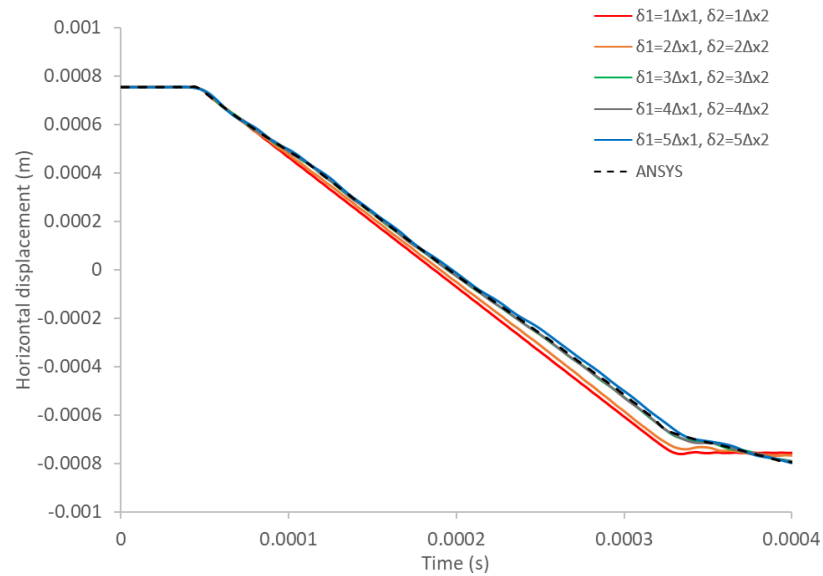


Fig. 5-2 Discretisation and horizons for refined grid-coarse grid case.

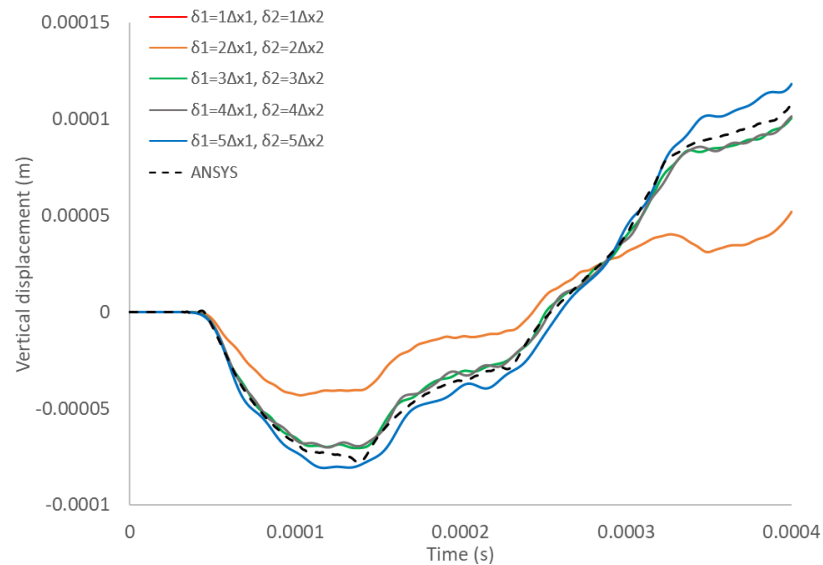
##### 5.4.1.1.1 Bond-based Peridynamics

Fig. 5-3 and Fig. 5-4 show the time histories of the horizontal and vertical displacements, respectively, for the selected material point under various combinations of locally defined horizon sizes ( $\delta_1$  and  $\delta_2$ ) in the bond-based formulation. The results indicate that peridynamic predictions become more consistent with the FEM solution as the horizon size increases. Configurations with  $\delta_1 = 3\Delta x_1$ ,  $\delta_2 = 3\Delta x_2$  and  $\delta_1 =$

$4\Delta x_1, \delta_2 = 4\Delta x_2$  yield the closest agreement with the FEM reference solutions. These findings are consistent with those obtained under uniform discretisation, confirming that a locally defined horizon size of  $\delta = 3\Delta x$  remains effective for non-uniform grids.



*Fig. 5-3 Variation of horizontal displacement of the material point located at (0.255 m, 0.255 m) with time in bond-based formulation, locally defined horizon size.*

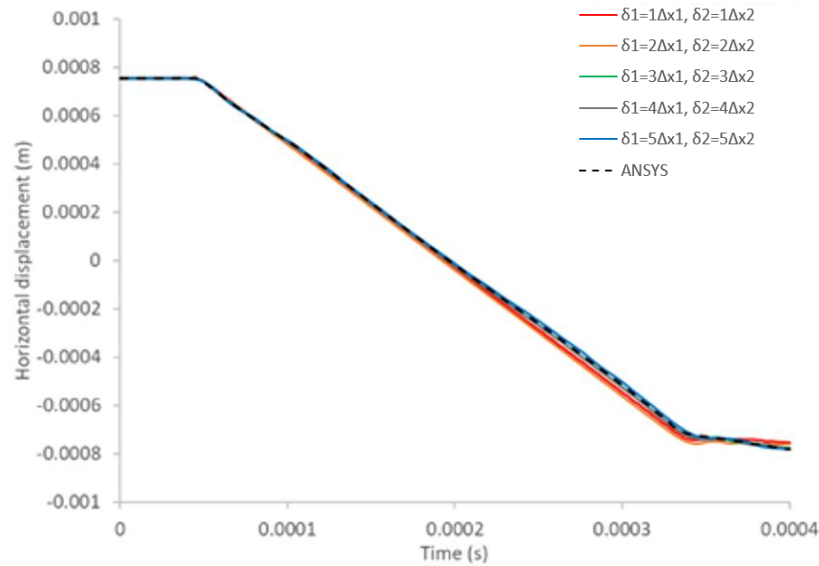


*Fig. 5-4 Variation of vertical displacement of the material point located at (0.255 m, 0.255 m) with time in bond-based formulation, locally defined horizon size.*

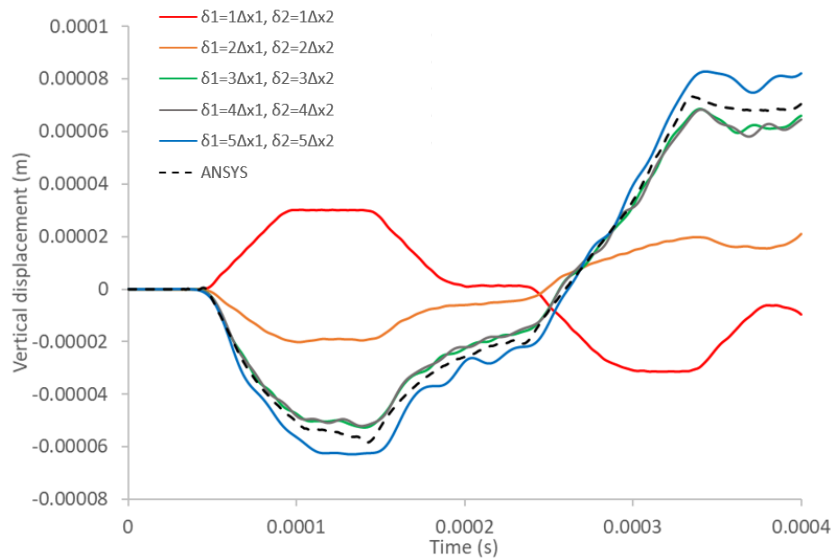
#### 5.4.1.1.2 Ordinary State-based Peridynamics

Fig. 5-5 and Fig. 5-6 show the time histories of the horizontal and vertical displacements at the selected material point for the ordinary state-based formulation.

Horizontal displacement predictions (Fig. 5-5) exhibit good agreement with the FEM results across all tested horizon sizes. For the vertical displacement (Fig. 5-6), the combinations,  $\delta_1 = 3\Delta x_1$ ,  $\delta_2 = 3\Delta x_2$  and  $\delta_1 = 4\Delta x_1$ ,  $\delta_2 = 4\Delta x_2$  show the closest correspondence with the FEM solution, a trend similar to the bond-based case.



*Fig. 5-5 Variation of horizontal displacement of the material point located at (0.255 m, 0.255 m) with time in ordinary state-based formulation, locally defined horizon size.*



*Fig. 5-6 Variation of vertical displacement of the material point located at (0.255 m, 0.255 m) with time in ordinary state-based formulation, locally defined horizon size.*

### 5.4.1.1.3 Non-ordinary State-based Peridynamics

For the non-ordinary state-based formulation, the time histories of horizontal and vertical displacements at the monitored material point are shown in Fig. 5-7 and Fig. 5-8. The results demonstrate that non-ordinary state-based formulation provides close agreement with the FEM solution for all tested horizon sizes, with specifically accurate predictions for smaller horizons ( $\delta_1 = 2\Delta x_1$ ,  $\delta_2 = 2\Delta x_2$ ).

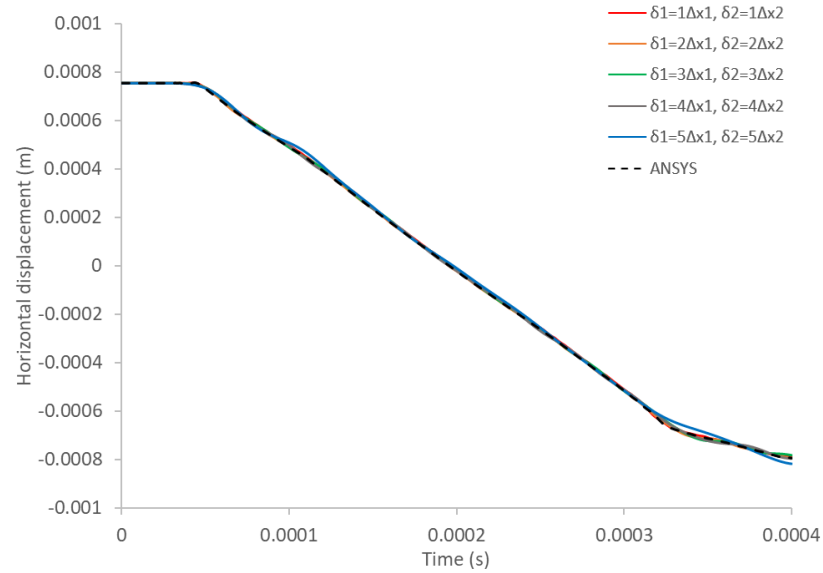
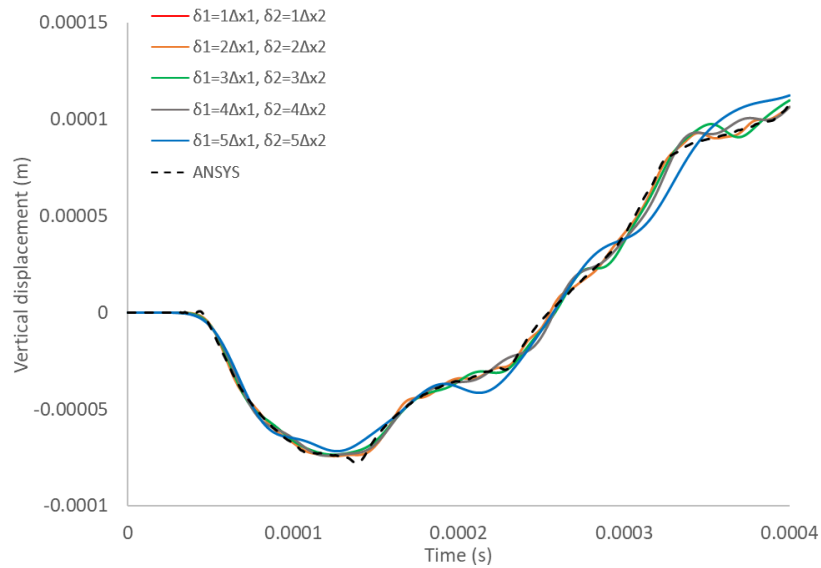


Fig. 5-7 Variation of horizontal displacement of the material point located at (0.255 m, 0.255 m) with time in non-ordinary state-based formulation, locally defined horizon size.



*Fig. 5-8 Variation of vertical displacement of the material point located at (0.255 m, 0.255 m) with time in non-ordinary state-based formulation, locally defined horizon size.*

#### 5.4.1.2 Effect of Constant Horizon Size

In the second set of investigations, the effect of adopting a constant horizon size throughout the non-uniformly discretised domain is examined. As shown in Fig. 5-9, the left half of the plate (Region 1) is discretised using a refined grid of  $\Delta x_1 = 0.005\text{m}$  while the right half (Region 2) employs a coarser grid of  $\Delta x_2 = 0.01\text{m}$ . The mesh ratio between the two regions is therefore  $k = \frac{\Delta x_2}{\Delta x_1} = 2$ .

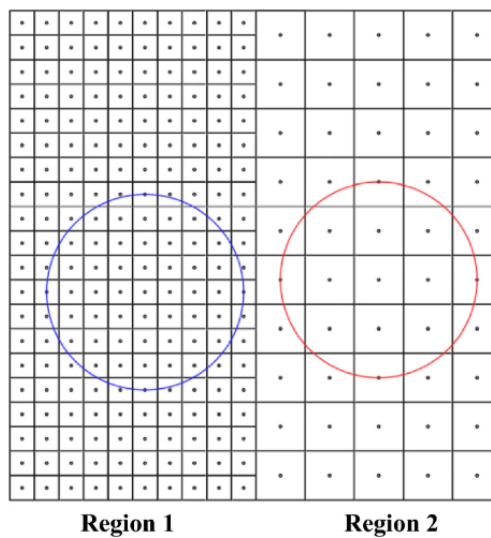


*Fig. 5-9 Discretisation and horizons for refined grid-coarse grid case*

However, in contrast to the previous case, where the horizon radius was defined locally for each region, all material points in the current analysis are assigned a constant horizon radius irrespective of their underlying mesh size, i.e.,  $\delta_1 = \delta_2 = nhor_2 \Delta x_2$ , with  $nhor_2$  varied from 1 to 5. As before, the dynamic response of the representative material point is monitored and compared to the FEM reference.

Furthermore, for each peridynamic formulation, the optimal results obtained from the constant horizon configuration in this section are directly compared to those from the locally defined horizon case in section 5.4.1.1.

#### 5.4.1.2.1 Bond-based Peridynamics

Fig. 5-10 and Fig. 5-11 present the horizontal and vertical displacement time histories for the material point at (0.255 m, 0.255 m). The closest agreement with the FEM reference is observed for horizon size combinations  $\delta_1 = 6\Delta x_1 = \delta_2 = 3\Delta x_2$ , and  $\delta_1 = 8\Delta x_1 = \delta_2 = 4\Delta x_2$ .

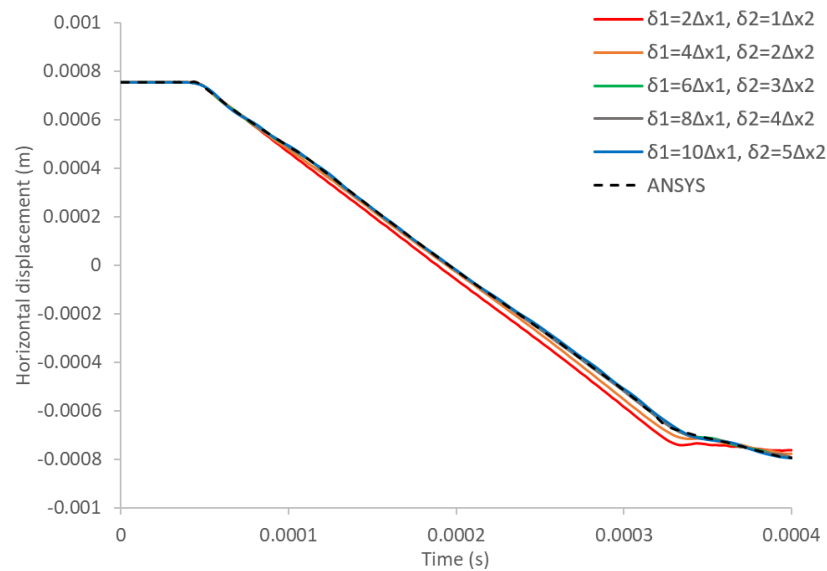
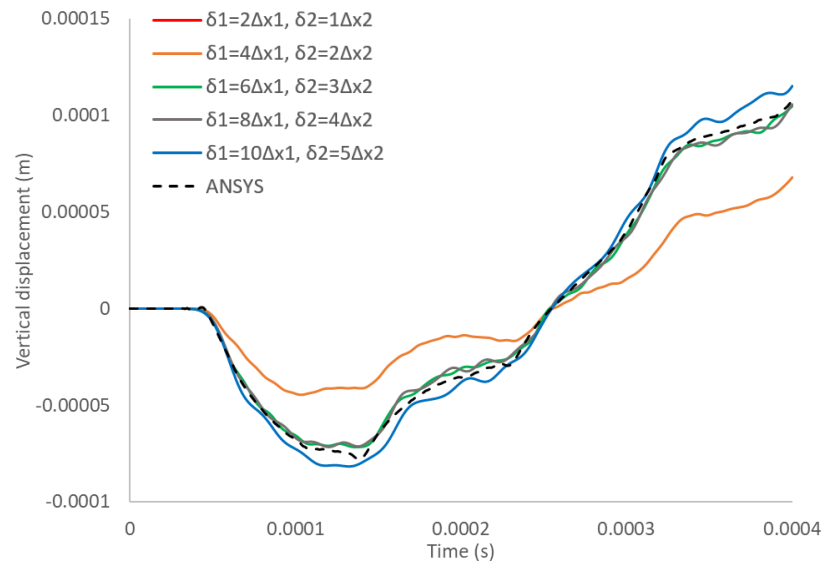
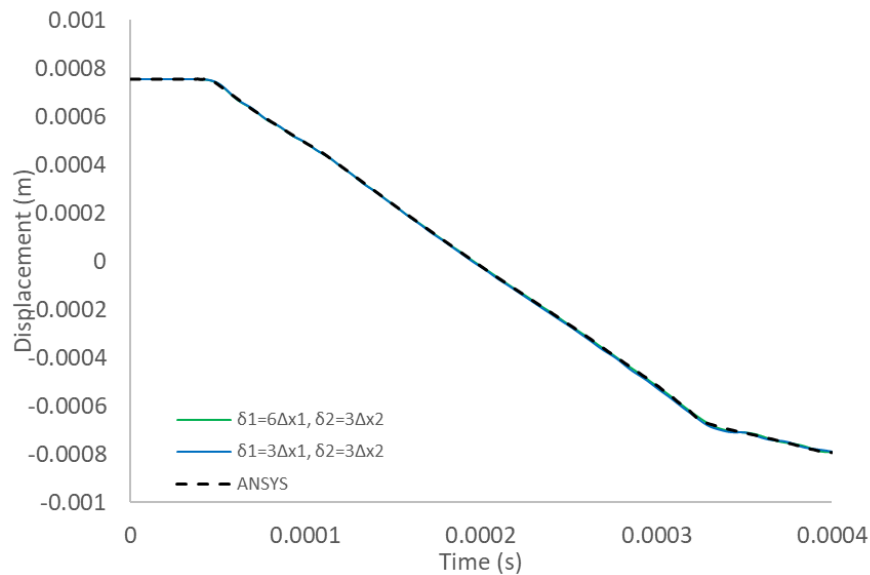


Fig. 5-10 Variation of horizontal displacement of the material point located at (0.255 m, 0.255 m) with time in bond-based formulation, constant horizon size.



*Fig. 5-11 Variation of vertical displacement of the material point located at (0.255 m, 0.255 m) with time in bond-based formulation, constant horizon size.*

A direct comparison between the locally defined and constant horizon approaches is provided for  $\delta_1 = 3\Delta x_1$ ,  $\delta_2 = 3\Delta x_2$  and  $\delta_1 = 6\Delta x_1 = \delta_2 = 3\Delta x_2$ . As shown in Fig. 5-12 and Fig. 5-13, the horizontal displacement predictions are similar for both approaches. However, vertical displacement results are improved when a constant horizon is used, attributable to the increased number of interacting material points within the horizon.



*Fig. 5-12 Comparison of horizontal displacement variation with time for the material point located at (0.255 m, 0.255 m) between locally defined and constant horizon size in the bond-based formulation.*

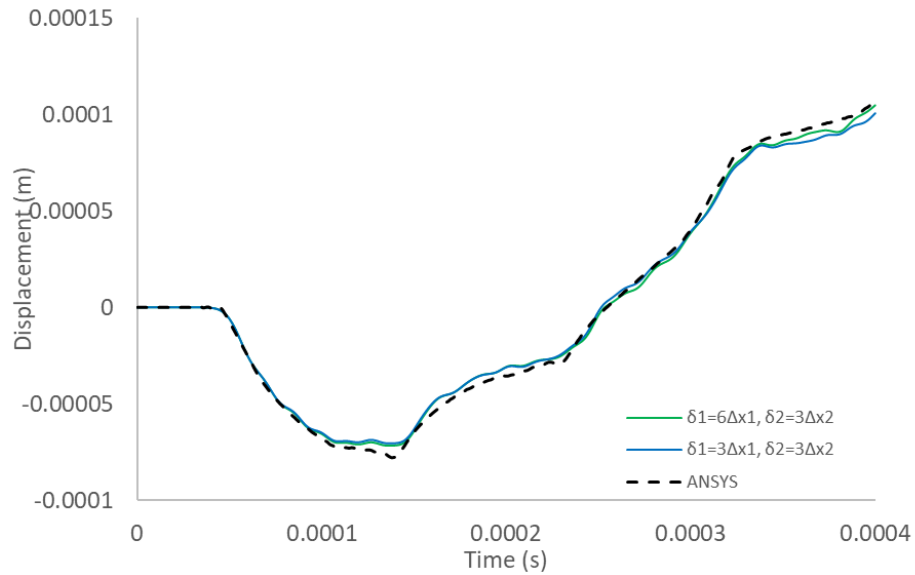


*Fig. 5-13 Comparison of vertical displacement variation with time for the material point located at (0.255 m,0.255 m) between locally defined and constant horizon size in the bond-based formulation.*

#### 5.4.1.2.2 Ordinary State-based Peridynamics

For the ordinary state-based formulation, the time histories of horizontal and vertical displacements for the constant horizon scenario are shown in Fig. 5-14 and Fig. 5-15. The horizontal displacement predictions remain consistent with the FEM results for all tested horizon sizes, whereas the vertical displacement (Fig. 5-15) shows more sensitivity to horizon size. The better agreement with FEM is achieved for  $\delta_1 = 6\Delta x_1 = \delta_2 = 3\Delta x_2$ , and  $\delta_1 = 8\Delta x_1 = \delta_2 = 4\Delta x_2$ .

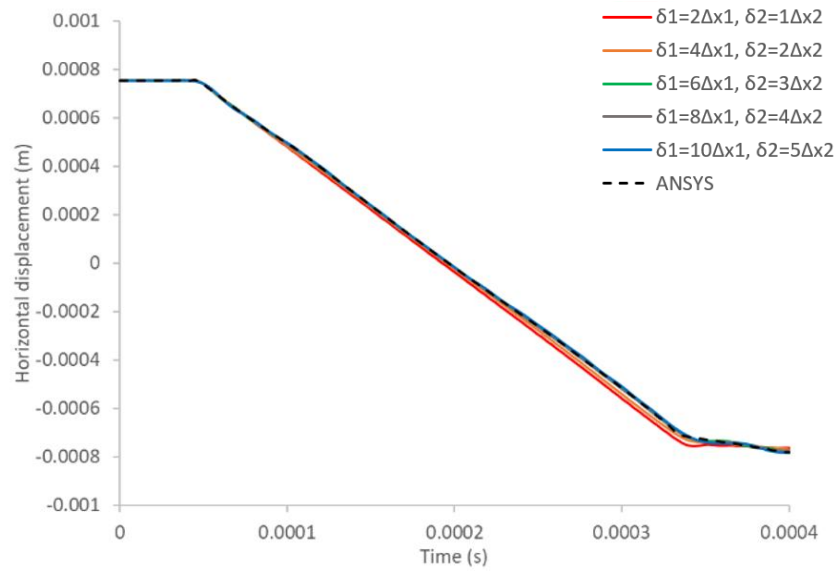


Fig. 5-14 Variation of horizontal displacement of the material point located at  $(0.255\text{ m}, 0.255\text{ m})$  with time in ordinary state-based formulation, constant horizon size.

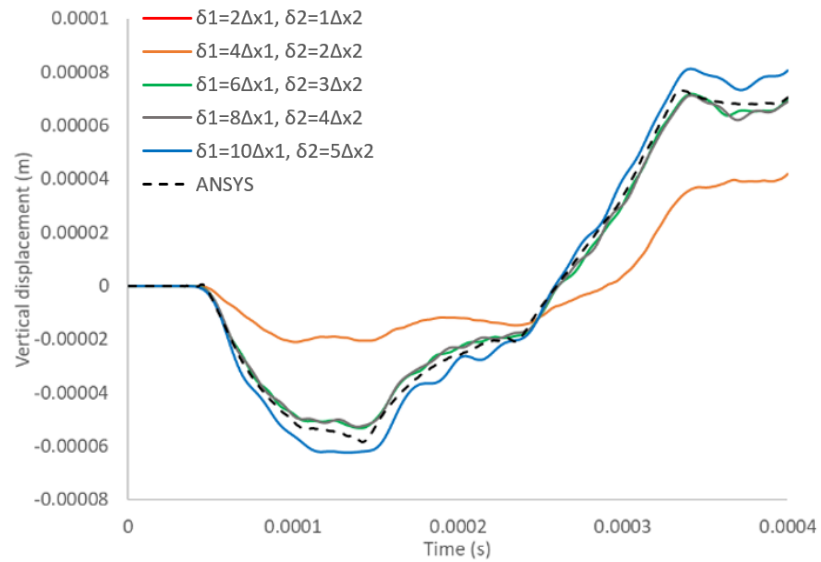
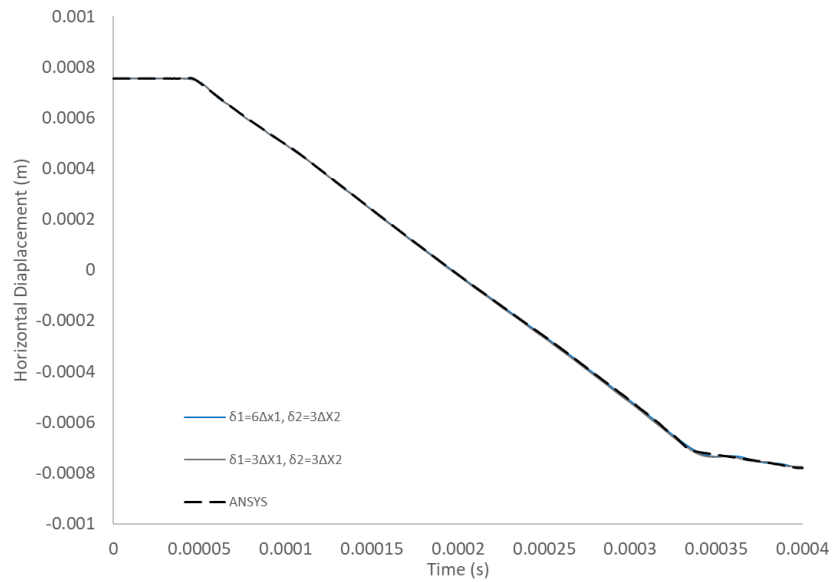
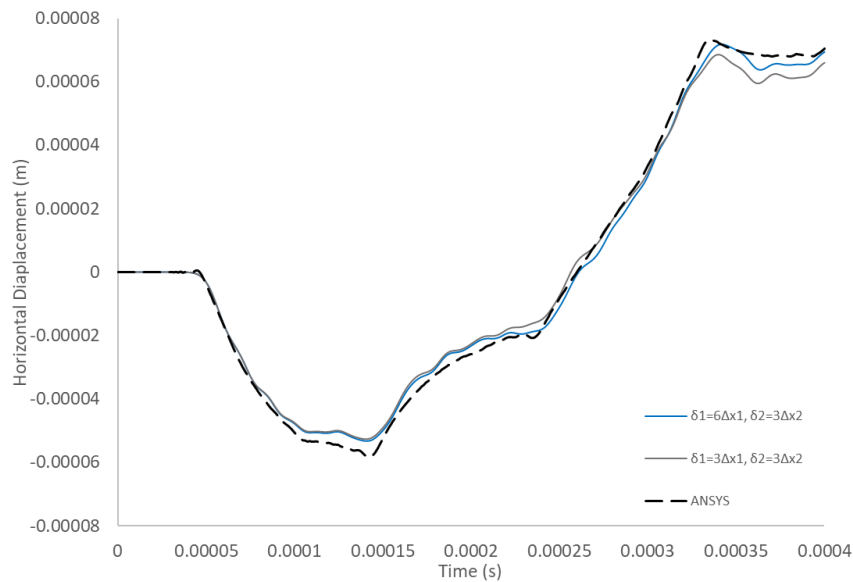


Fig. 5-15 Variation of vertical displacement of the material point located at  $(0.255\text{ m}, 0.255\text{ m})$  with time in ordinary state-based formulation, constant horizon size.

Comparison with the locally defined horizon case (Fig. 5-16 and Fig. 5-17) shows very similar horizontal displacement predictions for both strategies, with slightly improved vertical displacement accuracy for the constant horizon case, again due to a larger number of family members within the horizon.



*Fig. 5-16 Comparison of horizontal displacement variation with time for the material point located at (0.255 m,0.255 m) between locally defined and constant horizon size in the ordinary state-based formulation.*



*Fig. 5-17 Comparison of vertical displacement variation with time for the material point located at (0.255 m,0.255 m) between locally defined and constant horizon size in the ordinary state-based formulation.*

#### 5.4.1.2.3 Non-ordinary State-based Peridynamics

Finally, for the non-ordinary state-based formulation, Fig. 5-18 and Fig. 5-19 show that both the horizontal and vertical displacement histories exhibit good agreement with the FEM reference for all tested constant horizon sizes. The use of smaller

constant horizon values  $\delta_1 = 4\Delta x_1 = \delta_2 = 2\Delta x_2$  provide the closest match to FEM predictions.

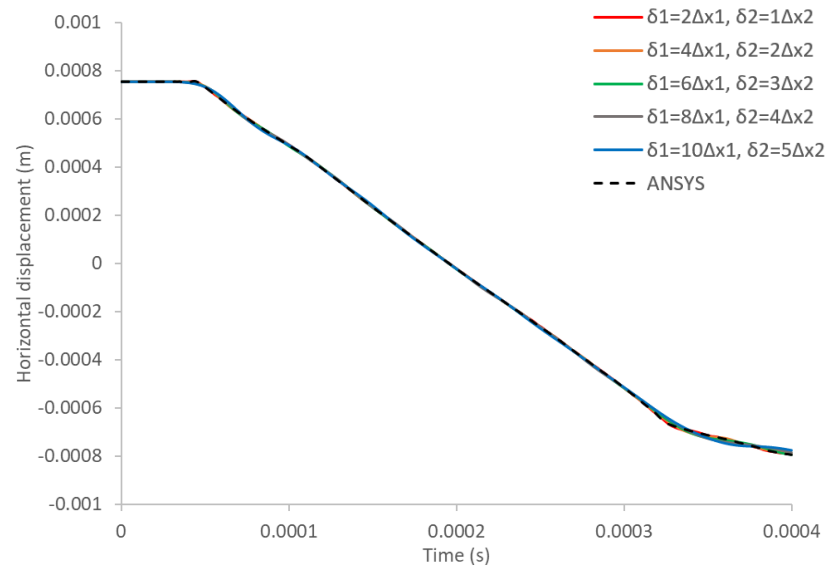


*Fig. 5-18 Variation of horizontal displacement of the material point located at (0.255 m, 0.255 m) with time in non-ordinary state-based formulation, constant horizon size.*

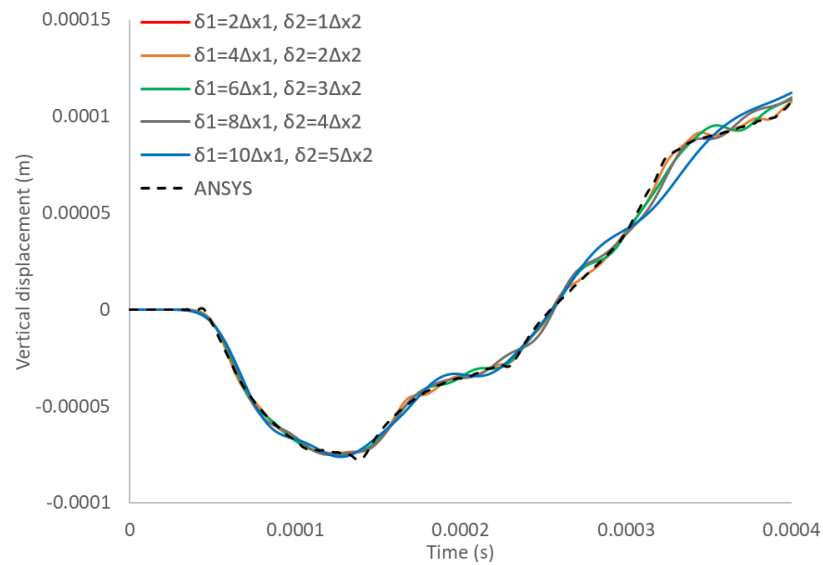


*Fig. 5-19 Variation of vertical displacement of the material point located at (0.255 m, 0.255 m) with time in non-ordinary state-based formulation, constant horizon size.*

A direct comparison between locally defined and constant horizon approaches is presented in Fig. 5-20 and Fig. 5-21. It is noticed that that both strategies yield nearly indistinguishable displacement responses at the monitoring point.

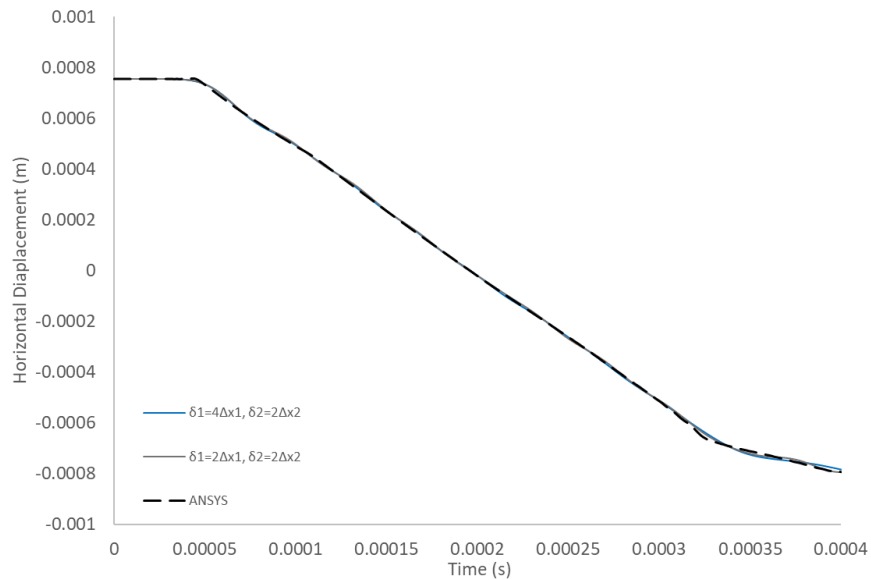


*Fig. 5-20 Comparison of horizontal displacement variation with time for the material point located at (0.255 m,0.255 m) between locally defined and constant horizon size in the non-ordinary state-based formulation.*

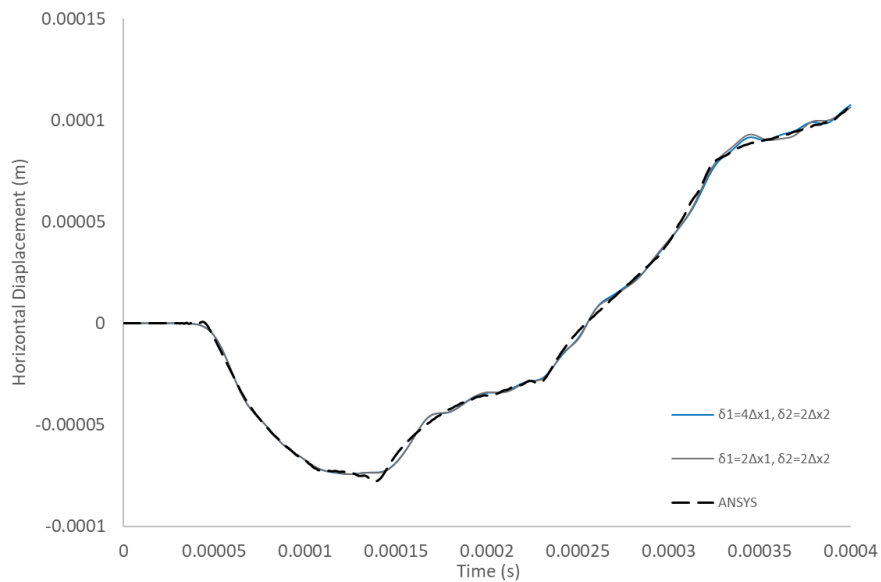


*Fig. 5-21 Comparison of vertical displacement variation with time for the material point located at (0.255 m,0.255 m) between locally defined and constant horizon size in the non-ordinary state-based formulation.*

#### 5.4.2 Plate Under Tension in Nonuniform Discretization

In this case study, a square plate of dimensions  $L = W = 1$  m with thickness of 0.01 m is subjected to a prescribed uniaxial tensile stress  $\sigma^* = 200$  MPa applied at the right edge, as illustrated in Fig. 4-12. This loading is imposed via a fictitious region at the right boundary, following the methodology outlined in Section 4.3.3 (see also Fig.

4-13). The left edge of the plate is fully fixed by using a fictitious region. The plate material is linear elastic with  $E = 200$  GPa and density  $\rho = 7850$  kg/m<sup>3</sup>. Poisson's ratio is taken as 1/3 for bond-based simulations, and non-ordinary state-based simulations, and 0.25 for ordinary state-based simulations. The steady-state response is obtained using the Adaptive Dynamic Relaxation technique (Underwood, 1983; Kilic and Madenci, 2010).

As in the previous plate vibration analysis, both locally defined horizon size and constant horizon size approaches are investigated. Each approach is implemented for the bond-based, ordinary state-based, and non-ordinary state-based peridynamic formulations. The peridynamic results are benchmarked against reference FEM solutions computed in Ansys. For each formulation, optimised cases from both horizon selection strategies are compared.

#### 5.4.2.1 Effect of Locally Defined Horizon Size

In this analysis, the solution domain is divided into two equal regions (Region 1 and Region 2), as illustrated in Fig. 5-2. The mesh size in Region 1  $\Delta x_1 = 0.005$  m, which is half that of Region 2 ( $\Delta x_2 = 0.01$  m), giving a mesh ratio of  $k = \frac{\Delta x_2}{\Delta x_1} = 2$ .

In each region, the horizon radius is defined as an integer multiple of the local grid size:  $\delta_1 = nhor_1 \Delta x_1$  for Region 1 and  $\delta_2 = nhor_2 \Delta x_2$  for Region 2 with  $nhor_1$  and  $nhor_2$  are varied simultaneously from 1 to 5.

##### 5.4.2.1.1 Bond-based Peridynamics

Fig. 5-22 and Fig. 5-23 present the horizontal and vertical displacement profiles along the central axes for the bond-based formulation. The results indicate that the better agreement with the FEM solution is achieved when horizon sizes are set to  $\delta_1 = 3\Delta x_1$ ,  $\delta_2 = 3\Delta x_2$ ,  $\delta_1 = 4\Delta x_1$ ,  $\delta_2 = 4\Delta x_2$  and  $\delta_1 = 5\Delta x_1$ ,  $\delta_2 = 5\Delta x_2$ .

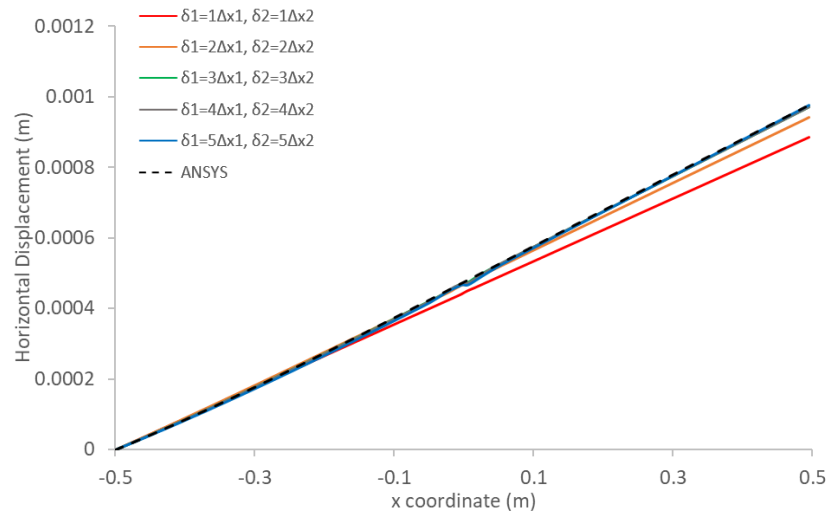


Fig. 5-22 Variation of horizontal displacements along the central axis ( $x, y = 0$ ) in bond-based formulation, locally defined horizon size.

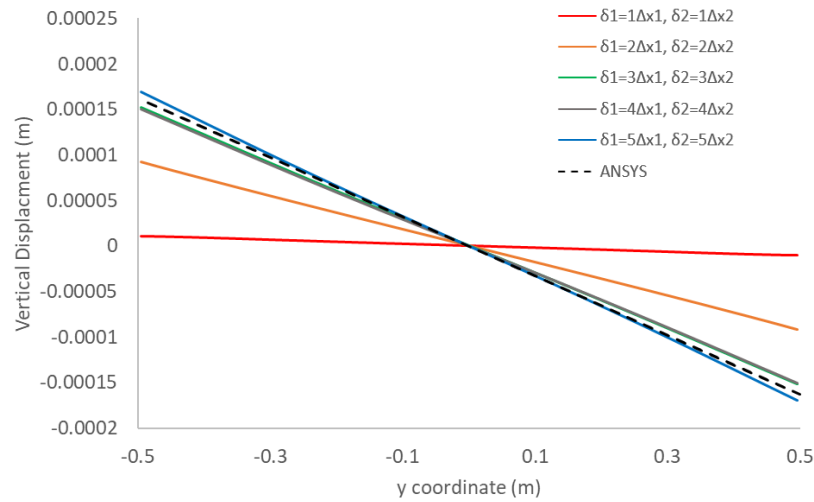


Fig. 5-23 Variation of vertical displacement along the central axis ( $x = 0, y$ ) in bond-based formulation, locally defined horizon size.

#### 5.4.2.1.2 Ordinary State-based Peridynamics

Fig. 5-24 and Fig. 5-25 show the horizontal and vertical displacements for the ordinary state-based formulation. Like the bond-based results, horizon configurations of  $\delta_1 = 3\Delta x_1$ ,  $\delta_2 = 3\Delta x_2$ ,  $\delta_1 = 4\Delta x_1$ ,  $\delta_2 = 4\Delta x_2$  and  $\delta_1 = 5\Delta x_1$ ,  $\delta_2 = 5\Delta x_2$  yield better agreement with the FEM reference. Smaller horizon values are insufficient to capture the correct displacement field, as previously observed.

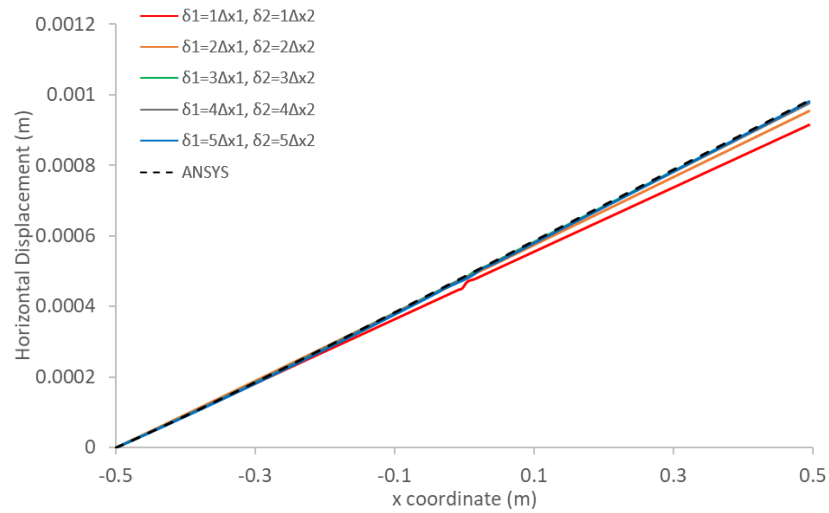


Fig. 5-24 Variation of horizontal displacements along the central axis ( $x, y = 0$ ) in ordinary state-based formulation, locally defined horizon size.

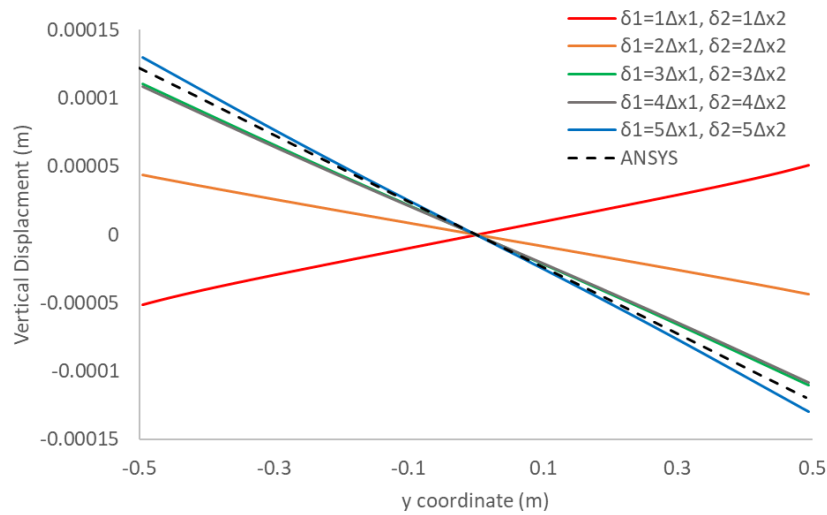


Fig. 5-25 Variation of vertical displacement along the central axis ( $x = 0, y$ ) in ordinary state-based formulation, locally defined horizon size.

#### 5.4.2.1.3 Non-ordinary State-based Peridynamics

Fig. 5-26 and Fig. 5-27 the horizontal and vertical displacement distributions for the non-ordinary state-based formulation. The closest correspondence with FEM is obtained for  $\delta_1 = 2\Delta x_1, \delta_2 = 2\Delta x_2$ . In contrast to bond-based and ordinary state-based results, the non-ordinary state-based formulation shows increasing horizontal displacement error at the interface as the horizon size increases.

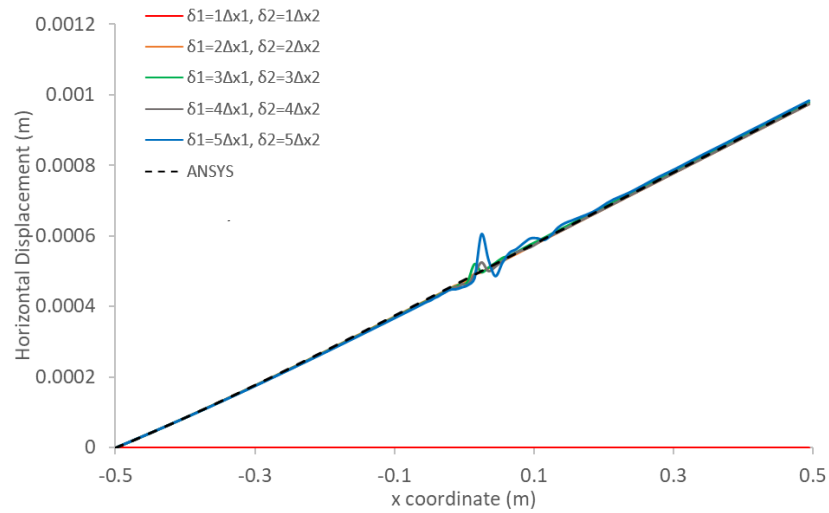


Fig. 5-26 Variation of horizontal displacements along the central axis ( $x, y = 0$ ) in non-ordinary state-based formulation, locally defined horizon size.

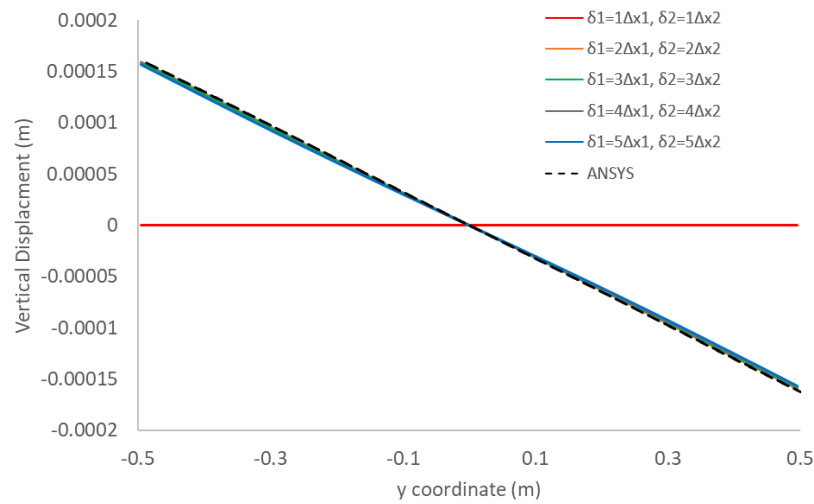


Fig. 5-27 Variation of vertical displacement along the central axis ( $x = 0, y$ ) in non-ordinary state-based formulation, locally defined horizon size.

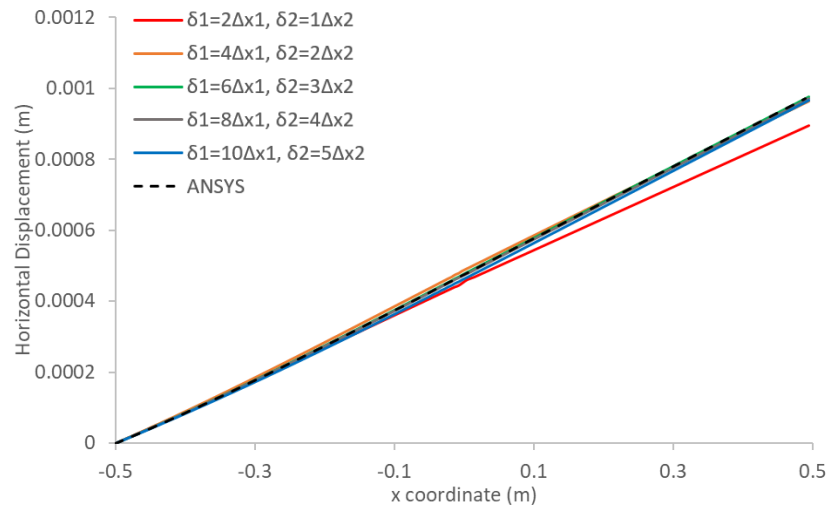
#### 5.4.2.2 Effect of Constant Horizon Size

In this set of analyses, all material points across both regions are assigned a constant horizon size, irrespective of local grid spacing. Specifically, the horizon size is taken as  $\delta_1 = \delta_2 = nhor_2 \Delta x_2$ , with  $nhor_2$  varied from 1 to 5.

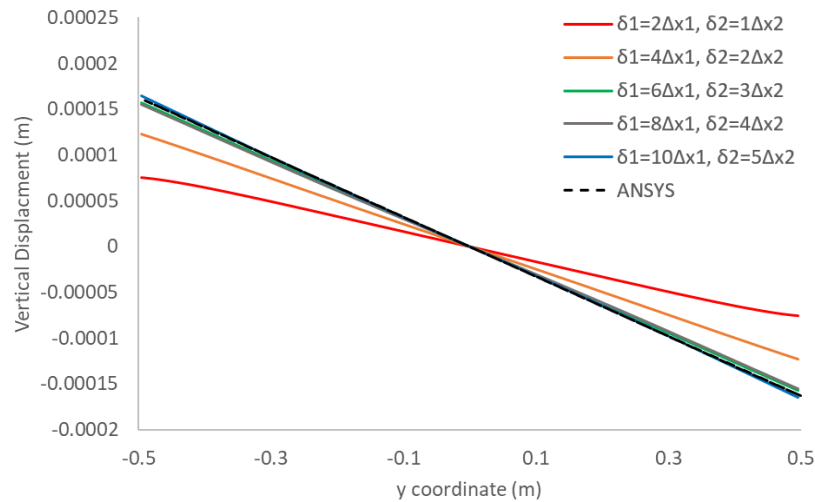
##### 5.4.2.2.1 Bond-based Peridynamics

Fig. 5-28 and Fig. 5-29 present the horizontal and vertical displacement fields for the bond-based formulation with constant horizon size. The results demonstrate that horizon values of  $\delta_1 = 6\Delta x_1 = \delta_2 = 3\Delta x_2$ ,  $\delta_1 = 8\Delta x_1 = \delta_2 = 4\Delta x_2$  and  $\delta_1 =$

$10\Delta x_1 = \delta_2 = 5\Delta x_2$  provide a better agreement with the FEM solution for both horizontal and vertical displacements.



*Fig. 5-28 Variation of horizontal displacements along the central axis ( $x, y = 0$ ) in bond-based formulation, constant horizon size.*



*Fig. 5-29 Variation of vertical displacement along the central axis ( $x = 0, y$ ) in bond-based formulation, constant horizon size.*

A direct comparison between the constant and locally defined horizon cases (Fig. 5-30 and Fig. 5-31) shows that while horizontal displacements are nearly identical, the constant horizon approach results in improved vertical displacement accuracy. This improvement can be attributed to the increased number of neighbouring points within the constant horizon, especially in the refined region.

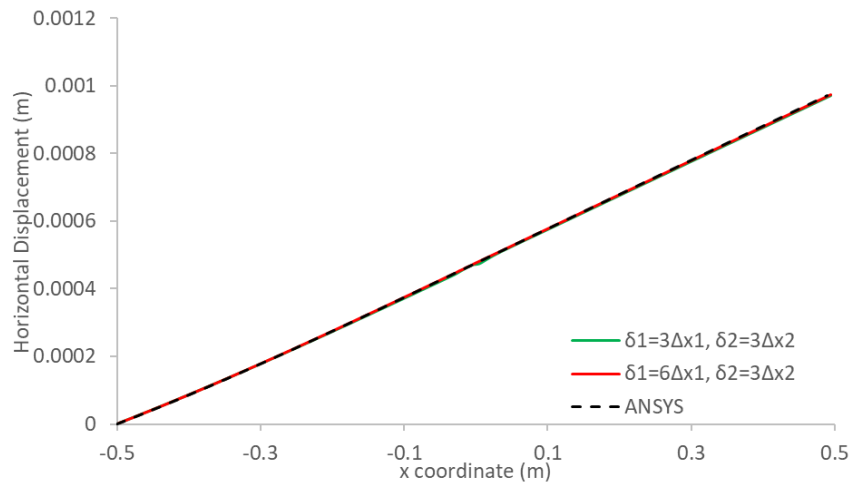


Fig. 5-30 Comparison of horizontal displacements along the central axis ( $x, y = 0$ ) between locally defined and constant horizon size in the bond-based formulation.

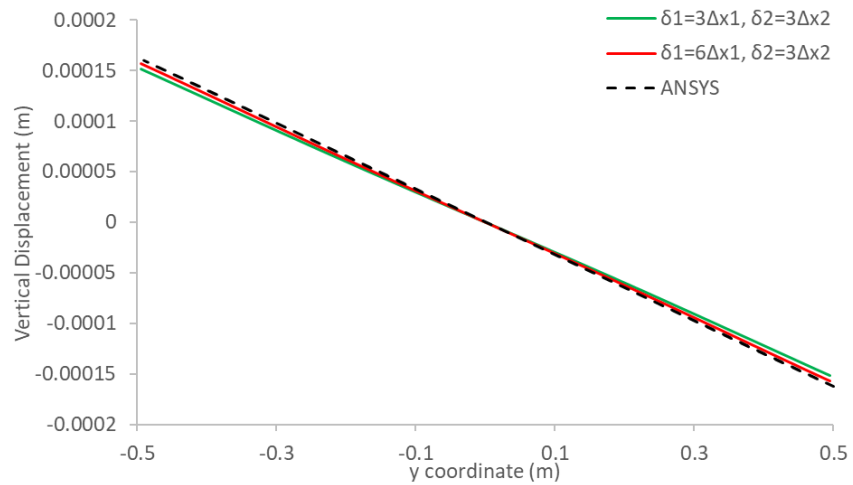
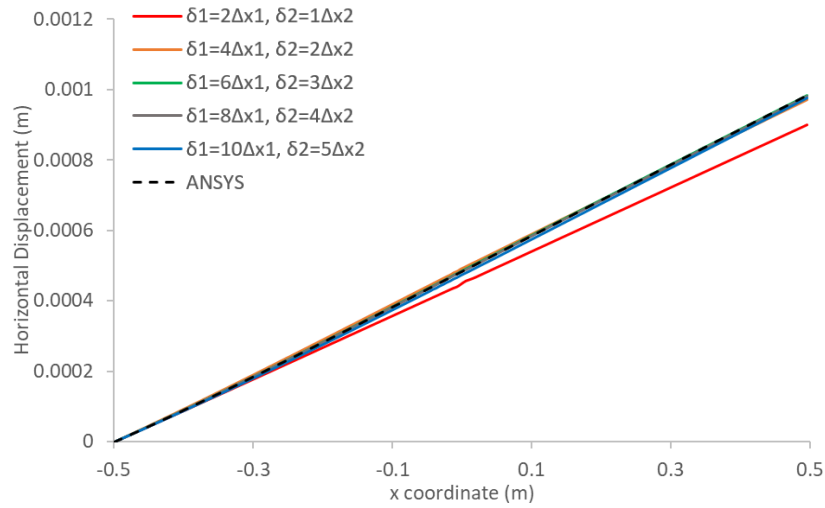


Fig. 5-31 Comparison of vertical displacements along the central axis ( $x = 0, y$ ) between locally defined and constant horizon size in the bond-based formulation.

#### 5.4.2.2.2 Ordinary State-based Peridynamics

Fig. 5-32 and Fig. 5-33 show the horizontal and vertical displacements for the ordinary state-based formulation under the constant horizon strategy. The horizon sizes  $\delta_1 = 6\Delta x_1 = \delta_2 = 3\Delta x_2$ ,  $\delta_1 = 8\Delta x_1 = \delta_2 = 4\Delta x_2$  and  $\delta_1 = 10\Delta x_1 = \delta_2 = 5\Delta x_2$  yield better agreement with FEM results.



*Fig. 5-32 Variation of horizontal displacements along the central axis ( $x, y = 0$ ) in ordinary state-based formulation, constant horizon size.*

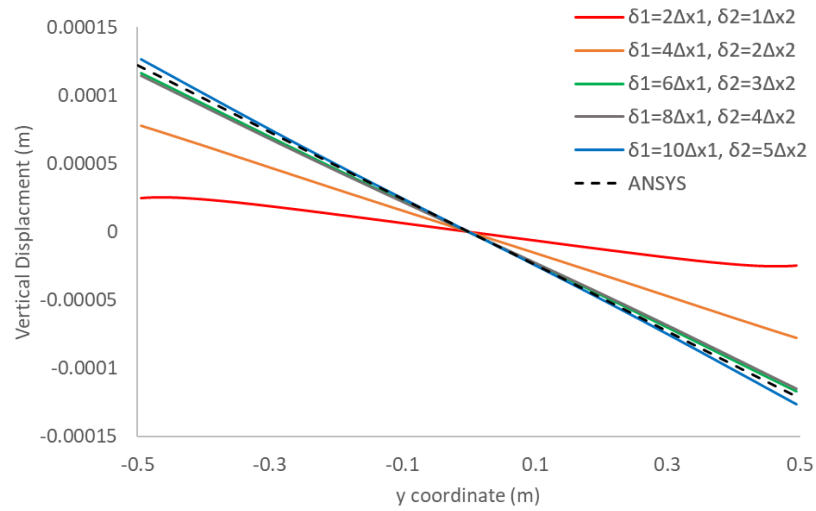


*Fig. 5-33 Variation of vertical displacement along the central axis ( $x = 0, y$ ) in ordinary state-based formulation, constant horizon size.*

Comparison between locally defined and constant horizon approaches (Fig. 5-34 and Fig. 5-35) confirms that horizontal displacement predictions are indistinguishable for the optimised horizon sizes, while the constant horizon case yields more accurate vertical displacement due to a larger number of material points within the horizon.

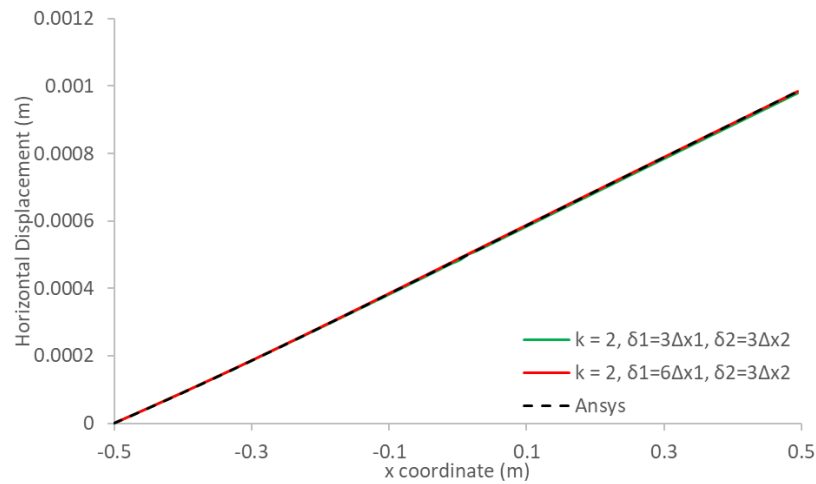


*Fig. 5-34 Comparison of horizontal displacements along the central axis ( $x, y = 0$ ) between locally defined and constant horizon size in ordinary state-based formulation.*

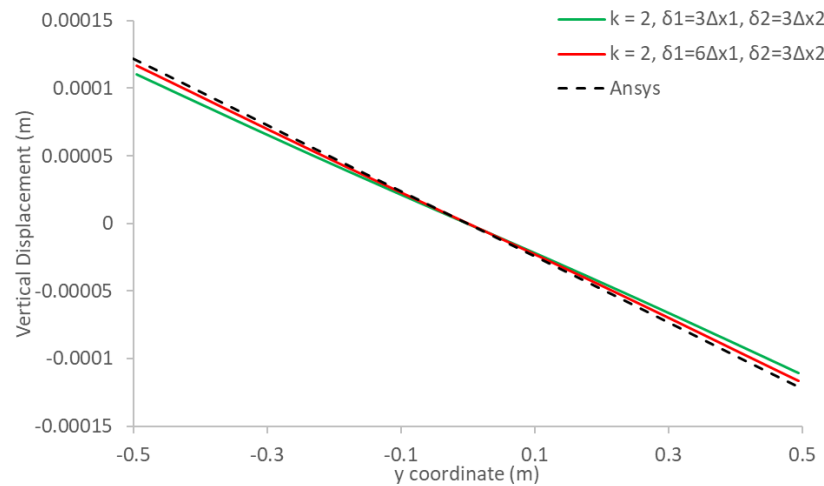


*Fig. 5-35 Comparison of vertical displacements along the central axis ( $x = 0, y$ ) between locally defined and constant horizon size in ordinary state-based formulation.*

#### 5.4.2.2.3 Non-ordinary State-based Peridynamics

Fig. 5-36 and Fig. 5-37 present the horizontal and vertical displacement distributions for the non-ordinary state-based formulation. For  $\delta_1 = 4\Delta x_1 = \delta_2 = 2\Delta x_2$ , the peridynamic predictions closely follow the FEM reference. Although increasing the horizon size introduces some interface error in the horizontal displacement, the magnitude of this error is less significant than that observed in the locally defined horizon approach.

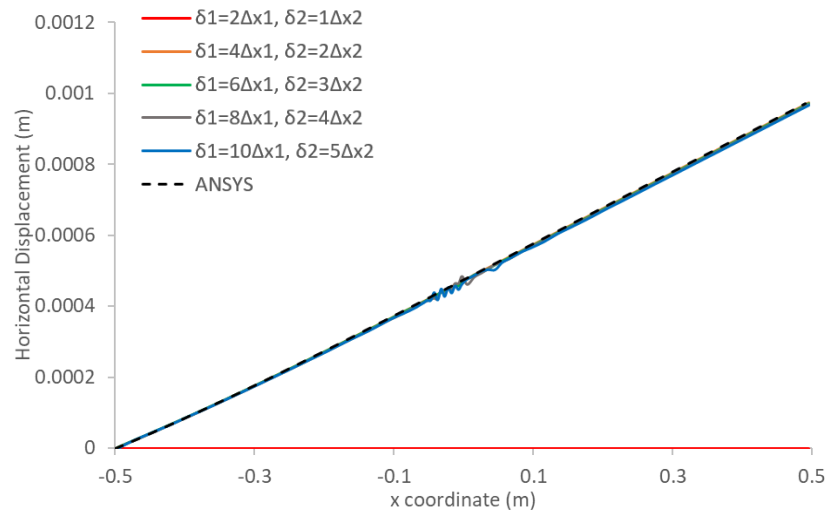


*Fig. 5-36 Variation of horizontal displacements along the central axis ( $x, y = 0$ ) in non-ordinary state-based formulation, constant horizon size.*

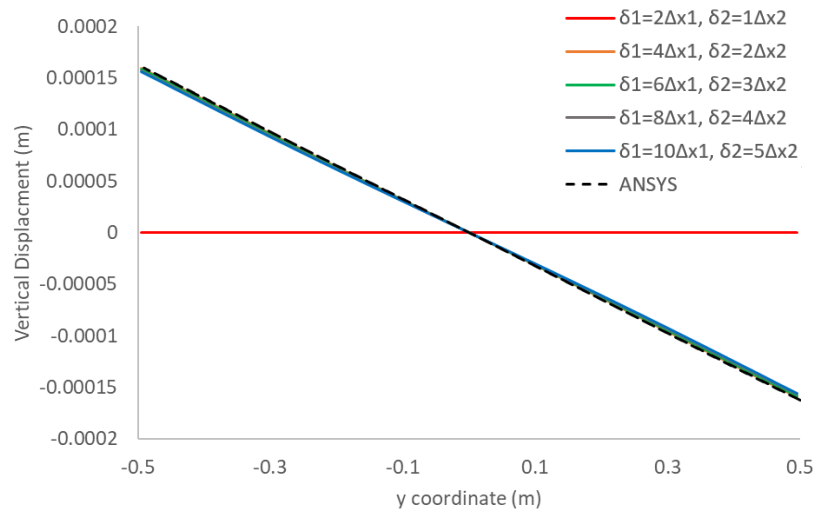


*Fig. 5-37 Variation of vertical displacement along the central axis ( $x = 0, y$ ) in non-ordinary state-based formulation, constant horizon size.*

Direct comparison (Fig. 5-38 and Fig. 5-39) shows that, for the optimised horizons ( $\delta_1 = 2\Delta x_1, \delta_2 = 2\Delta x_2$  for locally defined;  $\delta_1 = 4\Delta x_1 = \delta_2 = 2\Delta x_2$  for constant horizon), both strategies yield nearly identical displacement fields.

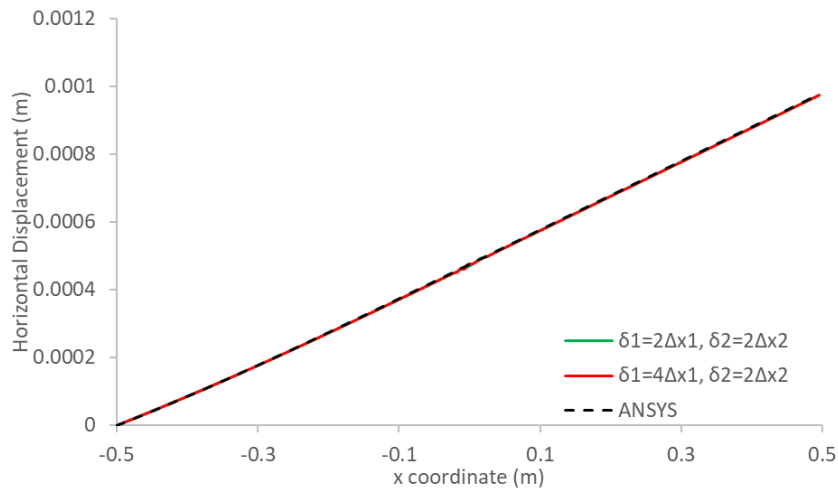


*Fig. 5-38 Comparison of horizontal displacements along the central axis ( $x, y = 0$ ) between locally defined and constant horizon size in non-ordinary state-based formulation.*

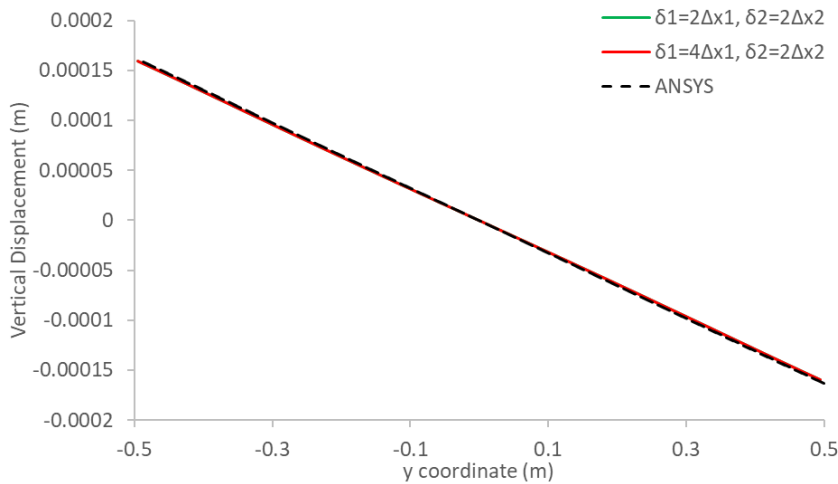


*Fig. 5-39 Comparison of vertical displacements along the central axis ( $x = 0, y$ ) between locally defined and constant horizon size in non-ordinary state-based formulation.*

Since a horizon size of  $3\Delta x$  is generally preferred in both bond-based and ordinary state-based formulations, the non-ordinary state-based formulation was also tested with comparable horizon values. As shown in Fig. 5-40 and Fig. 5-41, adopting the same horizon selection in non-ordinary state-based formulation does not result in significant loss of accuracy, but interface-related errors in horizontal displacement are more pronounced with locally defined horizons. Employing a constant horizon reduces the magnitude of such errors while maintaining comparable overall displacement predictions.

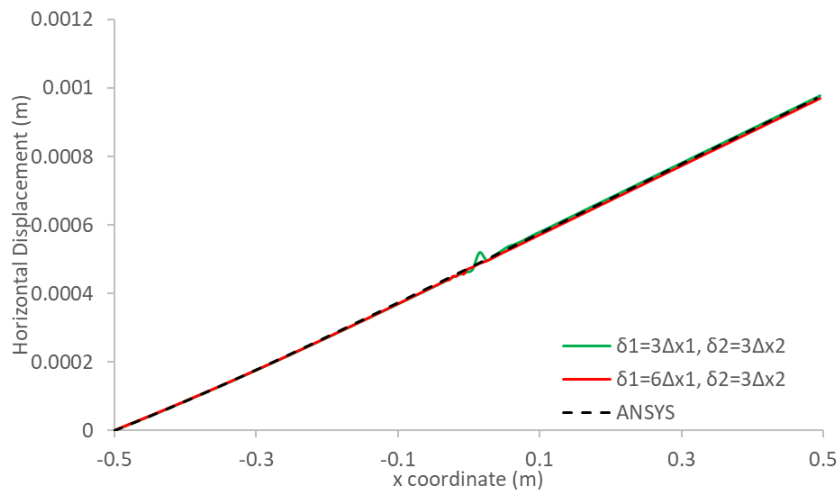


*Fig. 5-40 Comparison of horizontal displacements along the central axis ( $x, y = 0$ ) between locally defined and constant horizon size in non-ordinary state-based formulation.*

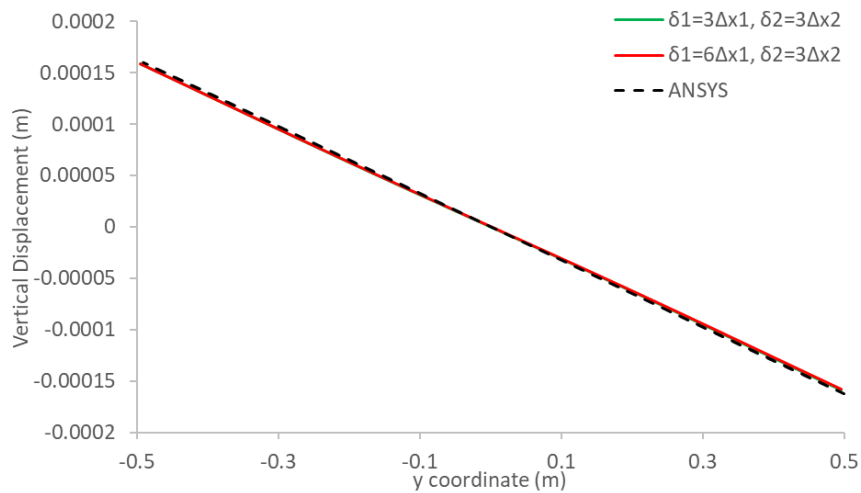


*Fig. 5-41 Comparison of vertical displacements along the central axis ( $x = 0, y$ ) between locally defined and constant horizon size in non-ordinary state-based formulation.*

## 5.5 Chapter Summary

This chapter has presented a derivation of the dual-horizon peridynamics formulation using the Euler-Lagrange equations. Dual-horizon peridynamics provides an effective framework for handling non-uniform discretisation and variable horizon sizes, both of which may be required for computational efficiency or to capture specific local features of complex engineering problems. The methodology has been systematically evaluated through numerical experiments involving both dynamic (plate vibration) and

static (plate under tension) benchmark problems, using bond-based, ordinary state-based, and non-ordinary state-based formulations.

The results demonstrate that, for both bond-based and ordinary state-based formulations, optimum accuracy is generally achieved when the horizon size is set to three times the local grid spacing ( $\delta = 3\Delta x$ ), in line with findings for uniform discretisation. Both locally defined and constant horizon strategies can deliver reliable predictions; however, the constant horizon approach tends to yield improved accuracy, attributed to the increased number of interacting material points.

For the non-ordinary state-based formulation, the optimal horizon size under non-uniform discretisation is found to be smaller ( $\delta = 2\Delta x$ ). In addition, the fluctuations observed in Fig. 5-26 occur when larger horizons are combined with locally defined strategies, leading to pronounced interface-related errors. At the transition between coarse and fine regions, the change in horizon size creates mismatched family sizes, which results in oscillatory behaviour. However, as shown in Fig. 5-40, this effect is mitigated when a constant horizon is applied across the domain.

Finally, with the advancement of AM technologies, the fabrication of complex materials such as microstructured materials is possible. peridynamic theory can be a suitable alternative for the analysis of microstructured materials to some other approaches presented in the literature (Placidi, 2016; Placidi and Barchiesi, 2018; Spagnuolo et al., 2017).

## Chapter 6 Thermal Diffusion Analysis by Using Dual-Horizon Peridynamics

### 6.1 Introduction

The preceding chapters have systematically developed the theoretical framework and numerical implementation of peridynamics for mechanical analysis, with a focus on the influence of discretisation and horizon size under both static and dynamic loadings. These investigations have established a foundation for the application of peridynamic methods to a broad range of mechanical engineering problems. However, AM and welding processes are inherently multiphysical, thermal effects are intrinsically coupled to the mechanical response, requiring robust modelling strategies that can capture the effects of nonlocal thermal diffusion and thermal discontinuities.

This chapter extends the peridynamic framework and introduces the dual-horizon peridynamic formulation to solve thermal diffusion problems. Lagrangian formalism is utilised to derive the governing equations. The proposed formulation allows utilisation of variable discretisation and horizon sizes inside the solution domain, which can result in significant benefits in terms of computational time. To demonstrate the capability of the Dual-Horizon Peridynamics formulation, three different example problems are considered, including a square plate with temperature and no flux boundary conditions, a square plate under thermal shock loading, and a square plate with an insulated crack. For all problems that are considered, good agreement is obtained between peridynamics predictions and FEM results.

### 6.2 Peridynamic Thermal Diffusion Formulation

The governing equation for peridynamic thermal diffusion can be derived by solving for the Euler–Lagrange equation (Oterkus et al., 2014)

$$\frac{d}{dt} \left( \frac{\partial L}{\partial \dot{\theta}} \right) - \frac{\partial L}{\partial \theta} = 0 \quad (6.1)$$

where  $\theta$  is the temperature, and  $L$  is the Lagrangian. The Lagrangian may be defined as

$$L = \int_V L dV \quad (6.2)$$

where  $L$  is the Lagrangian density. In peridynamic framework, the Lagrangian density at a material point can be defined as

$$L = Z + \rho \hat{s} \theta \quad (6.3)$$

in which  $Z$  is thermal potential,  $\rho$  is density, and  $\hat{s}$  represents the heat source per unit mass.

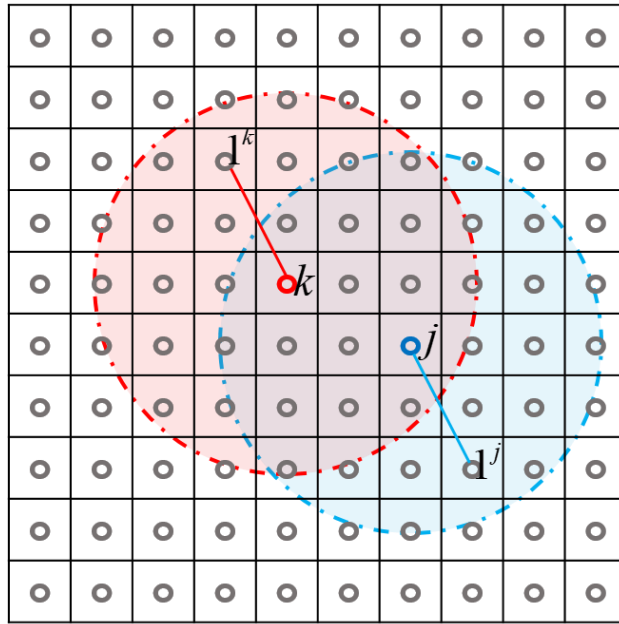


Fig. 6-1 Material points and the horizon (Oterkus et al., 2017).

In peridynamics the interactions between material points are nonlocal. Therefore, a material point exchanges heat energy through non-local interactions with its surrounding material points within its horizon,  $H_x$  with a size of,  $\delta$  (see Fig. 6-1) (Oterkus et al., 2014). Each material point possesses a thermal potential,  $Z_k$ , which depends on the temperatures of all neighbouring points inside its horizon.

For a given material point  $k$  at  $\mathbf{x}_k$ , the thermal potential  $Z_k$  is defined as the sum of microthermal potentials associated with its interactions. Specifically, due to the bidirectional heat exchange between two material points  $\mathbf{x}_k$  and  $\mathbf{x}_j$ , two microthermal potentials  $z_{kj}$  and  $z_{jk}$  arise. Microthermal potential,  $z_{kj}$  depends on the temperature

difference between the material point  $\mathbf{x}_k$  and the material points that it is interacting with inside its horizon.

Therefore, the thermal potential  $Z_k$  at material point  $\mathbf{x}_k$  can be defined as

$$Z_k = \frac{1}{2} \sum_{j=1}^{N_k} \frac{1}{2} \left\{ \begin{array}{l} z_{kj} [\theta_{1^k} - \theta_k, \dots, \theta_{N_k^k} - \theta_k] + \\ z_{jk} [\theta_{1^j} - \theta_j, \dots, \theta_{N_j^j} - \theta_j] \end{array} \right\} V_j \quad (6.4)$$

in which  $N_k$  and  $N_j$  are the number of material points inside the horizon of material points  $\mathbf{x}_k$  and  $\mathbf{x}_j$ , respectively,  $\theta_k$  is the temperature of material point  $\mathbf{x}_k$ ,  $\theta_{1^k}$  is the temperature of the first material point that interacts with point  $\mathbf{x}_k$ , by the same token for  $j$ , and  $V_j$  is the volume associated with the material point  $\mathbf{x}_j$ . The equation represents that the thermal potential at a material point  $\mathbf{x}_k$  is the sum of all microthermal potentials associated with that point.

Using the Euler–Lagrange equation given in Eq.( 6.1 ) for the material point  $\mathbf{x}_k$  yields the peridynamic governing equation for the thermal diffusion as

$$\sum_{j=1}^{N_k} [-\mathfrak{H}_{kj} + \mathfrak{H}_{jk}] V_j + \rho_k \hat{s}_k = 0 \quad (6.5)$$

where

$$\mathfrak{H}_{kj} = \frac{1}{2} \frac{1}{V_j} \left[ \sum_{i=1}^{N_k} \frac{\partial z_{ki}}{\partial (\theta_j - \theta_k)} V_i \right] \quad (6.6)$$

and

$$\mathfrak{H}_{jk} = \frac{1}{2} \frac{1}{V_k} \left[ \sum_{i=1}^{N_j} \frac{\partial z_{ji}}{\partial (\theta_k - \theta_j)} V_i \right] \quad (6.7)$$

The first term in Eq.( 6.5 ) represents the heat flow density,  $\mathfrak{H}_{kj}$ , from  $\mathbf{x}_j$  to  $\mathbf{x}_k$ , while the second term,  $\mathfrak{H}_{jk}$ , corresponds to the reverse interaction.

Moreover, the heat source  $\hat{s}_k$  in Eq.( 6.5 ) can be further defined as

$$\hat{S}_k = \dot{\epsilon}_{s,k} - S_{b,k} \quad (6.8)$$

in which  $S_{b,k}$  is the heat source due to volumetric heat generation per unit mass.

The rate of heat energy stored,  $\dot{\epsilon}_s$  when heat flow varies over a short period can be expressed as (Oterkus et al., 2014)

$$\dot{\epsilon}_s = C_v \frac{\partial \theta}{\partial t} \quad (6.9)$$

where  $C_v$  is the specific heat capacity.

Therefore, the peridynamic thermal diffusion equation given in Eq.( 6.5 ) can rewritten as

$$\rho_k C_v \dot{\theta}_k = \sum_{j=1}^{N_k} [\mathbb{H}_{kj} - \mathbb{H}_{jk}] V_j + h_{q,k} \quad (6.10)$$

where heat source due to volumetric heat generation can expressed as

$$h_{q,k} = \rho_k S_{b,k} \quad (6.11)$$

If bond-based peridynamic thermal diffusion model is considered, the heat flow density between two material points is assumed to be a function of the temperature difference between only the interacting material points. Thus,

$$\mathbb{H}_{kj} = \frac{1}{2} \frac{\partial z_{kj}}{\partial (\theta_j - \theta_k)} \quad (6.12)$$

and

$$\mathbb{H}_{jk} = \frac{1}{2} \frac{\partial z_{jk}}{\partial (\theta_k - \theta_j)} \quad (6.13)$$

For microthermal potentials,

$$\partial z_{kj} = \frac{1}{2} \frac{\kappa (\theta_j - \theta_k)^2}{2 |\mathbf{x}_j - \mathbf{x}_k|} \quad (6.14)$$

and

$$z_{jk} = \frac{1}{2} \frac{\kappa (\theta_k - \theta_j)^2}{2 |\mathbf{x}_k - \mathbf{x}_j|} \quad (6.15)$$

As a result, the corresponding heat flow densities in Eq.( 6.12 ) and Eq.( 6.13 ) can be re-written as

$$\mathbf{H}_{kj} = \frac{\kappa}{2} \frac{\theta_j - \theta_k}{|\mathbf{x}_j - \mathbf{x}_k|} \quad (6.16)$$

and

$$\mathbf{H}_{jk} = \frac{\kappa}{2} \frac{\theta_k - \theta_j}{|\mathbf{x}_k - \mathbf{x}_j|} \quad (6.17)$$

where peridynamic microconductivity,  $\kappa$  can be expressed for 2-Dimensional solution domains as (Oterkus et al., 2014)

$$\kappa = \frac{6k}{\pi h \delta^3} \quad (6.18)$$

in which  $k$  is the heat conductivity,  $h$  is the thickness of the geometry, and  $\delta$  is the horizon size.

### 6.3 Dual-horizon Peridynamics for Thermal Diffusion

The uniform discretization with constant horizon size is commonly used in peridynamic simulations since it is simple to implement for the whole geometry. However, for some problems, using finer discretization size at all locations inside the solution domain can be computationally time consuming. Thus, it is essential to use finer discretization size at locations with high temperature gradient and coarse discretization size can be used elsewhere. Moreover, utilizing variable horizon sizes can also be required either due to computational or problem specific reasons.

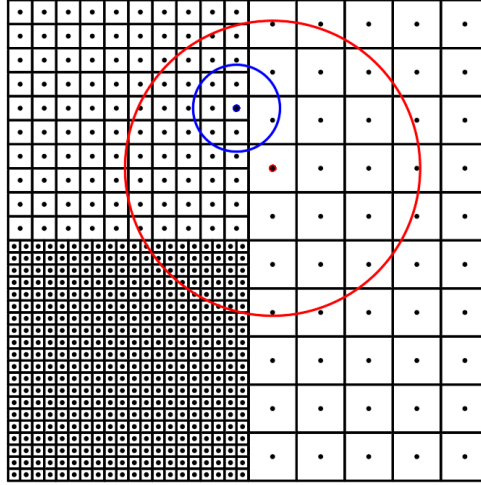


Fig. 6-2 Non-uniform discretization with different horizon sizes.

It should be noted that in Eq.( 6.12 ) and Eq.( 6.13 ), the microthermal potential is zero if one material point does not lie within the horizon of the other. As shown in Fig. 6-2, although a material point associated with a smaller (blue) horizon may fall within the horizon of another point with a larger (red) horizon, the reverse is not necessarily true.

Accordingly, the heat flow densities between material points  $\mathbf{x}_k$  and  $\mathbf{x}_j$  ,as given in Eq.( 6.16 ) and Eq.( 6.17 ) can be reformulated for the variable horizon case as

$$H_{kj} = \alpha_{kj} \frac{\kappa}{2} \frac{\theta_j - \theta_k}{|\mathbf{x}_j - \mathbf{x}_k|} \quad (6.19)$$

$$H_{jk} = \alpha_{jk} \frac{\kappa}{2} \frac{\theta_k - \theta_j}{|\mathbf{x}_k - \mathbf{x}_j|} \quad (6.20)$$

where the indicator functions are defined as

$$\alpha_{kj} = \begin{cases} 1, z_{kj} \neq 0 \\ 0, z_{kj} = 0 \end{cases} \quad (6.21)$$

$$\alpha_{jk} = \begin{cases} 1, z_{jk} \neq 0 \\ 0, z_{jk} = 0 \end{cases} \quad (6.22)$$

and the peridynamic microconductivities for material points  $\mathbf{x}_k$  and  $\mathbf{x}_j$  are given by

$$\kappa_k = \frac{6k}{\pi h \delta_k^3} \quad (6.23)$$

$$\kappa_j = \frac{6k}{\pi h \delta_j^3} \quad (6.24)$$

where  $\delta_k$  and  $\delta_j$  are the horizon sizes of the material points  $\mathbf{x}_k$  and  $\mathbf{x}_j$ , respectively.

#### 6.4 Thermal Diffusion Case Studies

To demonstrate the capabilities of the current dual-horizon peridynamics thermal diffusion formulation, three different problems are considered including a square plate with temperature and no flux boundary conditions, a square plate under thermal shock with insulated boundaries and a square plate with an insulated crack. Uniform or non-uniform discretization was utilized with constant or variable horizon size. Peridynamic predictions are compared with FEM results obtained by using ANSYS, a commercial finite element software.

##### 6.4.1 Plate with Temperature and No Flux Boundary Conditions

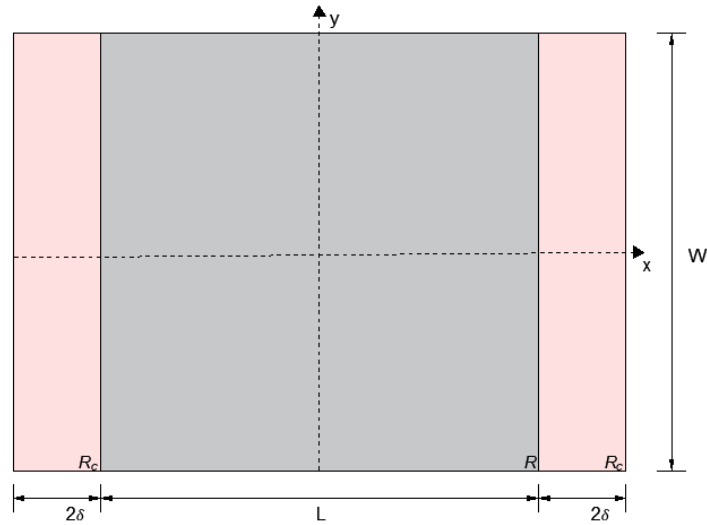


*Fig. 6-3 Peridynamic model of the plate.*

For the first example problem, an isotropic square plate with dimensions of length ( $L$ ) = width ( $W$ ) = 0.01 m is considered (Fig. 6-3). The plate has a thickness of  $h = 0.001$  m and is subjected to temperature boundary conditions of  $\theta(x = -0.005, y) = 0$  °C and  $\theta(x = 0.005, y) = 10$  °C at the left and right edges, respectively. The upper and

bottom boundaries are insulated boundaries. Boundary conditions are applied by introducing fictitious regions,  $R_c$  and following the approach described in Oterkus et al., (2014). Specific heat capacity  $C_v$ , thermal conductivity  $k$  and mass density  $\rho$  are specified as 64 J/kgK, 233 W/mK and 260 kg/m<sup>3</sup>, respectively.

The geometry is discretized in various forms in peridynamic model. The solution domain is split into two equal regions as Region 1 and Region 2 from the vertical axis,  $y$ . Mesh ratio  $k$  between these two regions is defined as

$$k = \frac{\Delta_1}{\Delta_2} \quad (6.25)$$

where  $\Delta_1$  indicates the spacing between the material points in Region 1 and  $\Delta_2$  indicates the spacing between the material points in Region 2.

The cases are evaluated with various horizon size combinations and horizon size ratio  $m$  is defined as

$$m = \frac{\delta_1}{\delta_2} \quad (6.26)$$

where  $\delta_1$  is the horizon size in Region 1 and  $\delta_2$  is the horizon size in Region 2. The relationship between horizon size and spacing is given as

$$\delta_i = n\Delta_i \quad (6.27)$$

where  $i = 1, 2$  represents Regions 1 and 2, respectively, whereas  $n = 1, \dots, 5$  represents the size the horizon. For example, if  $\delta_2 = 3\Delta_2$ , the horizon in Region2 has a size of three material points in radius.

### 6.4.1.1 Plate with Uniform Discretisation and Identical Horizon Sizes

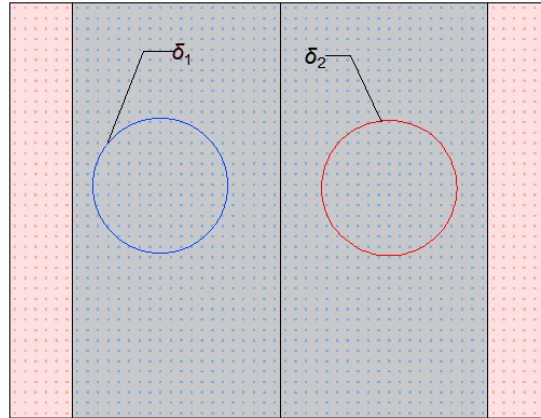


*Fig. 6-4 Peridynamic model with uniform discretisation and identical horizon sizes.*

In the first case, as shown in the Fig. 6-4, the plate is discretised uniformly with the spacing between material points  $\Delta_1 = \Delta_2 = 1.0 \times 10^{-4}$  m in horizontal and vertical directions. All material points have an identical horizon size ( $\delta_1 = \delta_2$ ). Therefore,  $k$  and  $m$  parameters defined in Eq.( 6.25 ) and Eq.( 6.26 ) are both equal to 1. The peridynamic solution of the temperature variations along the horizontal central axis are obtained by using explicit time integration with a time step size of  $1.0 \times 10^{-7}$  s, and compared with the finite element method results by using PLANE55 element in ANSYS.

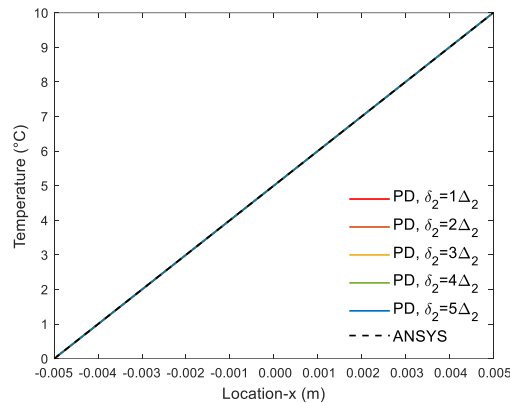


*Fig. 6-5 Temperature variations from peridynamic and FEM predictions at  $y = 0$  when  $k = 1$ ,  $m = 1$ .*

As can be seen in Fig. 6-5, the peridynamic predictions have a good agreement with FEM results for all horizon sizes for uniform discretization and identical horizon sizes.

### 6.4.1.2 Plate with Uniform Discretisation and Different Horizon Sizes

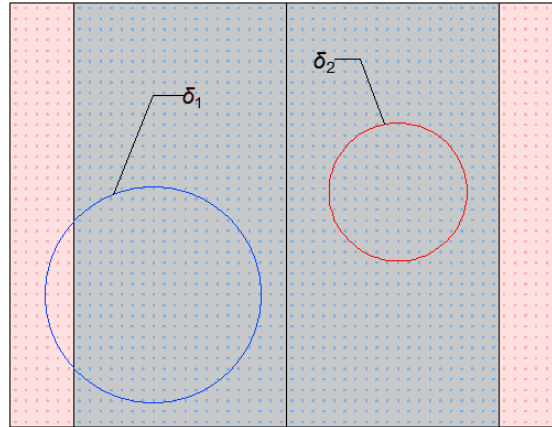


Fig. 6-6 Peridynamic model with uniform discretisation but different horizon sizes.

In order to investigate the capability of the dual-horizon concept, the square plate is discretised with the same discretization parameters ( $\Delta_1 = \Delta_2 = 1.0 \times 10^{-4}$  m) as in the former case. However, the horizon sizes in Regions 1 and 2 of the plate are different (see Fig. 6-6). The horizon size of Region 1 is set twice big of the horizon size of Region 2 ( $\delta_1 = 2\delta_2$ ). Therefore,  $k$  and  $m$  parameters are equal to 1 and 2, respectively.

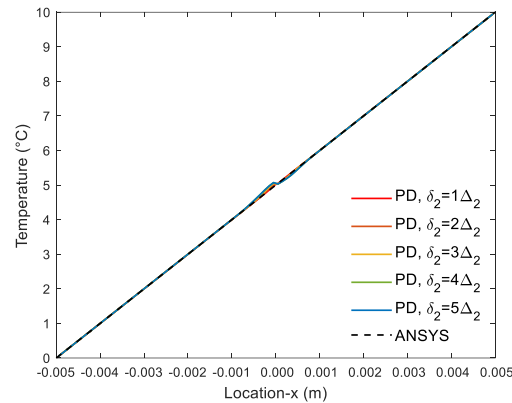
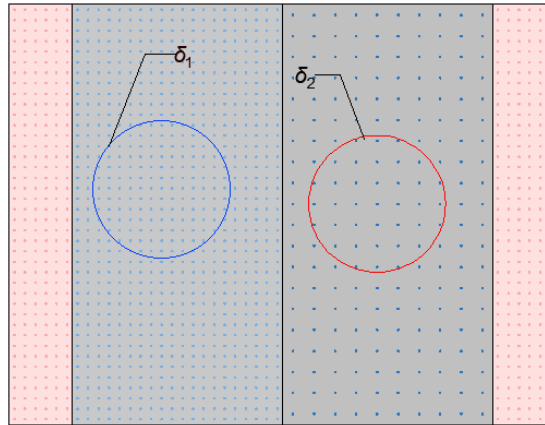


Fig. 6-7 Temperature variations from PD and FEM predictions at  $y = 0$  when  $k = 1$ ,  $m = 2$ .

The peridynamic solution of the temperature variations along horizontal central axis are obtained by using explicit time integration with a time step size of  $1.0 \times 10^{-7}$  s and compared with FEM results as shown in Fig. 6-7. The peridynamic predictions generally agree well with FEM. However, there is small difference at the interface of Regions 1 and 2 for larger horizon sizes and increases as the horizon size increases.

### 6.4.1.3 Plate with Non-uniform Discretisation and Identical Horizon Sizes



*Fig. 6-8 Peridynamic model with non-uniform discretisation but identical horizon sizes.*

In the third case, the square plate has the same geometric parameters, material properties and boundary conditions with the first case. Since refined discretisation increases the computational cost, in order to examine the non-uniform discretisation on heat conduction, the discretisation size in Region 2 is increased to a size of  $\Delta_2 = 2.0 \times 10^{-4}$  m in horizontal and vertical directions whereas the discretisation size in Region 1 is same as uniform cases which is  $\Delta_1 = 1.0 \times 10^{-4}$  m (Fig. 6-8). The horizon sizes remain the same in each region as the first uniform case. Therefore,  $k$  and  $m$  parameters are equal to 0.5 and 1, respectively.

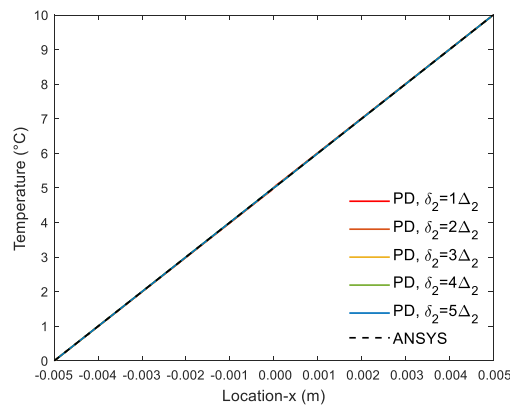


*Fig. 6-9 Temperature variations from PD and FEM predictions at  $y = 0$  when  $k = 0.5$ ,  $m = 1$ .*

The peridynamic solution of the temperature variations along the horizontal central axes are obtained by using explicit time integration with a time step size of  $1.0 \times 10^{-7}$  s. As shown in Fig. 6-9, the PD predictions for the temperature variations agree well with the FEM results for various horizon sizes.

#### 6.4.1.4 Plate with Non-uniform Discretisation and Different Horizon Sizes

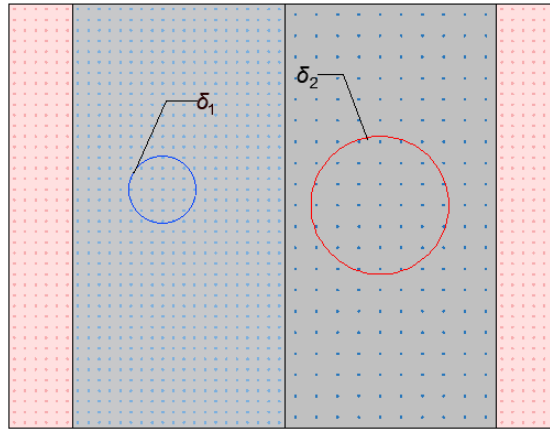


*Fig. 6-10 Peridynamic model with non-uniform discretisation but different horizon sizes.*

In peridynamic numerical simulations computational time depends on not only the discretisation size but also the number of material points within its horizon. The third case shows a good agreement of peridynamic and FEM predictions for various horizon sizes with a non-uniform discretisation. Therefore, this last case inherits the non-uniform discretisation from the third case and the horizon size in Region 1 is reduced to half of the horizon size in Region 2, i.e.  $\delta_2 = 2\delta_1$  (see Fig. 6-10). Since  $\Delta_2 = 2\Delta_1$  and  $\delta_2 = 2\delta_1$ , horizon in each region contains same number of material points within their horizon. Moreover,  $k$  and  $m$  parameters are both equal to 0.5, respectively.

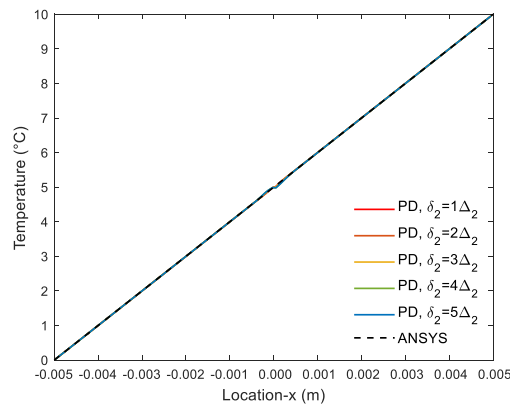


Fig. 6-11 Temperature variations from PD and FEM predictions at  $y = 0$  when  
 $k = 0.5, m = 0.5$ .

As can be observed in the Fig. 6-11, the peridynamic numerical results mostly agree well with the FEM results. However, as the horizon size grows, a slight difference is observed at the interface of Regions 1 and 2.

#### 6.4.2 Plate Under Thermal Shock with Insulated Boundaries

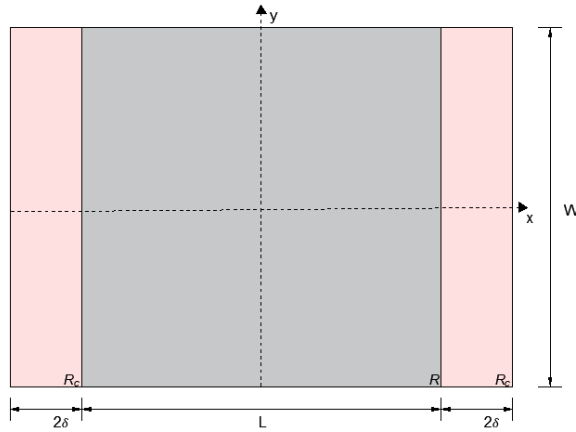


Fig. 6-12 Peridynamic model of the plate under thermal shock loading.

In the second example problem, an isotropic square plate with insulated boundaries is subjected to a thermal shock loading on the left edge. The geometric parameters are 10 m in length ( $L$ ) and width ( $W$ ) with a thickness of ( $h$ ) 1 m (see Fig. 6-12). The specific heat capacity  $C_v$ , thermal conductivity  $k$  and mass density  $\rho$  are specified as  $C_v = 1$  J/kgK,  $k = 1$  W/mk, and  $\rho = 1$  kg/m<sup>3</sup>, respectively. The initial condition and boundary conditions are stated as

$$\theta(x, y, t = 0) = 0 \text{ } ^\circ\text{C} \quad (6.28)$$

and

$$\theta, x(x = 5, y) = 0 \text{ } ^\circ\text{C}, \quad t > 0 \quad (6.29)$$

$$\theta, y(x, y = \pm 5) = 0 \text{ } ^\circ\text{C}, \quad t > 0 \quad (6.30)$$

$$\theta(x = -5, t) = 5te^{-2t}, \quad t > 0 \quad (6.31)$$

#### 6.4.2.1 Plate with Uniform Discretisation and Identical Horizon Sizes

In the first case, the peridynamic model has a uniform mesh with spacing  $\Delta_1 = \Delta_2 = 0.02$  m and identical horizon sizes in each region ( $\delta_1 = \delta_2$ ). Thus,  $k$  and  $m$  parameters are both equal to 1. The peridynamic solution of the temperature variations along central horizontal axis are obtained by using explicit time integration with a time step size of  $5.0 \times 10^{-4}$  s.

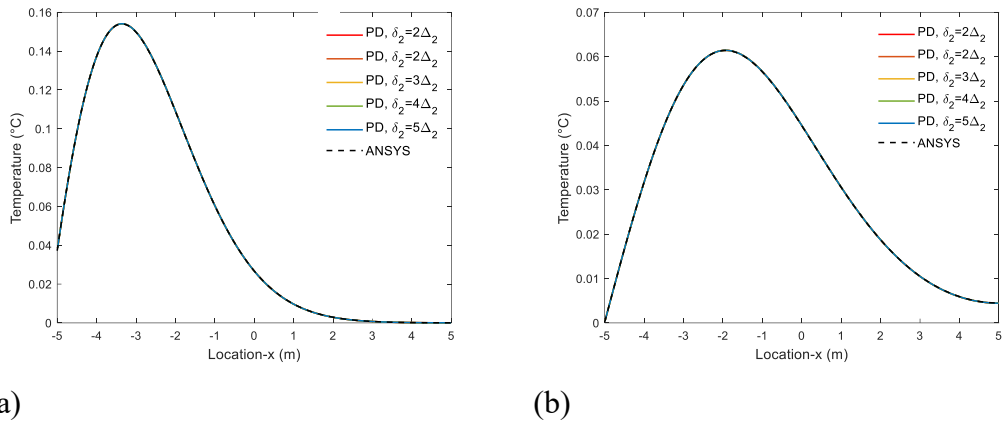


Fig. 6-13 Temperature variations from PD and FEM predictions when (a)  $t = 3$  s, (b)  $t = 6$  s at  $y = 0$ ,  $k = 1$ ,  $m = 1$ .

The results are assessed with various horizons and predicted at time  $t = 3$  s and  $t = 6$  s. Both peridynamic and FEM results are shown in Fig. 6-13. As can be observed, the peridynamic model results agree well with FEM results for various horizons with uniform discretisation.

#### 6.4.2.2 Plate with Uniform Discretisation and Different Horizon Sizes

In the second case, the numerical model has the same mesh configuration with the first case. In order to investigate the capability of the dual-horizon concept, horizon size in Region 2 is doubled, i.e.  $\delta_1 = 2\delta_2$ . Therefore,  $k$  and  $m$  parameters are equal to 1 and 2, respectively. The second case adopts the identical time step with the former case and the temperature variations along the central horizontal axis are plotted for time  $t = 3$  s and  $t = 6$  s for various horizons and compared with FEM results.

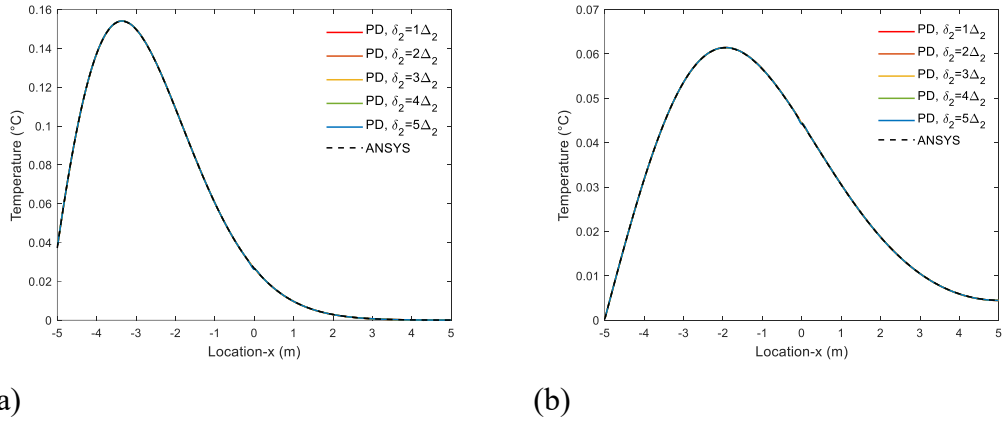


Fig. 6-14 Temperature variations from PD and FEM predictions when (a)  $t = 3$  s, (b)  $t = 6$  s at  $y = 0$ ,  $k = 1$ ,  $m = 2$ .

As shown in Fig. 6-14, peridynamic results for various horizon sizes generally agree well with FEM results. As the horizon size increases, a slight difference is observed at the interface of Regions 1 and 2 at both  $t = 3$  s and  $t = 6$  s.

#### 6.4.2.3 Plate with Non-uniform Discretisation and Identical Horizon Sizes

In the third case, the geometry is discretized with non-uniform discretisation. The spacing between material points in Region 2 is twice the spacing in Region 1, i.e.  $\Delta_1 = 0.02$  m,  $\Delta_2 = 0.04$  m. However, the horizon sizes are identical in each region, i.e.  $\delta_1 = \delta_2$ . Therefore,  $k$  and  $m$  parameters are equal to 0.5 and 1, respectively. The peridynamic solution of the temperature variations along the horizontal central axis at times  $t = 3$  s and  $t = 6$  s are evaluated with explicit time integration, with a time step size of  $5.0 \times 10^{-4}$  s and compared with FEM results.

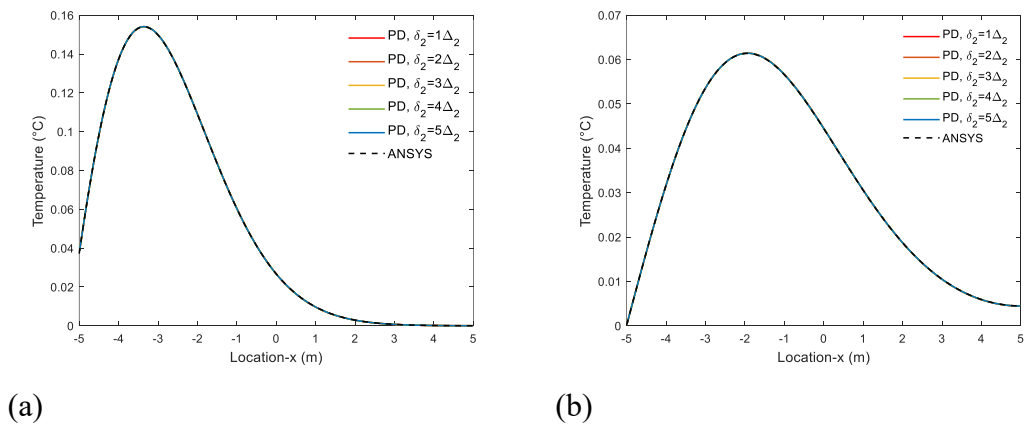


Fig. 6-15 Temperature variations from PD and FEM predictions when (a)  $t = 3$  s, (b)  $t = 6$  s at  $y = 0$ ,  $k = 0.5$ ,  $m = 1$ .

As can be observed from Fig. 6-15, results from peridynamic and FEM predictions for various horizons are in a good agreement.

#### 6.4.2.4 Plate with Non-uniform Discretisation and Different Horizon Sizes

The fourth case inherits the same discretisation configuration with the third case, i.e.  $\Delta_1 = 0.02$  m,  $\Delta_2 = 0.04$  m. However, the horizon size in Region 1 reduces to half size of the horizon size in Region 2, i.e.  $\delta_2 = 2\delta_1$ . Since both  $k$  and  $m$  parameters are equal to 0.5, each horizon has identical number of material points. Same time step size  $5.0 \times 10^{-4}$  s is adopted to obtain the temperature variations along the horizontal central axis when time  $t = 3$  s and  $t = 6$  s.

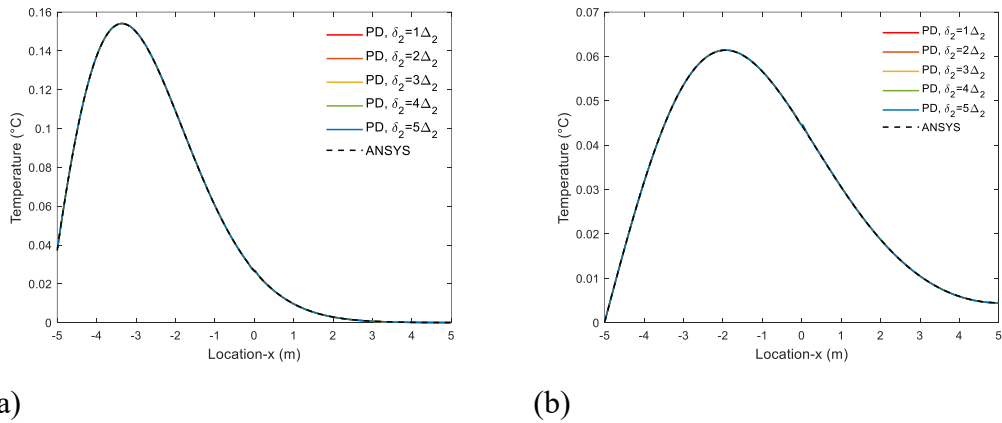


Fig. 6-16 Temperature variations from PD and FEM predictions when (a)  $t = 3$  s, (b)  $t = 6$  s at  $y = 0$ ,  $k = 0.5$ ,  $m = 0.5$ .

The peridynamic results mostly agree with FEM results for various horizon sizes (see Fig. 6-16). However, with the horizon size increases in each region, a slight difference is observed at the interface of Regions 1 and 2 for both  $t = 3$  s and  $t = 6$  s.

### 6.4.3 Square Plate with an Insulated Crack

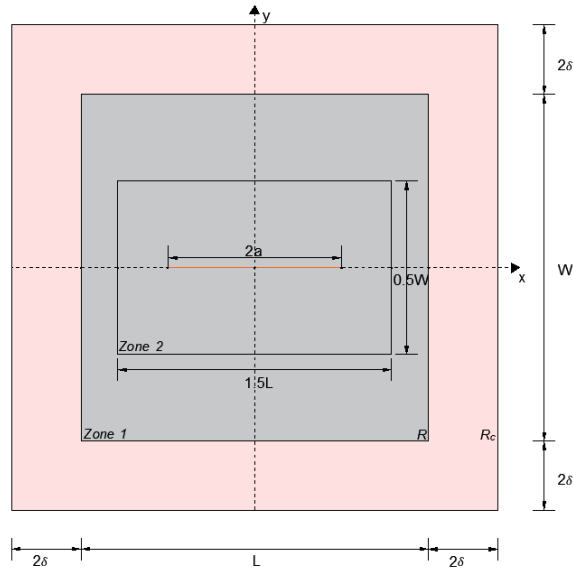


Fig. 6-17 Peridynamic model of the plate with an insulated crack.

For the final example problem as shown in Fig. 6-17, the isotropic square plate is considered with 2 cm in length ( $L$ ), 2 cm in width ( $W$ ) and 0.01 cm in thickness ( $h$ ). The plate has an insulated crack in the middle with a crack length of  $2a = 1$  cm. The specific heat capacity  $C_v$ , thermal conductivity  $k$  and mass density  $\rho$  are specified as  $C_v = 1$  J/kgK,  $k = 1.14$  W/cmK and  $\rho = 1$  kg/cm<sup>3</sup>, respectively. The plate is subjected to the following initial and boundary conditions

$$\theta(x, y, z, t = 0) = 0 \text{ } ^\circ\text{C} \quad -\frac{L}{2} \leq x \leq \frac{L}{2}, \quad -\frac{W}{2} \leq y \leq \frac{W}{2} \quad (6.32)$$

and

$$\theta\left(x, \frac{W}{2}, t\right) = 100 \text{ } ^\circ\text{C}, \quad \theta\left(x, -\frac{W}{2}, t\right) = -100 \text{ } ^\circ\text{C}, \quad t > 0 \quad (6.33)$$

$$\theta, x\left(\frac{L}{2}, y, t\right) = 0 \text{ } ^\circ\text{C}, \quad \theta, x\left(-\frac{L}{2}, y, t\right) = 0 \text{ } ^\circ\text{C}, \quad t > 0 \quad (6.34)$$

Since there is an insulated crack in the geometry, in order to evaluate the effect of dual horizon concept and non-uniform discretization, the geometry is split into two regions in peridynamic model as in the previous two numerical examples. Note that the definition of regions (zones) in this numerical example is different than the previous

two numerical examples. Moreover,  $k$  and  $m$  parameters are defined similarly as in the previous two examples.

#### 6.4.3.1 Plate with Uniform Discretisation and Identical Horizon Sizes

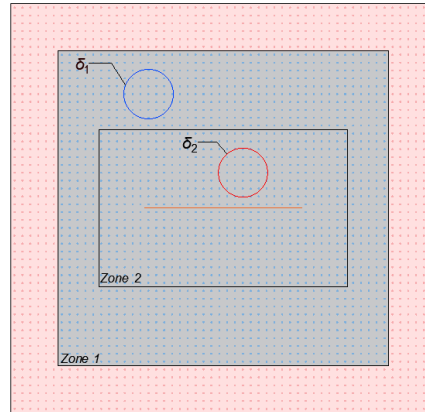


*Fig. 6-18 PD model with uniform discretisation and identical horizon sizes.*

As shown in Fig. 6-18, in this initial case the plate is uniformly discretised ( $k = 1$ ) with 0.01 cm spacing and the same horizon size is used in both zones ( $m = 1$ ). The peridynamic solution of the temperature variations along the vertical central axis is evaluated with a time step size of  $1.0 \times 10^{-5}$  s for various horizon sizes and compared with FEM results.

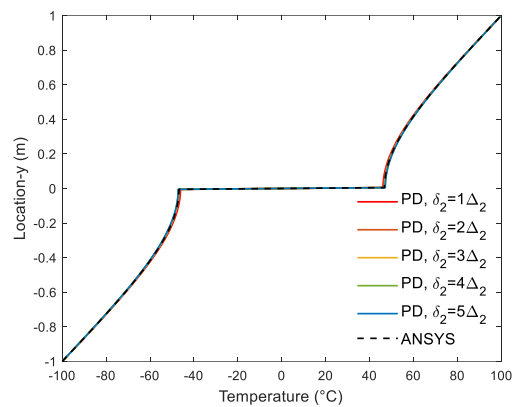


*Fig. 6-19 Temperature variations from PD and FEA predictions at  $x = 0$  when  $k = 1$ ,  $m = 1$ .*

As can be seen in Fig. 6-19, the numerical results from peridynamic analyses for various horizon sizes with uniform discretisation agree well with FEM results.

### 6.4.3.2 Plate with Uniform Discretisation and Different Horizon Sizes

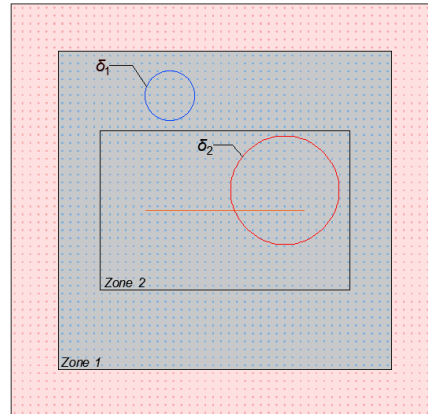


Fig. 6-20 PD model with uniform discretisation and different horizon sizes.

To investigate the dual-horizon size concept, this second case (see Fig. 6-20) utilizes uniform discretization as in the first case ( $k = 1$ ,  $\Delta_1 = 0.01$  cm,  $\Delta_2 = 0.01$  cm) and the horizon size in Region 2 is doubled due to the existence of insulated crack in this region ( $m = 0.5$ ,  $\delta_2 = 2\delta_1$ ). This case adopts the same time step size as the first case.

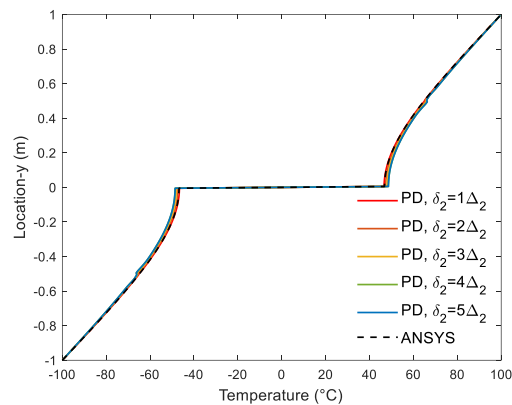


Fig. 6-21 Temperature variations from PD and FEA predictions at  $x = 0$  when  $k = 1$ ,  $m = 0.5$ .

As shown in Fig. 6-21, there is a good agreement between peridynamic and FEM results obtained along the vertical central axis. However, as the horizon size increases, a slight difference is observed at the interface between Region 1 and Region 2.

### 6.4.3.3 Plate with Non-uniform Discretisation and Identical Horizon Sizes

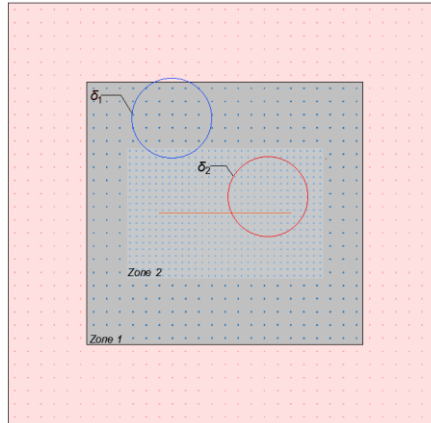


Fig. 6-22 PD model with non-uniform discretisation and identical horizon sizes.

Since coarse mesh requires less computational time, in this third case, the spacing in Region 1 is increased by two times compared with the first case ( $k = 2$ ,  $\Delta_1 = 0.02$  cm,  $\Delta_2 = 0.01$  cm). To evaluate the effect of non-uniform discretization, this third case (see Fig. 6-22) utilizes same horizon sizes in all regions ( $m = 1$ ,  $\delta_2 = \delta_1$ ). The time step size is the same as the first case.

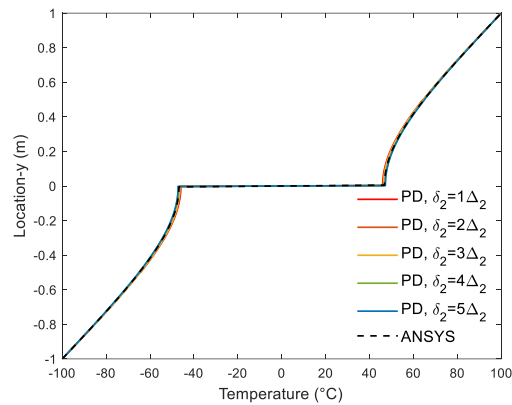


Fig. 6-23 Temperature variations from PD and FEM predictions at  $x = 0$  when  $k = 2$ ,  $m = 1$ .

As can be observed in Fig. 6-23, the peridynamic predictions for the temperature variations along the vertical central axis agree well with the FEM results for various horizon sizes.

#### 6.4.3.4 Plate with Non-uniform Discretisation and Different Horizon Sizes

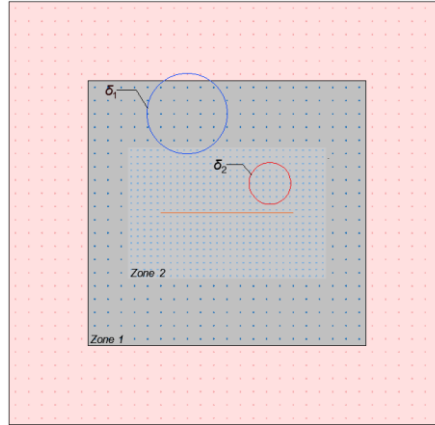


Fig. 6-24 PD model with non-uniform discretisation and different horizon sizes.

If horizon contains more material points, the computational time will increase. Therefore, in the last case, horizon size in Region 2 is reduced to half size compared with the horizon size in Region 1 ( $m = 2, \delta_1 = 2\delta_2$ ) as shown in Fig. 6-24. The discretization size is the same as in the third case ( $k=2, \Delta_1 = 0.02 \text{ cm}, \Delta_2 = 0.01 \text{ cm}$ ). Since both mesh ratio,  $k$  and horizon size ratio,  $m$  have values of 2, horizons in Regions 1 and 2 contain identical number of material points.

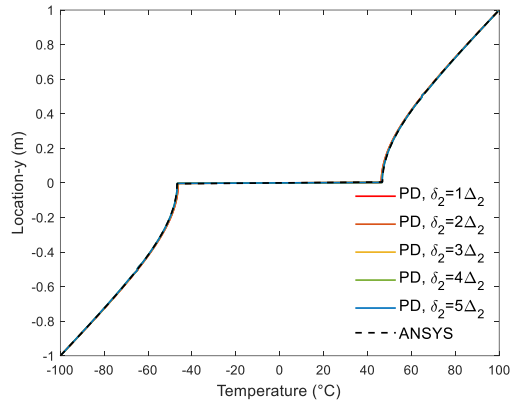


Fig. 6-25 Temperature variations from PD and FEM predictions at  $x = 0$  when  $k = 2$ ,  $m = 2$ .

As shown in Fig. 6-25, the perdynamic temperature predictions obtained along the vertical central axis agree well with FEM results. As the horizon size increases, a small difference is observed at the interface between Regions 1 and 2.

## 6.5 Chapter Summary

In this chapter, the dual-horizon peridynamic formulation is presented for the analysis of thermal diffusion problems. The framework enables the use of variable discretisation and horizon sizes within the computational domain, offering significant advantages in terms of computational efficiency for peridynamic simulations. To illustrate the capabilities of the dual-horizon approach, three representative case studies are examined: a square plate with imposed temperature and no-flux boundary conditions, a square plate subjected to thermal shock loading, and a square plate containing an insulated crack.

For each example, the solution domain is partitioned into two regions, each potentially characterised by distinct discretisation and horizon sizes. A range of five different horizon sizes is considered to systematically investigate the effect of horizon size on the results. Across all cases, good agreement is observed between peridynamic predictions and finite element method (FEM) solutions. However, when different discretisation or horizon sizes are employed in separate regions, minor discrepancies may arise at the interface, with the magnitude of these differences increasing as the horizon size ratio becomes larger. Overall, the findings indicate that the proposed Dual-Horizon Peridynamic formulation can be effectively applied to problems involving variable discretisation and horizon size, offering a practical balance between computational efficiency and accuracy.

## **Chapter 7 Thermomechanical Phase Change Peridynamic Model for Welding Analysis**

### **7.1 Introduction**

AM and welding are increasingly recognised as transformative technologies within advanced manufacturing, offering flexibility in fabricating complex geometries. However, these processes involve highly complex and transient thermomechanical environments, where rapid heating and cooling, strong coupling between thermal and mechanical responses, and phase transformations such as melting and solidification collectively determine the final microstructure of manufactured components. Consequently, the development of accurate and robust numerical models capable of simulating these coupled multiphysics phenomena has become essential for optimising process parameters and minimising costly trial-and-error experimentation.

The preceding chapters of this thesis have systematically developed a theoretical and computational framework for peridynamic modelling of both mechanical and thermal analysis. Building upon these developments, this chapter advances the peridynamic approach to address the challenges posed by AM and welding, with focus on the modelling of heat transfer and phase change scenarios. Furthermore, a central aspect of any numerical model for AM or welding is the representation of the heat source. Inaccuracies in the heat source model can lead to errors in predicting the transient temperature field, which in turn propagate into mechanical analyses, affecting displacement and residual stress predictions.

In this chapter, a new non-linear transient peridynamic model employing a variety of heat source models is developed to predict the temperature distribution and displacement variation. More importantly, as an essential physical phenomenon in heat conduction, phase transformation is considered in the peridynamic model. The importance of how the latent heat in the phase change can affect the temperature distribution and displacement field is also emphasised. The simulation results are compared with the FEM results. Close agreements are observed, which demonstrates the capability of the proposed non-linear transient peridynamic model for thermomechanical phase change analysis for AM and welding modelling.

## 7.2 Peridynamic Thermomechanics Theory

### 7.2.1 Peridynamic Thermo-Mechanical Governing Equations

The bond-based thermomechanical heat transfer equation for material point at  $\mathbf{x}$  is given by (Oterkus et al., 2014)

$$\rho(\mathbf{x})C_v\dot{\theta}(\mathbf{x}, t) = \int_{H_x} f_h dV' + h_q(\mathbf{x}, t) \quad (7.1)$$

where  $\rho$  is the density,  $C_v$  is the effective heat capacity, and  $\theta$  is the temperature. The term  $h_q$  represents the volumetric heat generation. In welding and AM process,  $h_q$  can represent the heat raised from the heat source.

The heat flow density (Oterkus et al., 2014),  $f_h$ , in Eq.( 7.1 ) can be expressed as

$$f_h = \kappa \frac{\tau}{|\xi|} \quad (7.2)$$

where  $\kappa$  is the micro-thermal conductivity,  $\xi = |\mathbf{x}' - \mathbf{x}|$  is the relative position between material points  $\mathbf{x}'$  and  $\mathbf{x}$  in the reference configuration. For two-dimensional structure, micro-thermal conductivity,  $\kappa$ , is provided in Eq.( 6.18 ). For three-dimensional structures, it is defined as (Oterkus et al., 2014)

$$\kappa = \frac{6k}{\pi\delta^4} \quad (7.3)$$

where  $k$  is the thermal conductivity, and  $\delta$  is the horizon size.

In addition, the notation  $\tau$  in Eq. ( 7.2 ) represents the temperature difference between a pair of material points  $\mathbf{x}'$  and  $\mathbf{x}$ , and this can be obtained by

$$\tau(\mathbf{x}, \mathbf{x}', t) = \theta(\mathbf{x}', t) - \theta(\mathbf{x}, t) \quad (7.4)$$

On the other hand, the general form of the coupled thermo-elasticity in bond-based peridynamics is provided by Oterkus et al. (2014). The equation of motion can be expressed as

$$\rho(\mathbf{x})\ddot{\mathbf{u}}(\mathbf{x}, t) = \int \left[ c \left( s(\mathbf{u}' - \mathbf{u}, \mathbf{x}' - \mathbf{x}) - \alpha \frac{\theta + \theta'}{2} \right) \frac{\mathbf{y}' - \mathbf{y}}{|\mathbf{y}' - \mathbf{y}|} \right] dV' + \mathbf{b}(\mathbf{x}, t) \quad (7.5)$$

where  $c$  represents the bond constant and is provided in Eq.( 3.6 ) and Eq.( 3.7 ) for two- and three-dimensional structure, respectively,  $s$  represents the stretch between the two material points as given in Eq.( 3.5 ),  $\alpha$  is the coefficient of thermal expansion,  $\mathbf{u}$  is the displacement of material point  $\mathbf{x}$ , and the term  $\mathbf{y}$  represent its position in the deformed configuration, thus  $\mathbf{y} = \mathbf{x} + \mathbf{u}$ .

### 7.2.2 Description of Time Dependent Heat Sources

Heat source modelling can be classified as a point heat source, a planar distribution heat source, and a volumetric distributed heat source. These sources are used to act on the numerical model depending on the actual manufacturing process model and the topographic characteristics of the weld.

#### 7.2.2.1 Point Heat Source

In the case of welding arc/laser beam acting on the surface of thick workpieces, the arc supplied with power  $Q$  can be treated as a point heat source. As shown in Fig. 7-1, a point heat source, so-called a concentrated source, is considered for thermal analysis in the peridynamic welding model.

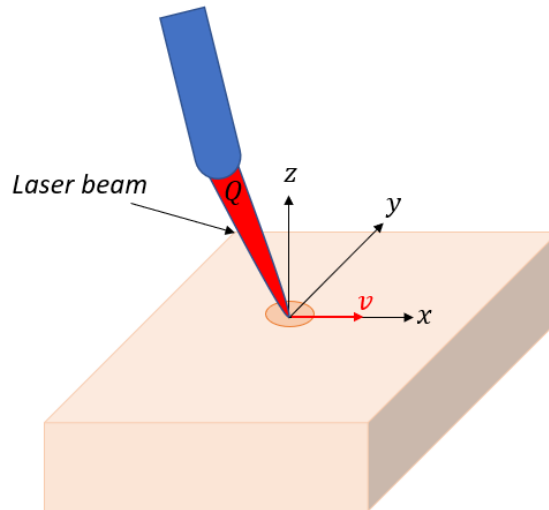


Fig. 7-1 Point heat source moving on the surface of a thick workpiece.

This is a simplified approximation of a physical situation but can provide a good temperature prediction under certain conditions. Rosenthal (1941) provides the solution for the temperature distribution of a steady state moving point heat source acted on a semi-infinite plate as

$$\theta - \theta_0 = \frac{Q}{2\pi kR} e^{-\frac{\bar{v}(x - \bar{v}t + R)}{2a}} \quad (7.6)$$

where  $\theta_0$  is the initial temperature of the workpieces,  $Q$  is the net heat input per unit time (heat source power),  $R$  is the distance to the centre of the welding arc,  $\bar{v}$  is the speed of arc,  $t$  is current time and  $a$  is the thermal diffusivity.

As can be observed from Eq.( 7.6 ), the temperature field in the welding arc centre tends to approach infinity when  $R \rightarrow 0$ , which does not have a physical meaning in the real welding process. However, the analytical temperature distribution for the point heat source model provides a reasonable temperature field prediction at the positions of the substance far from the heat source (Christensen, 1965).

#### 7.2.2.2 Gaussian Distribution Heat Source

The laser beam arc is a commonly used heat source in the selective laser melting technique. The source model can be accurately represented by a Gaussian distribution heat source as (Eagar and Tsai, 1983)

$$q(x, y, t) = q_m e^{-\frac{(x - \bar{v} * t)^2 + y^2}{2\sigma^2}} \quad (7.7)$$

and

$$q_m = \frac{Q}{2\pi\sigma^2} \quad (7.8)$$

where  $q_m$  is the maximum heat density at the welding arc centre  $(x - \bar{v} * t, y)$ ,  $\bar{v}$  is the speed of the moving heat source,  $Q$  is the power of laser beam, and  $\sigma$  is a distribution parameter.  $q(x, y, t)$  represents the heat flux at a point  $(x, y)$  at time  $t$ .

### 7.2.2.3 Volumetric Distribution Heat Source

In order to consider high-energy beam welding with heat flow penetration effect in the physical manufacturing process, a volumetric distributed model, named as semi-ellipsoidal heat source model, shown in Fig. 7-2 has been proposed by Goldak (1985).

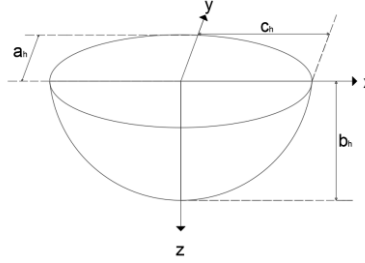


Fig. 7-2 Semi-ellipsoidal heat source model.

The mathematical form of heat source is given as (Goldak, 1985)

$$q(x, y, z, t) = q_m \exp\left(-\frac{3(x - v * t)^2}{c_h^2} - \frac{3y^2}{a_h^2} - \frac{3z^2}{b_h^2}\right) \quad (7.9)$$

where  $a_h$ ,  $b_h$ , and  $c_h$  are ellipsoidal heat source parameters as presented,  $q(x, y, z, t)$  is heat flux at a point  $(x, y, z)$  at time  $t$ .  $q_m$  is the maximum heat density at the centre of the welding arc which is given as (Goldak, 1985)

$$q_m = \frac{6\sqrt{Q}}{a_h b_h c_h \pi \sqrt{\pi}} \quad (7.10)$$

where  $Q$  is the net heat input per unit time.

### 7.3 Peridynamic Thermomechanics Coupled with Phase Change

Heat transfer scenarios with temperature variation often come with phase change. The characteristics of non-linearity, due to the multi-physical nature of the processes, make phase transformation challenging.

Phase change refers to the physical process in which a material transitions between different states, such as solid to liquid (melting) or liquid to solid (solidification). The energy required for a material to undergo such a transition, without a temperature change, is known as latent heat. During phase change, a material can absorb or release large amounts of latent heat at the transformation temperature. In the context of

welding and AM, where rapid heating and cooling occur, phase changes such as melting and solidification are common. Therefore, it is essential to account for the effects of latent heat in the peridynamic heat conduction equation to accurately model the thermal response of materials exposed to the high-energy heat source.

In the present work, the latent heat  $L_T$  is implicitly considered by effective heat capacity, in which the specific heat capacity of the material is artificially increased at mushy zone. Mushy zone is a temperature interval around the phase change temperature that the matter processes the phase transformation. The artificially increased specific heat capacity in the mushy zone can be defined as

$$C_p = \frac{L_T}{\theta_l - \theta_s} \quad (7.11)$$

where  $\theta_s$  is the substance solidification temperature and  $\theta_l$  is the substance fusion temperature. With the considered latent heat at phase change scenarios, consequently, the effective heat capacity  $C_v$  in the bond-based peridynamic heat conduction equation at different phases can be written as

$$C_v = \begin{cases} C_s & \theta < \theta_s & \text{solid phase} \\ C_p & \theta_s \leq \theta \leq \theta_l & \text{solid/liquid phase} \\ C_l & \theta > \theta_l & \text{liquid phase} \end{cases} \quad (7.12)$$

where  $C_s$ ,  $C_p$  and  $C_l$  are the specific heat capacities of the substance at solidus, mushy zone, and liquidus state, respectively. The effective heat capacity at each material point is determined based on its local temperature. If the temperature at a material point is below the melting point, the specific heat capacity corresponding to the solid phase is used in the heat conduction equation.

In addition, the mechanical properties of most materials used in welding and manufacturing are strongly affected by temperature. Specifically, for most metals, increasing temperature leads to a reduction in material stiffness, while lower temperatures result in higher stiffness.

To account for the temperature-dependent variation in material stiffness during arc welding scenarios involving phase change, a non-local approach is adopted to model. In the conventional bond-based peridynamics, the interaction between two material

points  $\mathbf{x}'$  and  $\mathbf{x}$  is linked by a ‘bond’. The bond constant in terms of Young’s Modulus,  $E$  for a two- and three-dimensional structure as given by Eq.( 3.6 ) and Eq.( 3.7 ), respectively. Without considering the temperature influence in the mechanical analysis, the parameter  $c$  is a constant value.

However, in the thermomechanical phase change peridynamic model for welding, Young’s modulus in the mechanical analysis is treated as a temperature-dependent property, denoted  $E(\theta)$ . As presented in Fig. 7-3, the bonds in the thermomechanical formulation are referred to as “thermo-mechanical bonds,” in which the effect of temperature on material stiffness is explicitly incorporated and can be defined as follows

$$c(\mathbf{x}, \theta_x) = \frac{9E(\theta_x)}{\pi h \delta^3} \quad (7.13)$$

and

$$c(\mathbf{x}', \theta_{x'}) = \frac{9E(\theta_{x'})}{\pi h \delta^3}$$

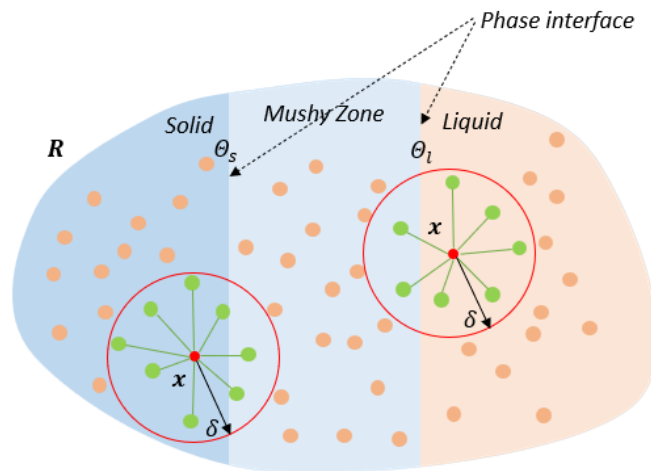


Fig. 7-3 Peridynamic horizon and its thermal-mechanical bonds (green line).

Therefore, the effect of temperature on material stiffness is incorporated through the bond constant. As the temperature varies at each material point and its neighbours, the bond constant is updated accordingly. Thus, the bond constant between two material points can be expressed as

$$c(\mathbf{x}, \mathbf{x}', \theta_x, \theta_{x'}) = \frac{c(\mathbf{x}, \theta_x) + c(\mathbf{x}', \theta_{x'})}{2} \quad (7.14)$$

With the temperature-dependent bond constant, the equation of motion for coupled thermo-elasticity in bond-based peridynamics can be re-written as

$$\rho(\mathbf{x})\ddot{\mathbf{u}}(\mathbf{x}, t) = \int \left[ c(\mathbf{x}, \mathbf{x}', \theta_x, \theta_{x'}) \left( s(\mathbf{u}' - \mathbf{u}, \mathbf{x}' - \mathbf{x}) - \alpha \frac{\theta + \theta'}{2} \frac{\mathbf{y}' - \mathbf{y}}{|\mathbf{y}' - \mathbf{y}|} \right) dV' + \mathbf{b}(\mathbf{x}, t) \right] \quad (7.15)$$

where all terms are as previously defined, and the temperature dependence of the bond constant directly links the local thermal environment to the mechanical response.

#### 7.4 Application of Initial and Boundary Conditions

The initial condition of the temperature distribution can be specified at time  $t = 0$

$$\theta(\mathbf{x}, t = 0) = \theta_0(\mathbf{x}) \quad (7.16)$$

where  $\theta_0$  is the initial temperature. If pre-heat treatment is adapted in the manufacturing process,  $\theta_0$  is defined as pre-heating temperature.

The boundary conditions in the heat conduction can be specified as temperature, heat flux, and the heat generation.

##### 7.4.1 Temperature

In peridynamics, the application of prescribed boundary temperatures differs from the approaches used in CCM. Rather than imposing the boundary temperature as a direct point load or distributed load on the physical boundary, peridynamics employs a fictitious layer, denoted as  $R_C$ , which is introduced outside the actual material region,  $R_t$  and shown in Fig. 7-4 (Oterkus et al., 2014; Madenci and Oterkus, 2016).

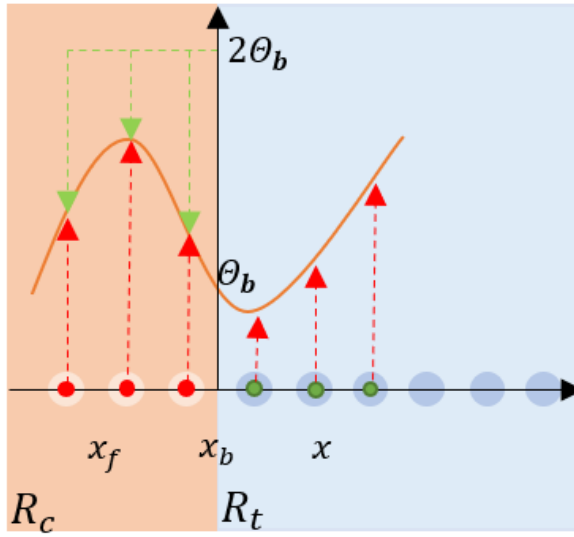


Fig. 7-4 Material real domain,  $R_t$  and its fictitious domain,  $R_C$ .

As illustrated in Fig. 7-4, the specified boundary temperature,  $\theta_b(\mathbf{x}_b, t)$ , along the real material surface is imposed within the fictitious layer by assigning temperature values to the corresponding material points in  $R_C$ . Specifically, the temperature at a fictitious material point,  $\mathbf{x}_f$ , is determined using the following relationship (Oterkus et al., 2014),

$$\theta_f(\mathbf{x}_f, t + \Delta t) = 2\theta_b(\mathbf{x}_b, t + \Delta t) - \theta(\mathbf{x}, t + \Delta t) \quad (7.17)$$

where  $\theta_f$  and  $\theta$  are the temperature of material points in the fictitious region  $R_C$  and real region  $R_t$ , respectively. Note that the material points at  $\mathbf{x}_f$  and  $\mathbf{x}$  are symmetrically located with respect to the location of the boundary  $\mathbf{x}_b$ . In the case of  $\theta_b(\mathbf{x}_b, t) = 0$ , this represents the insulated boundary condition.

#### 7.4.2 Heat Flux

The implementation of the heat flux from the heat source in the peridynamic heat transfer equation can be achieved by evaluating the rate of heat flow into the surface area and transforming it into a volumetric heat generation term,  $h_q(\mathbf{x}, t)$ . Therefore, the heat flux is applied as a volumetric heat source at the relevant material points and can be expressed as (Oterkus et al., 2014)

$$h_q(\mathbf{x}, t) = -\frac{q(\mathbf{x}, t) \cdot \mathbf{n}}{\Delta x} \quad (7.18)$$

where  $q(\mathbf{x}, t)$  is the heat flux,  $\Delta x$  is the spacing between material points and  $\mathbf{n}$  is the normal vector to the surface.

#### 7.4.3 Time-dependent Point Heat Source

For the numerical implementation of a moving point heat source on the workpiece, a birth-and-death procedure for material points is introduced in this work. Specifically, the point heat source is represented as a time-dependent volumetric heat generation, applied only to selected material points at each time step as the source moves along its prescribed path. When the heat source coincides with a particular material point, that point is assigned the corresponding volumetric heat generation. As the heat source advances and moves away from a given material point, the heat generation at that point is set to zero.

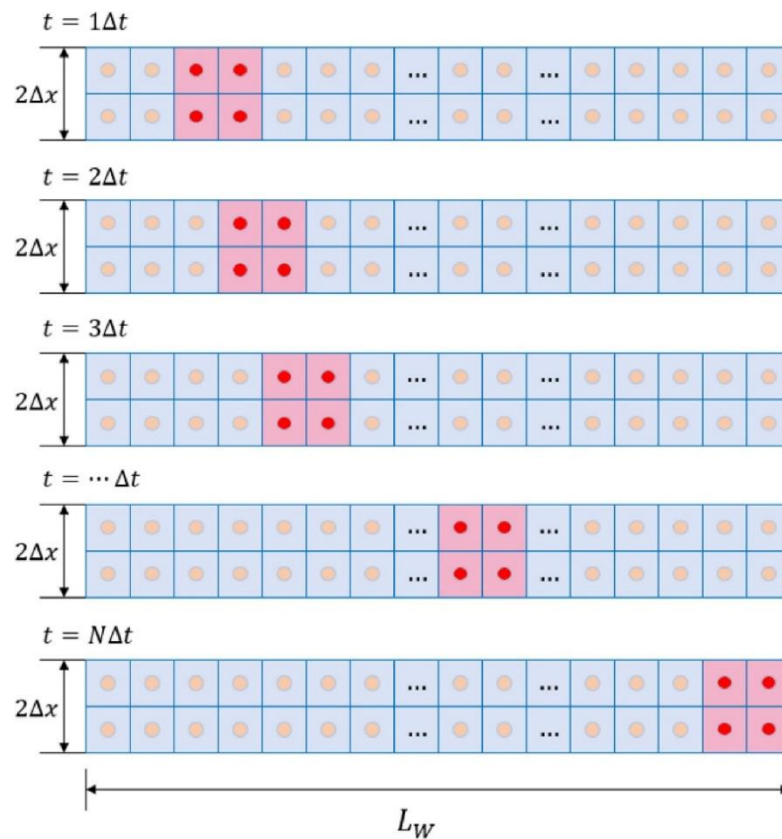


*Fig. 7-5 Demonstration of implementing moving point heat source in numerical model.*

The principle for implementing the moving point heat source in the numerical study is illustrated in Fig. 7-5. The total length of the welding track is denoted as  $L_W$ , which is

discretised into  $N$  material points. The total time required for the welding arc to travel the entire welding track is  $t_T$ . Accordingly, the time interval during which the heat source remains active on each material point can be obtained as

$$\Delta t = \frac{t_T}{N} \quad (7.19)$$

## 7.5 Numerical Results

### 7.5.1 Stefan's Solidification Problem

Classical Stefan's solidification problem (Jiji, 2009) is considered first. This is a moving boundary problem that describes the evolution of the interface  $x_i$  between two phases as the material undergoes a phase change. As presented in Fig. 7-6, the scenario assumes that the entire substance initially remains at the fusion temperature  $\theta_l$ . At time  $t = 0$  s, the temperature at the left edge of the material is suddenly reduced and maintained at  $\theta_b < \theta_s$ , initiating the solidification process. As a result, a solidification front begins to propagate from the cooled boundary, while the remainder of the substance remains in the liquid phase at the fusion temperature.

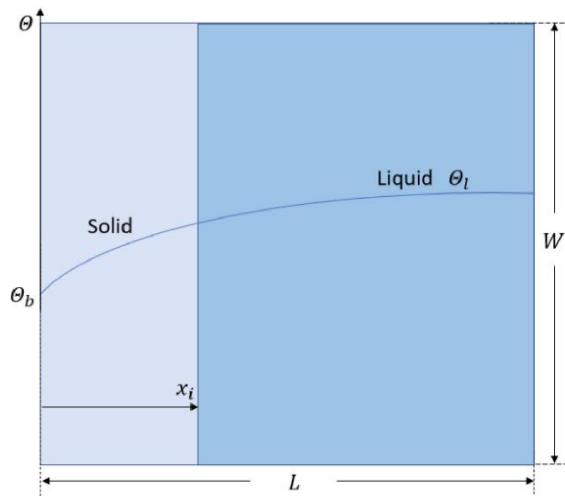


*Fig. 7-6 Physical illustration of Stefan's solidification problem.*

The Stefan solidification problem was reproduced from the ANSYS Verification Manual (ANSYS, Inc. 2013). In this scenario, the solidification process of a liquid region is examined, as demonstrated in Fig. 7-7(a). The region has a length of  $L = 0.01$  m and width of  $W = 0.01$  m.

Initially, the entire liquid field is maintained at the fusion temperature,  $\theta_l = 0^\circ\text{C}$ . At  $t = 0$  s, the temperature at the left edge ( $x = -\frac{L}{2}$ ) is suddenly subjected to a free surface temperature  $\theta_b = -5^\circ\text{C}$ , triggering the onset of solidification. As a result, the interface between the solid and liquid phases  $x_i$  begins to move inward from the cooled boundary. The thermal conductivity and density of the material are specified as  $k = 0.6 \text{ W/m}^\circ\text{C}$  and  $\rho = 1000 \text{ kg/m}^3$ , respectively.

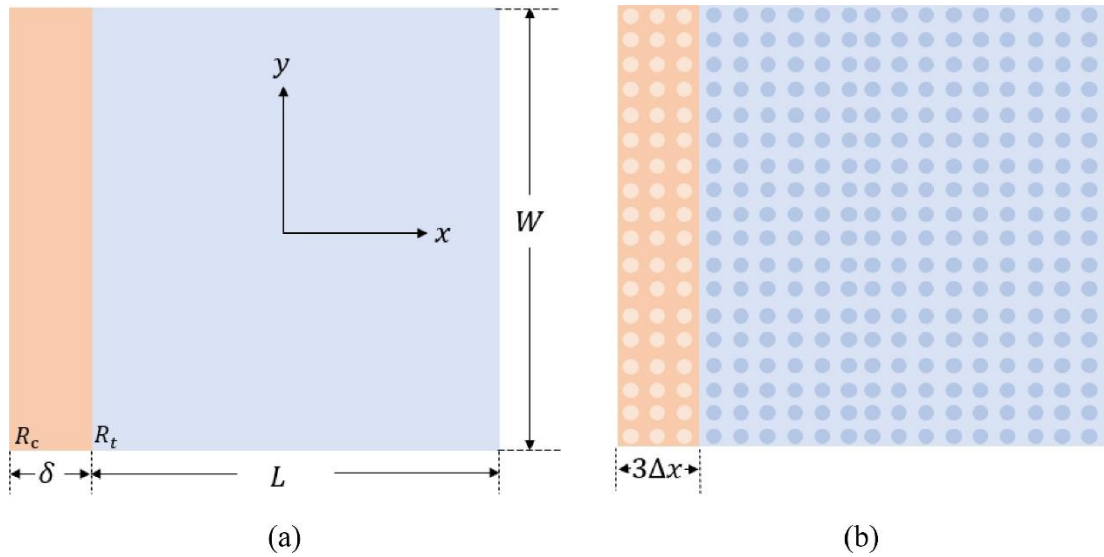


Fig. 7-7 Stefan's solidification problem illustration (a) geometry and (b) peridynamic discretization.

In this study, the substance is assumed to undergo phase change within the transformation temperature range

$$\theta_s = -1^\circ\text{C} \leq \theta \leq \theta_l = 0^\circ\text{C} \quad (7.20)$$

The latent heat  $L_T$  associated with this phase change is taken as 42000 J/kg. Hence, the effective heat capacity in the mushy zone is calculated as

$$C_{in} = \frac{L_T}{\theta_l - \theta_s} = 42000 \text{ J/kg}^\circ\text{C} \quad (7.21)$$

Consequently, the specific heat capacity at different temperatures is arranged as

$$C_v = \begin{cases} C_s = 4200 \text{ J/kg}^\circ\text{C} & \theta < -1^\circ\text{C} \\ C_p = 42000 \text{ J/kg}^\circ\text{C} & -1^\circ\text{C} \leq \theta \leq 0^\circ\text{C} \\ C_l = 4200 \text{ J/kg}^\circ\text{C} & \theta > 0^\circ\text{C} \end{cases} \quad (7.22)$$

Fig. 7-7(b) presents the numerical setup, the peridynamic discretization uses a spacing of  $\Delta x = L/100$ , with the horizon chosen as  $\delta = 3\Delta x$ . Time step size of  $\Delta t = 3 \times 10^{-2}$  s is adopted.

The initial temperature is set to the fusion temperature, i.e.,

$$\theta(x, y, t = 0) = \theta_l = 0^\circ\text{C} \quad (7.23)$$

To implement the temperature boundary condition, a fictitious boundary  $R_c$  with one horizon size is added at  $(x = -\frac{L}{2})$ , where the temperature is prescribed as

$$\theta\left(x = -\frac{L}{2}, y, t\right) = \theta_b = -5^\circ\text{C} \quad (7.24)$$

The evolution of the temperature distribution is computed numerically using the peridynamic formulation and compared with finite element results obtained in ANSYS. The FEM model employed PLANE55 elements with a uniform mesh size of  $\Delta x = 0.001$  m. The same material properties and boundary conditions as in the peridynamic model were applied. The transient analysis was performed up to  $t = 900$  s using automatic time stepping. The mesh size was determined following a convergence check, which confirmed that further refinement produced negligible changes in the thermal field. The case setup follows the ANSYS Verification Manual (ANSYS, Inc. 2013).

As shown in Fig. 7-8, the temperature profiles along the central axis ( $x, y = 0$ ) at selected time intervals ( $t = 300$  s,  $t = 600$  s,  $t = 900$  s) demonstrate good agreement between the peridynamic and FEM solutions.

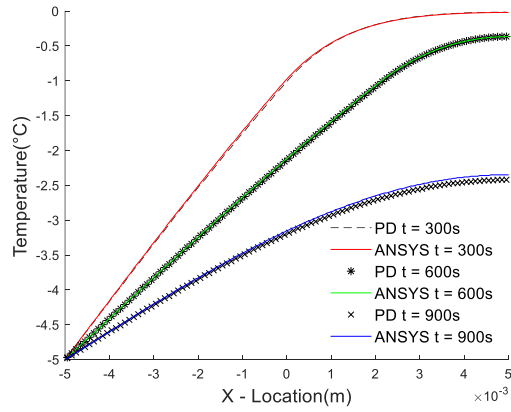


Fig. 7-8 Temperature comparison along axial axis at  $(x, y = 0)$ .

A comparison of the temperature variation as a function of time at the point  $(x = \frac{L}{2}, y = 0)$  between the peridynamic and FEM models is shown in Fig. 7-9. For the time between 787.82 and 797.82 s, the temperature at  $x = \frac{L}{2}, y = 0$  reaches  $\theta_s = -1\text{ }^\circ\text{C}$  which is the time that substance completely solidifies.

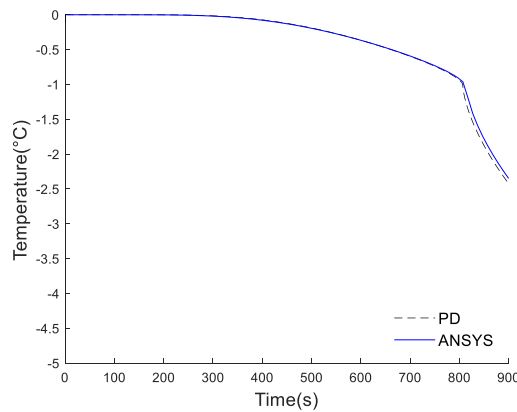


Fig. 7-9 Temperature variation at  $(x = \frac{L}{2}, y = 0)$ .

Further, the comparison of temperature distributions across the plate at 600 s for both the peridynamic and FEM models is illustrated Fig. 7-10, the temperature field across the plate predicted by the peridynamic model agrees with the FEM model.

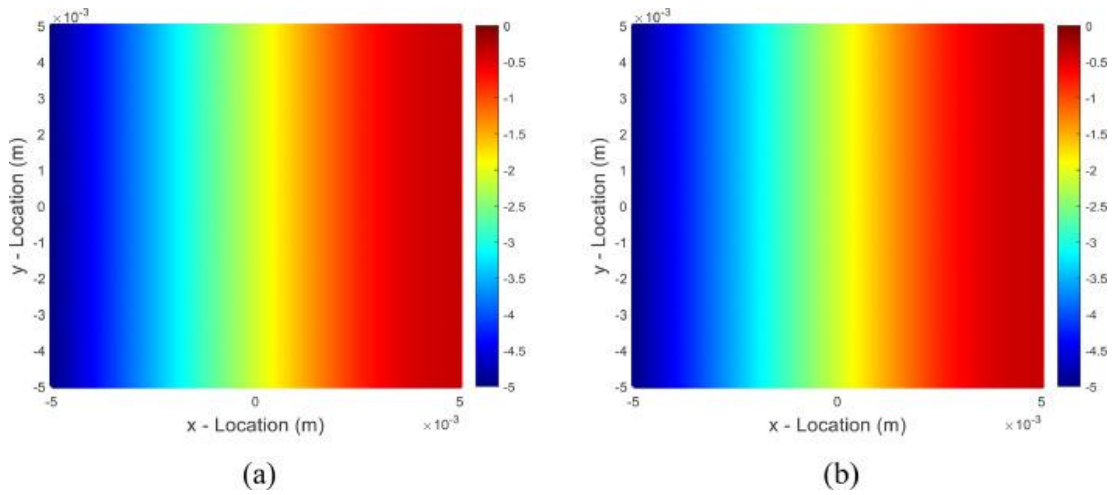


Fig. 7-10 Temperature distribution at  $t = 600s$  (a) peridynamic (b) FEM model.

To further illustrate the effect of latent heat during phase change, the Stefan solidification problem is also solved without accounting for latent heat effects. The resulting temperature distribution along the central axis ( $x, y = 0$ ) at  $t = 900 s$  is presented in Fig. 7-11. As observed, the inclusion of latent heat leads to differences in the predicted temperature profile. This is because latent heat is the energy absorbed or released during a phase change without a corresponding change in temperature. Neglecting latent heat results in inaccurate temperature predictions.

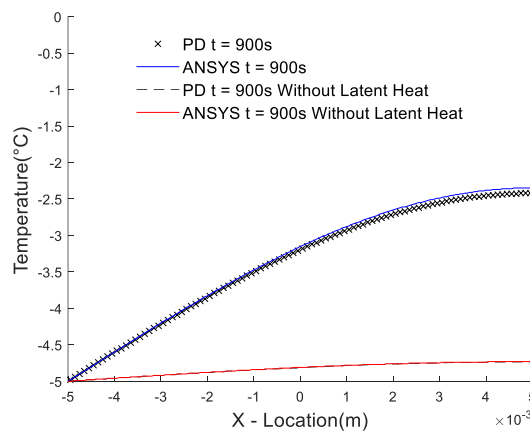


Fig. 7-11 Temperature distribution at  $(x, y = 0)$  at  $t = 900 s$ .

### 7.5.2 Neumann's Solidification Problem

Neumann (Jiji, 2009) extends the classical Stefan problem to cases where the initial temperature of the substance,  $\theta_i$ , exceeds the fusion temperature,  $\theta_l$ . As shown in Fig. 7-12, the material initially remains at a uniform temperature  $\theta_i$ , and then the left

boundary at  $x = -\frac{L}{2}$  is suddenly maintained at  $\theta_b < \theta_i$ . This abrupt cooling initiates solidification at the boundary, and the solid-liquid interface propagates into the liquid phase.

For the numerical study, the geometry and material properties are identical to those in the Stefan problem (see Fig. 7-7(a)): a plate of length  $L = 0.01$  m and width of  $W = 0.01$  m, with  $k = 0.6$  W/m°C, and  $\rho = 1000$  kg/m<sup>3</sup>.

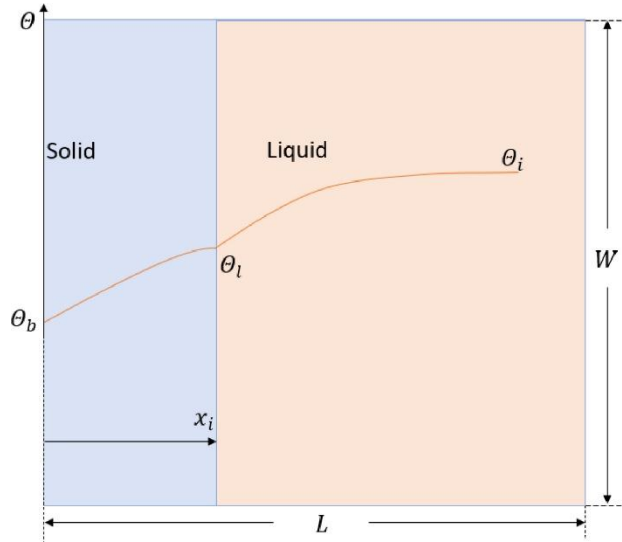


Fig. 7-12 Physical illustration of Neumann's solidification problem.

The initial temperature throughout the domain is set to  $\theta_i = 2$  °C, , which is above the melting point. The left edge is then maintained at  $\theta_b = -5$  °C, causing the phase boundary to advance from  $x = -\frac{L}{2}$ . The phase change is accounted for using the same latent heat treatment as in the previous section (Eq.( 7.22 )).

As shown in Fig. 7-7(b), discretization employs a mesh size of  $\Delta x = L/100$  with a horizon size of  $\delta = 3\Delta x$ , and a time step  $\Delta t = 3 \times 10^{-2}$  s.

The initial temperature is applied as

$$\theta(x, y, t = 0) = \theta_i = 2 \text{ °C} \quad ( 7.25 )$$

Fictitious boundary  $R_c$  with one horizon size is added to apply the temperature boundary condition, i.e.

$$\theta \left( x = -\frac{L}{2}, y, t \right) = \theta_b = -5 \text{ } ^\circ\text{C} \quad (7.26)$$

The Neumann solidification problem was also implemented in ANSYS using PLANE55 elements. A uniform mesh size of  $\Delta x = 0.001$  m was adopted following a convergence test with element sizes of 0.002 m, 0.001 m, and 0.0005 m. The transient thermal analysis was performed up to  $t = 1500$  s using automatic time stepping.

Temperature distributions along the central axis ( $x, y = 0$ ) at several time intervals ( $t = 300$  s,  $t = 600$  s,  $t = 900$  s) are shown in Fig. 7-13. The results show a linear temperature profile between  $-5$   $^\circ\text{C}$  and  $-1$   $^\circ\text{C}$  (the solid region), and a smooth, non-linear transition in the phase change region between  $-1$   $^\circ\text{C}$  and  $0$   $^\circ\text{C}$ , as the latent heat is accounted for phase change at this temperature interval.

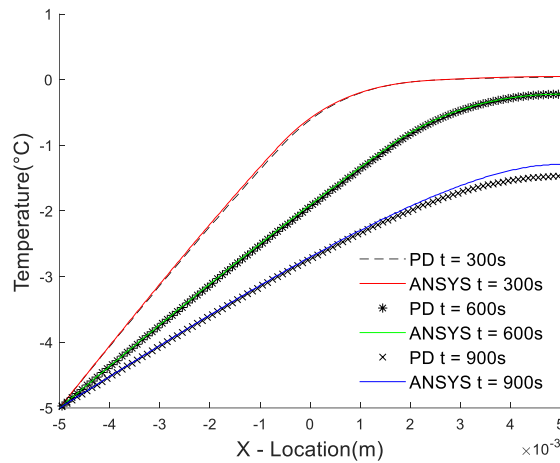


Fig. 7-13 Temperature comparison along ( $x, y = 0$ ) at several time intervals.

Time-dependent temperature responses at two material points,  $M \left( x = -\frac{4L}{5}, y = 0 \right)$  and  $N \left( x = \frac{L}{2}, y = 0 \right)$ , are compared in Fig. 7-14. As can be observed, the temperature at point M drops sharply at the onset, as it is closer to the cooling boundary and is reached by the moving solidification front sooner than point N.

The temperature at N has a quick drop between 2 and 0  $^\circ\text{C}$  while the curvature tends to smooth between 0 and -1  $^\circ\text{C}$  due to the latent heat effect. When the temperature is below -1  $^\circ\text{C}$ , the substance completely solidifies. Hence, the temperature variation has the similar curvature with the temperature between 2 and 0  $^\circ\text{C}$ .

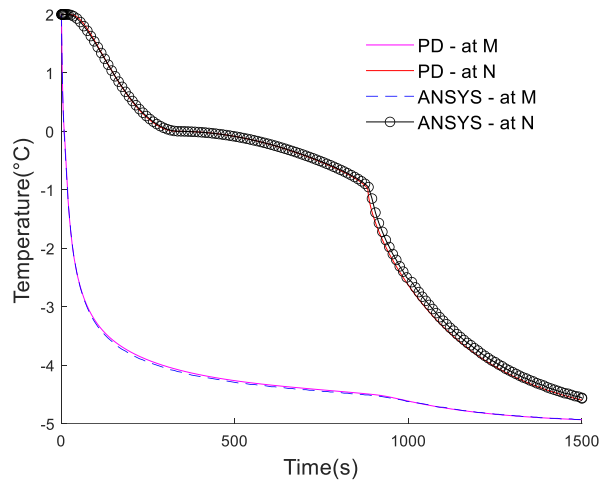


Fig. 7-14 Temperature variation at  $M \left( x = -\frac{4L}{5}, y = 0 \right)$  and  $N \left( x = \frac{L}{2}, y = 0 \right)$ .

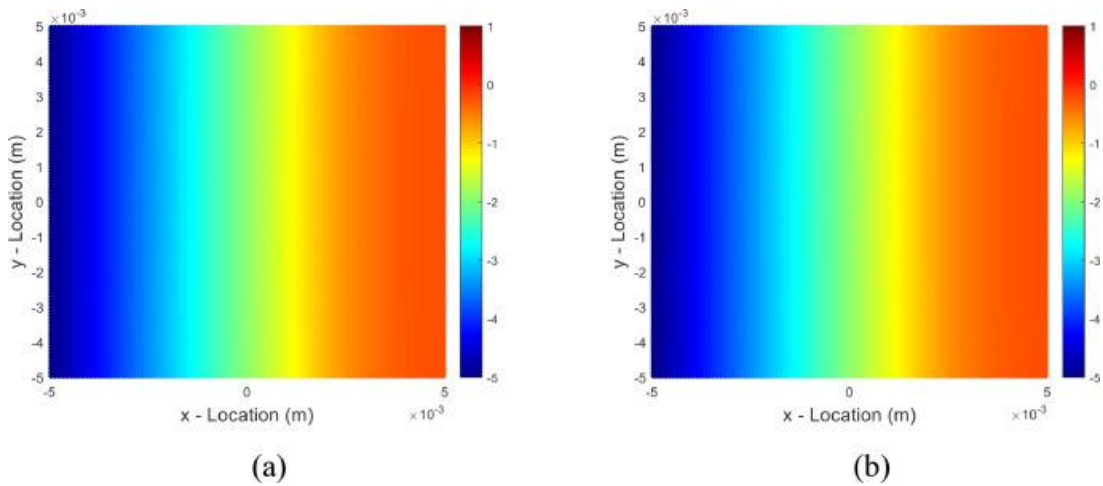


Fig. 7-15 Temperature distribution at  $t = 600$  s (a) peridynamic (b) FEM model.

Fig. 7-15 presents the spatial temperature distribution at 600 s as predicted by both the peridynamic and FEM models. As seen, the peridynamic predictions closely match the FEM results

### 7.5.3 Thermal Analysis for a Plate with a Moving Point Heat Source

An isotropic square plate with dimensions  $L = W = 0.1$  m and thickness  $H = 0.01$  m is presented in Fig. 7-16. The plate is subjected to a traveling point heat source with power  $Q = 3200$  W, which is initially located at the centre of the plate and moves towards to the positive  $x$  coordinate direction with a velocity of  $\bar{v} = 0.005$  m/s. The specific heat capacity, thermal conductivity and density are specified as  $C_v = 460$  J/kg,  $k = 50$  W/m°C, and  $\rho = 7820$  kg/m<sup>3</sup>, respectively.

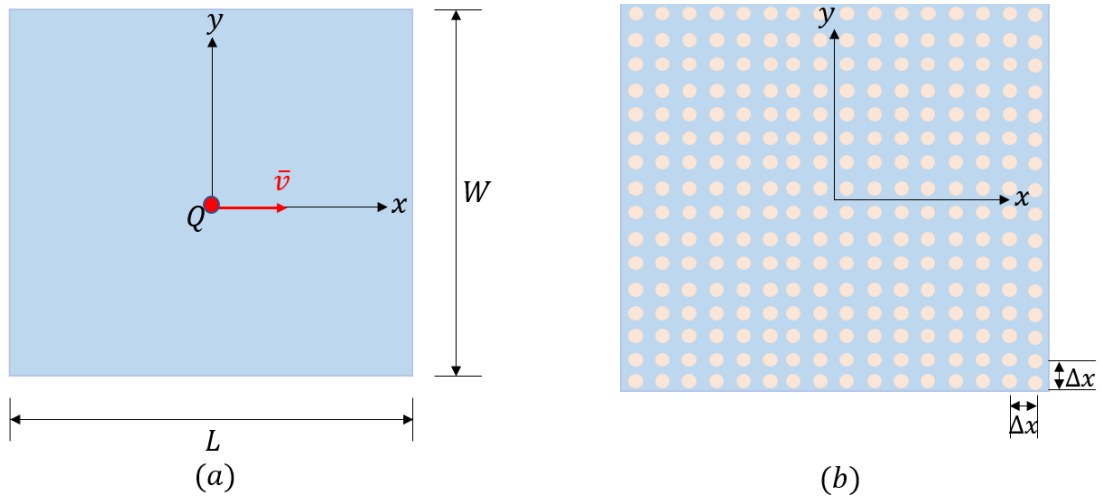


Fig. 7-16 Point heat source model illustration (a) geometry and (b) peridynamic discretization.

As shown in Fig. 7-16(b), the material points are discretised with a uniform spacing  $\Delta x = 0.0004$  m in  $x$  and  $y$  directions, respectively. The time step size is specified as  $\Delta t = 5 \times 10^{-4}$  s. The horizon is chosen as  $\delta = 3\Delta x$ .

The FEM model was implemented in ANSYS using PLANE55 elements. However, the transient thermal analysis does not directly incorporate a concentrated point heat source; instead, the standard practice is to approximate the point source as a volumetric heat generation applied to the elements. A similar approach is adopted in the peridynamic model, where the point source is converted into a volumetric heat generation distributed over four material points surrounding the source location, as depicted Fig. 7-17.

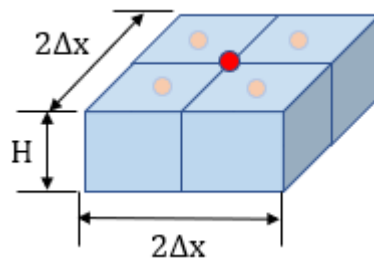


Fig. 7-17 Point heat source converted to heat generation.

The time-dependent point heat source is implemented using the birth-death procedure for material points, as described in Section 7.4.3. The volumetric heat generation assigned to each material point is obtained as

$$h_q(x, t) = \frac{Q}{4\Delta x^2 H} \quad (7.27)$$

The initial temperature of the plate is stated as

$$\theta_0(x, y, t = 0) = 0 \text{ }^\circ\text{C} \quad (7.28)$$

To validate the peridynamic implementation, the temperature distribution along the central axis ( $x, y = 0$ ) at  $t = 4 \text{ s}$  is compared with the analytical solution of Rosenthal (1941) and FEM results, as shown in Fig. 7-18.

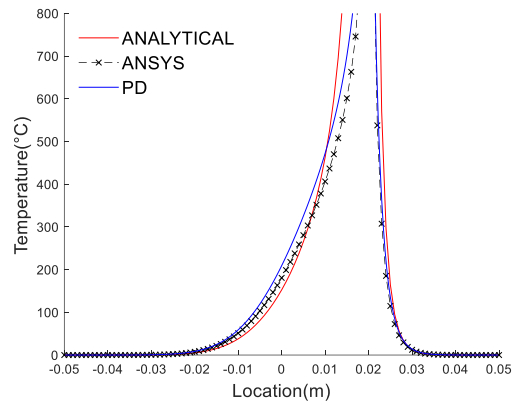


Fig. 7-18 Temperature variation at along ( $x, y = 0$ ) at  $t = 4 \text{ s}$ .

As expected from Eq.( 7.6 ), the analytical solution predicts a singularity at the centre of the heat source ( $\theta$  approach infinity when  $R \rightarrow 0$ ), which is not physically realized in numerical simulations. Both peridynamic and FEM results closely agree with the analytical solution at locations away from the moving source.

It should be noted that the analytical model assumes instantaneous travel of the point heat source to any location, while the numerical implementation distributes the heat as volumetric generation over discrete material points. Consequently, the predicted temperature field is sensitive to the discretization parameters. The discrepancy between numerical and analytical models can be reduced by employing finer spatial

and temporal discretization, though this comes at the expense of increased computational effort.

#### 7.5.4 Thermal Analysis for a Block with a Moving 3D Ellipsoidal Heat Source

To further demonstrate the capability of the proposed peridynamic formulation for welding heat conduction analysis, a three-dimensional moving ellipsoidal heat source is applied to a rectangular metal block. As shown in Fig. 7-19, the block has a dimension of  $L = W = 0.1$  m with a thickness of  $H = 0.01$  m. The ellipsoidal heat source with  $Q = 3200$  W, moves with a speed of  $\bar{v} = 0.005$  m/s in positive  $x$ -direction from the centre of the block. The thermal conductivity and density of the material are set as  $k = 50$  W/m°C and  $\rho = 7820$  kg/m<sup>3</sup>, respectively.

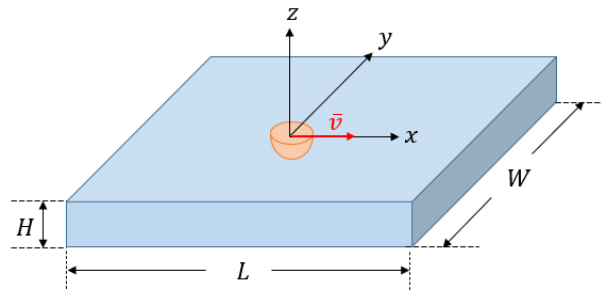


*Fig. 7-19 Geometrical illustration of ellipsoidal heat source acting on a rectangular block.*

The parameters for the ellipsoidal heat source are defined as

$$a_h = 0.001 \text{ m} \quad (7.29)$$

$$b_h = 0.001 \text{ m}$$

$$c_h = 0.0005 \text{ m}$$

The block is discretised with uniform spacing  $\Delta x = 4 \times 10^{-4}$  m in  $x$ ,  $y$  and  $z$  directions. The horizon is chosen as  $\delta = 3\Delta x$ . Time step size of  $\Delta t = 5 \times 10^{-4}$  s is used.

The initial temperature is set as

$$\theta(x, y, t = 0) = \theta_i = 0 \text{ }^\circ\text{C} \quad (7.30)$$

#### 7.5.4.1 Without Phase Change

In the first simulation, the effect of phase change is neglected, and the specific heat capacity is set as  $C_p = 490 \text{ J/kg}$ . For comparison, a finite element model is constructed using ANSYS Solid 70 elements with mesh sizes of 0.001 m in  $x$  and  $y$ -directions, and 0.0001 m in the  $z$ -direction.

The temperature profile along the heat source path ( $x, y = 0, z = \frac{H}{2}$ ) at  $t = 4 \text{ s}$  is presented in Fig. 7-20 for both peridynamic and FEM simulations. The developed peridynamic heat conduction model for ellipsoidal heat source is closely agreed with the FEM model.

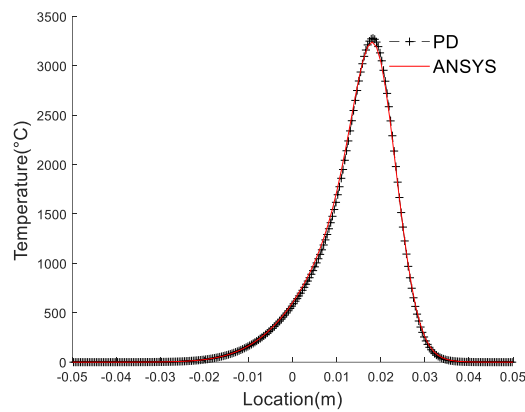


Fig. 7-20 Temperature variation at  $(x, y = 0, z = \frac{H}{2})$  at  $t = 4 \text{ s}$ .

The spatial temperature distributions predicted by the peridynamic and FEM models are also illustrated in Fig. 7-21. As observed, the predicted temperature distribution on the block has a good agreement with the FEM model.

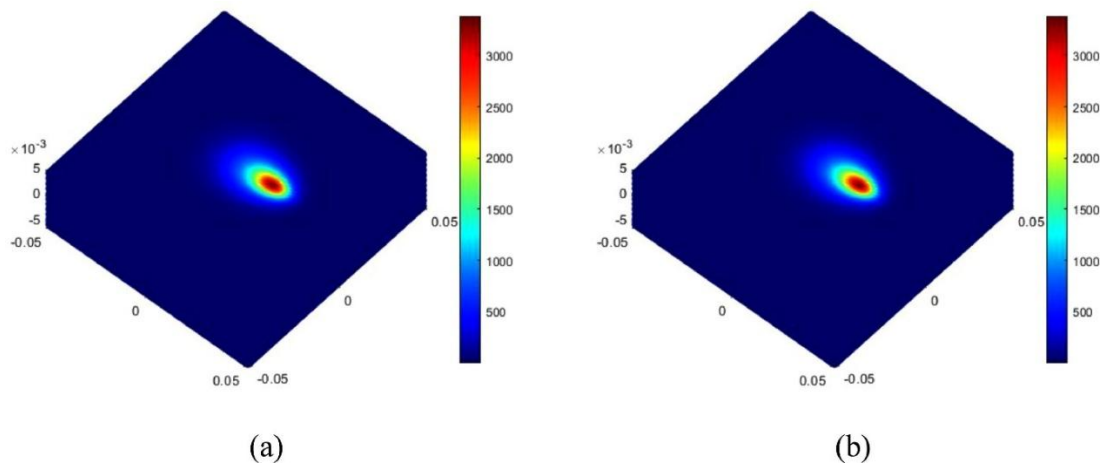


Fig. 7-21 Temperature distribution at  $t = 4$  s (a) peridynamic (b) FEM model.

#### 7.5.4.2 Considering Phase Change

In second investigation for ellipsoidal heat source model, phase change is considered. The mushy zone for metal is considered as  $\theta_s = 1385$  °C  $< \theta < \theta_l = 1450$  °C. The total latent heat required for the phase change completed is 260 kJ/kg.

Therefore, the effective heat capacity for metal at mushy zone is defined as

$$C_{in} = \frac{L_T}{\theta_l - \theta_s} = 4000 \text{ J/kg}^\circ\text{C} \quad (7.31)$$

Thus, the effective specific heat capacity at different temperatures can be expressed as

$$C_v = \begin{cases} C_s = 490 \text{ J/kg}^\circ\text{C} & \theta < 1385 \text{ }^\circ\text{C} \\ C_p = 4000 \text{ J/kg}^\circ\text{C} & 1385 \text{ }^\circ\text{C} < \theta < 1450 \text{ }^\circ\text{C} \\ C_l = 490 \text{ J/kg}^\circ\text{C} & \theta > 1450 \text{ }^\circ\text{C} \end{cases} \quad (7.32)$$

Fig. 7-22 compares the temperature distribution along  $(x, y = 0, z = \frac{H}{2})$  when the phase change is considered in the heat conduction model. The corresponding spatial temperature distribution is shown in Fig. 7-23.

As can be observed from the figures, when the phase change is considered in the model, the predicted temperature field shows a slow variation at the phase change temperature interval. The temperature is changed to steep variation again when the phase change has been completed. During the phase change, a large amount of energy is absorbed without significant temperature variation. As a result, the predicted maximum temperature in the phase change case is lower when compared with the case the phase change is neglected.

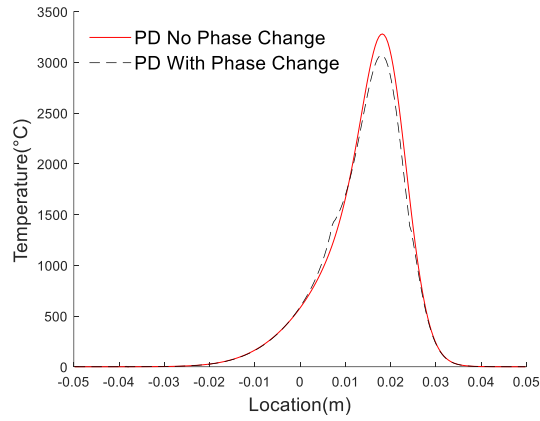


Fig. 7-22 Temperature variation at  $(x, y = 0, z = \frac{H}{2})$  at  $t = 4$  s.

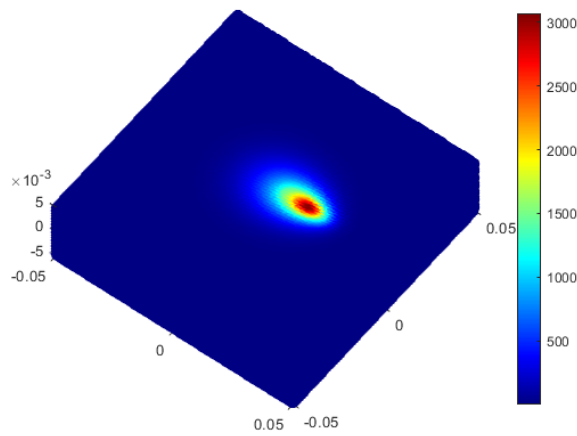


Fig. 7-23 Temperature distribution at  $t = 4$  s with phase change considered in peridynamic model.

### 7.5.5 Thermomechanical Analysis for a Plate with Moving 2D Gaussian Heat Source

Laser beam arcs are commonly employed in welding and AM processes, and their thermal effects are often modelled using a moving Gaussian heat source. To demonstrate the capability of the peridynamic approach for thermomechanical phase change analysis in such contexts, a two-dimensional plate subjected to a moving Gaussian heat source is investigated.

As shown in Fig. 7-24(a), plate has  $L = 0.1$  m in length,  $W = 0.1$  m in width, and a thickness of  $H = 0.01$  m. The Gaussian heat source, with a power of  $Q = 3200$  W is moving with a speed of  $\bar{v} = 0.025$  m/s in positive  $x$ -direction from the centre of

the plate. The thermal conductivity, density and thermal expansion coefficient are specified as  $k = 50 \text{ W/m}^\circ\text{C}$ ,  $\rho = 7820 \text{ kg/m}^3$  and  $\alpha = 13 \times 10^{-6} \text{ }^\circ\text{C}^{-1}$ .

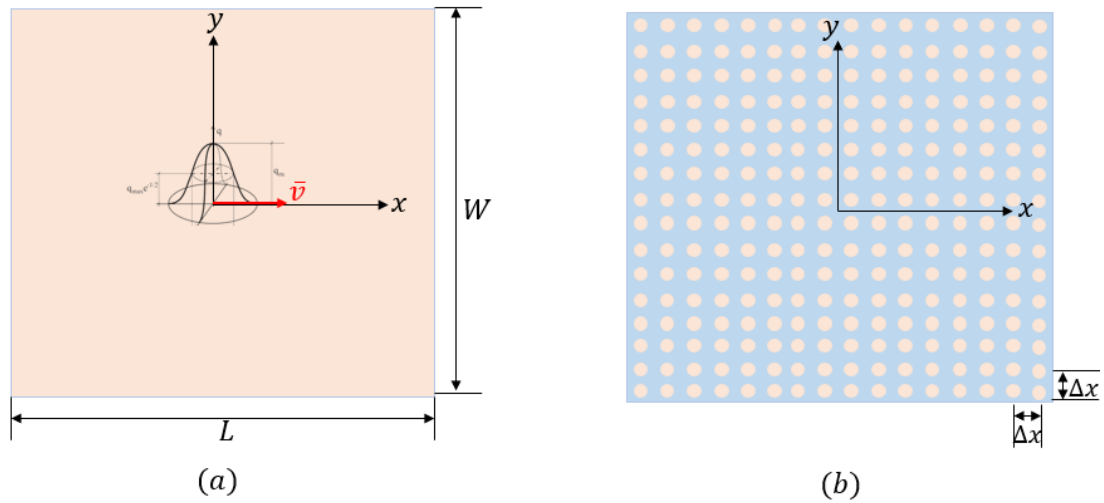


Fig. 7-24 Gaussian heat source model illustration (a) geometry and (b) peridynamic discretization.

Fig. 7-24(b) presents the peridynamic discretization model. The plate is meshed with a uniform spacing of  $\Delta x = 4 \times 10^{-4} \text{ m}$  with a horizon size of  $\delta = 3\Delta x$ . The time step size is taken as  $\Delta t = 1 \times 10^{-7} \text{ s}$ .

The Gaussian heat source distribution parameter is selected as  $\sigma = 0.0007 \text{ m}$ . The proposed Gaussian distributed heat flux is converted to volumetric heat generation for peridynamic implementation as

$$h_q(x, y, t) = \frac{q(x, y, t)}{\Delta x} \quad (7.33)$$

The initial temperature condition is specified as

$$\theta(x, y, t = 0) = \theta_i = 0 \text{ }^\circ\text{C} \quad (7.34)$$

#### 7.5.5.1 Without Phase Change

In the first scenario, latent heat effects are neglected, and the specific heat capacity is fixed at  $C_v = 490 \text{ J/kg}$ . The Young's Modulus is specified as  $E = 200 \text{ GPa}$ . To verify temperature and displacement fields in the peridynamic model, a finite element model is constructed using ANSYS PLANE223 elements with a mesh size  $\Delta = 0.001 \text{ m}$  in  $x$  and  $y$ -directions. PLANE223 is a two-dimensional coupled-field

element that models both thermal conduction and structural response, and is therefore adapted for verification in FEM.

Fig. 7-25 and Fig. 7-26 compare the temperature field and displacement field at  $t = 0.08$  s along the heat source moving track ( $x, y = 0$ ), respectively. Both temperature and displacement results show close agreement between peridynamic and FEM models.

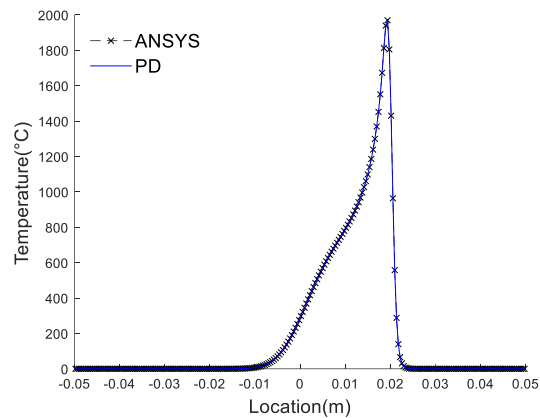


*Fig. 7-25 Temperature variation along  $(x, y = 0)$  at  $t = 0.08$  s.*

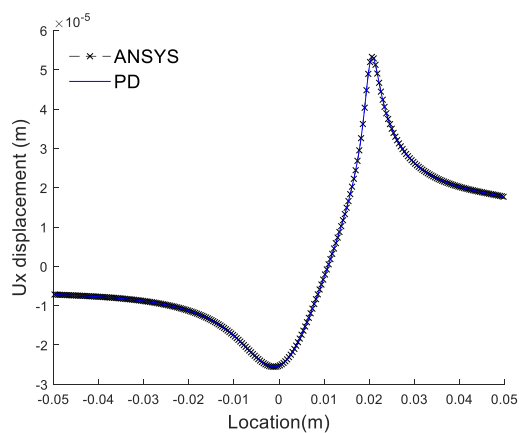


*Fig. 7-26 Displacement variation along  $(x, y = 0)$  at  $t = 0.08$  s.*

Fig. 7-27 presents the temperature field of the plate in peridynamic and FEM models. The FEM model results agree with the temperature field results predicted by the peridynamic model.

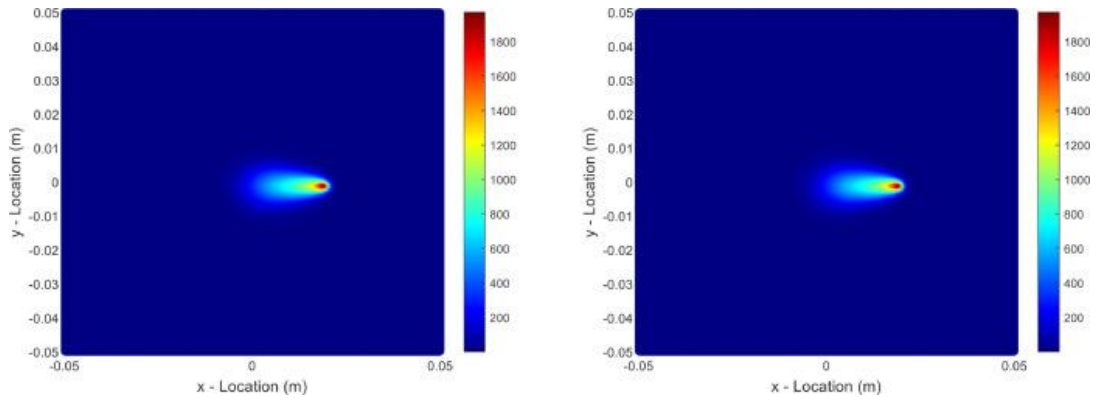


Fig. 7-27 Temperature field distribution at  $t = 0.08$  s (a) peridynamic (b) FEM model.

### 7.5.5.2 Considering Phase Change

In the second case, phase change is considered. The latent heat in phase transformation is implicitly applied in effective heat capacity and same as stated in Eq. ( 7.32 ). The temperature-dependent Young's Modulus  $E(\theta)$  is provided in Table 7-1.

Table 7-1 Temperature-dependent Young's Modulus

$\theta$ (K)	$E(\theta)$ (GPa)
298	200
473	187
673	172
873	157
973	141
1673	106
1573	10

Fig. 7-28 compares the temperature distribution along  $(x, y = 0)$  at  $t = 0.08$  s with and without phase change. The inclusion of latent heat in the phase change scenario leads to a lower maximum temperature and a plateau in the temperature profile within the phase change interval, which is characteristic of energy absorption during melting. The horizontal displacement field along  $(x, y = 0)$  is presented in Fig. 7-29. In addition, Fig. 7-30(a) and (b) present the two-dimensional displacement fields when

phase change is considered and omitted, respectively. It can be noticed that when the effect of temperature is considered for Young's Modulus, it has a significant effect on the displacement field.

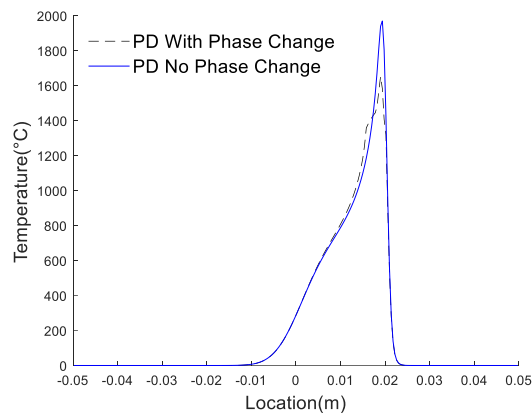


Fig. 7-28 Temperature variation along  $(x, y = 0)$  at  $t = 0.08$  s.

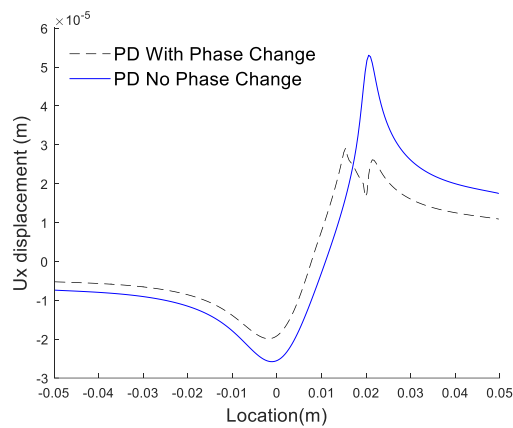
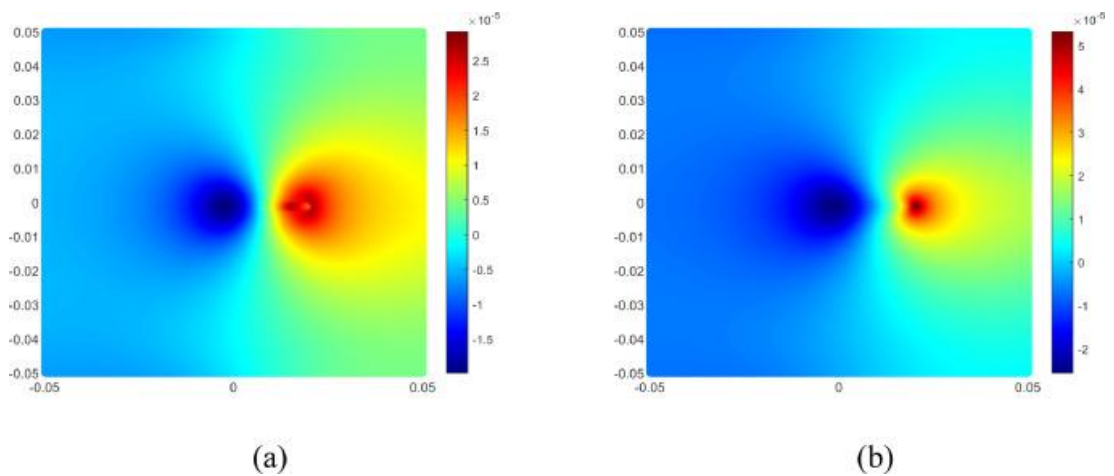


Fig. 7-29 Horizontal displacement variation along  $(x, y = 0)$  at  $t = 0.08$  s.



*Fig. 7-30 Horizontal displacement field at  $t = 0.08$  s(a) With phase change (b) without phase change.*

## **7.6 Chapter Summary**

In this chapter, a new non-linear transient peridynamic model has been proposed for the thermomechanical analysis of the welding and AM process. Phase change, as a common physical process in heat transfer scenarios, is considered in the model. Several classical phase change problems, i.e., Stefan's and Neumann's solidification problems, are simulated by the proposed model. In addition, a wide range of commonly utilised time-dependent heat source models, i.e., Point, Gaussian, and volumetric distributed heat source models, which are related to the different methods in the manufacturing process, have been considered in the peridynamic heat transfer model and thermoelastic analysis. The predicted thermal and mechanical fields have been verified with the finite element model. The peridynamic predicted results have a good agreement with the FEM model results. The phase change is a critical phenomenon in heat transfer. This is highlighted in the Gaussian and ellipsoidal heat source model. The effect of phase change on temperature and displacement fields is presented. Without considering the latent heat in the phase transformation can result in inaccurate temperature and displacement fields.

## **Chapter 8 Nonlocal Modelling of Multiphase Flow Wetting and Thermo-capillary Flow by Using Peridynamic Differential Operator**

### **8.1 Introduction**

The AM and welding processes are governed not only by mechanical and thermal interactions but also by fluid dynamics and interfacial phenomena at the microscale. Thermo-capillary effect, often referred to as the Marangoni effect, which arises from temperature-dependent surface tension gradients. In AM and welding, this effect drives fluid flow within melt pools, strongly influencing pool shape, solidification behaviour, microstructural evolution, and ultimately the mechanical integrity of the fabricated components. Accurately capturing these multiphysics interactions is therefore essential for the predictive modelling of AM and welding processes.

Recognising the importance of interfacial phenomena and multiphase interactions, this chapter extends the peridynamic modelling framework by leveraging the Peridynamic Differential Operator (PDDO) to address nonlocal multiphase flow motion and the thermo-capillary effects characteristic of AM and welding environments. Interfaces in multiphase flows are affected by surface tension, which is further complicated by the fact that temperature gradients induce tangential surface tension at the fluid interface. These effects also govern the wetting behaviour of fluids in contact with solid boundaries, which makes it difficult to accurately describe wetting phenomena. By utilising the PDDO, which expresses derivatives of any order through integral equations, the fundamental governing equations for multiphase fluid motion are reformulated in a nonlocal context.

In this chapter, a novel nonlocal peridynamic approach is developed for modelling multiphase fluid motion, explicitly incorporating thermal effects on surface tension. The nonlocal form of the continuum surface force (CSF) model is presented to accurately describe surface tension forces in both normal and tangential directions. Furthermore, to address inaccuracies in unit normal vectors at three-phase contact regions, an improved treatment is introduced. The validity and accuracy of the proposed methodology are demonstrated through several benchmark cases, including square droplet deformation, surface wetting, and droplet migration under thermo-capillary flow. The results confirm that the developed nonlocal model can capture the surface tension and thermo-capillary effects in multiphase fluid dynamics, thereby

providing a robust tool for the simulation of phenomena in AM and welding applications.

## 8.2 The Governing Equations of Motion for Multiphase Fluid Flow

Fluid dynamics in multiphase fluid flow is governed by continuity equation, Navier–Stokes equation, and energy equation.

### 8.2.1 Mass Conservation

The mass conservation in multiphase fluid flow motion can be described by the continuity equation as

$$\frac{\partial \rho}{\partial t} = -\rho \nabla \cdot \mathbf{v} \quad (8.1)$$

in which  $\rho$  is density,  $\mathbf{v}$  is velocity, and  $t$  is time.

### 8.2.2 Momentum Conservation

The Navier-Stokes equation in Lagrangian description has the form of (Brackbill et al., 1992)

$$\rho \frac{\partial \mathbf{v}}{\partial t} = \nabla \cdot \boldsymbol{\sigma} + \mathbf{b} + \mathbf{F}_s \quad (8.2)$$

where  $\mathbf{b}$  represents the body force, and  $\mathbf{F}_s$  is the surface tension force. The divergence of stress  $\nabla \cdot \boldsymbol{\sigma}$  can be represented as (Gao and Oterkus, 2019)

$$\nabla \cdot \boldsymbol{\sigma} = \nabla \cdot (-p\mathbf{I} + \boldsymbol{\tau}) \quad (8.3)$$

in which  $p$  is the hydrostatic pressure, and  $\mathbf{I}$  is the second order unit tensor. The shear-rate tensor  $\boldsymbol{\tau}$  can be defined as (Gao and Oterkus, 2019)

$$\boldsymbol{\tau} = 2\mu \dot{\boldsymbol{\epsilon}} \quad (8.4)$$

in which  $\mu$  is the dynamic viscosity, and  $\dot{\boldsymbol{\epsilon}}$  is the shear strain rate. The divergence of the shear-rate tensor can be represented as (Gao and Oterkus, 2019)

$$\nabla \cdot \boldsymbol{\tau} = \nabla \cdot (2\mu \dot{\boldsymbol{\epsilon}}) = \dot{\boldsymbol{\epsilon}} \cdot \nabla 2\mu + 2\mu \nabla \cdot \dot{\boldsymbol{\epsilon}} \quad (8.5)$$

If the dynamic viscosity  $\mu$  is assumed as a constant after substituting Eq.( 8.3 ) - Eq.( 8.5 ) into Eq. ( 8.2 ), the Navier-Stokes equation can be re-written as (Gao and Oterkus, 2019)

$$\rho \frac{\partial \mathbf{v}}{\partial t} = -\nabla p + 2\mu \nabla \cdot \boldsymbol{\varepsilon} + \mathbf{b} + \mathbf{F}_s \quad (8.6)$$

In addition, the shear strain rate tensor  $\boldsymbol{\varepsilon}$  can be expressed as (Gao and Oterkus, 2019)

$$\boldsymbol{\varepsilon} = \frac{1}{2} [\nabla \otimes \mathbf{v} + (\nabla \otimes \mathbf{v})^T] \quad (8.7)$$

If the fluid is incompressible, Eq.( 8.7 ) can be further simplified by continuity equation. As a result, the Navier-Stokes equation for incompressible fluid flow becomes (Hopp-Hirschler et al., 2018)

$$\rho \frac{\partial \mathbf{v}}{\partial t} = -\nabla p + \mu \Delta \mathbf{v} + \mathbf{b} + \mathbf{F}_s \quad (8.8)$$

The continuum surface force method (Brackbill et al., 1992) is adopted for modelling the surface tension force in multiphase fluid flow as the pressure jump occurred at the phase interface. The surface tension force is applied as a volumetric force and is distributed along a transition band (Fig. 8-1) along the interface. A weight function is acted on the transition band area to convert surface tension  $\mathbf{f}_s$  into force per unit volume  $\mathbf{F}_s$  (Morris, 2000). This can be represented as (Brackbill et al., 1992)

$$\mathbf{F}_s = \mathbf{f}_s \delta_{lg} \quad (8.9)$$

where  $\delta_{lg}$  is the weight function for surface tension that represents the magnitude distribution of the surface tension force at the transition band, which has a peak at the interface and decays with the distance away from the interface. The weight function,  $\delta_{lg}$ , is further described in section 8.3.2.3.

The volumetric surface tension force  $\mathbf{F}_s$  comprises the contributions from normal and tangential directions (Morris, 2000), which can be expressed as

$$\mathbf{F}_s = (\mathbf{f}_{s,n} + \mathbf{f}_{s,t}) \delta_{lg} = \mathbf{F}_{s,n} + \mathbf{F}_{s,t} \quad (8.10)$$

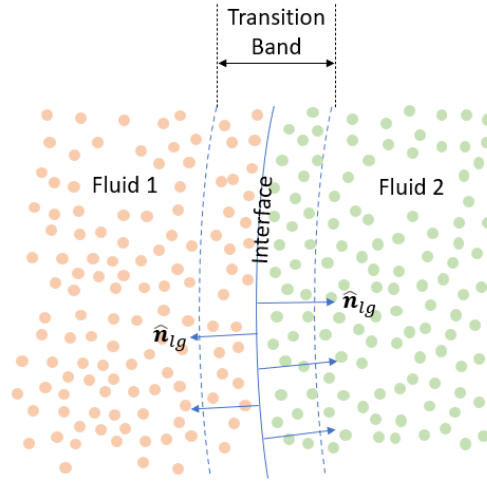


Fig. 8-1 The transition band and unit normal vectors between two fluids.

The normal component of surface tension force  $\mathbf{F}_{s,n}$  represents the surface tension force due to the local curvature at the transition band area. This can be defined as

$$\mathbf{F}_{s,n} = \gamma \tilde{\kappa} \hat{\mathbf{n}}_{lg} \delta_{lg} \quad (8.11)$$

in which  $\gamma$  is the temperature dependent surface tension coefficient in N/m,  $\tilde{\kappa}$  is the interface curvature, and  $\hat{\mathbf{n}}_{lg}$  is the unit normal vector at the interface between two different fluids.

The temperature dependent surface tension coefficient can be written as (Hopp-Hirschler et al., 2018)

$$\gamma = \gamma_0 - \frac{d\gamma(T)}{dT} (T - T_{\gamma_0}) \quad (8.12)$$

in which  $\frac{d\gamma(T)}{dT}$  is the surface tension temperature coefficient (Meier et al., 2021),  $T$  is the current temperature, and  $\gamma_0$  is the surface tension coefficient at reference temperature  $T_{\gamma_0}$ .

As the surface tension coefficient  $\gamma$  is a function of temperature, the surface tension force in tangential direction can occur due to temperature gradient and lead to Marangoni convection (Hopp-Hirschler et al., 2018). Therefore, the term,  $\mathbf{F}_{s,t}$ , on the right-hand side of Eq.( 8.10 ) represents the Marangoni force and acts tangentially to the interface, which drives the fluid from low surface tension region to high tension

regions. The tangential component of the surface tension force is given as (Morris, 2000)

$$\mathbf{F}_{s,t} = \nabla_S \gamma \delta_{lg} \quad (8.13)$$

where  $\nabla_S$  is the surface gradient, and  $\nabla_S \gamma$  can be represented as (Russell et al., 2018)

$$\nabla_S \gamma = \frac{d\gamma(T)}{dT} \nabla_S T \quad (8.14)$$

in which  $\nabla_S T$  is the surface temperature gradient and can be expressed (Russell et al., 2018)

$$\nabla_S T = [\nabla T - (\nabla T \cdot \hat{\mathbf{n}}_{lg}) \hat{\mathbf{n}}_{lg}] \quad (8.15)$$

As a result, the Marangoni force can be written as

$$\mathbf{F}_{s,t} = \frac{d\gamma(T)}{dT} [\nabla T - (\nabla T \cdot \hat{\mathbf{n}}_{lg}) \hat{\mathbf{n}}_{lg}] \delta_{lg} \quad (8.16)$$

### 8.2.3 Equation of State

Assuming the fluid is barotropic, an additional equation is required to uncouple the mass and momentum equations (Batchelor, 2000). In this study, the incompressible fluid flow motion is constrained by a weakly compressible equation of state, whose density is only a function of pressure. A typical equation of state is given as (Morris et al., 1997)

$$p = \frac{\rho_0 c_0^2}{\alpha} \left[ \left( \frac{\rho}{\rho_0} \right)^\alpha - 1 \right] + p_0 \quad (8.17)$$

in which  $\rho_0$  is the initial density,  $c_0$  is the numerical speed of sound, and  $\alpha$  is the adiabatic exponent.  $p_0$  is the background pressure which prevents a negative pressure field and provides tension stabilities (Colagrossi and Landrini, 2003). As the density changes and it is updated by using continuity equation given in Eq.( 8.1 ). The pressure field is calculated by the change between the updated density,  $\rho$  and its initial density,  $\rho_0$  in the equation of state (Eq.( 8.17 )). In two-phase fluid flow motion, the equation of state for each type of fluid flow can be expressed as (Zhang et al., 2015)

$$p_l = \frac{\rho_{0,l} c_{0,l}^2}{\alpha_l} \left[ \left( \frac{\rho_l}{\rho_{0,l}} \right)^{\alpha_l} - 1 \right] + p_{0,l} \quad (8.18)$$

and

$$p_g = \frac{\rho_{0,g} c_{0,g}^2}{\alpha_g} \left[ \left( \frac{\rho_g}{\rho_{0,g}} \right)^{\alpha_g} - 1 \right] + p_{0,g} \quad (8.19)$$

where the subscripts  $l$  and  $g$  denote the denser and lighter fluids, respectively.

The adiabatic exponent  $\alpha$  defines the degree of incompressibility and pressure of fluid response to density perturbations. As density perturbations increase, a high adiabatic exponent can cause progressively large error in the pressure field. For laminar flow with low Reynolds numbers, the adiabatic exponent is taken as one ( $\alpha_l = \alpha_g = 1$ ) to keep the error in density and pressure proportional (Morris et al., 1997).

In weakly compressible approach, the density variation  $\Delta\rho$  in each fluid domain need to be (Meier et al., 2021)

$$\frac{\Delta\rho}{\rho} \ll 1 \quad (8.20)$$

This criterion is checked at the end of the simulation in each case.

The numerical speed of sound,  $c_0$ , in Eq.( 8.17 ) needs to be chosen large enough to limit the density change threshold up to 1% (Meier et al., 2021). On the other hand, the numerical stability is dependent on the time step size. The numerical speed of sound should not be too large to make the time step excessively small (Morris et al., 1997).

In this study, as the fluid domain is composed of multiphase flows with different density ratios, the numerical speed of the sound is estimated by the highest pressure change  $\Delta p$  in the denser fluid as (Grenier et al., 2013)

$$c_{0,g} \gg \sqrt{\frac{\Delta p}{\rho_{0,l}}} \quad (8.21)$$

For gravity-based flow, the maximum pressure variation in Eq.( 8.21 ) is estimated by (Morris et al., 1997)

$$\Delta p = \rho_{0,l}gH \quad ( 8.22 )$$

where  $g$  is the force of gravity, and  $H$  is the reference depth.

For surface tension-driven flows, the pressure changes in Eq.( 8.21 ) is approximated by using Young–Laplace equation (Breinlinger et al., 2013). The work carried out by the pressure on an interfacial area can be represented as

$$\Delta p = \gamma \frac{dA}{dV} \quad ( 8.23 )$$

in which  $dV$  and  $dA$  are infinitely small volume and area at the interface, respectively.

For a two-dimensional circular droplet, the pressure change at the interfacial area can be computed as

$$\Delta p = \gamma \frac{dA}{dV} = \gamma \frac{dA}{dr} \frac{dr}{dV} = \gamma \frac{1}{R} \quad ( 8.24 )$$

where  $r$  is the radius and  $R$  is the characteristic radius of droplet curvature. The surface tension coefficient,  $\gamma$ , is calculated from Eq.( 8.12 ).

On the other hand, the numerical speed of sound in lighter fluid is calculated as (Zhang et al., 2015)

$$c_{0,g} = \sqrt{\frac{\rho_{0,l}c_{0,l}^2\alpha_g}{\alpha_l\rho_{0,g}}} \quad ( 8.25 )$$

in which  $c_{0,l}$  is obtained from Eq.( 8.21 ).

Note that by comparing the numerical speed of sound in denser in Eq.( 8.21 ) and lighter fluids in Eq.( 8.25 ), it can be found that the numerical speed of sound  $c_{0,g}$  in lighter fluid is higher than the numerical speed of sound  $c_{0,l}$  in denser fluid when the density ratio  $\rho_{0,l}/\rho_{0,g}$  is significant.

### 8.2.4 Energy Equation

The local form of total energy in a fluid system can be represented as (Incropera et al., 1996)

$$\frac{\partial}{\partial t} \rho \left( e + \frac{1}{2} |\mathbf{v}|^2 \right) = -\nabla \cdot \mathbf{q} + S - \nabla \cdot (p\mathbf{v}) + \nabla \cdot (\boldsymbol{\tau} \cdot \mathbf{v}) + \rho(\mathbf{b} \cdot \mathbf{v}) \quad (8.26)$$

in which  $e$  is the internal energy per unit mass,  $\frac{1}{2} |\mathbf{v}|^2$  is the kinetic energy per unit mass, and  $S$  is the source term. The first term on right-hand side,  $\nabla \cdot \mathbf{q}$ , is the net rate of heat addition due to conduction. The third term on the right-hand side,  $\nabla \cdot (p\mathbf{v})$ , represents the rate of doing work against pressure. The term  $\nabla \cdot (\boldsymbol{\tau} \cdot \mathbf{v})$  represents the rate of doing work against viscous force, and the term  $\rho(\mathbf{b} \cdot \mathbf{v})$  represents the rate of doing work against the body force.

Using product rule within the divergence operator ( $\nabla \cdot$ ), the rate of doing work against pressure and viscous force can be rewritten as

$$\nabla \cdot (p\mathbf{v}) = \mathbf{v} \cdot \nabla p + p \nabla \cdot \mathbf{v} \quad (8.27)$$

and

$$\nabla \cdot (\boldsymbol{\tau} \cdot \mathbf{v}) = \boldsymbol{\tau} : (\nabla \otimes \mathbf{v}) + \mathbf{v} \cdot (\nabla \cdot \boldsymbol{\tau}) \quad (8.28)$$

The mechanical energy equation can be derived from the momentum equation by multiplying velocity with momentum equation which leads to (Incropera et al., 1996)

$$\frac{\partial}{\partial t} \frac{1}{2} \rho |\mathbf{v}|^2 = -(\nabla p) \cdot \mathbf{v} + (\nabla \cdot \boldsymbol{\tau}) \cdot \mathbf{v} + (\rho \mathbf{b}) \cdot \mathbf{v} \quad (8.29)$$

Using Eq.( 8.27 ) - Eq.( 8.28 ), mechanical energy equation in Eq.( 8.29 ) can be rewritten as (Incropera et al., 1996)

$$\begin{aligned} \frac{\partial}{\partial t} \frac{1}{2} \rho |\mathbf{v}|^2 + \nabla \cdot \left( \frac{1}{2} \rho \mathbf{v} |\mathbf{v}|^2 \right) & \quad (8.30) \\ = -\nabla \cdot (p\mathbf{v}) + p \nabla \cdot \mathbf{v} + \nabla \cdot (\boldsymbol{\tau} \cdot \mathbf{v}) - \boldsymbol{\tau} : (\nabla \otimes \mathbf{v}) + (\rho \mathbf{b}) & \\ \cdot \mathbf{v} & \end{aligned}$$

In this study, the fluid is assumed to be incompressible for which the speed of fluid flow is lower than the compressible flow. Therefore, the mechanical energy can be subtracted from the total energy equation and leads to the internal energy equation as (Incropera et al., 1996)

$$\frac{\partial \rho e}{\partial t} = -\nabla \cdot q + S - p\nabla \cdot \mathbf{v} + \boldsymbol{\tau} : (\nabla \otimes \mathbf{v}) \quad (8.31)$$

Defining internal energy as (Incropera et al., 1996)

$$e = C_p T \quad (8.32)$$

in which  $C_p$  is the specific heat capacity and substituting Eq.( 8.32 ) into Eq.( 8.31 ) leads to (Incropera et al., 1996)

$$\frac{\partial \rho C_p T}{\partial t} = -\nabla \cdot q + S - p\nabla \cdot \mathbf{v} + \boldsymbol{\tau} : (\nabla \otimes \mathbf{v}) \quad (8.33)$$

The heat flux  $q$  based on Fourier's Law can be represented as (Incropera et al., 1996)

$$q = -k\nabla T \quad (8.34)$$

where  $k$  is the thermal conductivity.

In the case of sudden expansion or compression phenomenon, the term  $p\nabla \cdot \mathbf{v}$  represents energy for the cooling or heating a fluid internally (Bird, 2002). Since the focus of this study is on multiphase flow and there are no significant sudden volume changes in the fluid domain, this term is omitted from the energy equation. On the other hand, the term  $\boldsymbol{\tau} : (\nabla \otimes \mathbf{v})$  representing the motion energy is irreversibly exchanged into thermal energy, and it is considerable if the speed of the fluid is relatively high (Bird, 2002). As the current study focuses on the multi-phase flow motion at a low Reynolds number, this term is also not considered in the energy equation. The thermal conductivity  $k$  is assumed to be a constant number as a result, the internal energy can be rewritten as

$$\frac{\partial \rho C_p T}{\partial t} = k\nabla^2 T + S \quad (8.35)$$

### 8.3 PDDO Governing Equations

Peridynamic differential operator (PDDO) can express partial differentials of any order by integral equations. Therefore, the governing equations for multiphase fluid motion, such as the Navier–Stokes equations and energy equations, can be reformulated in terms of integral equations. The mathematical formulations of peridynamic functions are introduced in section 3.3.

#### 8.3.1 Non-local Form of Continuity Equation

Velocity divergence in local form can be written as

$$\nabla \cdot \mathbf{v}(\mathbf{x}) = \sum_{i=1}^2 \frac{\partial v_i(\mathbf{x})}{\partial x_i} = \frac{\partial v_1(\mathbf{x})}{\partial x_1} + \frac{\partial v_2(\mathbf{x})}{\partial x_2} \quad (8.36)$$

The partial derivative terms in velocity divergence can be replaced by the first order peridynamic function as

$$\frac{\partial v_1(\mathbf{x})}{\partial x_1} = \int_{H_x} g_1^{10}(\xi) (v_1(\mathbf{x}') - v_1(\mathbf{x})) dV' \quad (8.37)$$

$$\frac{\partial v_2(\mathbf{x})}{\partial x_2} = \int_{H_x} g_1^{01}(\xi) (v_2(\mathbf{x}') - v_2(\mathbf{x})) dV'$$

Therefore, the velocity divergence in non-local form can be constructed as

$$\begin{aligned} \nabla \cdot \mathbf{v}(\mathbf{x}) &= \int_{H_x} \begin{pmatrix} g_1^{10}(\xi) & g_1^{01}(\xi) \end{pmatrix} \begin{pmatrix} v_1(\mathbf{x}') - v_1(\mathbf{x}) \\ v_2(\mathbf{x}') - v_2(\mathbf{x}) \end{pmatrix} dV' \\ &= \int_{H_x} \mathbf{g}_1(\xi) \cdot (\mathbf{v}(\mathbf{x}') - \mathbf{v}(\mathbf{x})) dV' \end{aligned} \quad (8.38)$$

As a result, the non-local form of mass conservation can be represented as

$$\frac{\partial \rho(\mathbf{x})}{\partial t} = -\rho(\mathbf{x}) \int_{H_x} \mathbf{g}_1(\xi) \cdot (\mathbf{v}(\mathbf{x}') - \mathbf{v}(\mathbf{x})) dV' \quad (8.39)$$

where the first order peridynamic functions  $\mathbf{g}_1(\xi)$  are represented as

$$\mathbf{g}_1(\boldsymbol{\xi}) = \begin{pmatrix} g_1^{10}(\boldsymbol{\xi}) \\ g_1^{01}(\boldsymbol{\xi}) \end{pmatrix} \quad (8.40)$$

### 8.3.2 Non-local Form of Terms in Navier-Stokes Equation

As discussed in Section 8.2.2, the Navier-Stokes equation incorporates terms for pressure gradient, viscosity, surface tension, and body forces. The non-local form of each term is expressed in this session.

#### 8.3.2.1 Pressure Gradient

The pressure gradient term  $\nabla \cdot (-p\mathbf{I})$  in local form can be written as

$$\nabla p(\mathbf{x}) = \begin{pmatrix} \frac{\partial p(\mathbf{x})}{\partial x_1} \\ \frac{\partial p(\mathbf{x})}{\partial x_2} \end{pmatrix} \quad (8.41)$$

Correspondingly, by using the first order peridynamic function, its nonlocal form can be expressed as

$$\begin{aligned} \nabla p(\mathbf{x}) &= \int_{H_x} (p(\mathbf{x}') - p(\mathbf{x})) \begin{pmatrix} g_1^{10}(\boldsymbol{\xi}) \\ g_1^{01}(\boldsymbol{\xi}) \end{pmatrix} dV' \\ &= \int_{H_x} (p(\mathbf{x}') - p(\mathbf{x})) \mathbf{g}_1(\boldsymbol{\xi}) dV' \end{aligned} \quad (8.42)$$

#### 8.3.2.2 Viscous Force

Local form of the velocity gradient can be written as

$$\nabla \otimes \mathbf{v}(\mathbf{x}) = \begin{pmatrix} \frac{\partial}{\partial x_1} \\ \frac{\partial}{\partial x_2} \end{pmatrix} (v_1(\mathbf{x}) \quad v_2(\mathbf{x})) = \begin{bmatrix} \frac{\partial v_1(\mathbf{x})}{\partial x_1} & \frac{\partial v_2(\mathbf{x})}{\partial x_1} \\ \frac{\partial v_1(\mathbf{x})}{\partial x_2} & \frac{\partial v_2(\mathbf{x})}{\partial x_2} \end{bmatrix} \quad (8.43)$$

The velocity gradient matrix can be transformed into its non-local form by using peridynamic function which can be expressed as

$$\begin{aligned}
\nabla \otimes \mathbf{v}(\mathbf{x}) &= \int_{H_x} \begin{pmatrix} g_1^{10}(\xi) \\ g_1^{01}(\xi) \end{pmatrix} ((v_1(\mathbf{x}') - v_1(\mathbf{x})) \quad (v_2(\mathbf{x}') - v_2(\mathbf{x}))) dV' \quad (8.44) \\
&= \int_{H_x} \mathbf{g}_1(\xi) (\mathbf{v}(\mathbf{x}') - \mathbf{v}(\mathbf{x}))^T dV' \\
&= \int_{H_x} \mathbf{g}_1(\xi) \otimes (\mathbf{v}(\mathbf{x}') - \mathbf{v}(\mathbf{x})) dV'
\end{aligned}$$

Local form of Laplacian operator is defined by the divergence of the gradient as

$$\begin{aligned}
\Delta \mathbf{v}(\mathbf{x}) &= \nabla \cdot (\nabla \otimes \mathbf{v}(\mathbf{x})) = (\nabla \otimes \mathbf{v}(\mathbf{x}))^T \cdot \nabla = \begin{bmatrix} \frac{\partial v_1^2(\mathbf{x})}{\partial x_1^2} + \frac{\partial v_1^2(\mathbf{x})}{\partial x_2^2} \\ \frac{\partial v_2^2(\mathbf{x})}{\partial x_1^2} + \frac{\partial v_2^2(\mathbf{x})}{\partial x_2^2} \end{bmatrix} \quad (8.45) \\
&= \text{tr} \left( \begin{bmatrix} \frac{\partial^2}{\partial x_1^2} & \frac{\partial^2}{\partial x_1 \partial x_2} \\ \frac{\partial^2}{\partial x_1 \partial x_2} & \frac{\partial^2}{\partial x_2^2} \end{bmatrix} \right) \begin{pmatrix} v_1(\mathbf{x}) \\ v_2(\mathbf{x}) \end{pmatrix}
\end{aligned}$$

Hence, the non-local form Laplacian operator can be constructed as

$$\begin{aligned}
\Delta \mathbf{v}(\mathbf{x}) &= \text{tr} \left( \begin{bmatrix} \frac{\partial^2}{\partial x_1^2} & \frac{\partial^2}{\partial x_1 \partial x_2} \\ \frac{\partial^2}{\partial x_1 \partial x_2} & \frac{\partial^2}{\partial x_2^2} \end{bmatrix} \right) \begin{pmatrix} v_1(\mathbf{x}) \\ v_2(\mathbf{x}) \end{pmatrix} \quad (8.46) \\
&= \int_{H_x} \text{tr}(\mathbf{g}_2(\xi)) \begin{pmatrix} v_1(\mathbf{x}') - v_1(\mathbf{x}) \\ v_2(\mathbf{x}') - v_2(\mathbf{x}) \end{pmatrix} dV'
\end{aligned}$$

in which  $\mathbf{g}_2(\xi)$  is represented as

$$\mathbf{g}_2(\xi) = \begin{bmatrix} g_2^{02}(\xi) & g_2^{11}(\xi) \\ g_2^{11}(\xi) & g_2^{20}(\xi) \end{bmatrix} \quad (8.47)$$

Subsequently, the non-local form of viscous force in a compact form can be written as

$$\mu \Delta \mathbf{v}(\mathbf{x}) = \mu \int_{H_x} \text{tr}(\mathbf{g}_2(\xi)) (\mathbf{v}(\mathbf{x}') - \mathbf{v}(\mathbf{x})) dV' \quad (8.48)$$

### 8.3.2.3 Surface Tension Force in Normal Direction

The classical form of normal surface tension  $\mathbf{F}_{s,n}$  represented in terms of surface tension coefficient  $\gamma$ , unit normal vector  $\hat{\mathbf{n}}_{lg}$ , weight function  $\delta_{lg}$  and interface curvature  $\tilde{\kappa}$  is denoted in Eq.( 8.11 ). To construct the normal surface tension in a non-local form, it is first necessary to construct the fluid interface normal vector,  $\hat{\mathbf{n}}_{lg}$ , and curvature,  $\tilde{\kappa}$ , in a nonlocal form.

According to the continuous surface force method (Brackbill et al., 1992), as the colour function has a unit jump at the interface, it can be used to identify and track the position of the interface. The normal vectors between fluid and gas interface can be represented by the gradient of the colour function,  $\nabla c_{lg}(\mathbf{x})$ , as

$$\begin{aligned} \nabla c_{lg}(\mathbf{x}) &= \begin{pmatrix} \frac{\partial c_{lg}(\mathbf{x})}{\partial x_1} \\ \frac{\partial c_{lg}(\mathbf{x})}{\partial x_2} \end{pmatrix} = \int_{H_x} (c_{lg}(\mathbf{x}') - c_{lg}(\mathbf{x})) \begin{pmatrix} g_1^{10}(\xi) \\ g_1^{01}(\xi) \end{pmatrix} dV' \\ &= \int_{H_x} (c_{lg}(\mathbf{x}') - c_{lg}(\mathbf{x})) \mathbf{g}_1(\xi) dV' \end{aligned} \quad (8.49)$$

where  $c_{lg}(\mathbf{x})$  is the colour function at material point  $\mathbf{x}$ . The difference of colour function between a pair of material points can be represented by

$$c_{lg}(\mathbf{x}') - c_{lg}(\mathbf{x}) = \begin{cases} 1, & \text{if } \mathbf{x} \text{ and } \mathbf{x}' \text{ are in same fluid domain} \\ 0, & \text{otherwise} \end{cases} \quad (8.50)$$

In numerical simulations, if there is a large density difference between two fluids at the interface, a weighted-density approach is used as an alternative method to determine the difference of colour function (Adami et al., 2010), i.e.

$$c_{lg}(\mathbf{x}') - c_{lg}(\mathbf{x}) = \begin{cases} \frac{2\rho_x}{\rho_x + \rho_{x'}} & \text{if } \mathbf{x} \text{ and } \mathbf{x}' \text{ are in same fluid domain} \\ 0, & \text{otherwise} \end{cases} \quad (8.51)$$

where  $\rho_x$  is the density of material point located at  $\mathbf{x}$ , and  $\rho_{x'}$  is density of material point located at  $\mathbf{x}'$ .

Following the approach purposed by Morris (2000), the unit normal vector between two fluid domains,  $\hat{\mathbf{n}}_{lg}(\mathbf{x})$ , as shown in Fig. 8-1, then can be formulated by using the gradient of colour function in Eq.( 8.49 ) as

$$\hat{\mathbf{n}}_{lg}(\mathbf{x}) = \frac{\nabla c_{lg}(\mathbf{x})}{|\nabla c_{lg}(\mathbf{x})|} = \frac{\int_{H_x} (c_{lg}(\mathbf{x}') - c_{lg}(\mathbf{x})) \mathbf{g}_1(\boldsymbol{\xi}) dV'}{\left| \int_{H_x} (c_{lg}(\mathbf{x}') - c_{lg}(\mathbf{x})) \mathbf{g}_1(\boldsymbol{\xi}) dV' \right|} \quad (8.52)$$

In addition, the weight function for surface tension in Eq.( 8.11 ) in continuum surface force method is taken as the magnitude of the gradient of the colour function (Morris, 2000) and its non-local form is provided as (Gao and Oterkus, 2020)

$$\delta_{lg}(\mathbf{x}) = |\nabla c_{lg}(\mathbf{x})| = \left| \int_{H_x} (c_{lg}(\mathbf{x}') - c_{lg}(\mathbf{x})) \mathbf{g}_1(\boldsymbol{\xi}) dV' \right| \quad (8.53)$$

the weight function for surface tension is used to convert the surface tension force into volumetric force, and distribute the force along the fluid interface transition band area.

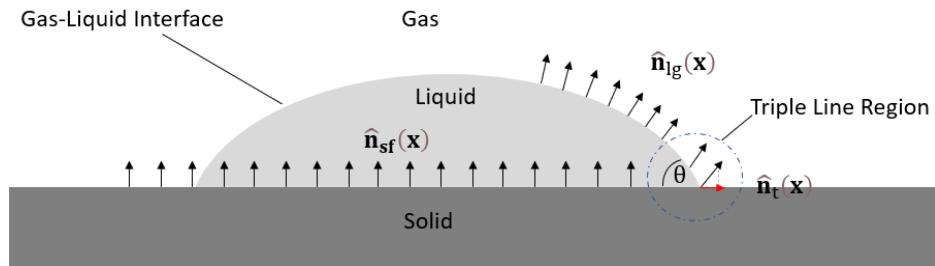


*Fig. 8-2 Two fluids come into contact at a solid surface, and the triple line region at the point of contact.*

Fig. 8-2 shows a droplet surrounded by a gaseous fluid and resting on a solid surface. The unit normal vectors,  $\hat{\mathbf{n}}_{lg}(\mathbf{x})$ , from Eq.( 8.52 ) represent the normal direction of the interface between liquid and gaseous fluid, and they can be accurately computed when material points in each fluid domain fully interact with their family material. However, at the triple line region, where the liquid–gas interface meets the solid-liquid interface in Fig. 8-2, the material points in the fluid domain close to the solid wall do not have enough family material points to contribute to the integral equation, unit normal vectors between fluids calculated according to Eq.( 8.52 ) can be corrupted. Moreover, as the curvature is calculated from the divergence of unit normal vectors at the

interface, these corrupted unit normal vectors result in erroneous curvature calculations.

Therefore, consideration is required when computing unit normal vectors at the triple line region. In this study, the corrupted unit normal vectors at this region are corrected through a normal prescription scheme (Breinlinger et al., 2013).

The unit normal vectors at the triple line region,  $\hat{\mathbf{n}}_{lg,cor}(\mathbf{x})$ , as shown in Fig. 8-3 can be prescribed as (Breinlinger et al., 2013)

$$\hat{\mathbf{n}}_{lg,cor}(\mathbf{x}) = \hat{\mathbf{n}}_t(\mathbf{x}) \sin\theta_{eq} - \hat{\mathbf{n}}_{sf}(\mathbf{x}) \cos\theta_{eq} \quad (8.54)$$

in which  $\hat{\mathbf{n}}_t$  is the projection of unit normal vector,  $\hat{\mathbf{n}}_{lg}(\mathbf{x})$ , between the denser fluid and the lighter fluid on the solid-fluid interface,  $\hat{\mathbf{n}}_{sf}(\mathbf{x})$  is the unit normal vector between solid phase and fluid phase, and  $\theta_{eq}$  is the equilibrium contact angle.

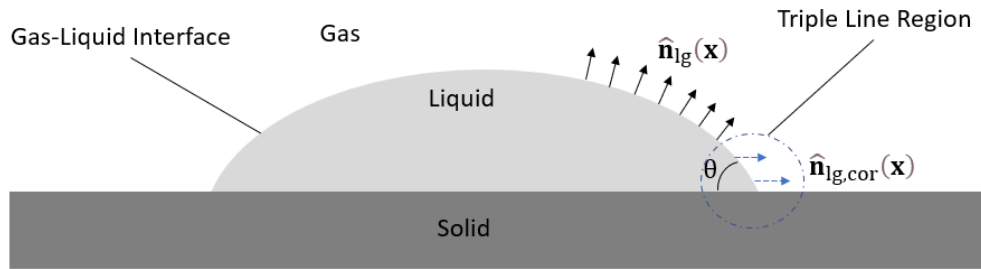


Fig. 8-3 Unit normal vector  $\hat{\mathbf{n}}_{lg,cor}(\mathbf{x})$  at the triple line region and ordinary computed unit normal vector  $\hat{\mathbf{n}}_{lg}(\mathbf{x})$ .

When a droplet is in contact with a solid surface, the balance between the adhesive and cohesive forces in the droplet forms the equilibrium contact angle  $\theta_{eq}$ . Eq.( 8.54 ) prescribes unit normal vectors at the triple line region point in the direction of the interface normal that forms the equilibrium contact angle  $\theta_{eq}$ . If a droplet comes into contact with a solid surface and forms an instantaneous contact angle  $\theta$  not equal to the equilibrium contact angle  $\theta_{eq}$ , the curvature obtained by the divergence of the prescribed unit normal vectors  $\hat{\mathbf{n}}_{lg,cor}(\mathbf{x})$  will drive the interface to move until the droplet forms an equilibrium contact angle with the solid interface (Breinlinger et al., 2013).

Following a similar approach introduced in continuum surface force method, the unit normal vector between solid phase and fluid phase,  $\hat{\mathbf{n}}_{sf}(\mathbf{x})$ , in Eq.( 8.54 ), can be formulated as (Meier et al., 2021)

$$\hat{\mathbf{n}}_{sf}(\mathbf{x}) = \frac{\nabla c_{sf}(\mathbf{x})}{|\nabla c_{sf}(\mathbf{x})|} \quad (8.55)$$

in which  $\nabla c_{sf}(\mathbf{x})$  is the gradient of the colour function between fluid and solid phase. Similarly, its non-local form can be represented as

$$\begin{aligned} \nabla c_{sf}(\mathbf{x}) &= \begin{pmatrix} \frac{\partial c(\mathbf{x})}{\partial x_1} \\ \frac{\partial c(\mathbf{x})}{\partial x_2} \end{pmatrix} = \int_{H_x} (c_{sf}(\mathbf{x}') - c_{sf}(\mathbf{x})) \begin{pmatrix} g_1^{10}(\boldsymbol{\xi}) \\ g_1^{01}(\boldsymbol{\xi}) \end{pmatrix} dV' \\ &= \int_{H_x} (c_{sf}(\mathbf{x}') - c_{sf}(\mathbf{x})) \mathbf{g}_1(\boldsymbol{\xi}) dV' \end{aligned} \quad (8.56)$$

where  $c_{sf}(\mathbf{x})$  is the colour function at material point  $\mathbf{x}$  for distinguishing fluid and solid phase. The difference of colour function between a pair of material points can be defined as

$$c_{sf}(\mathbf{x}') - c_{sf}(\mathbf{x}) = \begin{cases} 1, & \text{if } \mathbf{x} \text{ and } \mathbf{x}' \text{ are in same phase} \\ 0, & \text{otherwise} \end{cases} \quad (8.57)$$

Consequently, the projection of unit normal vector between liquid and gaseous fluid on the solid-fluid interface,  $\hat{\mathbf{n}}_t(\mathbf{x})$ , in Eq.( 8.54 ) can be computed as (Breinlinger et al., 2013)

$$\hat{\mathbf{n}}_t(\mathbf{x}) = \frac{\hat{\mathbf{n}}_{lg}(\mathbf{x}) - (\hat{\mathbf{n}}_{lg}(\mathbf{x}) \cdot \hat{\mathbf{n}}_{sf}(\mathbf{x})) \hat{\mathbf{n}}_{sf}(\mathbf{x})}{|\hat{\mathbf{n}}_{lg}(\mathbf{x}) - (\hat{\mathbf{n}}_{lg}(\mathbf{x}) \cdot \hat{\mathbf{n}}_{sf}(\mathbf{x})) \hat{\mathbf{n}}_{sf}(\mathbf{x})|} \quad (8.58)$$

where  $\hat{\mathbf{n}}_{sf}(\mathbf{x})$  is provided in Eq.( 8.55 ) and  $\hat{\mathbf{n}}_{lg}(\mathbf{x})$  is provided in Eq.( 8.52 ).

The ordinary computed unit normal vectors  $\hat{\mathbf{n}}_{lg}(\mathbf{x})$  from Eq.( 8.52 ) and prescribed unit normal vectors  $\hat{\mathbf{n}}_{lg,cor}(\mathbf{x})$  at the triple line region from Eq.( 8.54 ) are represented in Fig. 8-3. Since the calculation of  $\hat{\mathbf{n}}_{lg,cor}(\mathbf{x})$  depends on the equilibrium contact

angle  $\theta_{eq}$ , when current contact angle  $\theta$  is greatly different from equilibrium contact angle  $\theta_{eq}$ , a sharp transition can be observed between  $\hat{\mathbf{n}}_{lg}(\mathbf{x})$  and  $\hat{\mathbf{n}}_{lg,cor}(\mathbf{x})$ . This sharp transition will cause a discontinuity when computing the curvature. As a result, a smoothed unit normal correction scheme is implemented here to ensure a smooth transition from prescribed unit normal vectors to ordinary computed unit normal vectors, the smoothed interface unit normal vectors can be obtained as

$$\hat{\mathbf{n}}_{lg}^*(\mathbf{x}) = \frac{f_{w,x}\hat{\mathbf{n}}_{lg}(\mathbf{x}) + (1 - f_{w,x})\hat{\mathbf{n}}_{lg,cor}(\mathbf{x})}{|f_{w,x}\hat{\mathbf{n}}_{lg}(\mathbf{x}) + (1 - f_{w,x})\hat{\mathbf{n}}_{lg,cor}(\mathbf{x})|} \quad (8.59)$$

where  $\hat{\mathbf{n}}_{lg,cor}(\mathbf{x})$  can be calculated from Eq. ( 8.52 ) and  $\hat{\mathbf{n}}_{lg}(\mathbf{x})$  can be calculated from Eq. ( 8.54 ). The parameter  $f_{w,x}$  is a transition function and determines the influence of the prescribed normal vector at the triple line region which depends on the distance to the wall. It is provided as

$$f_{w,x} = \begin{cases} 0 & d_w < 0 \\ d_w/d_{max} & \text{if } 0 < d_w < d_{max} \\ 1 & d_w > d_{max} \end{cases} \quad (8.60)$$

in which  $d_w$  is the distance between fluid material points and the solid-fluid interface. The  $d_{max}$  in Eq.( 8.60 ) is denoted as the maximum smooth distance from the wall, in this work, it is taken as  $2\Delta x$ , where  $\Delta x$  is the spacing between material point. The schematic diagram of the smoothed interface unit normal vectors calculated from Eq.( 8.59 ) is shown in Fig. 8-4. Section 8.5.2 gives a numerical example of the effectiveness of this smoothing correction method.

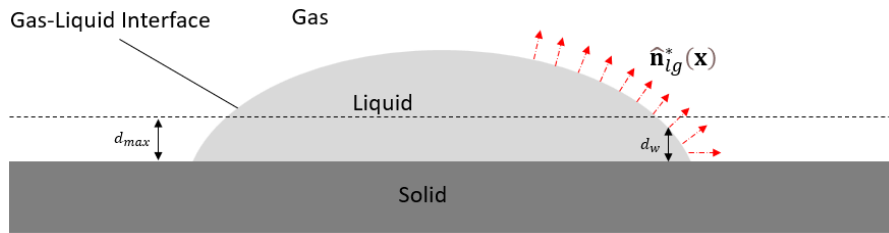


Fig. 8-4 Corrected unit normal vectors distributed along the fluid interface.

Subsequently, the surface curvature  $\tilde{\kappa}$  in Eq.( 8.11 ) then can be calculated via the divergence of the smoothed interface unit normal vector, i.e.

$$\tilde{\kappa}(\mathbf{x}) = -\nabla \cdot \hat{\mathbf{n}}_{lg}^*(\mathbf{x}) = -\int_{H_x} \mathbf{g}_1(\xi) \cdot (\hat{\mathbf{n}}_{lg}^*(\mathbf{x}') - \hat{\mathbf{n}}_{lg}^*(\mathbf{x})) dV' \quad (8.61)$$

As suggested in Morris' work (2020), curvature directly computed from Eq.( 8.61 ) can lead to errors at the edges of the transition region, as the smoothed interface unit normal vectors are relatively small and can have erroneous directions when they are away from the interface. Therefore, the surface curvature cannot be approximated accurately. This problem can be addressed by introducing selection criteria to determine if a ‘reliable’ normal vector can be obtained for divergence computation. A function at each material point is used to distinguish ‘reliable’ normal vectors that can contribute to the curvature approximation in Eq.( 8.61 ) (Morris, 2000), i.e.

$$N_x = \begin{cases} 1, & \text{if } |f_{w,x} \hat{\mathbf{n}}_{lg}(\mathbf{x}) + (1 - f_{w,x}) \hat{\mathbf{n}}_{lg,cor}(\mathbf{x})| > \epsilon \\ 0, & \text{otherwise} \end{cases} \quad (8.62)$$

and

$$\hat{\mathbf{n}}_{lg}^*(\mathbf{x}) = \begin{cases} \frac{f_{w,x} \hat{\mathbf{n}}_{lg}(\mathbf{x}) + (1 - f_{w,x}) \hat{\mathbf{n}}_{lg,cor}(\mathbf{x})}{|f_{w,x} \hat{\mathbf{n}}_{lg}(\mathbf{x}) + (1 - f_{w,x}) \hat{\mathbf{n}}_{lg,cor}(\mathbf{x})|}, & \text{if } N_x = 1 \\ 0, & \text{otherwise} \end{cases}, \quad (8.63)$$

where  $\epsilon \ll 1$  is a user-defined tolerance (Morris, 2000). As the unit normal vectors below the tolerance are not contributed to the curvature computation, an intermediate curvature estimation needs to be used to sum over reliable normal vectors (Morris, 2000). As a result, the curvature in Eq.( 8.61 ) can be recomputed as

$$\tilde{\kappa}^*(\mathbf{x}) = -\int_{H_x} \min(N_{x'}, N_x) \mathbf{g}_1(\xi) \cdot (\hat{\mathbf{n}}_{lg}^*(\mathbf{x}') - \hat{\mathbf{n}}_{lg}^*(\mathbf{x})) dV' \quad (8.64)$$

On the other side, considering material points at the edge of the phase transition region, whose family material points are within the horizon but outside the transition region, the interface unit normal vectors at these family material points are zeros. As a result, a correction factor is used to consider the truncated material points, and it can be represented as (Gao and Oterkus, 2020)

$$\zeta = \frac{\int_{H_x} \min(N_{x'}, N_x) \omega(\xi) dV'}{\int_{H_x} \omega(\xi) dV'} \quad (8.65)$$

in which  $\omega(\xi)$  is the weight function as represented in Eq.( 3.28 ).

Based on Eq.( 8.59 ),the smoothed interface unit normal vectors, $\hat{\mathbf{n}}_{lg}^*(\mathbf{x})$  obtained for material points at each fluid domain always point from themselves to the fluid interface. Considering a pair of material points which  $\mathbf{x}$  is in one fluid domain and  $\mathbf{x}'$  is in the other fluid domain, the direction of their unit normal vectors will opposite with each other. Therefore, a phase normal coefficient  $\varphi_x^{x'}$  is added to reverse the unit normal vector direction if it is opposite from the unit normal vector at material point  $\mathbf{x}$  (Zhang et al., 2015). Hence, the interface curvature in this study is computed as

$$\tilde{\kappa}^{**}(\mathbf{x}) = \frac{\tilde{\kappa}^*(\mathbf{x})}{\zeta} = - \frac{\int_{H_x} \min(N_{x'}, N_x) \mathbf{g}_1(\xi) \cdot \left( \varphi_x^{x'} \hat{\mathbf{n}}_{lg,x'}^* - \hat{\mathbf{n}}_{lg,x}^* \right) dV'}{\frac{\int_{H_x} \min(N_{x'}, N_x) \omega(\xi) dV'}{\int_{H_x} \omega(\xi) dV'}} \quad (8.66)$$

with

$$\varphi_x^{x'} = \begin{cases} -1, & \text{if } \mathbf{x}' \text{ is not in the same fluid domain with } \mathbf{x} \\ 1, & \text{if } \mathbf{x}' \text{ is in the same fluid domain with } \mathbf{x} \end{cases} \quad (8.67)$$

Finally, the non-local form of the normal surface tension can be expressed as

$$\mathbf{F}_{s,n} = \gamma \tilde{\kappa}^{**}(\mathbf{x}) \hat{\mathbf{n}}_{lg}^*(\mathbf{x}) \delta_{lg}(\mathbf{x}) \quad (8.68)$$

in which  $\gamma$  is given by Eq.( 8.12 ),  $\tilde{\kappa}^{**}(\mathbf{x})$  is the curvature as described in Eq.( 8.66 ),  $\hat{\mathbf{n}}_{lg}^*(\mathbf{x})$  is the smoothed unit normal vector between liquid-gas interface as described in Eq. ( 8.59 ) and  $\delta_{lg}(\mathbf{x})$  is weight function for surface tension as described in Eq.( 8.53 ).

#### 8.3.2.4 Marangoni Force

The classical form of the Marangoni force is given in Eq.( 8.16 ).

To evaluate the non-local form of Marangoni force, the temperature gradient  $\nabla T$  in non-local form needs to be developed. The temperature gradient  $\nabla T$  in local form is given as

$$\nabla T(\mathbf{x}) = \begin{pmatrix} \frac{\partial T(\mathbf{x})}{\partial x_1} \\ \frac{\partial T(\mathbf{x})}{\partial x_2} \end{pmatrix} \quad (8.69)$$

Therefore, the non-local form of the temperature gradient by using the peridynamic function can be expressed as

$$\nabla T(\mathbf{x}) = \int_{H_x} (T(\mathbf{x}') - T(\mathbf{x})) \begin{pmatrix} g_1^{10}(\boldsymbol{\xi}) \\ g_1^{01}(\boldsymbol{\xi}) \end{pmatrix} dV' = \int_{H_x} (T_{x'} - T_x) \mathbf{g}_1(\boldsymbol{\xi}) dV' \quad (8.70)$$

As a result, the non-local form of Marangoni force can be represented as

$$\mathbf{F}_{s,t} = \frac{d\gamma(T)}{dT} \left[ \nabla T(\mathbf{x}) - \left( \nabla T(\mathbf{x}) \cdot \hat{\mathbf{n}}_{lg}^*(\mathbf{x}) \right) \hat{\mathbf{n}}_{lg}^*(\mathbf{x}) \right] \delta_{lg}(\mathbf{x}) \quad (8.71)$$

where  $\nabla T(\mathbf{x})$  is calculated from Eq.( 8.70 ),  $\hat{\mathbf{n}}_{lg}^*(\mathbf{x})$  is calculated from Eq.( 8.59 ), and  $\delta_{lg}$  is calculated from Eq.( 8.53 ).

### 8.3.3 Thermal Model

The classical form of the energy equation is given in Eq.( 8.35 ). The local form of the divergence of the heat flux in the equation can be written as

$$\nabla \cdot \mathbf{q}(\mathbf{x}) = -k \left( \frac{\partial}{\partial x_1} \quad \frac{\partial}{\partial x_2} \right) \begin{pmatrix} \frac{\partial T(\mathbf{x})}{\partial x_1} \\ \frac{\partial T(\mathbf{x})}{\partial x_2} \end{pmatrix} = -k \left( \frac{\partial^2 T(\mathbf{x})}{\partial x_1^2} + \frac{\partial^2 T(\mathbf{x})}{\partial x_2^2} \right) \quad (8.72)$$

The second order partial derivative for temperature can be represented by second order peridynamic function as

$$\frac{\partial^2 T}{\partial x_1^2} = \int_{H_x} g_2^{20}(\boldsymbol{\xi}) (T(\mathbf{x}') - T(\mathbf{x})) dV' \quad (8.73)$$

$$\frac{\partial^2 T}{\partial x_2^2} = \int_{H_x} g_2^{02}(\xi)(T(\mathbf{x}') - T(\mathbf{x})) dV'$$

As a result, the Lagrangian description of internal energy equation in non-local form can be written as

$$\rho(\mathbf{x}) \frac{\partial C_p(\mathbf{x})T(\mathbf{x})}{\partial t} = k \int_{H_x} \text{tr}(\mathbf{g}_2(\xi))(T(\mathbf{x}') - T(\mathbf{x})) dV' + S(\mathbf{x}) \quad (8.74)$$

#### 8.4 Numerical Implementation

The non-local form of governing equations is solved numerically. The fluid domain is discretized into a series of material points, and each material point carries information such as material density, viscosity, pressure, velocity, displacement, and temperature. Since PDDO inherits analogous concepts with peridynamics theory, the long-range force is considered in the simulation domain representing a material point interacting with a series of family material points within a horizon. As shown in Fig. 8-5,  $\mathbf{x}_i^n$  represents the current coordinate of the material point  $i$  at time  $t = t_n$ , and material point  $i$  interacts with family material points  $j$  at  $\mathbf{x}_j^n$  within a range of  $\delta$ . With the updated Lagrangian description, the location of the material points changes at every time step. Therefore, a material point may interact with different family material points at time  $t = t_{n+1}$  and the peridynamics function needs to be reconstructed based on the updated configuration.

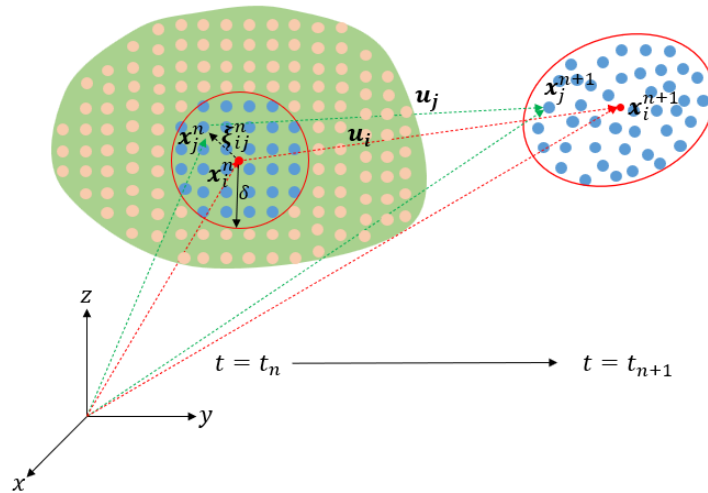


Fig. 8-5 Location of material point  $\mathbf{x}_i^n$  with its family members at  $t = t_n$ , and the updated location at  $t = t_{n+1}$ .

#### 8.4.1 Discretized Form of Governing Equations by Using PDDO

To ensure the mass conservation is maintained at the fluid domain, each material point in the simulation domain is assigned with an initial mass after the simulation domain is discretized. The mass at each material point remains same during simulation, as the density field of the material point is updated by continuity equation, the volume of material point can be updated correspondingly at each time step as

$$V_i^n = \frac{m_i}{\rho_i^n} \quad (8.75)$$

where  $m_i$  is the initial mass of material point  $i$ , and  $\rho_i^n$  is the density at the current time step.

The discretized form of the peridynamic function up to second order is given as

$$\mathbf{g}_1(\boldsymbol{\xi}_{ij}^n) = \begin{pmatrix} g_1^{10}(\boldsymbol{\xi}_{ij}^n) \\ g_1^{01}(\boldsymbol{\xi}_{ij}^n) \end{pmatrix} \quad (8.76)$$

and

$$\mathbf{g}_2(\boldsymbol{\xi}_{ij}^n) = \begin{bmatrix} g_2^{02}(\boldsymbol{\xi}_{ij}^n) & g_2^{11}(\boldsymbol{\xi}_{ij}^n) \\ g_2^{11}(\boldsymbol{\xi}_{ij}^n) & g_2^{20}(\boldsymbol{\xi}_{ij}^n) \end{bmatrix} \quad (8.77)$$

in which the relative distance vector between a pair of material points  $i$  and  $j$  can be represented as

$$\boldsymbol{\xi}_{ij}^n = \mathbf{x}_j^n - \mathbf{x}_i^n = \begin{bmatrix} \xi_{ij}^{1n} \\ \xi_{ij}^{2n} \end{bmatrix} \quad (8.78)$$

where superscript  $n$  represents the current time step.

As introduced in Eq.( 3.31 ), peridynamic function up to second order is represented as

$$\begin{cases} \mathbf{g}_1^{01}(\boldsymbol{\xi}_{ij}^n) \\ \mathbf{g}_2^{02}(\boldsymbol{\xi}_{ij}^n) \\ \mathbf{g}_1^{10}(\boldsymbol{\xi}_{ij}^n) \\ \mathbf{g}_2^{11}(\boldsymbol{\xi}_{ij}^n) \\ \mathbf{g}_2^{20}(\boldsymbol{\xi}_{ij}^n) \end{cases} = \begin{cases} a_{01}^{01n} & a_{02}^{01n} & a_{10}^{01n} & a_{11}^{01n} & a_{20}^{01n} \\ a_{01}^{02n} & a_{02}^{02n} & a_{10}^{02n} & a_{11}^{02n} & a_{20}^{02n} \\ a_{01}^{10n} & a_{02}^{10n} & a_{10}^{10n} & a_{11}^{10n} & a_{20}^{10n} \\ a_{01}^{11n} & a_{02}^{11n} & a_{10}^{11n} & a_{11}^{11n} & a_{20}^{11n} \\ a_{01}^{20n} & a_{02}^{20n} & a_{10}^{20n} & a_{11}^{20n} & a_{20}^{20n} \end{cases} \begin{cases} \omega(|\boldsymbol{\xi}_{ij}^n|)(\boldsymbol{\xi}_{ij}^{1n})^0(\boldsymbol{\xi}_{ij}^{2n})^1 \\ \omega(|\boldsymbol{\xi}_{ij}^n|)(\boldsymbol{\xi}_{ij}^{1n})^0(\boldsymbol{\xi}_{ij}^{2n})^2 \\ \omega(|\boldsymbol{\xi}_{ij}^n|)(\boldsymbol{\xi}_{ij}^{1n})^1(\boldsymbol{\xi}_{ij}^{2n})^0 \\ \omega(|\boldsymbol{\xi}_{ij}^n|)(\boldsymbol{\xi}_{ij}^{1n})^1(\boldsymbol{\xi}_{ij}^{2n})^1 \\ \omega(|\boldsymbol{\xi}_{ij}^n|)(\boldsymbol{\xi}_{ij}^{1n})^2(\boldsymbol{\xi}_{ij}^{2n})^0 \end{cases} \quad (8.79)$$

in which coefficient matrix in Eq.( 8.79) is obtained by numerically solving Eq.( 3.32)

as

$$\sum_{j=1}^{N_i} \omega(|\boldsymbol{\xi}_{ij}^n|) [\mathbf{C}^n] V_j^n [\mathbf{a}^n] = \begin{bmatrix} 1 & 0 & 0 & 0 & 0 \\ 0 & 2 & 0 & 0 & 0 \\ 0 & 0 & 1 & 0 & 0 \\ 0 & 0 & 0 & 1 & 0 \\ 0 & 0 & 0 & 0 & 2 \end{bmatrix} \quad (8.80)$$

with

$$[\mathbf{a}^n] = \begin{cases} a_{01}^{01n} & a_{02}^{01n} & a_{10}^{01n} & a_{11}^{01n} & a_{20}^{01n} \\ a_{01}^{02n} & a_{02}^{02n} & a_{10}^{02n} & a_{11}^{02n} & a_{20}^{02n} \\ a_{01}^{10n} & a_{02}^{10n} & a_{10}^{10n} & a_{11}^{10n} & a_{20}^{10n} \\ a_{01}^{11n} & a_{02}^{11n} & a_{10}^{11n} & a_{11}^{11n} & a_{20}^{11n} \\ a_{01}^{20n} & a_{02}^{20n} & a_{10}^{20n} & a_{11}^{20n} & a_{20}^{20n} \end{cases} \quad (8.81)$$

$$[\mathbf{C}^n] \quad (8.82)$$

$$= \begin{bmatrix} (\boldsymbol{\xi}_{ij}^{1n})^0(\boldsymbol{\xi}_{ij}^{2n})^2 & (\boldsymbol{\xi}_{ij}^{1n})^0(\boldsymbol{\xi}_{ij}^{2n})^3 & (\boldsymbol{\xi}_{ij}^{1n})^1(\boldsymbol{\xi}_{ij}^{2n})^1 & (\boldsymbol{\xi}_{ij}^{1n})^1(\boldsymbol{\xi}_{ij}^{2n})^2 & (\boldsymbol{\xi}_{ij}^{1n})^2(\boldsymbol{\xi}_{ij}^{2n})^1 \\ (\boldsymbol{\xi}_{ij}^{1n})^0(\boldsymbol{\xi}_{ij}^{2n})^3 & (\boldsymbol{\xi}_{ij}^{1n})^0(\boldsymbol{\xi}_{ij}^{2n})^4 & (\boldsymbol{\xi}_{ij}^{1n})^1(\boldsymbol{\xi}_{ij}^{2n})^2 & (\boldsymbol{\xi}_{ij}^{1n})^1(\boldsymbol{\xi}_{ij}^{2n})^3 & (\boldsymbol{\xi}_{ij}^{1n})^2(\boldsymbol{\xi}_{ij}^{2n})^2 \\ (\boldsymbol{\xi}_{ij}^{1n})^1(\boldsymbol{\xi}_{ij}^{2n})^1 & (\boldsymbol{\xi}_{ij}^{1n})^1(\boldsymbol{\xi}_{ij}^{2n})^2 & (\boldsymbol{\xi}_{ij}^{1n})^2(\boldsymbol{\xi}_{ij}^{2n})^0 & (\boldsymbol{\xi}_{ij}^{1n})^2(\boldsymbol{\xi}_{ij}^{2n})^1 & (\boldsymbol{\xi}_{ij}^{1n})^3(\boldsymbol{\xi}_{ij}^{2n})^0 \\ (\boldsymbol{\xi}_{ij}^{1n})^1(\boldsymbol{\xi}_{ij}^{2n})^2 & (\boldsymbol{\xi}_{ij}^{1n})^1(\boldsymbol{\xi}_{ij}^{2n})^3 & (\boldsymbol{\xi}_{ij}^{1n})^2(\boldsymbol{\xi}_{ij}^{2n})^1 & (\boldsymbol{\xi}_{ij}^{1n})^2(\boldsymbol{\xi}_{ij}^{2n})^2 & (\boldsymbol{\xi}_{ij}^{1n})^3(\boldsymbol{\xi}_{ij}^{2n})^1 \\ (\boldsymbol{\xi}_{ij}^{1n})^2(\boldsymbol{\xi}_{ij}^{2n})^1 & (\boldsymbol{\xi}_{ij}^{1n})^2(\boldsymbol{\xi}_{ij}^{2n})^2 & (\boldsymbol{\xi}_{ij}^{1n})^3(\boldsymbol{\xi}_{ij}^{2n})^0 & (\boldsymbol{\xi}_{ij}^{1n})^3(\boldsymbol{\xi}_{ij}^{2n})^1 & (\boldsymbol{\xi}_{ij}^{1n})^4(\boldsymbol{\xi}_{ij}^{2n})^0 \end{bmatrix}$$

and

$$\omega(|\boldsymbol{\xi}_{ij}^n|) = \exp\left(-\left(\frac{2|\boldsymbol{\xi}_{ij}^n|}{\delta}\right)^2\right) \quad (8.83)$$

where  $V_j^n$  is the volume of family material point  $j$ ,  $N_i$  represents the number of family material points of material point  $i$ .

As a study investigated by Madenci et al. (2019), horizon size in the numerical simulation is chosen as maximum order of differentiation plus one. Since, the maximum order of differentiation is two, the horizon size is chosen as  $3\Delta x$ , in which  $\Delta x$  is spacing between material points at the initial configuration.

The discretized form of the continuity equation is given as

$$\rho_i^{n+1} = \rho_i^n - \rho_i^n \Delta t \sum_{j=1}^{N_i} [\mathbf{g}_1(\xi_{ij}^n) \cdot (\mathbf{v}_j^n - \mathbf{v}_i^n)] V_j^n \quad (8.84)$$

in which  $\rho_i^{n+1}$  is the updated density,  $\Delta t$  is the time step size, and term  $\mathbf{v}_i^n$  and  $\mathbf{v}_j^n$  represent the velocity field of material point  $i$  and  $j$ , respectively.

In addition, the pressure field of the material material point  $i$  at time  $t = t_n$  is computed by equation of state as expressed in Eq.( 8.17 ) as

$$p_i^n = \frac{\rho_{0,i} c_{0,i}^2}{\alpha_i} \left[ \left( \frac{\rho_i^n}{\rho_{0,i}} \right)^{\alpha_i} - 1 \right] + p_{0,i} \quad (8.85)$$

in which  $p_i^n$  is the pressure at the current time step and  $p_{0,i}$  is the background pressure. The background pressure in this study is estimated as

$$p_{0,i} = 0.05 \times \frac{\rho_{0,i} c_{0,i}^2}{\alpha_i} \quad (8.86)$$

Depending on the type of the fluid motion, the numerical speed of sound  $c_{0,i}$  of material points in denser and lighter fluid phase is estimated by using Eq.( 8.21 ) and Eq.( 8.25 ), respectively.

After the pressure field at each material point is computed by Eq.( 8.85 ), the discretized form of the pressure gradient in momentum equation then can be represented as

$$\nabla p_i^n = \sum_{j=1}^{N_i} [(p_j^n - p_i^n) \mathbf{g}_1(\xi_{ij}^n)] V_j^n \quad (8.87)$$

The discretized form of the viscous force in momentum equation can be computed as

$$\mu_i^n \Delta \mathbf{v}_i^n = \sum_{j=1}^{N_i} \mu_i^n \left[ \text{tr} \left( \mathbf{g}_2(\xi_{ij}^n) \right) (\mathbf{v}_j^n - \mathbf{v}_i^n) \right] V_j^n \quad (8.88)$$

The discretized form of the normal surface tension force in momentum equation is calculated from Eq.( 8.68 ) as

$$\begin{aligned} \mathbf{F}_{s,n_i}^n & \quad (8.89) \\ &= -\gamma \frac{\sum_{j=1}^{N_i} \min(N_j, N_i) \left[ \mathbf{g}_1(\xi_{ij}^n) \cdot \left( \varphi_i^j \hat{\mathbf{n}}_{lg_j}^{*n} - \hat{\mathbf{n}}_{lg_i}^{*n} \right) \right] V_j}{\frac{\sum_{j=1}^{N_i} \min(N_j, N_i) \omega(\xi_{ij}^n) V_j}{\sum_{j=1}^{N_i} \omega(\xi_{ij}^n) V_j'}} \hat{\mathbf{n}}_{lg_i}^{*n} \left| \sum_{j=1}^{N_i} \left[ (c_{lg_j}^n - c_{lg_i}^n) \mathbf{g}_1(\xi_{ij}^n) \right] V_j^n \right| \end{aligned}$$

in which  $\gamma$  is the temperature dependent surface tension coefficient and is computed from Eq.( 8.12 ). The term  $c_{lg_j}^n - c_{lg_i}^n$  represents the difference of colour index between a pair of material points, and  $\varphi_i^j$  is the phase normal coefficient.  $\hat{\mathbf{n}}_{lg_i}^{*n}$  is the smoothed interface unit normal, at time  $t = t_n$  this can be expressed as

$$\hat{\mathbf{n}}_{lg_i}^{*n} = \frac{f_{w,i} \hat{\mathbf{n}}_{lg_i}^n + (1 - f_{w,i}) \hat{\mathbf{n}}_{lg,cor_i}^n}{\left| f_{w,i} \hat{\mathbf{n}}_{lg_i}^n + (1 - f_{w,i}) \hat{\mathbf{n}}_{lg,cor_i}^n \right|} \quad (8.90)$$

where  $f_{w,i}$  is the transition function. The ordinary computed unit normal vector,  $\hat{\mathbf{n}}_{lg_i}^n$ , is calculated as

$$\hat{\mathbf{n}}_{lg_i}^n = \frac{\sum_{j=1}^{N_i} \left[ (c_{lg_j}^n - c_{lg_i}^n) \mathbf{g}_1(\xi_{ij}^n) \right] V_j^n}{\left| \sum_{j=1}^{N_i} \left[ (c_{lg_j}^n - c_{lg_i}^n) \mathbf{g}_1(\xi_{ij}^n) \right] V_j^n \right|} \quad (8.91)$$

and the prescribed unit normal vector at triple line region ,  $\hat{\mathbf{n}}_{lg,cor_i}^n$ , is calculated as

$$\hat{\mathbf{n}}_{lg,cor_i}^n = \hat{\mathbf{n}}_{t_i}^n \sin \theta_{eq} - \hat{\mathbf{n}}_{sf_i}^n \cos \theta_{eq} \quad (8.92)$$

with

$$\hat{\mathbf{n}}_{sf_i}^n = \frac{\sum_{j=1}^{N_i} [(c_{sf_j}^n - c_{sf_i}^n) \mathbf{g}_1(\boldsymbol{\xi}_{ij}^n)] V_j^n}{\left| \sum_{j=1}^{N_i} [(c_{sf_j}^n - c_{sf_i}^n) \mathbf{g}_1(\boldsymbol{\xi}_{ij}^n)] V_j^n \right|} \quad (8.93)$$

and

$$\hat{\mathbf{n}}_{t_i}^n(\mathbf{x}) = \frac{\hat{\mathbf{n}}_{lg_i}^n(\mathbf{x}) - \left( \hat{\mathbf{n}}_{lg_i}^n(\mathbf{x}) \cdot \hat{\mathbf{n}}_{sf_i}^n(\mathbf{x}) \right) \hat{\mathbf{n}}_{sf_i}^n(\mathbf{x})}{\left| \hat{\mathbf{n}}_{lg_i}^n(\mathbf{x}) - \left( \hat{\mathbf{n}}_{lg_i}^n(\mathbf{x}) \cdot \hat{\mathbf{n}}_{sf_i}^n(\mathbf{x}) \right) \hat{\mathbf{n}}_{sf_i}^n(\mathbf{x}) \right|} \quad (8.94)$$

in which the term  $c_{sf_j}^n - c_{sf_i}^n$  represents the difference of colour index for distinguishing fluid and solid phase between a pair of material points.  $\theta_{eq}$  is a user predefined equilibrium contact angle before simulation.

$N_i$  is the unit normal index and is calculated as

$$N_i = \begin{cases} 1, & \text{if } \left| f_{w,i} \hat{\mathbf{n}}_{lg_i}^n + (1 - f_{w,i}) \hat{\mathbf{n}}_{lg,cor_i}^n \right| > \epsilon \\ 0, & \text{otherwise} \end{cases} \quad (8.95)$$

The discretized form of the Marangoni force in momentum equation then can be calculated from Eq.( 8.71 ) as

$$\begin{aligned} \mathbf{F}_{s,t_i}^n = \frac{d\gamma(T)}{dT} & \left[ \sum_{j=1}^{N_i} [(T_j^n - T_i^n) \mathbf{g}_1(\boldsymbol{\xi}_{ij}^n)] V_j^n \right. \\ & - \left( \sum_{j=1}^{N_i} [(T_j^n - T_i^n) \mathbf{g}_1(\boldsymbol{\xi}_{ij}^n)] V_j^n \right. \\ & \left. \left. \cdot \hat{\mathbf{n}}_{lg_i}^n \right) \hat{\mathbf{n}}_{lg_i}^n \right] \left| \sum_{j=1}^{N_i} [(c_{lg_j}^n - c_{lg_i}^n) \mathbf{g}_1(\boldsymbol{\xi}_{ij}^n)] V_j^n \right| \end{aligned} \quad (8.96)$$

in which  $\frac{d\gamma(T)}{dT}$  is the surface tension temperature coefficient as shown in Eq.( 8.12 ).

As a result, the discretized form of momentum equation can be represented as

$$\mathbf{a}_i^{n+1} = \frac{1}{\rho_i^{n+1}} \left[ -\nabla p_i^n + \mu_i^n \Delta \mathbf{v}_i^n + \mathbf{F}_{s,n_i}^n + \mathbf{F}_{s,t_i}^n \right] + \frac{1}{\rho_i^{n+1}} \mathbf{b}_i \quad (8.97)$$

where  $\mathbf{a}_i^{n+1}$  is the updated acceleration at  $t = t_{n+1}$  and  $\mathbf{b}_i$  is the body force density. When the density ratio between two fluids is relatively large, the discontinuity of the fluid density and viscosity field will present at the transition band of the interface. As PDDO is a non-local approach, the discontinuity will cause stability issues. In order to reduce numerical oscillations and prevent material points' penetration during the simulation, the density and viscosity coefficient can be smoothed by harmonic means as

$$\rho_i^{n+1} = \frac{2\rho_i^{n+1}\rho_j^{n+1}}{\rho_i^{n+1} + \rho_j^{n+1}} \quad (8.98)$$

and

$$\mu_i^n = \frac{2\mu_i\mu_j}{\mu_i + \mu_j} \quad (8.99)$$

The harmonic means for density and viscosity treatment is validated for multiphase flow fluid motion at low Reynold's number. In the case of the flow motion with high Reynold's number, additional numerical treatments are required (Gao and Oterkus, 2020). In this study, only the flow with low Reynold's number is investigated.

The discretized form of the internal energy equation can be represented as

$$T_i^{n+1} = T_i^n + \frac{\Delta t}{\rho_i^{n+1} C_{p,i}} \left[ \sum_{j=1}^{N_i} k_i^n \left[ \text{tr} \left( \mathbf{g}_2(\boldsymbol{\xi}_{ij}^n) \right) (T_j^n - T_i^n) \right] V_j^n + S_i \right] \quad (8.100)$$

Similarly, to prevent numerical oscillation in energy equation and to have a smooth transition of the heat conductivity coefficient at the interface region, the coefficient  $k_i^n$  in Eq.( 8.100 ) is also smoothed by harmonic means as

$$k_i^n = \frac{2k_i k_j}{k_i + k_j} \quad (8.101)$$

#### 8.4.2 Boundary Conditions

As shown in Fig. 8-6, the boundary conditions are implemented through fictitious layers in the numerical simulation, which is widely adopted in peridynamic studies (Oterkus et al., 2014). Three variables are considered in boundaries, which are velocity, pressure, and temperature.

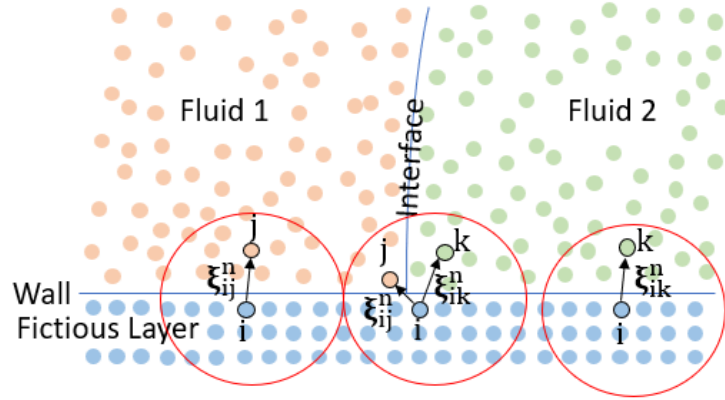


Fig. 8-6 Schematic drawing of interface between two fluids and the boundary material points.

Slip or no-slip velocity boundary conditions are used at wall boundary and implemented by material points in fictitious layers. The velocities of the material points in fictitious layers are computed based on the velocities of material points in the fluid domain. Different methods for implementing these boundary conditions are used in numerical simulations, such as mirroring material points at boundary approach as suggested in Oterkus et al., (2014), so that the variable at a material point in the fictitious layers is mirrored by a material point at the fluid domain. Since the fluid particles are moving during the simulation, instead of mirroring the moving fluid particles, a simplified boundary implementation using weighted average approach is used to keep the material points in the fictitious region at fixed locations (Gao and Oterkus, 2020).

For slip or no-slip velocity boundary conditions, the velocity of material point  $i$  in a fictitious layer at the current time step  $n$  is calculated as

$$\mathbf{v}_i^n = 2\mathbf{v}_{wall} - \varphi_w \frac{\sum_{j=1}^{N_1} \omega_0(\xi_{ij}^n) \mathbf{v}_j^n + \sum_{k=1}^{N_2} \omega_0(\xi_{ik}^n) \mathbf{v}_k^n}{\sum_{j=1}^{N_1} \omega_0(\xi_{ij}^n) + \sum_{k=1}^{N_2} \omega_0(\xi_{ik}^n)} \quad (8.102)$$

with

$$\varphi_w = \begin{cases} 1 & \text{for no - slip boundary condition} \\ -1 & \text{for slip boundary condition with } \mathbf{v}_{wall} = 0 \end{cases} \quad (8.103)$$

in which  $\mathbf{v}_{wall}$  is the wall velocity, the subscripts  $j$  and  $k$  represent the family material points of  $i$  in fluid 1 and fluid 2, respectively. The superscript  $N_1$  and  $N_2$  represents the material point  $i$  in the fictitious layer has  $N_1$  family material points in fluid 1 and  $N_2$  family material points in fluid 2, respectively. The velocity of family material points of  $i$  in fluid 1 and fluid 2 at current time step  $n$  are denoted by  $\mathbf{v}_j^n$  and  $\mathbf{v}_k^n$ , respectively.

The weight function in Eq.( 8.102 ) between a pair of material points is computed as (Colagrossi and Landrini, 2003)

$$\omega_0(\xi_{ij}^n) = \frac{\left( e^{-\left(\frac{|\xi_{ij}^n|}{\Delta x}\right)^2} - e^{-9} \right)}{\Delta x^3 \pi (1 - 10e^{-9})} \quad (8.104)$$

Without considering the gravity force, the pressure of material points in fictitious layers are calculated from the pressure of the material points in fluid domain as (Gao and Oterkus, 2020)

$$p_i^n = \frac{\sum_{j=1}^{N_1} \omega_0(\xi_{ij}^n) p_j^n + \sum_{k=1}^{N_2} \omega_0(\xi_{ik}^n) p_k^n}{\sum_{j=1}^{N_1} \omega_0(\xi_{ij}^n) + \sum_{k=1}^{N_2} \omega_0(\xi_{ik}^n)} \quad (8.105)$$

in which  $p_j^n$  and  $p_k^n$  are the pressure of family material points of  $i$  in fluid 1 and fluid 2 at current time step  $n$ .

Dirichlet and Neuman temperature boundary conditions are also implemented by material points in fictitious layers. With the analogous ideas of computing velocity and pressure for material points at fictitious layers, the temperature of material point  $i$  at current time step  $n$  is computed from its family material points temperature  $T_j^n$  and  $T_k^n$  in fluid 1 and fluid 2 as

$$T_i^n = 2T_{wall} - \varphi_T \frac{\sum_{j=1}^{N_1} \omega_0(\xi_{ij}^n) T_j^n + \sum_{k=1}^{N_2} \omega_0(\xi_{ik}^n) T_k^n}{\sum_{j=1}^{N_1} \omega_0(\xi_{ij}^n) + \sum_{k=1}^{N_2} \omega_0(\xi_{ik}^n)} \quad (8.106)$$

with

$$\varphi_T = \begin{cases} 1 & \text{for Dirichlet boundary condition} \\ -1 & \text{for Neuman boundary condition with } T_{wall} = 0 \end{cases} \quad (8.107)$$

in which  $T_{wall}$  is the wall temperature.

#### 8.4.3 Time Stepping Scheme

The momentum equation is integrated explicitly in time using Velocity Verlet scheme as (Adami et al., 2013)

$$\mathbf{v}_i^{n+1} = \mathbf{v}_i^n + \frac{1}{2}(\mathbf{a}_i^{n+1} + \mathbf{a}_i^n)\Delta t \quad (8.108)$$

and the displacement field at each material point in fluid domain is updated by

$$\mathbf{u}_i^{n+1} = \mathbf{u}_i^n + \mathbf{v}_i^n \Delta t + \frac{1}{2} \mathbf{a}_i^n \Delta t^2 \quad (8.109)$$

As a result, the updated location of the material points can be found as

$$\mathbf{x}_i^{n+1} = \mathbf{x}_i^0 + \mathbf{u}_i^{n+1} \quad (8.110)$$

in which the superscript 0 represents at time step  $n = 0$ .

To maintain the numerical stability in time integration, the time step size  $\Delta t$  is constrained by the Courant–Friedrichs–Lewy (CFL) condition (Courant et al., 1928). The CFL condition in time integration is based on several conditions. The time step size for numerical speed of sound condition is (Adami et al., 2013)

$$\Delta t_s \leq 0.25 \frac{\Delta x}{c_{max} + |\mathbf{v}_{max}|} \quad (8.111)$$

in which  $c_{max}$  is the maximum numerical speed of sound among all phases. The estimation of numerical speed of sound in each fluid phase is provided in Eq.( 8.21 ) and Eq.( 8.25 ), and  $\mathbf{v}_{max}$  is the maximum velocity in the simulation domain.

The time step size for viscous condition is constrained as (Adami et al., 2013)

$$\Delta t_v \leq 0.125 \frac{\Delta x^2}{\left(\frac{\mu}{\rho_0}\right)_{max}} \quad (8.112)$$

where  $\left(\frac{\mu}{\rho_0}\right)_{max}$  is the maximum kinematic viscosity among all phases.

The time step size for body force condition is applied as (Adami et al., 2013)

$$\Delta t_b \leq 0.25 \sqrt{\frac{\Delta x}{g}} \quad (8.113)$$

in which  $g$  is the gravity acceleration.

The time step size for surface tension condition is implemented as (Adami et al., 2010)

$$\Delta t_{sf} \leq 0.25 \sqrt{\frac{\rho_0 \Delta x^3}{2\pi\gamma}} \quad (8.114)$$

In addition, the time step size in thermal analysis is restricted as (Cleary, 1988)

$$\Delta t_t \leq 0.125 \frac{\rho_0 C_p \Delta x^2}{k} \quad (8.115)$$

In processing the numerical time integration, the time step size is chosen as the minimum of above criteria as

$$\Delta t = \min\{\Delta t_v, \Delta t_b, \Delta t_{sf}, \Delta t_t\} \quad (8.116)$$

#### 8.4.4 Material Points Shifting Technique

Since distorted material points induce stability issues in processing the numerical integration (Xu et al., 2009), the position shifting technique is applied at material points at each time step in fluid domain to avoid clustering problems. The application of position shifting technique is introduced in Gao and Oterkus, (2020) for PDDO. At each time step, the displacement for each material point in fluid domain  $\mathbf{u}_i^{n+1}$  is corrected by a shifted distance  $(\Delta \mathbf{u}_i^{n+1})^*$ , which is represented as

$$(\mathbf{u}_i^{n+1})^* = \mathbf{u}_i^{n+1} + (\Delta \mathbf{u}_i^{n+1})^* \quad (8.117)$$

The shifting distance is defined as (Gao and Oterkus, 2020)

$$(\Delta \mathbf{u}_i^{n+1})^* = C \alpha_{MPST} \mathbf{U}_i \quad (8.118)$$

in which  $\mathbf{U}_i$  is the displacement shifting vector. To ensure the shifted distance can sufficiently prevent the instability and do not cause accuracy issues, the constant  $C$  is typically taken between 0.01-0.1. The shifting magnitude  $\alpha_{MPST}$  is set as (Xu et al., 2009)

$$\alpha_{MPST} = v_{max} \Delta t \quad (8.119)$$

In addition, the displacement shifting vector in Eq.( 8.118 ) is provided as (Gao and Oterkus, 2020)

$$\mathbf{U}_i = \sum_j^{N_i} \frac{\bar{\xi}_i^{-2}}{|\xi_{ij}^n|^2} \xi_{ij}^n \quad (8.120)$$

The summation of distance vectors in Eq.( 8.120 ) describes the anisotropy of the spacing between material points, and  $\frac{\bar{\xi}_i^{-2}}{|\xi_{ij}^n|^2}$  is used as a weight function to evaluate the influence from material point  $j$ . The averaged material points spacing  $\bar{\xi}_i$  in Eq.( 8.120 ) is defined as (Xu et al., 2009)

$$\bar{\xi}_i = \frac{1}{N_i} \sum_j^{N_i} |\xi_{ij}^n| \quad (8.121)$$

#### 8.4.5 Moving Least Square Method

In Lagrangian method, the position of material points is tracked and updated at each time step. When position of material points in the fluid domain changes continuously, the number of family material points may decrease. In this case, the calculated density may be smaller than normal. Therefore, the equation of state predicts wrong pressure values, leading to a gradual deterioration of the entire field (Dilts, 1999). To avoid mass conservation issues, and oscillations at the density, pressure, and velocity of

material points at fluid domain are smoothed using moving least square method (Dilts, 1999).

The velocity field in the fluid domain is smoothed as (Gao and Oterkus, 2020)

$$(\mathbf{v}_i^n)^{smoothed} = \frac{\sum_j^{N_i} \mathbf{v}_j^n \omega_{MLS}(\boldsymbol{\xi}_{ij}^n) V_j^n}{\sum_j^{N_i} \omega_{MLS}(\boldsymbol{\xi}_{ij}^n) V_j^n} \quad (8.122)$$

The pressure field in the fluid domain is smoothed as (Gao and Oterkus, 2020)

$$(p_i^n)^{smoothed} = \frac{\sum_j^{N_i} p_j^n \omega_{MLS}(\boldsymbol{\xi}_{ij}^n) V_j^n}{\sum_j^{N_i} \omega_{MLS}(\boldsymbol{\xi}_{ij}^n) V_j^n} \quad (8.123)$$

The density field in the fluid domain is smoothed as (Gao and Oterkus, 2020)

$$(\rho_i^n)^{smoothed} = \frac{\sum_j^{N_i} \bar{\rho}_j^n \omega_{MLS}(\boldsymbol{\xi}_{ij}^n) V_j^n}{\sum_j^{N_i} \omega_{MLS}(\boldsymbol{\xi}_{ij}^n) V_j^n} \quad (8.124)$$

with

$$\bar{\rho}_j^n = \left[ \frac{(p_j^n - p_{0,j}) \alpha_j}{\rho_{0,j} c_{0,j}^2} + 1 \right]^{\frac{1}{\alpha_i}} \rho_{0,i} \quad (8.125)$$

The weight function,  $\omega_{MLS}$ , for smoothing variables in above equations at fluid domain is provided as (Colagrossi and Landrini, 2003)

$$\omega_{WLS}(\boldsymbol{\xi}_{ij}^n) = [\beta_0(\mathbf{x}_i^n) + \beta_1(\mathbf{x}_i^n)(-\xi_{ij}^{1n}) + \beta_2(\mathbf{x}_i^n)(-\xi_{ij}^{2n})] \omega_0(\boldsymbol{\xi}_{ij}^n) \quad (8.126)$$

in which

$$\boldsymbol{\beta}(\mathbf{x}_i^n) = \begin{pmatrix} \beta_0(\mathbf{x}_i^n) \\ \beta_1(\mathbf{x}_i^n) \\ \beta_2(\mathbf{x}_i^n) \end{pmatrix} = \mathbf{S}^{-1}(\mathbf{x}_i^n) \begin{bmatrix} 1 \\ 0 \\ 0 \end{bmatrix} \quad (8.127)$$

and

$$\mathbf{S}(\mathbf{x}_i^n) = \sum_j^{N_i} \omega_0(\xi_{ij}^n) \begin{bmatrix} 1 & -\xi_{ij}^{1n} & -\xi_{ij}^{2n} \\ -\xi_{ij}^{1n} & (\xi_{ij}^{1n})^2 & \xi_{ij}^{1n} \xi_{ij}^{2n} \\ -\xi_{ij}^{2n} & \xi_{ij}^{1n} \xi_{ij}^{2n} & (\xi_{ij}^{2n})^2 \end{bmatrix} \quad (8.128)$$

In addition, to reduce the numerical computation time, the velocity, pressure and density field only being corrected over a period of time steps by using moving least square method, and this is optional in numerical simulation. For benchmark cases moving least square method is used for dynamic cases (Section 8.5.1, 8.5.3 and 8.5.5), however this method is not needed for static cases (Section 8.5.2 and 8.5.4).

### 8.5 Numerical Simulations

In this section, five numerical cases are considered by using the developed PDDO for modelling the surface tension forces in multiphase fluid flow motion. First, a two-dimensional square droplet deformation is studied to examine the non-local form of surface tension force model in normal direction. Second, when fluid flow is in contact with a solid surface, the difference between unit normal vectors at the triple line region before and after using the unit normal vector prescription scheme are compared through a static droplet wetting case. Third, simulation of droplet contact angle development on a solid surface is performed to show the effect of prescribed normal vectors at the triple line region. Afterwards, capillary stresses tangential to the interface are computed under a heat conduction phenomenon to validate the non-local form of the Marangoni force formulation. Finally, a two-dimensional droplet migration in a thermocapillary flow is presented to test the combination of the surface tension forces in the normal direction and the tangential direction. The predicted migration velocity of the circular droplet in the thermocapillary flow is compared with the volume of fluid method.

#### 8.5.1 Droplets Deformation

In the first case, a two-dimensional square droplet deformation is conducted to validate the surface tension force model by using PDDO. As shown in Fig. 8-7(a), the square droplet with dimensions of 0.6 m × 0.6 m is filled with fluid 2 and surrounded by fluid 1. The fluid domain has a box of size  $L = W = 1$  m. The density for fluid 1 and fluid 2 are specified as  $\rho_1 = 10 \text{ kg/m}^3$  and  $\rho_2 = 1 \text{ kg/m}^3$ , respectively. Fluid 1 has a

viscosity coefficient of  $\mu_1 = 1 \text{ Pa} \cdot \text{s}$  while fluid 2 has  $\mu_2 = 0.2 \text{ Pa} \cdot \text{s}$ . The surface tension coefficient between fluid 1 and fluid 2 is independent with the temperature and chosen as  $\gamma = 1 \text{ N/m}$ .

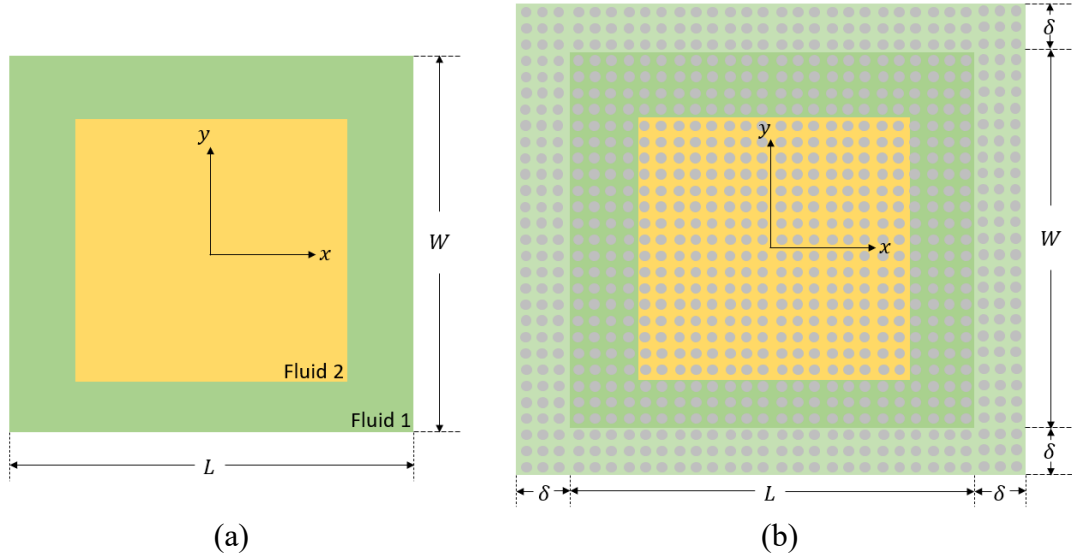


Fig. 8-7 Investigation of square droplet deformation (a) geometry (b) PDDO discretisation.

The fluid is initially at rest for which the initial condition can be illustrated as

$$u = 0, v = 0 \text{ at } t = 0 \quad (8.129)$$

No-slip boundary conditions are applied at four edges of the fluid 1 as

$$v_x = v_y = 0 \text{ at } x = -\frac{L}{2}, x = \frac{L}{2}, y = -\frac{W}{2}, y = \frac{W}{2} \quad (8.130)$$

In processing the numerical simulation, as shown in Fig. 8-7(b), three layers for fictitious material points are wrapped along the edges of the fluid domain. No-slip boundary conditions are implemented on these fictitious material points by using Eq.( 8.102 ) - Eq.( 8.103 ) with  $\mathbf{v}_{wall} = 0 \text{ m/s}$ . The pressure field for fictitious material points is computed by using Eq.( 8.105 ).

The deformation of the square droplet is driven by surface tension force, which transforms square droplet in a circular shape at equilibrium state. With incompressibility hypothesis, the radius of the final circular droplet can be estimated as

$$R = \frac{0.6}{\sqrt{\pi}} \approx 0.034 \text{ m} \quad (8.131)$$

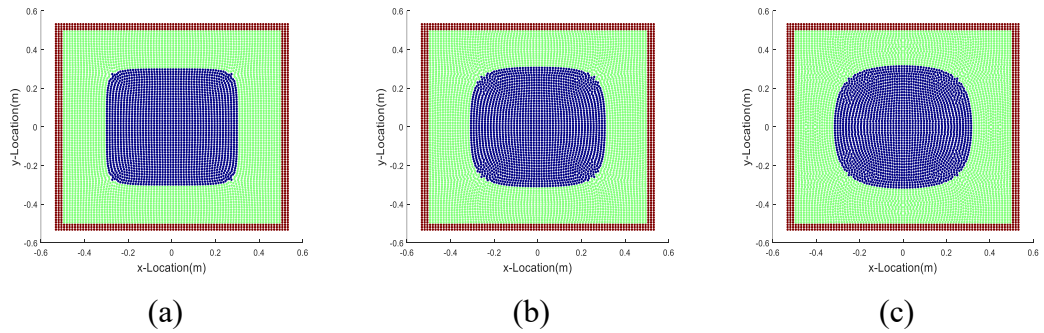
Therefore, the pressure changes  $\Delta p$  between fluid 1 and fluid 2 can be estimated by using Young-Laplace equation as

$$\Delta p = \frac{\gamma}{R} \approx 2.94 \text{ Pa} \quad (8.132)$$

As introduced in section 8.2.3, the incompressible fluid motion is constrained by a weakly compressible equation of state, and the numerical speed of sound in the equation of state is computed based on the pressure change. As a result, the numerical speed of sound for fluid 1 can be estimated by using Eq.( 8.21 ), and the numerical speed of sound for fluid 2 can be obtained by Eq.( 8.25 ). In this case, numerical speed of sound for fluid 1 is taken as  $c_1 = 6 \text{ m/s}$ , and for fluid 2 as  $c_2 = 18.97 \text{ m/s}$ .

As shown in Fig. 8-7(b), the fluid domain is discretised with a uniform spacing of  $\Delta x = 0.0125 \text{ m}$ . The horizon size is selected as  $\delta = 3\Delta x$ . Simulation is processed for a total time of  $t = 2.56 \text{ s}$  and the time step size is set as  $\Delta t = 8 \times 10^{-5} \text{ s}$ . The displacement field of the material points in fluid domain is obtained by velocity Verlet scheme.

In addition, the moving least square method introduced in section 8.4.5 is used to correct the density, pressure, and velocity field at fluid domain at every 20-time steps. In order to obtain a smooth distribution of material points in the fluid domain, the material points shifting technique is utilized in every time step of the simulation to smooth the displacement field. The constant  $C$  is taken as 0.01 in this case.



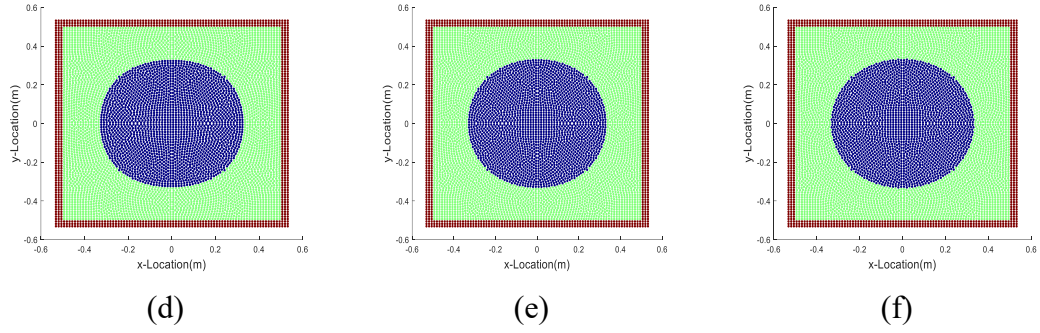


Fig. 8-8 Evolution of droplet deformation at (a)  $t = 0.128$  s, (b)  $t = 0.384$  s, (c)  $t = 0.64$  s, (d)  $t = 1.28$  s, (e)  $t = 1.92$  s, (f)  $t = 2.56$  s.

Fig. 8-8 shows the snapshots of the droplet transformation from square shape to circular shape. As can be observed from Fig. 8-8(f), at the final state, the droplet has an average radius of 0.0338 m, which is close to the estimated value given in Eq.( 8.131 ). The time history of average pressure difference between fluid 1 and fluid 2 is presented in Fig. 8-9(a). As can be observed from the figure, the pressure difference reaches an equilibrium state after  $t = 1.5$  s. The pressure changes  $\Delta p$  between fluid 1 and fluid 2 predicted by PDDO shows a close agreement with the analytical solution as computed by Eq.( 8.132 ). The final pressure profile of the fluid domain at  $t = 2.56$  s is presented in Fig. 8-9(b). The square droplet transforms into a circular shape with a smooth material point distribution, and the pressure difference between droplet and surrounding fluids match with the analytical value from Young-Laplace equation. It can be concluded that the current surface tension model utilizing the PDDO can accurately capture the surface tension effect in the normal direction in multiphase flow.

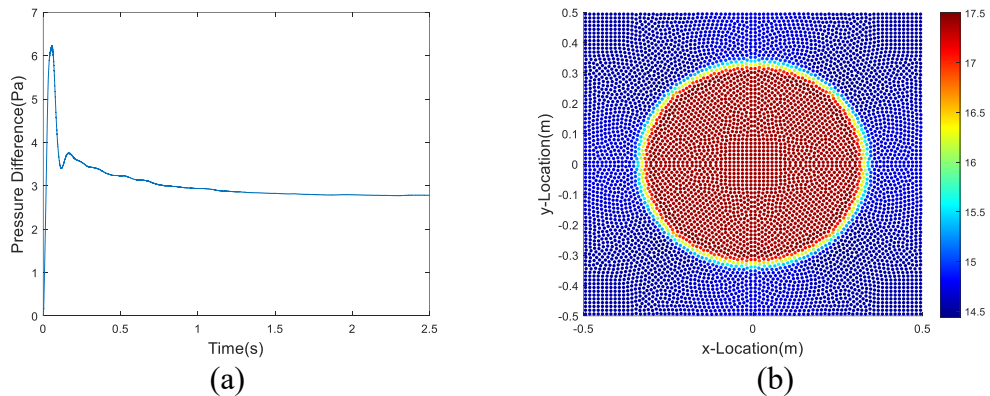
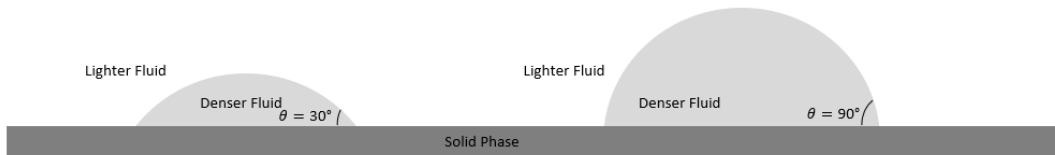


Fig. 8-9 Pressure profile (a) time history of pressure difference between the droplet and surrounding fluid (b) distribution at  $t=2.56$  s.

### 8.5.2 Unit Normal Vector Correction at Triple Line Region

The first case demonstrates the effectiveness of surface tension force model in normal direction. However, this only validates the case when fluid 2 is fully surrounded by fluid 1. When both fluids are in contact with a solid interface, additional processing of the unit normal vectors between the two fluids at the triple line region is required to prevent curvature errors. As shown in Fig. 8-10, this section uses cases of droplets forming two different contact angles on a solid surface to demonstrate the difference between the unit normal vectors obtained before and after normal prescription scheme at triple line region.



*Fig. 8-10 Demonstration of two droplets lying on a solid surface with 30° contact angle and 90° contact angle.*

As shown in Fig. 8-11, two denser fluid droplets with radius  $r = 0.0125$  m are surrounded by lighter fluid, and they are both being placed in a rectangular box. The box has a size of 0.1 m in length and 0.05 m in width. The density for denser fluid is  $\rho_1 = 1000$  kg/m<sup>3</sup> and for lighter fluid is  $\rho_2 = 1.2$  kg/m<sup>3</sup>. Two denser fluid droplets contact with the solid surface and form a contact angle of 30° and 90°, respectively. The spacing between material point is set as  $\Delta x = 0.0013$  m.

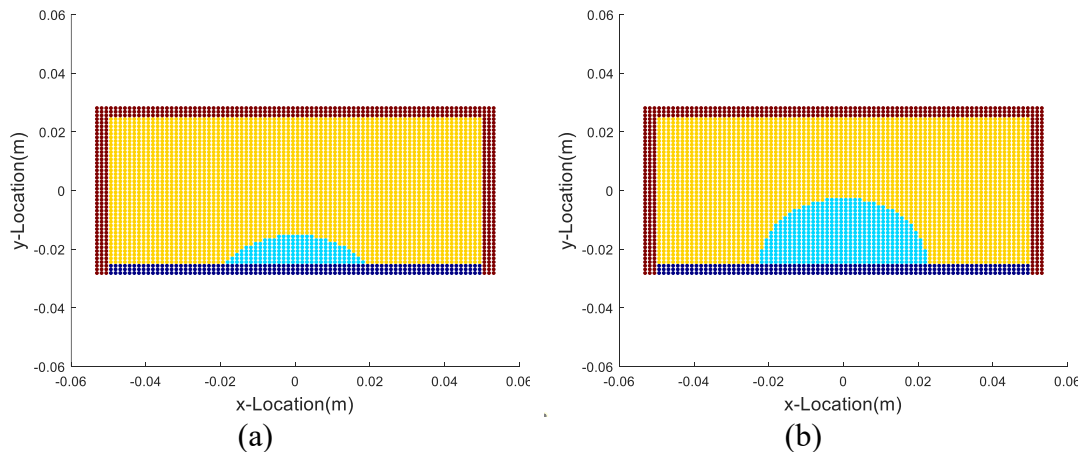


*Fig. 8-11 PDDO discretisation of droplet contact on solid interface (a) 30° contact angle (b) 90° contact angle.*

The unit normal vectors between the denser and lighter fluid domains, calculated according to Eq.( 8.52 ), are shown in Fig. 8-12. It can be observed that in the case of a  $30^\circ$  contact angle, the unit normal vectors  $\hat{n}_{lg}$  at the triple line region in the lighter fluid domain is pointed towards the wrong direction. The issues are also reflected in the  $90^\circ$  contact angle case. This is because, at the triple line region, there are not enough family material points to contribute to the integral equation when computing the unit normal for the lighter fluid. Therefore, incorrect unit normal vectors will result in incorrect curvature calculations and affect the surface tension force modelling.

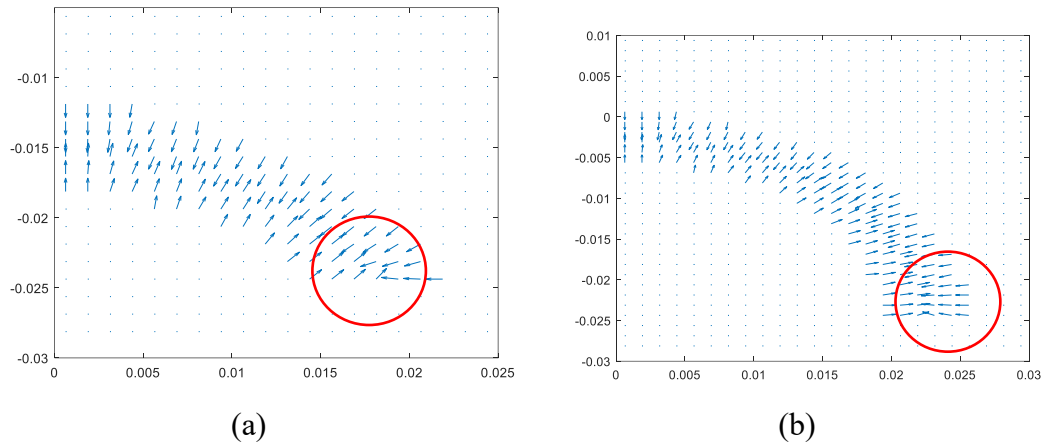


Fig. 8-12 The unit normal vectors between fluid domains before correction (a)  $30^\circ$  contact angle (b)  $90^\circ$  contact angle.

Considering that the same droplet forms contact angles of  $30^\circ$  and  $90^\circ$ , respectively, the prescription normal vectors  $\hat{n}_{lg,cor}$  at triple line region computed based on Eq.( 8.54 ), and interface unit normal vectors  $\hat{n}_{lg}$  not at the triple line region obtained based on Eq.( 8.52 ) are presented in Fig. 8-13.

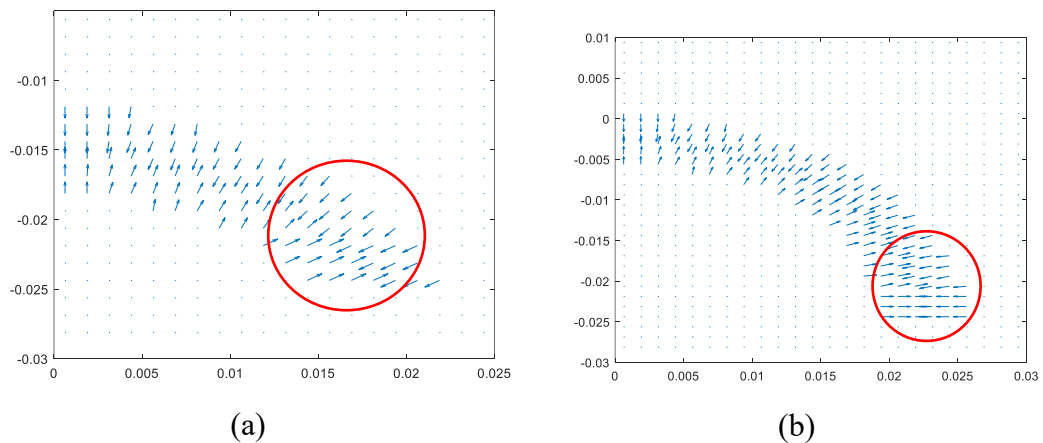


Fig. 8-13 The corrected unit normal vectors at triple line region (a)  $30^\circ$  contact angle (b)  $90^\circ$  contact angle.

As shown in Fig. 8-13, while the incorrect unit normal vectors at the triple line region are resolved in both contact angle cases, a sharper transition is observed between the two types of unit normal vectors. Therefore, calculating the curvature of the interface remains problematic.

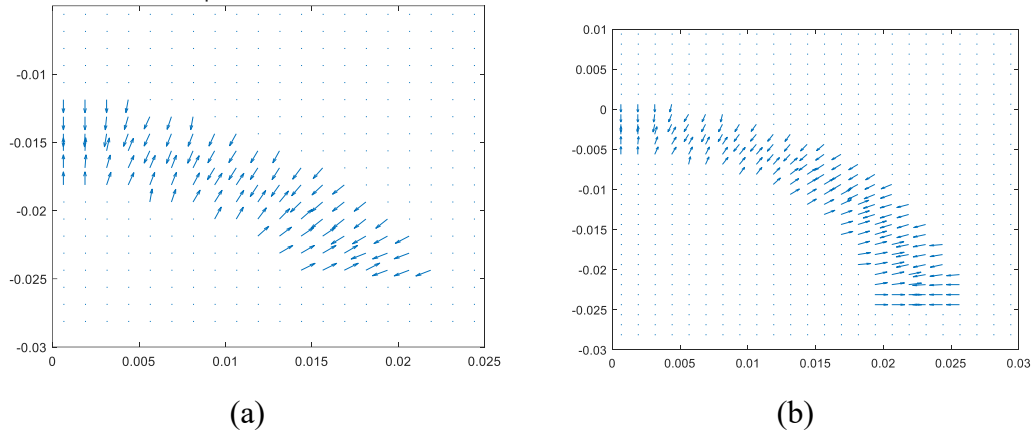


Fig. 8-14 Smoothed unit normal vectors at fluid interface (a)  $30^\circ$  contact angle (b)  $90^\circ$  contact angle.

In order to prevent discontinuity of the unit normal vectors not at the triple line region, the unit normal vectors at the triple line region are smoothed according to Eq.( 8.59 ). The unit normal vectors between denser and lighter fluid domains after smoothing are presented in Fig. 8-14. As can be observed, the unit normal vectors close to the triple line region comply with the corrected unit normal vector  $\hat{n}_{lg,cor}$  while far from the triple line region unit normal vector is computed from  $\hat{n}_{lg}$ . When the instantaneous contact angle  $\theta$  formed by a droplet contacting a solid surface is not equal to the equilibrium contact angle  $\theta_{eq}$ , the curvature creates a force to move the triplet until the equilibrium contact angle is reached.

### 8.5.3 Static Contact Angle Development

After demonstrating the influence of treatment for unit normal vectors at the triple line region, in this section, a two-dimensional liquid droplet deformation on a rigid wall is investigated to study the characteristics of droplet wetting in different stages. As shown in Fig. 8-15(a), a rectangular liquid droplet with a dimension of  $2.25 \times 10^{-2} \text{ m}^2$  in length and  $1.25 \times 10^{-2} \text{ m}^2$  in width is placed in a rectangular box with a dimension of  $0.1 \times 0.05 \text{ m}^2$ . The liquid droplet on the wall is surrounded by gas fluids. The density and viscosity coefficient of the gas phase are specified as  $\rho_1 = 1.2 \text{ kg/m}^3$  and  $\mu_1 = 1 \times 10^{-3} \text{ Pa} \cdot \text{s}$ , respectively. The density and viscosity coefficient for liquid is

set as  $\rho_2 = 1000 \text{ kg/m}^3$  and  $\mu_2 = 3.16 \times 10^{-5} \text{ Pa} \cdot \text{s}$ , respectively. To focus on the physical characteristics of droplet wetting, the surface tension coefficient between liquid and gas fluids is chosen as  $\gamma = 0.07 \text{ N/m}$ , which is independent of the temperature variation.

The fluid gravitational acceleration is disregarded in this example. The initial condition of the fluid is provided as

$$u = 0, v = 0 \text{ at } t = 0 \quad (8.133)$$

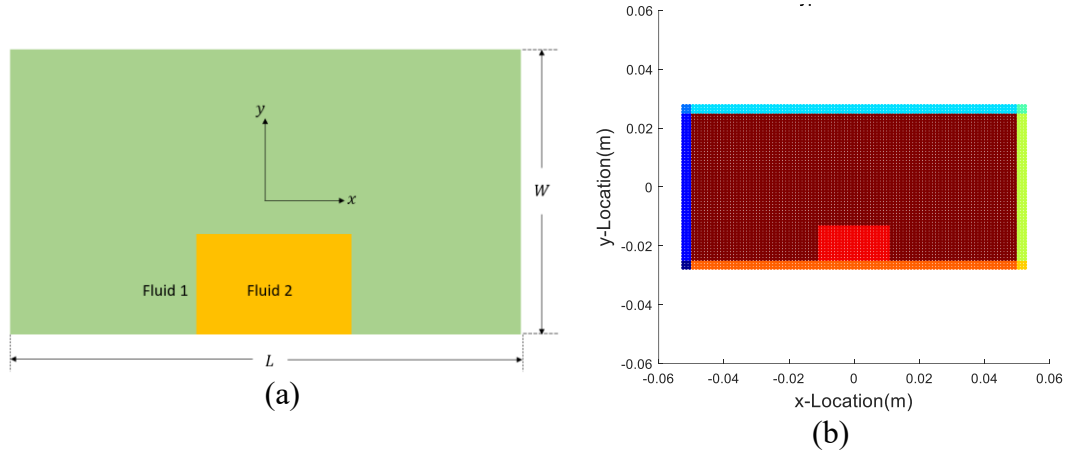


Fig. 8-15 Investigation of square droplet wetting on a solid surface (a) geometry of the fluid domain (b) PDDO discretisation of the simulation domain.

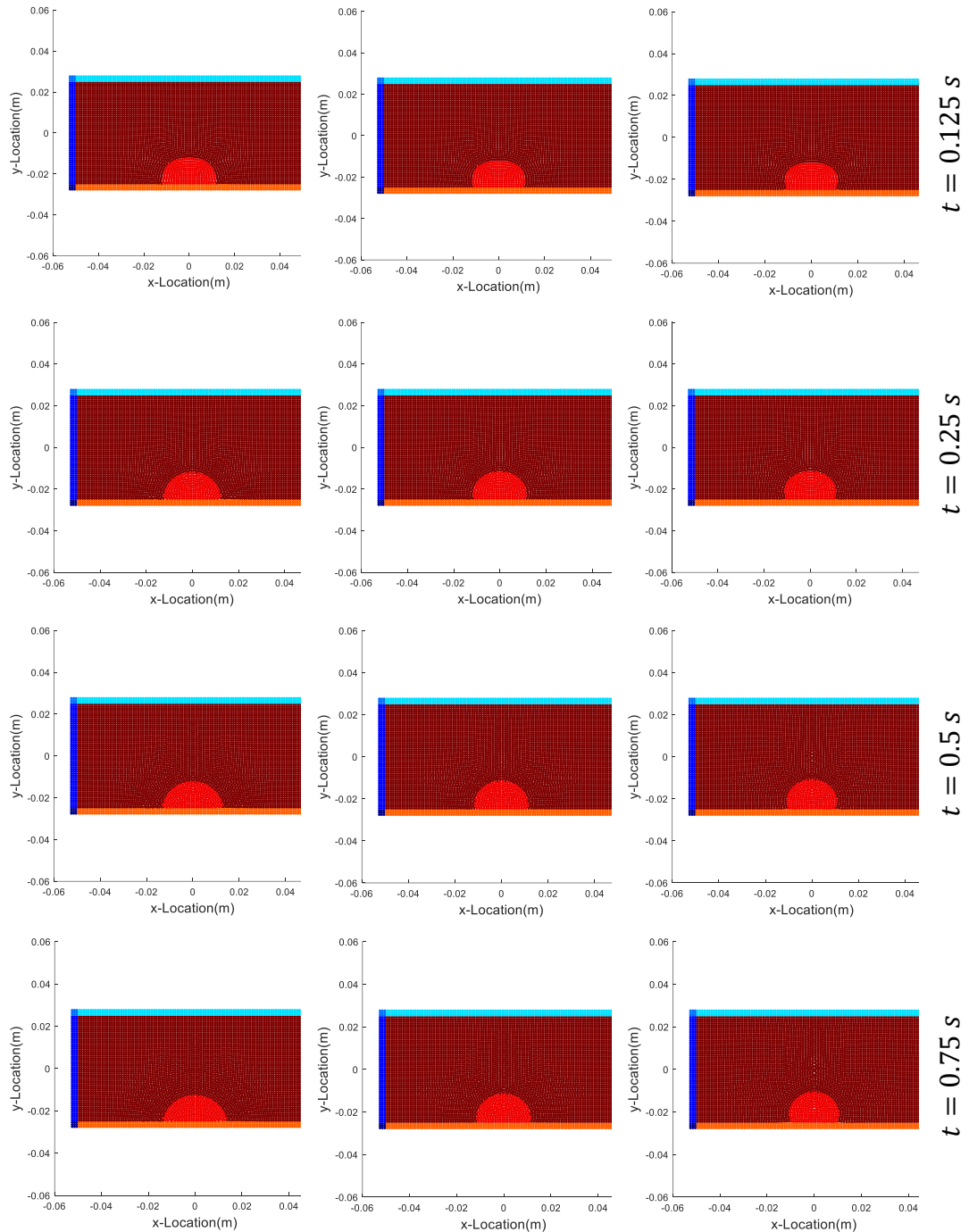
Fig. 8-15(b) shows the numerical simulation domain. The domain is discretized with a uniform spacing of  $\Delta x = 1.0 \times 10^{-3} \text{ m}$ . The horizon size is chosen as  $\delta = 3\Delta x$ . The material points in the fluid 1 and fluid 2 are presented in dark red and red, respectively. The gas and liquid fluid are wrapped by three layers of fictitious material points while the rigid solid wall boundary is presented in orange colour. The no-slip boundary conditions are implemented as

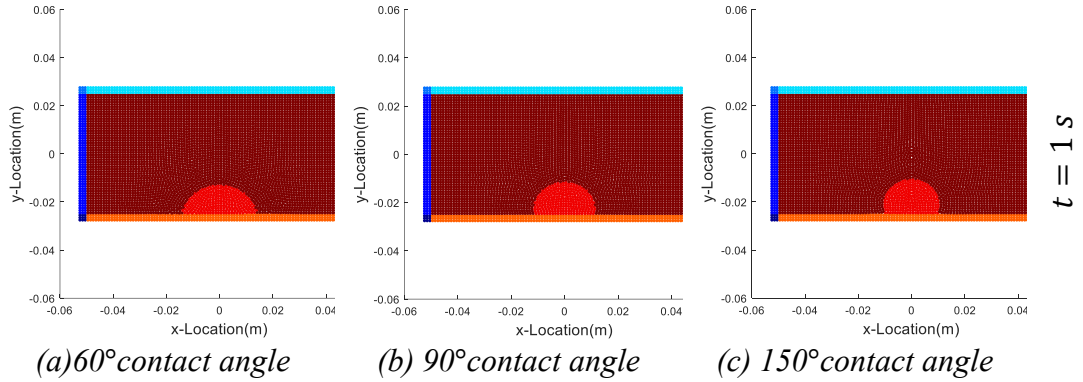
$$v_x = v_y = 0 \text{ at } x = -\frac{L}{2}, x = \frac{L}{2}, y = -\frac{W}{2}, y = \frac{W}{2} \quad (8.134)$$

Therefore, the velocities at fictitious material points are computed based on Eq.( 8.102 ) - Eq.( 8.103 ) with  $v_{wall} = 0 \text{ m/s}$ . The pressure field at fictitious material points is calculated according to Eq.( 8.105 ).

The time step size is set as  $\Delta t = 5 \times 10^{-5} \text{ s}$  with a total simulation time of  $t = 1 \text{ s}$ . The displacement field of the material points in fluid domain is acquired by using

velocity Verlet scheme. In this case, the moving least squares technique is applied in the simulation every 20 steps to smooth the velocity, pressure, and density fields. In addition, the material points shifting technology is used in the simulation, and the constant  $C$  in Eq.( 8.118 ) is taken as 0.01 to ensure the smooth distribution of material points at each time step.





(a)  $60^\circ$  contact angle      (b)  $90^\circ$  contact angle      (c)  $150^\circ$  contact angle  
 Fig. 8-16 Evolution of liquid droplet wetting on a solid surface for various contact angles.

Fig. 8-16 presents snapshots of the two-dimensional liquid droplet formation on the solid wall for three different cases  $\theta_{eq} = 60^\circ$  (hydrophilic wetting),  $\theta_{eq} = 90^\circ$  and  $\theta_{eq} = 150^\circ$  (hydrophobic wetting). The droplet initially stays as a rectangular shape. The unit normal vectors between the gas and liquid phases at the triple line region are corrected and smoothed based on the prescribed equilibrium contact angle by using Eq.( 8.59 ). The unit normal vectors form a smooth curvature at the interface between gas and liquid. The curvature obtained from the corrected unit normal vectors induced a force along the fluid interface to deform the droplet until the prescribed equilibrium contact angle is reached.

#### 8.5.4 Capillary Stress Tangential to Interface

After investigating the surface tension force in normal direction, in this section, the developed non-local Marangoni force formulation is examined by considering a heat conduction test case. As shown in Fig. 8-17(a), two-layered fluids are placed in a square simulation domain with 5.75 mm in length and width. The heat conduction and Marangoni force at the fluid interface are simulated by using the developed PDDO model. The left and right sides of the fluid domain are filled with liquid 1 and liquid 2, respectively. Two fluids have identical density and viscosity coefficients as  $\rho_1 = \rho_2 = 250 \text{ kg/m}^3$  and  $\mu_1 = \mu_2 = 0.012 \text{ Pa} \cdot \text{s}$ . The specific heat capacity and heat conduction coefficient for fluid 1 and fluid 2 are taken as  $c_{p1} = c_{p2} = 0.5 \times 10^{-4} \text{ J/kgK}$  and  $k_1 = k_2 = 1.2 \times 10^{-6} \text{ W/mK}$ . As this case focuses on verifying the heat conduction and Marangoni force models, only the energy equation is involved in this model, and the Marangoni force is numerically computed by using PDDO based on Eq.( 8.16 ). In addition, the surface tension coefficient is a temperature dependent

property which is given in Eq.( 8.12 ), in which the surface tension temperature coefficient is chosen to be  $\frac{d\gamma(T)}{dT} = 0.002 \text{ N/mK}$ .

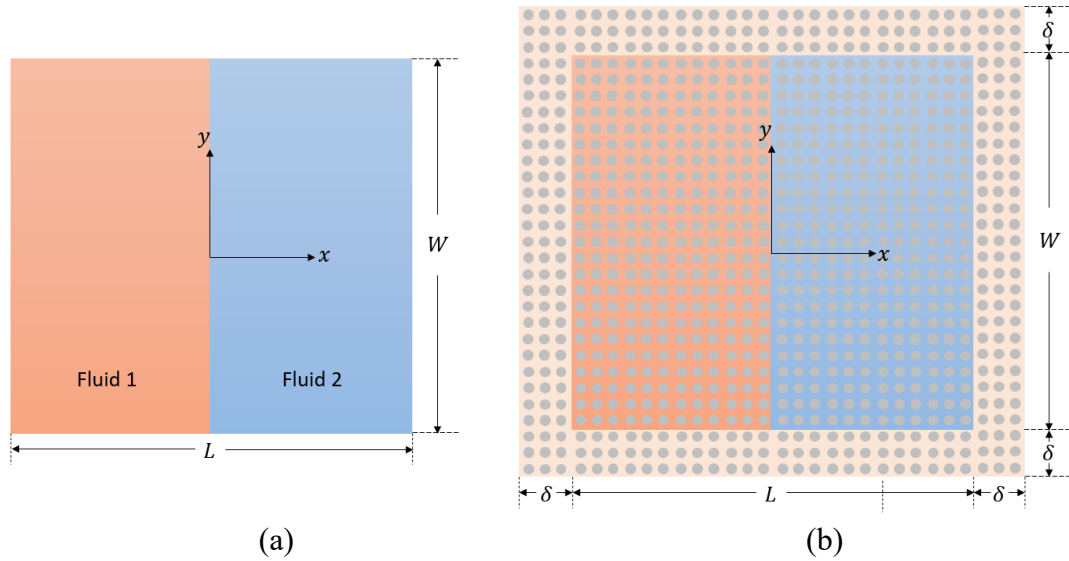


Fig. 8-17 Investigation of Marangoni force at the interface between two fluids (a) geometry (b) PDDO discretisation.

The time step size is chosen as  $\Delta t = 1 \times 10^{-5} \text{ s}$ , and the total simulation time is  $t = 0.1 \text{ s}$ .

At the initial state, the temperature distribution of the fluid domain is set to zero as

$$T = 0 \text{ at } t = 0 \quad (8.135)$$

The boundary conditions are implemented by using the fictitious layers as shown in Fig. 8-17(b) and defined as

$$T = 0 \text{ K at } y = -\frac{W}{2} \quad (8.136)$$

$$T = 1.152 \text{ K at } y = \frac{W}{2}$$

$$\frac{\partial T}{\partial x} = 0 \text{ at } x = -\frac{L}{2} = \frac{L}{2}$$

In order to accurately capture the Marangoni force distribution at the interface, the heat conduction model is first examined with a mesh size of  $\Delta x = 9.0 \times 10^{-5} \text{ m}$ . The horizon size is chosen as  $\delta = 3\Delta x$ . The temperature distribution predicted by using

PDDO at  $t = 0.1$  s is compared with ANSYS and presented in Fig. 8-18. A good agreement is observed between the two methods, which validates the heat conduction model. In addition, as can be computed from the temperature field and the analytical solution, a temperature gradient of  $\nabla T = 200$  K/m is distributed along the width of the simulation domain. As a result, Marangoni force is developed vertically at the interface. The theoretical Marangoni force distributed along the interface is computed as  $f_{s,t} = \nabla_s \gamma = 0.4$  N/m<sup>2</sup>.

The Marangoni force is examined under different spacings between material points, in which the mesh size is chosen as  $\Delta x = 1.8 \times 10^{-4}$  m,  $\Delta x = 9.0 \times 10^{-5}$  m and  $\Delta x = 4.5 \times 10^{-5}$  m. Fig. 8-19 presents Marangoni force vectors distributed along the interface by using a mesh size of  $\Delta x = 9.0 \times 10^{-5}$  m. The profile of the Marangoni force vectors is perpendicular to the interface. As the continuum surface force method is adopted in the model, the volume Marangoni force is smoothed and distributed symmetrically along the transition band of the fluid interface.

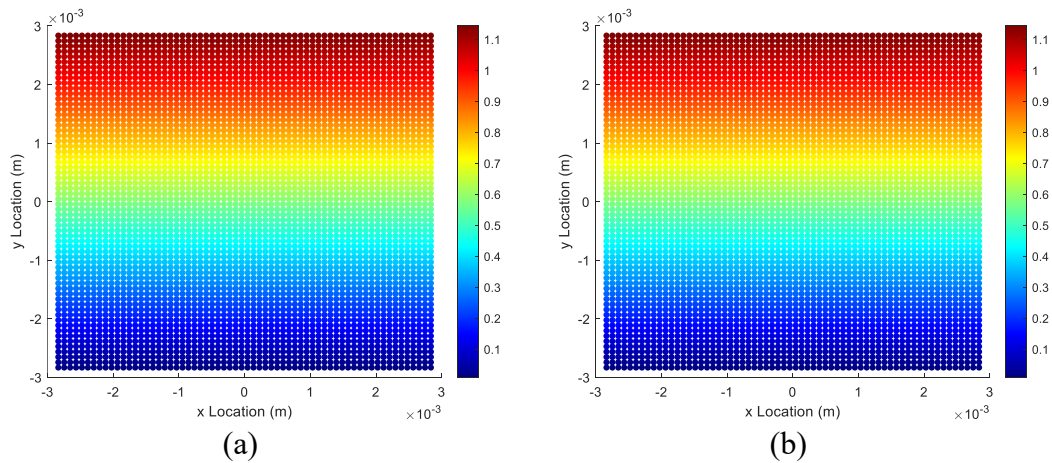
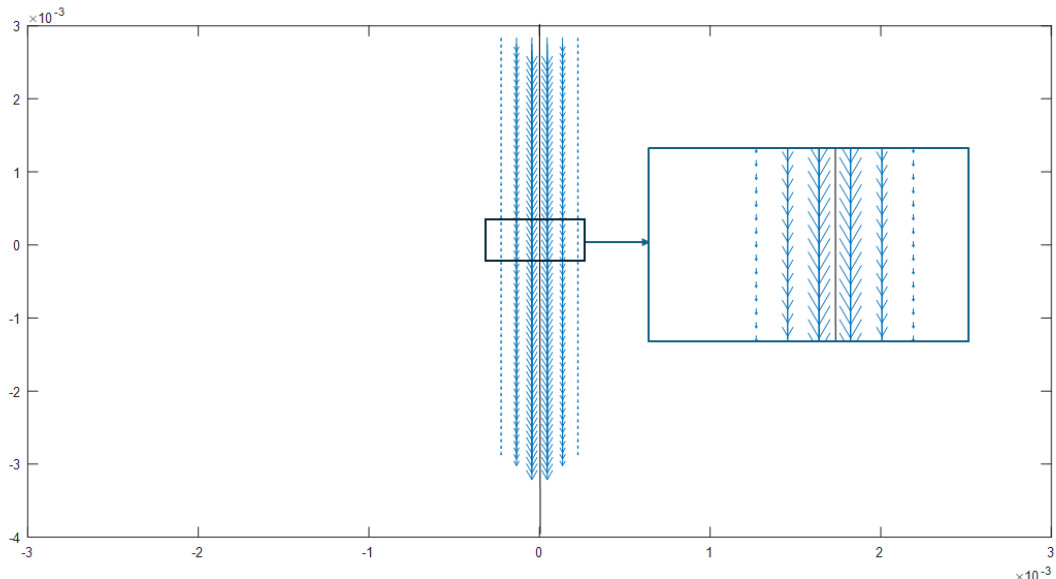
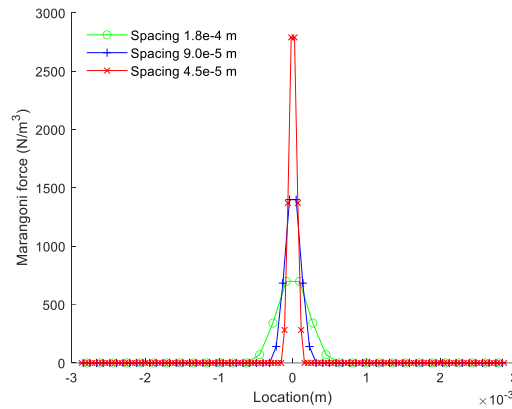


Fig. 8-18 Temperature distribution of the simulation domain at  $t=0.1$  s (a)PDDO (b)ANSYS.



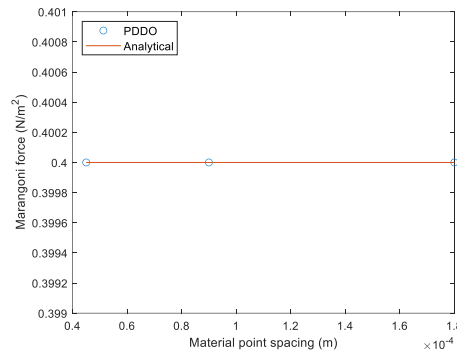
*Fig. 8-19 Marangoni force vectors distributed along the interface with  $\Delta x = 9.0 \times 10^{-5} \text{ m}$ .*

Fig. 8-20 shows the Marangoni force magnitude distribution profile in the horizontal direction at the centre of the simulation domain by using various mesh sizes. It can be noticed that the maximum Marangoni force decreases as the material point spacing increases. The continuum surface force model handles the local Marangoni forces at the fluid interface by applying them to material points in the transition zone between the two fluids. As the horizon size is taken as  $\delta = 3\Delta x$ , material points adjacent to the interface but beyond a horizon size from the interface do not capture surface tension forces. As a result, only three layers of material points on either side of the interface capture the Marangoni force regardless of the spacing chosen. The magnitude distribution of the Marangoni force at these material points is governed by a weighting function that controls the decay of the Marangoni force with increasing distance from the interface.



*Fig. 8-20 Volumetric Marangoni force distribution computed at interfaces of different mesh sizes using PDDO.*

To compare the numerically computed Marangoni force with the analytical solution, Fig. 8-21 presents the integral of the Marangoni force distributed at the three-layer material points along the interface for different spacings between material points. As can be observed, the calculated Marangoni force has a good agreement with the analytical solution despite the spacing between material points being different. Therefore, the presented Marangoni force formulation can accurately capture the Marangoni force due to the temperature gradient.



*Fig. 8-21 Comparison between the PDDO prediction and analytical solution of interfacial Marangoni force.*

### 8.5.5 Two-dimensional Droplet Migration in Thermocapillary Flow

After validating the surface tension formulation in normal direction, the Marangoni force formulation, and heat conduction model, in this case, surface tension in normal and tangential directions are combined to investigate the motion of a droplet in thermocapillary flow. Thermocapillary flow motion was studied in the past decades experimentally and numerically (Young et al., 1959; Balasubramaniam and Chai, 1987;

Wozniak et al., 2001). In this case, the flow motion is simulated by using PDDO. As shown in Fig. 8-22(a), a circular droplet with radius  $R = 0.00144$  m is initially located at the centre of the simulation domain, and it is filled with fluid 1. The density and viscosity coefficient for fluid 1 are set as  $\rho_1 = 250$  kg/m<sup>3</sup> and  $\mu_1 = 0.012$  Pa · s., respectively. The droplet is surrounded by fluid 2 in a square box with a dimension of  $L = W = 0.00576$  m. The density and viscosity coefficient for fluid 2 are specified as  $\rho_2 = 500$  kg/m<sup>3</sup> and  $\mu_2 = 0.024$  Pa · s. In heat conduction model, the specific heat capacity for fluid 1 and fluid 2 is  $c_{p1} = 0.5 \times 10^{-4}$  J/kgK and  $c_{p2} = 1.0 \times 10^{-4}$  J/kgK, respectively. The heat conduction coefficient for fluid 1 and fluid 2 is chosen as  $k_1 = 1.2 \times 10^{-6}$  W/mK and  $k_2 = 2.4 \times 10^{-6}$  W/mK, respectively.

As the incompressible fluid motion is constrained by a weakly compressible equation of state, the numerical speed of sound in the equation of state for each fluid domain is set as  $c_1 = 1.666$  m/s and  $c_2 = 1.178$  m/s, and the material constants are  $\alpha_1 = \alpha_2 = 1$ . The surface tension coefficient is dependent on the temperature as given in Eq.( 8.12 ). The reference surface tension coefficient, reference temperature, and surface tension temperature coefficient are chosen as  $\gamma_0 = 0.01$  N/m,  $T_{\gamma_0} = 290$  K, and  $\frac{d\gamma(T)}{dT} = 0.002$  N/mK.

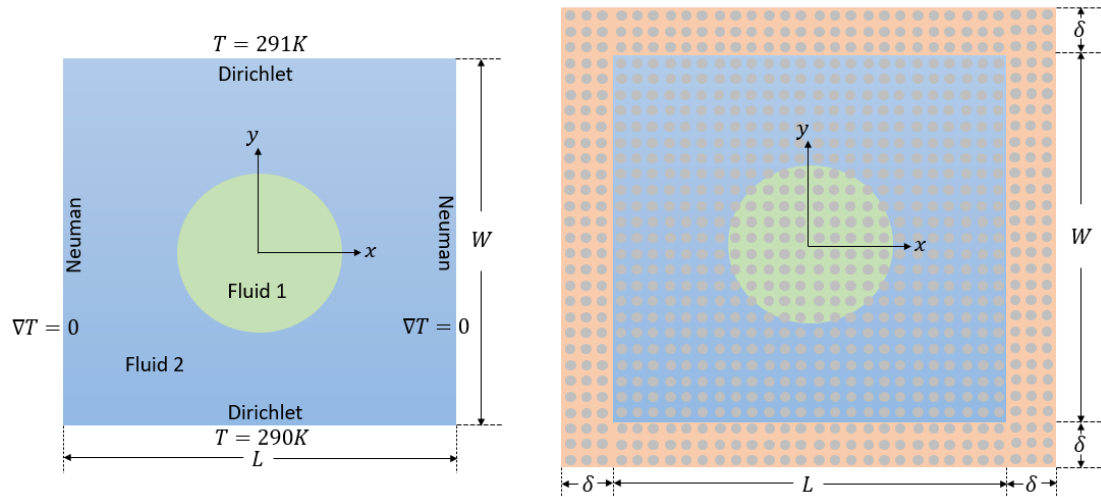


Fig. 8-22 Thermocapillary flow migration (a) geometry (b) PDDO discretisation.

The fluid is initially at rest for which the initial displacement and velocity conditions can be represented as

$$\mathbf{u} = 0, \mathbf{v} = 0 \text{ at } t = 0 \quad (8.137)$$

In addition, a linearly varying temperature profile is initially applied to the fluid domain with temperature gradient  $|\nabla T| = 200 \text{ K/m}$  and points upwards. This can be represented as

$$T(x, y) = |\nabla T| \left( x + \frac{L}{2} \right) \text{ at } t = 0 \quad (8.138)$$

No-slip boundary conditions for velocity are applied to the top and bottom edges of the fluid domain as

$$v_x = v_y = 0 \text{ at } y = -\frac{W}{2}, y = \frac{W}{2} \quad (8.139)$$

Free-slip condition for velocity is applied to the lateral edges of the fluid domain. In addition, a Dirichlet temperature boundary condition is applied on the top and bottom edges of the square box as

$$T = 290 \text{ K at } y = -\frac{W}{2} \quad (8.140)$$

$$T = 291.152 \text{ K at } y = \frac{W}{2}$$

The Neumann boundary condition is applied on the lateral edges of the square box. As represented in Fig. 8-22(b), the fluid domain is wrapped with three layers of material points for implementing the temperature, pressure, and velocity boundary conditions. No-slip and free slip boundary conditions are implemented on these fictitious material points by using Eq.( 8.102 ) - Eq.( 8.133) and the pressure field at fictitious material points is calculated by using Eq.( 8.105 ). In addition, Dirichlet and Neumann temperature boundary condition for fluid domain are implemented by using Eq.( 8.106 ) - Eq.( 8.107 ) for material points at fictitious region.

The fluid domain is discretised with a uniform spacing of  $\Delta x = 9 \times 10^{-5} \text{ m}$  and the horizon size is taken as  $\delta = 3\Delta x$ . The simulation is conducted with a total time of  $t = 0.12 \text{ s}$  and the time step size is chosen as  $\Delta t = 1 \times 10^{-5} \text{ s}$ . Material points shifting technique is implemented, and the constant  $C$  is taken as 0.01. In addition, the density,

pressure, and velocity field are smoothed by moving least square method every 20-time steps.

The interface between the circular droplet and surrounding fluid is subjected to the surface tension force in normal direction. The pressure difference between two fluids maintains the equilibrium of circular shape. The pressure field of the fluid domain at  $t = 0.12$  s is shown in Fig. 8-23. The pressure difference between two fluids interface can be analytically verified by Young-Laplace equation, in which  $\Delta P = 6.944$  N/m<sup>2</sup>. As can be seen from the figure, a good agreement with the analytical value is observed for the pressure difference between fluid 1 and fluid 2.

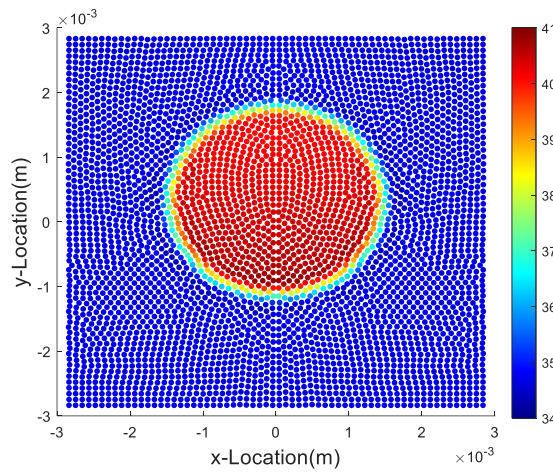


Fig. 8-23 Fluid field pressure distribution at  $t=0.12$  s.

The dimensionless parameters Reynolds number, Marangoni number, and capillary number are used to characterize thermocapillary migration. To compare the result with the Volume of Fluid (VOF) method, the dimensionless parameters are taken as the same as the case presented in the VOF method (Ma and Bothe, 2011). The dimensionless parameters in this case are set as

$$Re = \frac{\rho_2 R U_r}{\mu_2} = 0.72 \quad (8.141)$$

$$Ma = \frac{\rho_2 c_{p2} R U_r}{k_2} = 0.72 \quad (8.142)$$

and

$$Ca = \frac{\mu_2 U_r}{\gamma_0} = 0.0576 \quad (8.143)$$

in which  $U_r$  is the characteristic velocity, and it is being computed as

$$U_r = \frac{\frac{d\gamma(T)}{dT} |\nabla T| R}{\mu_2} = \frac{0.002 \times 200 \times 0.00144}{0.024} = 0.024 \frac{\text{m}}{\text{s}} \quad (8.144)$$

The migration of the circular droplet at different times is provided in Fig. 8-24. To visualise the migration of a droplet, the lowest location of the circular droplet at the initial stage is used as a reference location and presented as a dash line in the figure.

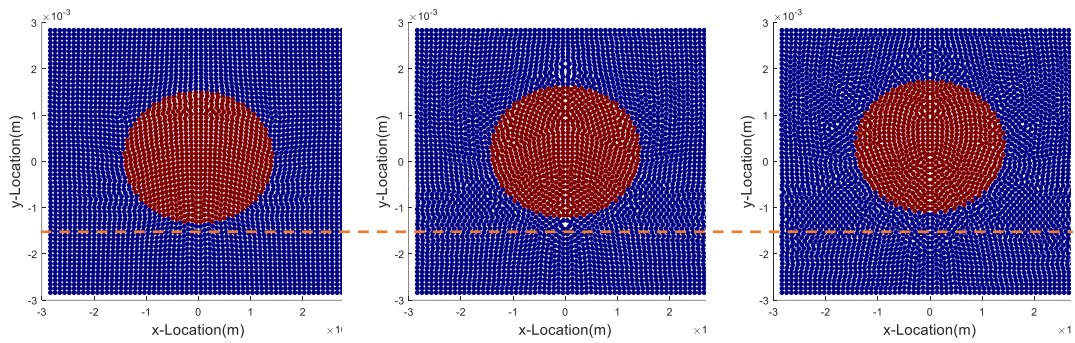
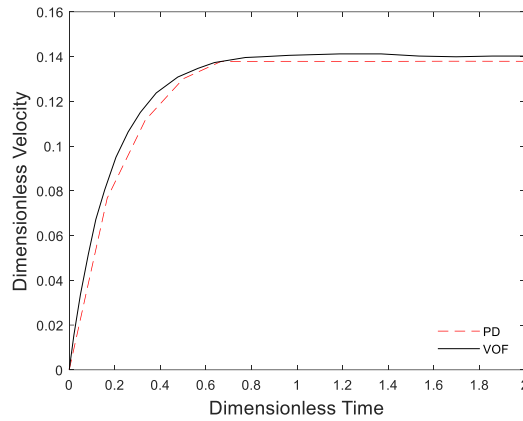


Fig. 8-24 Migration of the droplet at (a)  $t=0.04$  s (b)  $t=0.08$  s (c)  $t=0.12$  s.

The ratio between square box and the radius of the droplet is  $L/R = 4$ . The migration velocity of the circular droplet by using VOF method at this ratio is provided in Ma and Bothe, (2011). The comparison between PDDO method and VOF method for the time evolution of droplet migration velocity is presented in Fig. 8-25. The velocity is non-dimensionalized as  $U^* = U/U_r$ , and the time is non-dimensionalized as  $t^* = t/t_r$  with  $t_r = R/U_r$ . As can be observed from the figure, the migration velocity predicted by using the proposed method has a good agreement with the velocity predicted by using the VOF method.



*Fig. 8-25 Dimensionless velocity of the droplet migration over the dimensionless time.*

The temperature and velocity field of the fluid domain at  $t = 0.12$  s are provided in Fig. 8-26 and Fig. 8-27, respectively. The uneven temperature distribution in Fig. 8-26 causes a temperature gradient across the fluid domain. As a result, tangential forces are created at the interface between fluid 1 and fluid 2. Combining with the viscosity of the fluid, the droplet is pushed to move along the thermal gradient upwards, and the material points within the droplet recirculate along a pair of symmetrical vortices in the circular droplet.

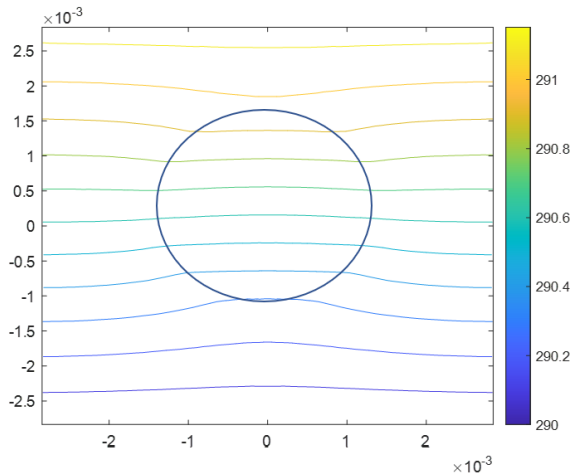


*Fig. 8-26 Isothermal distribution of the fluid domain at  $t=0.12$  s.*

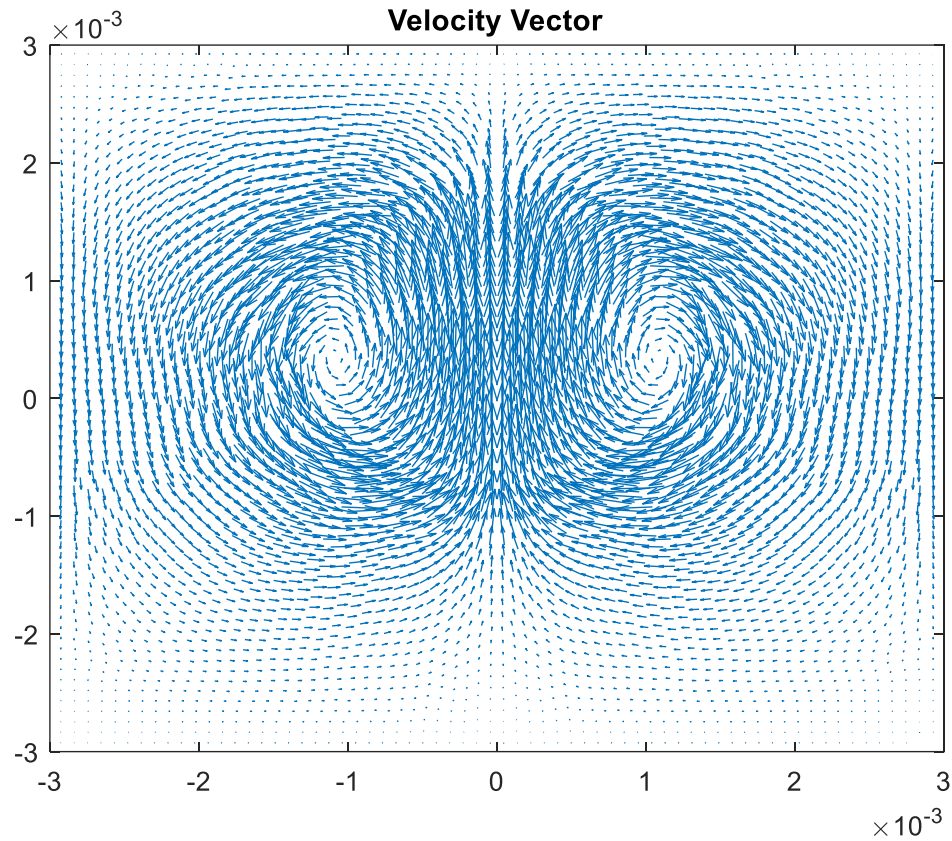


*Fig. 8-27 Velocity profile of the thermocapillary migration of the droplet at  $t=0.12$  s.*

### **8.6 Chapter Summary**

This chapter presents a new non-local surface tension model in multiphase fluid flow through the PDDO. The model considers surface tension in the normal direction, Marangoni forces, and surface wetting. The governing equations of multiphase flow motion are represented using the PDDO. The non-local form of normal surface tension is verified by simulating the deformation of a square droplet. Subsequently, this work explains the handling of the unit normal vector at the triple line region using the static and dynamic behaviour of droplet wetting on solid surfaces. Furthermore, this work validates the accuracy of the newly developed non-local form of the Marangoni force formulation via a heat conduction model. Finally, the normal surface tension and Marangoni forces formulations are simultaneously examined in the multiphase flow by simulating the migration of droplets in thermal capillary flow. A good agreement is observed by analysing the droplet migration speed and comparing the results with existing methods.

## Chapter 9 Conclusion

### 9.1 Achievement of Research Objectives

This thesis aimed to advance and validate peridynamic modelling approaches for simulating AM and welding processes, with a focus on thermomechanical behaviour, phase transformations, and multiphase flow phenomena. The achievement of each research objective is summarised as follows

- Objective 1: To investigate the influence of horizon size in peridynamics and provide optimal selection guidelines for achieving accurate and efficient numerical simulations.

Addressed in Chapter 4, this objective involved a systematic study of horizon size across bond-based, ordinary state-based, and non-ordinary state-based peridynamic formulations. The study of horizon size shows a trade-off between accuracy and computational efficiency. Smaller horizons, such as  $\delta = 1\Delta x$ , reduce the number of interactions per material point and therefore lower computational cost, but they fail to capture nonlocal effects and show poor agreement with FEM. Larger horizons improve accuracy, with optimal results found for  $\delta = 3 - 5\Delta x$  in bond-based and ordinary state-based formulations, while non-ordinary state-based formulations remain accurate at  $\delta = 2\Delta x$ . However, further increases in  $\delta$  provide little improvement in accuracy while increasing computational expense.

- Objective 2: To develop and implement a peridynamic formulation with variable horizon sizes and non-uniform discretisation, thereby reducing numerical simulation time while maintaining accuracy.

Chapter 5 introduced the dual-horizon peridynamics framework, which allows for non-uniform discretisation and variable horizon sizes throughout the computational domain. Through a series of static and dynamic benchmark problems investigation for a two-dimensional plate, practical guidelines for varying horizon sizes were provided. This approach also provides finer resolution where needed while maintaining computational efficiency elsewhere.

- Objective 3: To extend and validate the dual horizon peridynamic formulation for heat transfer analysis, addressing the challenges of non-uniform discretisation in thermal diffusion problems.

Chapter 6 developed a dual-horizon peridynamic formulation for thermal diffusion in non-uniformly discretised domains. Numerical case studies demonstrated that peridynamic predictions closely match temperature distributions and transient responses from FEM simulations. This approach overcomes computational efficiency limitations associated with uniform discretisation, enabling thermal analysis in complex geometries.

- Objective 4: To develop and validate a coupled thermomechanical peridynamic model incorporating phase change, thereby supporting predictive simulation of deformation during AM and welding processes.

In Chapter 7, a coupled thermomechanical peridynamic model was introduced, incorporating phase transformation phenomena such as solidification and melting. The formulation supports the predictive simulation of temperature evolution and structural deformation, including the effects of transient and moving heat sources.

- Objective 5: To extend the peridynamic modelling framework to simulate multiphase flow using a non-local differential operator, thereby improving the analysis of complex interfacial behaviours relevant to AM and welding. The thesis extends peridynamics with the PDDO, enabling meshless simulation of multiphase flows, wetting dynamics, and thermo-capillary (Marangoni) effects. Numerical studies validate the approach, with results demonstrating strong agreement with analytical and reference benchmarks.

## **9.2 Significance and Implications of Research Findings**

This research delivers several significant contributions to the field of computational mechanics and the modelling of advanced manufacturing processes. The systematic investigation of horizon size across multiple peridynamic formulations addresses a longstanding gap in the literature and results in practical guidelines for selecting optimal horizon sizes in engineering simulations.

To overcome the computational intensity of peridynamics relative to classical continuum methods like FEM, this thesis introduces and validates a dual-horizon peridynamic framework. By using non-uniform discretization, efficient large-scale modelling with peridynamics can be achieved while maintaining accuracy. For the first time, the dual-horizon concept is extended to thermal diffusion problems within the peridynamic framework. Numerical results confirm that the dual-horizon model reliably captures temperature fields with close agreement to FEM solutions.

The thesis further advances the field of multiphysics modelling by developing a coupled thermomechanical peridynamic model that incorporates phase changes, such as solidification and melting. This approach captures the interaction between thermal and mechanical fields and can simulate the effects of moving and transient heat sources, as well as latent heat during phase transformation, key features of AM and welding processes.

In the area of multiphase modelling, the introduction of the PDDO-based peridynamic framework allows for meshless simulation of interfacial phenomena, including droplet deformation, dynamic wetting, and Marangoni effects. Validation against analytical solutions and benchmark data demonstrates the accuracy of this approach for problems involving evolving interfaces that challenge traditional methods.

From an applied perspective, these developments provide more reliable predictions of deformation, temperature evolution, and multiphase flow in manufacturing scenarios where traditional numerical methods often struggle. Beyond these direct applications, this study's contributions are also relevant to the emerging field of digital twin technology. The systematic horizon size study improves predictive reliability while thermomechanical and multiphase flow models lay the foundation for integrating peridynamics into the digital twin framework.

Overall, the thesis advances both theoretical understanding and practical implementation of peridynamics, offering modelling tools that support improved process optimisation, defect reduction, and the design of reliable components in AM and welding. Together, these advances allow the creation of accurate and predictive digital replicas of manufacturing processes, supporting real-time monitoring, optimisation, and decision-making in AM and welding.

### 9.3 Limitations and Recommended Future Work

In Chapter 4, the investigation of horizon size was conducted under the assumption of undamaged structures. Under these conditions, the peridynamic solution is expected to converge to the CCM solution as the horizon size approaches zero, allowing analytical and FEM solutions to serve as effective reference solutions for validating peridynamic predictions and determining a suitable horizon size. However, this does not fully capture scenarios involving damage evolution within the material, where the nonlocal characteristics of peridynamics become critical and direct reference solutions may be unavailable. Future research should therefore focus on investigating the influence of horizon size on the prediction of crack initiation, propagation paths, and failure mechanisms.

Since peridynamics has a relatively high computational cost compared to the FEM, this can serve as a barrier to industrial applications. While this thesis demonstrates that the dual-horizon framework can already improve efficiency through non-uniform discretisation, further strategies are needed to make peridynamic simulations viable at an industrial scale. Future work should explore adaptive refinement to concentrate resolution in critical regions, parallel computing and GPU acceleration to reduce solution times, and hybrid FEM-peridynamic coupling to restrict the nonlocal formulation to regions where it is essential. These approaches would reduce computational demands and expand the feasibility of applying peridynamics to large-scale AM and welding problems.

While the coupled thermomechanical peridynamic model developed in this thesis captures key aspects of phase change and deformation during AM and welding, the treatment of material behaviour remains a limitation. The current formulations are based on simplified, primarily isotropic material properties and idealised phase transformation kinetics. However, AM applications increasingly involve functionally graded materials (FGMs), which offer tailored property distributions and enhanced performance. Extending the peridynamic approach to incorporate FGMs in thermomechanical analysis represents a promising direction for future research. This will require the development and validation of constitutive models that can represent gradations in elasticity, thermal conductivity, and phase transformation behaviour,

thereby improving the investigation of residual stress distribution, interface stability, and defect evolution in FGMs produced by AM.

Furthermore, this thesis has presented advanced peridynamic frameworks for thermomechanical analysis in solids (Chapter 7) and thermal-fluid analysis using the PDDO (Chapter 8). These models were developed and applied separately to establish and validate each framework independently, as they address distinct physical mechanisms and numerical challenges. However, the direct coupling between the PDDO-based thermal-fluid approach and peridynamic formulations for solid mechanics has not yet been investigated. As a result, the transition from dynamic melt pool behaviour during heating to subsequent solidification and mechanical response is not fully captured within a unified framework. Future research could focus on developing a fully coupled peridynamic approach that integrates PDDO-based thermal-fluid and bond-based or state-based solid mechanics models. Such an approach could simulate the entire process, from melt pool dynamics under a moving heat source through solidification, to the prediction of residual stresses, deformation, and potential defects in the final material.

Finally, the validation of this work relies primarily on comparisons with FEM and analytical solutions. To further improve the robustness of the models, future work can incorporate experimental measurements. Examples include thermocouple or infrared-based temperature monitoring, digital image correlation for strain fields, and high-speed imaging of melt pool dynamics. Such experimental benchmarks would provide independent validation of peridynamic predictions and support their application in real-world manufacturing scenarios.

In summary, the tools developed in this thesis lay the foundation for practical applications in AM and welding. This framework can be used to simulate melt pool evolution, capture multiphysics interactions, and predict deformation. This capability supports process optimisation and parameter selection, contributing to the development of more reliable and efficient manufacturing processes. Future work will extend this model to complex geometries, FGM materials and validate it with experimental data to confirm its robustness for industrial applications.

## References

- Abdulhameed, O., Al-Ahmari, A., Ameen, W. and Mian, S.H., 2019. Additive manufacturing: Challenges, trends, and applications. *Advances in Mechanical Engineering*, 11(2), p.1687814018822880.
- Adam, G.A. and Zimmer, D., 2015. On design for additive manufacturing: evaluating geometrical limitations. *Rapid Prototyping Journal*, 21(6), pp.662-670.
- Adami, S., Hu, X.Y. and Adams, N.A., 2010. A new surface-tension formulation for multi-phase SPH using a reproducing divergence approximation. *Journal of Computational Physics*, 229(13), pp.5011-5021.
- Adami, S., Hu, X.Y. and Adams, N.A., 2013. A transport-velocity formulation for smoothed particle hydrodynamics. *Journal of Computational Physics*, 241, pp.292-307.
- Al Hamahmy, M.I. and Deiab, I., 2020. Review and analysis of heat source models for additive manufacturing. *The International Journal of Advanced Manufacturing Technology*, 106(3), pp.1223-1238.
- Anderson, T.L., 2005. *Fracture mechanics: fundamentals and applications*. CRC press.
- ANSYS, Inc. (2013) *Mechanical APDL Verification Manual*, Release 15.0. Southpointe: ANSYS, Inc.
- Arrizubieta, J.I., Taberner, I., Ruiz, J.E., Lamikiz, A., Martinez, S. and Ukar, E., 2014. Continuous coaxial nozzle design for LMD based on numerical simulation. *Physics Procedia*, 56, pp.429-438.
- Balasubramaniam, R. and Chai, A.T., 1987. Thermocapillary migration of droplets: An exact solution for small Marangoni numbers. *Journal of colloid and interface science*, 119(2), pp.531-538.
- Batchelor, G.K., 2000. *An introduction to fluid dynamics*. Cambridge university press.
- Belytschko, T., Krongauz, Y., Organ, D., Fleming, M. and Krysl, P., 1996. Meshless methods: an overview and recent developments. *Computer methods in applied mechanics and engineering*, 139(1-4), pp.3-47.
- Bikas, H., Stavropoulos, P. and Chryssolouris, G., 2016. Additive manufacturing methods and modelling approaches: a critical review. *The International Journal of Advanced Manufacturing Technology*, 83(1), pp.389-405.
- Bian, P., Shao, X. and Du, J., 2019. Finite element analysis of thermal stress and thermal deformation in typical part during SLM. *Applied Sciences*, 9(11), p.2231.
- Biot, M.A., 1956. Thermoelasticity and irreversible thermodynamics. *Journal of applied physics*, 27(3), pp.240-253.
- Bird, R.B., 2002. Transport phenomena. *Applied Mechanics Reviews*, 55(1), pp.R1-R4.

- Bobaru, F. and Duangpanya, M., 2012. A peridynamic formulation for transient heat conduction in bodies with evolving discontinuities. *Journal of Computational Physics*, 231(7), pp.2764-2785.
- Brackbill, J.U., Kothe, D.B. and Zemach, C., 1992. A continuum method for modeling surface tension. *Journal of computational physics*, 100(2), pp.335-354.
- Breinlinger, T., Polfer, P., Hashibon, A. and Kraft, T., 2013. Surface tension and wetting effects with smoothed particle hydrodynamics. *Journal of Computational Physics*, 243, pp.14-27.
- Brennan, M.C., Keist, J.S. and Palmer, T.A., 2021. Defects in metal additive manufacturing processes.
- Cano-Lozano, J.C., Bolaños-Jiménez, R., Gutiérrez-Montes, C. and Martínez-Bazán, C., 2015. The use of volume of fluid technique to analyze multiphase flows: Specific case of bubble rising in still liquids. *Applied Mathematical Modelling*, 39(12), pp.3290-3305.
- Chen, Y., Peng, X., Kong, L., Dong, G., Remani, A. and Leach, R., 2021. Defect inspection technologies for additive manufacturing. *International Journal of Extreme Manufacturing*, 3(2), p.022002.
- Christensen, N., 1965. Distribution of temperatures in arc welding. *British Welding Journal*, pp.54-75.
- Cleary, P.W., 1998. Modelling confined multi-material heat and mass flows using SPH. *Applied Mathematical Modelling*, 22(12), pp.981-993.
- Colagrossi, A. and Landrini, M., 2003. Numerical simulation of interfacial flows by smoothed particle hydrodynamics. *Journal of computational physics*, 191(2), pp.448-475.
- Courant, R., Friedrichs, K. and Lewy, H., 1928. Über die partiellen Differenzgleichungen der mathematischen Physik. *Mathematische annalen*, 100(1), pp.32-74.
- De Meo, D., Zhu, N. and Oterkus, E., 2016. Peridynamic modeling of granular fracture in polycrystalline materials. *Journal of Engineering Materials and Technology*, 138(4), p.041008.
- De Meo, D., Russo, L. and Oterkus, E., 2017. Modeling of the onset, propagation, and interaction of multiple cracks generated from corrosion pits by using peridynamics. *Journal of Engineering Materials and Technology*, 139(4), p.041001.
- Dilts, G.A., 1999. Moving-least-squares-particle hydrodynamics—I. Consistency and stability. *International Journal for Numerical Methods in Engineering*, 44(8), pp.1115-1155.

- Dorduncu, M., Kutlu, A., Madenci, E. and Rabczuk, T., 2023. Nonlocal modeling of bi-material and modulus graded plates using peridynamic differential operator. *Engineering with Computers*, 39(1), pp.893-909.
- Eagar, T.W. and Tsai, N.S., 1983. Temperature fields produced by traveling distributed heat sources. *Welding journal*, 62(12), pp.346-355.
- Foster, J.T., Silling, S.A. and Chen, W., 2011. An energy based failure criterion for use with peridynamic states. *International Journal for Multiscale Computational Engineering*, 9(6).
- Gannon, L., 2011. *Effect of welding residual stress and distortion on ship hull structural performance* (Doctoral dissertation, Dalhousie University).
- Gao, Y. and Oterkus, S., 2019. Nonlocal numerical simulation of low Reynolds number laminar fluid motion by using peridynamic differential operator. *Ocean Engineering*, 179, pp.135-158.
- Gao, Y. and Oterkus, S., 2020. Multi-phase fluid flow simulation by using peridynamic differential operator. *Ocean Engineering*, 216, p.108081.
- Gerstle, W., Silling, S., Read, D., Tewary, V. and Lehoucq, R., 2008. Peridynamic simulation of electromigration. *Comput Mater Continua*, 8(2), pp.75-92.
- Goldak, J., 1985. A double ellipsoid finite element model for welding heat sources. *IIW Doc. No.*, 212.
- Goldak, J., Chakravarti, A. and Bibby, M., 1984. A new finite element model for welding heat sources. *Metallurgical transactions B*, 15(2), pp.299-305.
- Grenier, N., Le Touzé, D., Colagrossi, A., Antuono, M. and Colicchio, G., 2013. Viscous bubbly flows simulation with an interface SPH model. *Ocean Engineering*, 69, pp.88-102.
- Gu, X., Madenci, E. and Zhang, Q., 2018. Revisit of non-ordinary state-based peridynamics. *Engineering fracture mechanics*, 190, pp.31-52.
- Guski, V., Verestek, W., Oterkus, E. and Schmauder, S., 2020. Microstructural investigation of plasma sprayed ceramic coatings using peridynamics. *Journal of Mechanics*, 36(2), pp.183-196.
- Haleem, A. and Javaid, M., 2019. Additive manufacturing applications in industry 4.0: a review. *Journal of Industrial Integration and Management*, 4(04), p.1930001.
- Hirt CW, Nichols BD (1981) Volume of fluid (VOF) method for the dynamics of free boundaries. *J Comput Phys* 39(1):201–225
- Hoang, D.A., van Steijn, V., Portela, L.M., Kreutzer, M.T. and Kleijn, C.R., 2013. Benchmark numerical simulations of segmented two-phase flows in microchannels using the Volume of Fluid method. *Computers & Fluids*, 86, pp.28-36.

- Hopp-Hirschler, M., Shadloo, M.S. and Nieken, U., 2018. A smoothed particle hydrodynamics approach for thermo-capillary flows. *Computers & Fluids*, 176, pp.1-19.
- Hu, H. and Argyropoulos, S.A., 1996. Mathematical modelling of solidification and melting: a review. *Modelling and Simulation in Materials Science and Engineering*, 4(4), p.371.
- Incropera, F.P., DeWitt, D.P., Bergman, T.L. and Lavine, A.S., 1996. *Fundamentals of heat and mass transfer* (Vol. 6, p. 116). New York: Wiley.
- Jiji Latif, M., 2009. Heat conduction. *Berlin and Heidelberg: Springer-Verlag*.
- Katz-Demyanetz, A., Popov Jr, V.V., Kovalevsky, A., Safranchik, D. and Koptioug, A., 2019. Powder-bed additive manufacturing for aerospace application: Techniques, metallic and metal/ceramic composite materials and trends. *Manufacturing review*, 6.
- Kilic, B. and Madenci, E., 2010. An adaptive dynamic relaxation method for quasi-static simulations using the peridynamic theory. *Theoretical and Applied Fracture Mechanics*, 53(3), pp.194-204.
- Lapidus, L. and Pinder, G.F., 1999. *Numerical solution of partial differential equations in science and engineering*. John Wiley & Sons.
- Liao, Y., Liu, L., Liu, Q., Lai, X., Assefa, M. and Liu, J., 2017. Peridynamic simulation of transient heat conduction problems in functionally gradient materials with cracks. *Journal of Thermal Stresses*, 40(12), pp.1484-1501.
- Liu, X., He, X., Wang, J., Sun, L. and Oterkus, E., 2018. An ordinary state-based peridynamic model for the fracture of zigzag graphene sheets. *Proceedings of the Royal Society A: Mathematical, Physical and Engineering Sciences*, 474(2217), p.20180019.
- Luo, Z. and Zhao, Y., 2018. A survey of finite element analysis of temperature and thermal stress fields in powder bed fusion Additive Manufacturing. *Additive Manufacturing*, 21, pp.318-332.
- Ma, C. and Bothe, D., 2011. Direct numerical simulation of thermocapillary flow based on the volume of fluid method. *International Journal of Multiphase Flow*, 37(9), pp.1045-1058.
- Madenci, E. and Oterkus, E., 2013. Peridynamic theory. In *Peridynamic theory and its applications* (pp. 19-43). New York, NY: Springer New York.
- Madenci, E. and Oterkus, S., 2016. Ordinary state-based peridynamics for plastic deformation according to von Mises yield criteria with isotropic hardening. *Journal of the Mechanics and Physics of Solids*, 86, pp.192-219.
- Madenci, E. and Oterkus, S., 2017. Ordinary state-based peridynamics for thermoviscoelastic deformation. *Engineering Fracture Mechanics*, 175, pp.31-45.

- Madenci, E., Dorduncu, M., Barut, A. and Futch, M., 2017. Numerical solution of linear and nonlinear partial differential equations using the peridynamic differential operator. *Numerical Methods for Partial Differential Equations*, 33(5), pp.1726-1753.
- Madenci, E., Barut, A. and Futch, M., 2016. Peridynamic differential operator and its applications. *Computer Methods in Applied Mechanics and Engineering*, 304, pp.408-451.
- Madenci, E., Dorduncu, M. and Gu, X., 2019. Peridynamic least squares minimization. *Computer Methods in Applied Mechanics and Engineering*, 348, pp.846-874.
- Meier, C., Fuchs, S.L., Hart, A.J. and Wall, W.A., 2021. A novel smoothed particle hydrodynamics formulation for thermo-capillary phase change problems with focus on metal additive manufacturing melt pool modeling. *Computer Methods in Applied Mechanics and Engineering*, 381, p.113812.
- Mohanavel, V., Ali, K.A., Ranganathan, K., Jeffrey, J.A., Ravikumar, M.M. and Rajkumar, S.J.M.T.P., 2021. The roles and applications of additive manufacturing in the aerospace and automobile sector. *Materials Today: Proceedings*, 47, pp.405-409.
- Morris, J.P., Fox, P.J. and Zhu, Y., 1997. Modeling low Reynolds number incompressible flows using SPH. *Journal of computational physics*, 136(1), pp.214-226.
- Morris, J.P., 2000. Simulating surface tension with smoothed particle hydrodynamics. *International journal for numerical methods in fluids*, 33(3), pp.333-353.
- Nguyen, C.T., Oterkus, S., Oterkus, E., Amin, I., Ozdemir, M., El-Aassar, A.H. and Shawky, H., 2021. Modelling of Eulerian incompressible fluid flows by using peridynamic differential operator. *Ocean Engineering*, 239, p.109815.
- Ning, J., Sievers, D.E., Garmestani, H. and Liang, S.Y., 2019. Analytical thermal modeling of metal additive manufacturing by heat sink solution. *Materials*, 12(16), p.2568.
- Oterkus, E., Guven, I. and Madenci, E., 2010, June. Fatigue failure model with peridynamic theory. In *2010 12th IEEE intersociety conference on thermal and thermomechanical phenomena in electronic systems* (pp. 1-6). IEEE.
- Oterkus, E., Guven, I. and Madenci, E., 2012. Impact damage assessment by using peridynamic theory. *Open Engineering*, 2(4), pp.523-531.
- Oterkus, E. and Madenci, E., 2012, April. Peridynamics for failure prediction in composites. In *53rd AIAA/ASME/ASCE/AHS/ASC Structures, Structural Dynamics and Materials Conference 20th AIAA/ASME/AHS Adaptive Structures Conference 14th AIAA* (p. 1692).

- Oterkus, S., Fox, J. and Madenci, E., 2013, May. Simulation of electro-migration through peridynamics. In *2013 IEEE 63rd electronic components and technology conference* (pp. 1488-1493). IEEE.
- Oterkus, S., Madenci, E., Oterkus, E., Hwang, Y., Bae, J. and Han, S., 2014, May. Hygro-thermo-mechanical analysis and failure prediction in electronic packages by using peridynamics. In *2014 IEEE 64th electronic components and technology conference (ECTC)* (pp. 973-982). IEEE.
- Oterkus, S., Madenci, E. and Agwai, A., 2014. Fully coupled peridynamic thermomechanics. *Journal of the Mechanics and Physics of Solids*, *64*, pp.1-23.
- Oterkus, S., Madenci, E. and Agwai, A., 2014. Peridynamic thermal diffusion. *Journal of Computational Physics*, *265*, pp.71-96.
- Oterkus, S., Madenci, E. and Oterkus, E., 2017. Fully coupled poroelastic peridynamic formulation for fluid-filled fractures. *Engineering geology*, *225*, pp.19-28.
- Paskual, A., Álvarez, P. and Suárez, A., 2018. Study on arc welding processes for high deposition rate additive manufacturing. *Procedia Cirp*, *68*, pp.358-362.
- Placidi, L., 2016. A variational approach for a nonlinear one-dimensional damage-elasto-plastic second-gradient continuum model. *Continuum Mechanics and Thermodynamics*, *28*(1), pp.119-137.
- Placidi, L. and Barchiesi, E., 2018. Energy approach to brittle fracture in strain-gradient modelling. *Proceedings of the Royal Society A: Mathematical, Physical and Engineering Sciences*, *474*(2210), p.20170878.
- Reddy, J.N., 2013. *An introduction to continuum mechanics*. Cambridge university press.
- Ren, H., Zhuang, X., Cai, Y. and Rabczuk, T., 2016. Dual-horizon peridynamics. *International Journal for Numerical Methods in Engineering*, *108*(12), pp.1451-1476.
- Ren, H., Zhuang, X. and Rabczuk, T., 2017. Dual-horizon peridynamics: A stable solution to varying horizons. *Computer Methods in Applied Mechanics and Engineering*, *318*, pp.762-782.
- Rosenthal, D., 1941. Mathematical theory of heat distribution during welding and cutting. *Welding journal*, *20*(5), pp.220s-234s.
- Rumman, R., Lewis, D.A., Hascoet, J.Y. and Quinton, J.S., 2019. Laser metal deposition and wire arc additive manufacturing of materials: An overview. *Archives of Metallurgy and Materials*, pp.467-473.
- Russell, M.A., Souto-Iglesias, A. and Zohdi, T., 2018. Numerical simulation of Laser Fusion Additive Manufacturing processes using the SPH method. *Computer Methods in Applied Mechanics and Engineering*, *341*, pp.163-187.

- Schoinochoritis, B., Chantzis, D. and Salonitis, K., 2017. Simulation of metallic powder bed additive manufacturing processes with the finite element method: A critical review. *Proceedings of the Institution of Mechanical Engineers, Part B: Journal of Engineering Manufacture*, 231(1), pp.96-117.
- Sepe, R., Greco, A., De Luca, A., Caputo, F. and Berto, F., 2021. Influence of thermo-mechanical material properties on the structural response of a welded butt-joint by FEM simulation and experimental tests. *Forces in Mechanics*, 4, p.100018.
- Shravan, C., Radhika, N.N.H.D.K., Deepak Kumar, N.H. and Sivasailam, B., 2023. A review on welding techniques: properties, characterisations and engineering applications. *Adv. Mater. Process. Technol*, 10, pp.1126-1181.
- Silling, S.A., 2000. Reformulation of elasticity theory for discontinuities and long-range forces. *Journal of the Mechanics and Physics of Solids*, 48(1), pp.175-209.
- Silling, S.A. and Askari, E., 2005. A meshfree method based on the peridynamic model of solid mechanics. *Computers & structures*, 83(17-18), pp.1526-1535.
- Silling, S.A., Epton, M., Weckner, O., Xu, J. and Askari, E., 2007. Peridynamic states and constitutive modeling. *Journal of elasticity*, 88(2), pp.151-184.
- Silling, S.A., 2017. Stability of peridynamic correspondence material models and their particle discretizations. *Computer Methods in Applied Mechanics and Engineering*, 322, pp.42-57.
- Sola, A. and Nouri, A., 2019. Microstructural porosity in additive manufacturing: The formation and detection of pores in metal parts fabricated by powder bed fusion. *Journal of Advanced Manufacturing and Processing*, 1(3), p.e10021.
- Spagnuolo, M., Barcz, K., Pfaff, A., Dell'Isola, F. and Franciosi, P., 2017. Qualitative pivot damage analysis in aluminum printed pantographic sheets: numerics and experiments. *Mechanics Research Communications*, 83, pp.47-52.
- Strieby, S.F., 2024. Operationalizing Metal Additive Manufacturing for Expeditionary Employment by the United States Marine Corps.
- Taşdemir, A. and Nohut, S., 2021. An overview of wire arc additive manufacturing (WAAM) in shipbuilding industry. *Ships and Offshore Structures*, 16(7), pp.797-814.
- Tofail, S.A., Koumoulos, E.P., Bandyopadhyay, A., Bose, S., O'Donoghue, L. and Charitidis, C., 2018. Additive manufacturing: scientific and technological challenges, market uptake and opportunities. *Materials today*, 21(1), pp.22-37.
- Thompson, S.M., Bian, L., Shamsaei, N. and Yadollahi, A., 2015. An overview of Direct Laser Deposition for additive manufacturing; Part I: Transport phenomena, modeling and diagnostics. *Additive Manufacturing*, 8, pp.36-62.
- Underwood, P., 1983. Computational methods for transient analysis. *Dynamic relaxation*, pp.245-265.

- Udaykumar, H.S., Mittal, R. and Shyy, W., 1999. Computation of solid–liquid phase fronts in the sharp interface limit on fixed grids. *Journal of computational physics*, 153(2), pp.535-574.
- Van Elsen, M., Baelmans, M., Mercelis, P. and Kruth, J.P., 2007. Solutions for modelling moving heat sources in a semi-infinite medium and applications to laser material processing. *International Journal of heat and mass transfer*, 50(23-24), pp.4872-4882.
- Vastola, G., Zhang, G., Pei, Q.X. and Zhang, Y.W., 2016. Controlling of residual stress in additive manufacturing of Ti6Al4V by finite element modeling. *Additive Manufacturing*, 12, pp.231-239.
- Vazic, B., Oterkus, E. and Oterkus, S., 2020. In-plane and out-of plane failure of an ice sheet using peridynamics. *Journal of Mechanics*, 36(2), pp.265-271.
- Voller, V.R., Swaminathan, C.R. and Thomas, B.G., 1990. Fixed grid techniques for phase change problems: a review. *International journal for numerical methods in engineering*, 30(4), pp.875-898.
- Wang, L.J., Xu, J.F. and Wang, J.X., 2016. The Green's functions for peridynamic non-local diffusion. *Proceedings of the Royal Society A: Mathematical, Physical and Engineering Sciences*, 472(2193), p.20160185.
- Warren, T.L., Silling, S.A., Askari, A., Weckner, O., Epton, M.A. and Xu, J., 2009. A non-ordinary state-based peridynamic method to model solid material deformation and fracture. *International Journal of Solids and Structures*, 46(5), pp.1186-1195.
- Wong, K.V. and Hernandez, A., 2012. A review of additive manufacturing. *International scholarly research notices*, 2012(1), p.208760.
- Wozniak, G., Balasubramaniam, R., Hadland, P.H. and Subramanian, R.S., 2001. Temperature fields in a liquid due to the thermocapillary motion of bubbles and drops. *Experiments in fluids*, 31(1), pp.84-89.
- Xu, R., Stansby, P. and Laurence, D., 2009. Accuracy and stability in incompressible SPH (ISPH) based on the projection method and a new approach. *Journal of computational Physics*, 228(18), pp.6703-6725.
- Xue, T., Zhang, X. and Tamma, K.K., 2018. A two-field state-based peridynamic theory for thermal contact problems. *Journal of Computational Physics*, 374, pp.1180-1195.
- Yang, H. and He, Y., 2010. Solving heat transfer problems with phase change via smoothed effective heat capacity and element-free Galerkin methods. *International Communications in Heat and Mass Transfer*, 37(4), pp.385-392.

Yang, L., Hsu, K., Baughman, B., Godfrey, D., Medina, F., Menon, M. and Wiener, S., 2017. *Additive manufacturing of metals: the technology, materials, design and production* (Vol. 1). Cham: Springer.

Yang, Q., Zhang, P., Cheng, L., Min, Z., Chyu, M. and To, A.C., 2016. Finite element modeling and validation of thermomechanical behavior of Ti-6Al-4V in directed energy deposition additive manufacturing. *Additive Manufacturing*, 12, pp.169-177.

Young, N.O., Goldstein, J.S. and Block, M., 1959. The motion of bubbles in a vertical temperature gradient. *Journal of Fluid Mechanics*, 6(3), pp.350-356.

Zhang, A., Sun, P. and Ming, F., 2015. An SPH modeling of bubble rising and coalescing in three dimensions. *Computer Methods in Applied Mechanics and Engineering*, 294, pp.189-209.